Universitat Autònoma de Barcelona

Synthesis, Characterization and Nanostructuration of D–A systems based on Fc-PTM dyads

by

Dayana Morales Acosta

Doctoral Thesis
Programa de Doctorat en Ciència de Materials

Directors

Prof. Jaume Veciana and Dr. Imma Ratera
Institut de Ciència de Materials de Barcelona

Tutor

Dr. Cristina Palet
Departament de Química, Universitat Autònoma de Barcelona

Departament de Química
Facultad de Ciènces

January 2015

Memòria presentada per aspirar al Grau de Doctor per:

Dayana Morales Acosta

Vist i plau,

Els directors:

Prof. Jaume Veciana
Research Professor

Dr. Imma Ratera
Tenured Scientist

a Bellaterra, February 2, 2015

DECLARATION

I hereby declare that the work carried out in this Doctoral Thesis has not been previously submitted for any degree and is no currently being submitted in candidature for any other degree.

Signed .....
Dayana Morales Acosta
Candidate

The work of this Doctoral Thesis was carried out by the candidate at the Institut de Ciéncia de Materials de Barcelona under our supervision. Also, we certify that we have read this Doctoral Thesis and that, in our opinion, it is fully adequate in scope and quality as a Doctoral Thesis for the degree of Doctor of Philosophy.

Signed .....
Prof. Jaume Veciana
Research Professor
Institut de Ciència de Materials de Barcelona

Signed .....
Dr. Imma Ratera
Tenured Scientist
Institut de Ciència de Materials de Barcelona

Signed .....
Dr. Cristina Palet
Chemistry department
Universitat Autònoma de Barcelona

There are only two days in the year when nothing can be done. One is called yesterday and the other is called tomorrow, so today is the right day to love, believe, do and mostly live.

Dalai Lama

ACKNOWLEDGMENTS

El camino recorrido hasta hoy ha sido largo y la meta no se hubiese cumplido sin el apoyo, la confianza y el soporte científico y/o emocional de muchas personas. Por eso quiero agradecer en primer lugar a mi Padre Dios, por la vida y la salud a lo largo de todos estos años, por cada oportunidad que me ha dado, cada puerta que ha abierto, cada lágrima que ha enjugado con su amor, aún por las pruebas y las dificultades. Este trabajo demuestra que Dios es un Dios de pactos y que siempre cumple sus promesas, a Él la gloria y el honor.

En el ámbito académico quiero agradecer infinitamente a la Dr. Imma Ratera, quien apenas conociéndome supo ver en mí la capacidad para desarrollar este trabajo, gracias por la apertura que siempre me ha dado, por su dirección profesional y sus consejos personales. Sin su guía no hubiese sido posible desarrollar ésta tesis y menos aún verla plasmada en éste manuscrito. Gracias Imma por las puertas abiertas que siempre mantuviste para mí, por tu comprensión y tu esfuerzo porque yo sea cada día mejor y alcance ésta meta.

También quiero agradecer al Prof. Jaume Veciana y a la Prof. Concepciò Rovira por la oportunidad que me dieron de formar parte de su grupo de investigación, gracias por las palabras tan sabias que en su día supieron transmitirme, palabras que talvez no las terminaba de entender pero que hoy puedo decir con certeza, cuánta razón tenían!. Muchas gracias Dr. Imma y Prof. Jaume por el tiempo y la dedicación que han invertido en la edición de ésta tesis.

Al trabajar con estos sistemas dadores-aceptores se me dió la oportunidad de conocer y trabajar en el mundo de las técnicas de caracterización basadas en luz sincrotrón. Todo el conocimiento y la experiencia que adquirí no habrían sido posibles sin las valiosas explicaciones y soporte científico de los doctores Virginia Pérez y Carlos Escudero, científicos de línea (NAPP) en ALBA. Así como también gracias al Dr. Robert Acres ex-científico de línea (Materials Science) in ELETTRA y a la Prof. Maddalena Pedio. Gracias a todos por cada uno de los turnos de trabajo

que realizamos y por su gran colaboración.

También estoy muy agradecida con las personas que han colaborado en las medidas de potencial de superficie y conductividad de las SAMs presentadas en este trabajo, gracias al Dr. Makos Paradinas y a Li Yuan; así como también a la personas de los servicios internos y externos de caracterización: Amable, Vega, Guillaume y Daniel Gamarra.

Quiero agradecer a dos personas cuyos trabajos han significado la base y el soporte de ésta investigación, gracias Judit por tu legado y gracias Manel por tu colaboración. Finalmente, mi agradecimiento a todas las personas del grupo Nanomol quienes de una u otra manera han formado parte de ésta experiencia de vida. Mi eterna gratitud para Dolores, Estela, Paula, Lourdes y Elena por haber sido las amigas que necesité en tiempos difíciles, gracias por el tiempo compartido, las risas, los cafés, en una palabra gracias chicas por su AMISTAD.

El financiamiento de éstos cuatro años de beca pre-doctoral quiero agradecer a a la Secretaría de Educación Superior, Ciencia, Tecnología e Innovación (SENESCYT - Ecuador). También quiero hacer extensivo mi agradecimiento a la Universidad Técnica de Ambato y a la Facultad de Ciencia e Ingeniería en Alimentos, representadas por sus antiguas y actuales autoridades: Ing. Luis Amoroso, Dr. Galo Naranjo, Ing. Romel Rivera y Dr. Jacqueline Ortiz. Gracias por el contrato de auspicio.

A mi padre César y a mi tío Iván quiero agradecerles por la confianza depositada en mí al firmar una “carta en blanco" como garantía, estaré en deuda por siempre con ustedes!.

Agradece a la llama su luz, pero no olvides el pie del candil que paciente la sostiene

Rabindranath Tagore (1861-1941) Filósofo y escritor indio

La vida no me alcanzaría para agradecer a quienes han significado mi verdadero soporte e impulso cada día. Gracias a mis padres, César y Clarita por las bendiciones que desde Ecuador me enviaron día tras día. Gracias porque a pesar de lo que representó nuestra distancia siempre crearon el viento favorable para que

mis alas se desplieguen y yo pueda volar tan alto como mis sueños me llevasen. A ustedes les debo lo que soy y lo que he alcanzado!! A mis abuelitos Nahúm y Berthita porque han sido mis segundos padres, siempre pendientes de mí y apoyándome en todo. A mis pequeñas: Mary, Beli y Joce, por el amor incondicional, la alegría, la inocencia y la fortaleza que me han transmitido. A mi amado esposo Freddy, con quien inicié esta aventura, este sueño, este reto. Gracias amor por pacientemente estar a mi lado, cuidarme, animarme y nunca dejar de repetirme que crees en mí. La vida unió nuestros caminos y tú uniste nuestras vidas! Gracias por todo tu apoyo. A Martita y Estuardo†, por tener siempre una sonrisa y una bendición para mí. A mis tíos, tías, primos y primas, especialmente a quienes me supieron recibir como a hija durante mis visitas.

Finalmente quiero dar las gracias a Mn. Bruno, a la hermana Mercedes y a todas las personas que siempre me han tenido en sus oraciones.

MUCHAS GRACIAS A TOD@S, éste triunfo también les pertenece.

Research funded by:

SUMMARY

This Thesis is centered in the field of multifunctional molecular materials and more specifically in the area of molecular electronics. The work is focused on the design, synthesis and nanostructuration of molecular materials based on donor–acceptor (D–A) open-shell systems.

In general, in this work it has been studied how the electronic properties of D–A molecules are modified when moving from the tridimensionality (3D) of solution and crystals to the bidimentionality (2D) obtained when the dipolar molecules are oriented and nanostructured on a metallic surface as self-assembled monolayers (SAMs). Moreover, the influence of the electronic open-shell nature of such D–A molecules on the overall electronic properties of the oriented nanostructured system has been also evaluated.

Modulating and controlling the response given by multifunctional molecular materials by applying external stimuli is one of the foremost motivations in the field of micro- and nanoelectronics. Bistability is the extreme manifestation of the non-linear response of the material to an external stimulus and is only supported in systems with strong cooperative interactions and therefore it is a rare phenomenon in molecular materials. On the other hand, the possibility to switch a bistable molecular material between states having strikingly different properties by application of external stimuli opens the way to the development of molecular-based switches and memories. In this regard, the first part of the work is devoted to the study of the temperature and solvent induced electronic bistability phenomena in 3D (solution and crystals) of D–A systems based on ferrocene electron donor units bonded covalently to a polychlorotriphenylmethyl radical acceptor unit through an ethylenic spacer (Fc–PTM) in solution and also in solid state. Specifically, the role of the donor strength of the ferrocene moiety in the switchable intramolecular electron transfer phenomena where coexist neutral (D–A) and zwitterionic (D^+–A^-) states that show different magnetic and optical properties has been evaluated. It

has been demonstrated that with the methylation of the Fc units that enhances their donor-ability a higher percentage of the zwitterionic state in comparison with the non-methylated Fc–PTM dyad was found in solid state. In solution, it was demonstrated that playing with the polarity of the solvent it is possible to stabilize one (neutral) or other (zwitterionic) electronic state and more interestingly, using solvents with intermediate polarity like acetone or THF it was observed the coexistence of both stable electronic states.

The second part of the Thesis is focused on the use of different approaches to get bidimiensional nanostructuration of Fc–PTM D–A molecules on gold surfaces, as SAMs, to study its electronic properties. Initially, a two-steps approach has been used which after a lot of effort it was concluded that was not robust enough for further reliable electronic characterization. Then, the work moves to the use of a one-step approach, for the nanostructuration of D–A molecules on metallic substrates, which succeeded. All the SAMs were characterized using different surface analysis techniques like polarization-modulation infrared reflection adsorption spectroscopy (PM-IRRAS), X-ray photoelectron spectroscopy (XPS), time-of-flight secondary ions mass spectrometry (ToF-SIMS), contact angle (CA), atomic force microscopy (AFM) and cyclic voltammetry (CV). The stability of these SAMs was probed specially by CV measurements.

To get further insight into the electronic structure of such SAMs of molecular oriented dipoles on surfaces, synchrotron radiation techniques (PES, RPES and NEXAFS) have been used. The influence of the open-shell electronic structure of dyad **1** over the electronic properties of 2D nanostructures has been analysed in comparison to the closed-shell electronic structure of **1H**. We conclude that the dimensionality of the Fc–PTM D–A system determine its electronic properties and behavior. In fact, while in 3D structures, the bistability phenomena takes place thanks to cooperative intermolecular electrostatic interactions, with the experiments performed using external stimuli (solvent, T) to modify the electronic state of the 2D nanostructures (SAMs) no bistability was observed.

Oriented dipoles on surfaces are interesting molecular systems due to the possibility they offer to modify the surface potential of metallic electrodes of molecular electronic devices improving their performances. In this regard, the surface potential related with the work function (WF) of these SAMs, **S1** and **S1-H** have been studied by Kelvin Probe Force Microscopy (KPFM) showing for both cases an increase in the WF of the gold substrates used. The lower modification of the WF caused by the open-shell SAM **S1** in comparison with **S1-H** has been attributed to a higher effect of depolarization due to its larger polarizability. This effect gives place to a modification of its energy levels in order to preserve the equilibrium and stabilize the energy of the system formed by 2D oriented dipoles.

In the field of molecular electronics, there is a great interest in finding D−A molecules that are one way conductors and thus, can be used as rectifiers of electric current. In this regards, the last part of the Thesis has been devoted to the transport measurements of these D−A SAMs junctions of the type Au-SAM//Ga_2O_3/EGaIn. The studied rectifying molecule, Fc−PTM, was designed so that electrical conduction within it would be favored from the electron-rich subunit or moiety (electron donor) to an electron-poor moiety (electron acceptor), but disfavored (by several electron volts) in the reverse direction. The current measurements have shown that junctions based on the open-shell **S1** SAM have a high current density but do not rectify. However, junctions based on the closed-shell **S1-H** SAM show a lower current density at ±1.0 V but when the energy barrier imposed by the LUMO of the system is overcome at −2.0 V it rectifies, showing an interesting rectification ratio of 10^2.

Contents

List of Abbreviations

A Acceptor

4–ATP 4–Aminothiophenol

AES Auger Electron Spectroscopy

AFM Atomic Force Microscopy

BE Binding Energy

CA Contact Angle

CE Counter Electrode

CPD Contact Potential Difference

CT Charge Transfer

CV Cyclic Voltammetry

D Donor

D–A Donor–Acceptor

2D Two-Dimensions

3D Three-Dimensions

DMF *N N*-Dimethylformamide

DMSO Dimethyl Sulfoxide

EPR Electron Paramagnetic Resonance

ESR Electron Spin Resonance

Fc Ferrocene

Fc–PTM Ferrocene–Polychlorotriphenylmethyl

FET Field Effect Transistor

HIB Hole-Injection Barrier

HOMO Highest Occupied Molecular Orbital

HR-XPS High Resolution X-ray Photoelectron Spectroscopy

IET Intramolecular Electron Transfer

IP Ionization Potential

IR Infrared

IRRAS Infrared Reflection Adsorption Spectroscopy

KE Kinetic Energy

KPFM Kelvin Probe Force Microscopy

LED Light-Emitting Diode

LUMO Lowest Unoccupied Molecular Orbital

MALDI–TOF Matrix-Assisted Laser Desorption Ionization Time-of-Flight mass spectrometry

MCBJ Mechanically Controllable Break Junction

MO Molecular Orbital

M–S Metal–Sulfur

N Neutral

n-$\mathbf{Bu_4NPF_6}$ Tetrabutylammonium Hexafluorophosphate

NDR Negative Differential Resistance

NEXAFS Near-Edge X-ray Absorption Fine Structure spectroscopy

NIR Near-Infrared

NMR Nuclear Magnetic Resonance

OLED Organic Light Emitting Diode

PEDOT:PSS Poly(3,4-ethylenedioxythiophene)-poly(styrenesulfonate)

PES Photoemission Spectroscopy

PM–IRRAS Polarization-Modulation Infrared Reflection Adsorption Spectroscopy

PTM Polychlorotriphenylmethyl radical

QCM Quartz Crystal Microbalance

RE Reference Electrode

RF Radio-Frequency

RPES Resonant Photoemission Spectroscopy

SAM Self-assembled monolayer

SECO Secondary electron cut-off

SERS Surface-enhanced Raman scattering

SPR Surface Plasmon Resonance

SR Synchrotron radiation

STM Scanning Tunneling Microscopy

SUMO Singly Unoccupied molecular Orbital

TBAH Tetrabutylammonium hydroxide

TBAHFP Tetrabutylammonium Hexafluorophosphate

THF Tetrahydrofuran

TLC Thin layer chromatography

TMOF Trimethyl orthoformate

ToF–SIMS Time-of-flight secondary ion mass spectrometry

UHV Ultra-high vacuum

UPS Ultraviolet Photoemission Spectroscopy

UV–Vis–NIR Ultraviolet-visible-near-infrared spectroscopy

VB Valence band

WE Working electrode

XPS X-ray Photoelectron Spectroscopy

Z Zwitterionic

He who lives without discipline dies without honor

Icelandinc proverb

1

Introduction and Objectives

Everything in our environment is made by matter and energy. Every single day we are in contact with a huge variety of materials which make our life more comfortable. Such materials range from basic (i.e. clothes, appliances, food packaging, etc.) to complex (i.e. electronic devices) and there is no doubt that they have revolutionized our lives. We live in a technological era in which it is fundamental the development and understanding of new materials to further control and tune their properties.

In this framework, the development of computing and electronic devices has been one of the most developed areas in the last decades. In fact, the field of integrated electronics starts being active in the late 1950s[1] and the invention of the first junction transistor dates back to 1947[2]. In 1965 Gordon Moore, the co-founder of Intel, observed that the number of transistors per cm^2 of silicon doubled every year[1]. This statement is known as the "Moore's Law". Later, in 1975 this statement was revised by Moore to state that chip densities would double every 2 years[2]. From that moment, the reduction in size of the electronic components and also the increase in speed have been two of the foremost motivations of this field.

In the effort to make electronic components smaller and smaller in size, fundamental limits both in materials and processes currently used, are faced. Therefore, new processes and new materials need to be developed to extend the functionality of integrated circuits. It is this motivation that leads to the scientist community to focus on more fundamental components like are the molecules[2]. In effect, the eminent physics and visionary Richard Feynman in 1959 during his lecture entitled "There Plenty of Room at the Bottom already proposed shrinking computing devices toward their physical limits, where "wires should be 10 or 100 atoms in diameter, and the circuits should be a few thousand angstroms across[3]. At that moment, a new field of research was predicted: nanoscience and nanotechnology.

In the last decades, nanoscience and nanotechnology have emerged as promising fields to provide fundamental understanding of phenomena taking place in materials through the research at the atomic and molecular level which lead to the discovery of novel properties and functionalities[4]. Thus, significant advances have been observed in the development of new materials and processes at the nanoscale, as well as in the study and understanding of their properties. However, there is still a lot to do in this young research field. In order to move forward in this interdisciplinary field of research it is necessary the active collaboration of chemists, physicists, materials scientists, and electrical and chemical engineers.

Although nanoscience and nanotechnology are considered a modern research field, from a chemistry point of view, nanomaterials are anything but new[5]. However, advances in synthetic chemistry and in methods for the investigation and manipulation of individual or small ensembles of molecules, together with the capability to predict and analyze these systems have produced major advances in the field of molecular materials. Such advances, have facilitated the development of new materials and phenomena[5] that can be used for the fabrication of sustainable and low-cost molecular sized electronic components allowing to control and process signals[6,7]. These molecular materials show interesting properties that may differ very significantly from those of the corresponding bulk materials[5].

In fact, multifunctional molecular nanomaterials are considered materials that constitute basic building blocks for the fabrication of complex devices that

exploit desired functions. They can be used for several applications in diverse fields like: electronics, optoelectronics, information processing, catalysis, biomedical science, environmental science, energy conversion and storage, advanced defense technologies, among others[8]. In this context, molecular electronics is an emerging area of science focused on the development of new materials that show unique properties thanks to their nanoscale (at least one of their dimensions below 100 nm)[8]. Molecular electronics can be broadly defined as the technology that uses single or small groups of molecules to perform electronic functions[2].

In the last years, molecular materials have become a very active filed of research in materials science, as prove some existing devices that are commercially available such as organic light emitting diodes (OLED) or organic solar cells. Molecular materials are constituted by purely organic or metal-organic building blocks that can be easily obtained and modified by conventional synthetic methods. Thus, different functional groups can be introduced in a single molecule which can lead to molecule-based materials exhibiting two or more properties at the same time (electrical, optical and/or magnetic), introducing in this way a great versatility over the conventional inorganic materials. Moreover the properties of such molecular materials can be easily modulated and tuned by small structural modification of their chemical skeletons.

In this context, the design and synthesis of new molecules to be used as nanomaterial in a device must take into account three important issues. First, the properties of the individual molecule which correspond to those of isolated molecules either in a dilute solution, in a matrix, or on a surface. Second, the interaction between these molecules and how they affect the properties of its supramolecular structure (discrete ensembles of molecules). Finally, the interface with the outside world, which means the way to give inputs (i.e. energy or charge) and read the output characteristic of the device[5]. On the other hand, any molecular electronic candidate must meet certain basic requirements such as: *i)* show chemical stability, *ii)* be inert with respect to other molecules of the same type specially for devices involving charge-storage or redox-active molecules, *iii)* show reversible electron transfer from one element to the next, *iv)* make possible to exchange information

through the interaction with an interface, both on a microscopic and macroscopic level[2] and *v)* to be cost-effi cient[8]. All these requirements present challenges that need to be overcome before such materials can be used in real applications which is the framework of the research field of molecular nanomaterials.

For the fabrication of molecular nanomaterials, two complementary strategies can be used, the so called "top-down" or the "bottom-up". In the top-down approach, materials are generated by carving nanomaterials out of bulk materials or by breaking down a complex entity into its component parts. In contrast, the bottom-up approach is based on fabricating nanomaterials out of independent individual building blocks[9] (Figure 1.1). Given that the bottom-up approach is likely to become an integral part of nanomaterials manufacture, understanding each individual molecular building blocks, its structure, assembly process, properties and dynamic behavior is of real importance[9]. In particular, the chemical self-assembly or spontaneous organization of molecules to form ordered and well defined nanostructures thanks to the intermolecular forces (Figure 1.1). In general this is a simple and low cost process which can cover from the nano to the micrometer scale making the idea attractive from a technological point of view. In fact, this is the reason why during the last two decades much effort has been done in structuring matter by bottom-up self-assembling processes, one of the most promising fields of research in nanoscience and molecular materials.

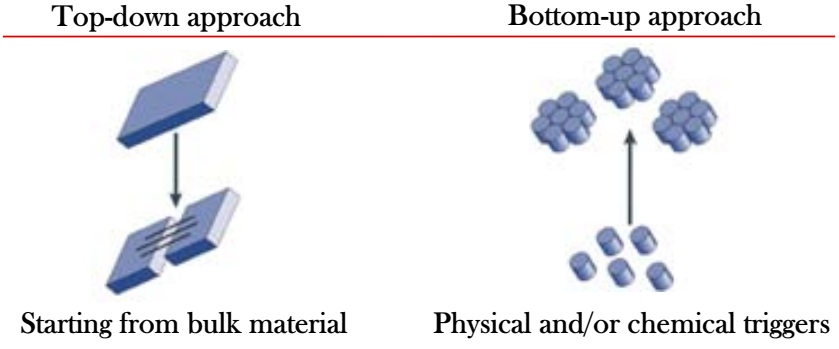

Figure 1.1: Approaches used for the fabrication of molecular nanomaterials[10].

Then, molecular self-assembly (Figure 1.2) is a powerful process for fabricating novel supramolecular architectures with unavailable properties from disordered systems of pre-existing molecules by controlling specific, local interactions among

the components themselves[8]. In fact, this process is present everywhere in the natural world, for instance lipid molecules form oil drops in water; four hemoglobin polypeptides form a functional tetrameric hemoglobin protein; ribosomal proteins and RNA coalesce into functional ribosomes[9]. Molecular self-assembly is driven by weak, noncovalent bonds (hydrogen bonds), ionic bonds (electrostatic interactions), hydrophobic interactions, van der Waals interactions, and water-mediated hydrogen bonds. Such bonds are relatively insignificant in isolation but when combined together as a whole, they govern the conformation of supramolecular structures[9]. As mentioned before, self-organization phenomena play an important role in the assembling of macroscopic structures with specific desired properties which can be exploited for the integration of different classes of nanaomaterials in devices[8].

Specially, self-assembled monolayers (SAMs) are a unique class of nanostructured mate- rials, formed by molecular assemblies through spontaneous adsorption of organic molecules on a substrate, with properties determined by their lattice structures and interactions with the substrate and environment[8,11–16]. Formation of SAMs take place through different steps[17] as it is represented in Figure 1.2. The process starts with the physisorption of the molecules present in solution, followed by the chemical interaction of the molecules with the surface atoms through their binding groups forming strong covalent bonds after a few minutes.

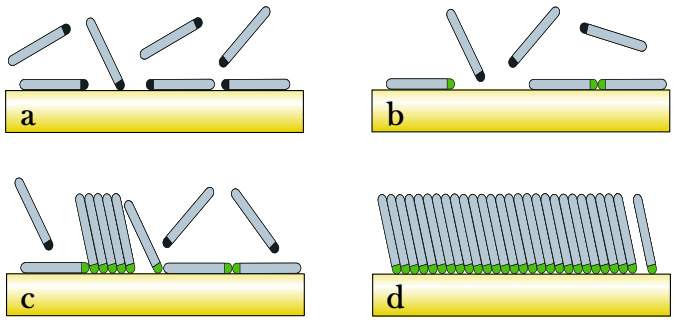

Figure 1.2: Scheme of the steps that take place during the self-assembly process of alkanethiols on Au: *a)* physisorption, *b)* lying down phase formation, *c)* nucleation of the standing up phase, and *d)* standing up phase[17].

The growth process of the monolayer comes with the nucleation of islands containing lying down molecules which finally grow increasing the surface coverage

to obtain a well packed monolayer with standing up molecules, in an ideal case. SAMs have been used to study interface phenomena, modification of the properties of different surfaces, modification of the work function of electrodes to favour the charge injection in electronic devices, molecular recognition, fabrication of nanodevices, among others. The study of these nanostructured materials is of fundamental importance due to the nonadditive, collective behaviors that usually appear in molecular materials as a result of intermolecular interactions[18].

In the effort to study, manipulate, understand and control the properties of nanostructured materials in the last decades, new and very sensitive techniques have been developed opening the door to the nanoworld. The techniques that allow the study of nanoscale objects are known as surface analysis techniques and can be roughly divided in microscopic techniques, like Scanning Tunneling Microscopy (STM) or Atomic Force Microscopy (AFM) and spectroscopic techniques such as: X-ray Photoelectron Spectroscopy (XPS), Auger Electron Spectroscopy (AES), Polarization-Modulation Infrared Reflection Adsorption Spectroscopy (PM-IRRAS), among others. In fact, in order to characterize and understand materials at the nanoscale usually more than one of these techniques is needed.

As we have previously mentioned, the properties of the same molecule structured in a different dimensionality can be very different. For instance, the same molecular unit in a tridimensional (3D) arrangement, in solution or in a crystal can present very different properties than the same unit forming a self-assembly monolayer (Figure 1.3).

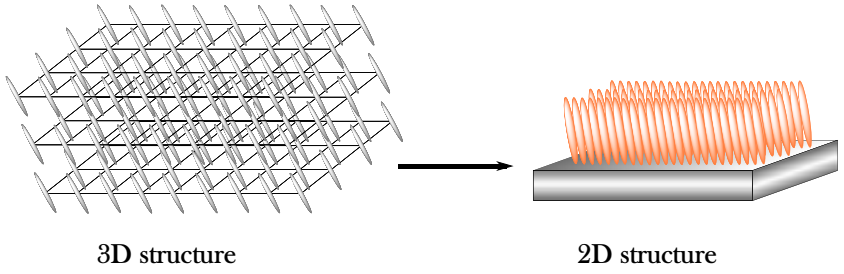

Figure 1.3: Schematic representation of 3D and 2D molecular structures.

In this way, new and interesting phenomena can be observed due to the change of dimensionality which can be used in different fields as previously men-

tioned. Thus, studying how the properties and characteristics of a multifunctional organic material change when passing from the bulk to the nanoscale, results very interesting to make a step forward towards molecular electronics.

1.1 Objectives

This Thesis will be focused on the design, synthesis and nanostructuration of molecular materials based on electron donor–acceptor (D–A) open-shell systems. The general objective will be the study of the electronic properties of multifunctional molecular systems based on an electronic donor unit linked to an electronic open-shell acceptor unit that shows interesting magnetics, electric and optic properties; when the systems pass from 3D (solution or crystal phase) to 2D (nanostructured self-assembled monolayers). In particular, the following specific objectives have been considered:

- Study the electronic bistability phenomena in bulk (3D) of D–A systems based on a ferrocene electron donor unit bonded to a polychlorotriphenylmethyl radical acceptor unit through an ethylenic spacer (Fc–PTM) in solution and in solid (crystalline) state induced by the solvent or the temperature, respectively. Specifically, the role of the donor strength of the ferrocene electron donor moiety in the bistability phenomena will be evaluated.

- Study different approaches to obtain robust bidimensional (2D) nanostructuration, as self-assembled monolayers (SAMs), of Fc–PTM open-shell derivatives on gold substrates.

- Study the electronic properties of SAMs of Fc–PTM open-shell molecules by different surface analysis techniques. To get further insight into the electronic structure of such molecular oriented dipoles on surfaces, synchrotron radiation will be used. Also the study of any possible temperature or solvent induced bistability of the molecular systems once nanostructured as SAM on gold is carried out.

- Study the capacity of surface potential or work function modification of the Fc−PTM open-shell SAMs in comparison with its closed-shell structure using two complementary techniques: Kelvin Probe Force Microscopy (KPFM) and Ultraviolet Photoemission Spectroscopy (UPS).

- Study the electron transport through these Fc−PTM, D−A SAMs using EGaIn top electrodes and analysis of the influence of the open-shell electronic structure on the mechanism of conduction and the possible rectification.

Bibliography

[1] B. G. E. Moore, "Cramming more components onto integrated circuits," *Electronics*, vol. 38, no. 8, 1965.

[2] R. L. Carroll and C. B. Gorman, "The genesis of molecular electronics.," *Angewandte Chemie*, vol. 41, no. 23, pp. 4378–400, 2002.

[3] R. P. Feynman, "Plenty of Room at the Bottom," 1959.

[4] H.-E. Schaefer, *Nanoscience: The Science of the Small in Physics, Engineering, Chemistry, Biology and Medicine.* Springer-Verlag Berlin Heidelberg, 2010.

[5] A. C. Grimsdale and K. Müllen, "The chemistry of organic nanomaterials.," *Angewandte Chemie*, vol. 44, no. 35, pp. 5592–629, 2005.

[6] B. Albinsson, M. P. Eng, K. Pettersson, and M. U. Winters, "Electron and energy transfer in donor-acceptor systems with conjugated molecular bridges.," *Physical chemistry chemical physics*, vol. 9, no. 44, pp. 5847–64, 2007.

[7] T. P. Radhakrishnan, "Molecular structure, symmetry, and shape as design elements in the fabrication of molecular crystals for second harmonic generation and the role of molecules-in-materials.," *Accounts of chemical research*, vol. 41, no. 3, pp. 367–76, 2008.

[8] Y. Yin and D. Talapin, "The chemistry of functional nanomaterials.," *Chemical Society reviews*, vol. 42, no. 7, pp. 2484–7, 2013.

[9] S. Zhang, "Fabrication of novel biomaterials through molecular self-assembly.," *Nature biotechnology*, vol. 21, no. 10, pp. 1171–8, 2003.

[10] G. a. Silva, "Neuroscience nanotechnology: progress, opportunities and challenges.," *Nature reviews. Neuroscience*, vol. 7, no. 1, pp. 65–74, 2006.

[11] C. D. Bain, E. B. Troughton, Y.-T. Tao, J. Evall, G. M. Whitesides, and R. G. Nuzzo, "Formation of monolayer films by the spontaneous assembly of organic thiols from solution onto gold," *Journal of American Chemical Society*, vol. 111, pp. 321–335, 1989.

[12] P. E. Laibinis, J. J. Hickman, M. S. Wrighton, and G. M. Whitesides, "Orthogonal Self-Assembled Monoalyers: Alkanethiols on Gold and Alkane Carboxylic Acids on Alumina," *Science*, vol. 245, pp. 845–847, 1989.

[13] P. E. Laibinis, G. M. Whitesides, D. L. Allara, Y.-T. Tao, A. N. Parikh, and R. G. Nuzzo, "Comparison of the Structures and Wetting Properties of Self-Assembled Monolayers of n-Alkanethiols on the Coinage Metal Surfaces, Cu, Ag, Au," *Journal of American Chemical Society*, vol. 113, pp. 7152–7167, 1991.

[14] P. E. Laibinis and G. M. Whitesides, "*w*-Terminated Alkanethiolate Monolayers on Surfaces of Copper, Silver, and Gold Have Similar Wettabilities," *Journal of the American Chemical Society*, vol. 114, pp. 1990–1995, 1992.

[15] A. Ulman, "Formation and Structure of Self-Assembled Monolayers.," *Chemical reviews*, vol. 96, no. 4, pp. 1533–1554, 1996.

[16] J. C. Love, L. a. Estroff, J. K. Kriebel, R. G. Nuzzo, and G. M. Whitesides, "Self-assembled monolayers of thiolates on metals as a form of nanotechnology.," *Chemical reviews*, vol. 105, pp. 1103–69, 2005.

[17] C. Vericat, M. E. Vela, G. Benitez, P. Carro, and R. C. Salvarezza, "Self-assembled monolayers of thiols and dithiols on gold: new challenges for a well-known system.," *Chemical Society reviews*, vol. 39, no. 5, pp. 1805–34, 2010.

[18] A. Painelli and F. Terenziani, "Multielectron Transfer in Clusters of Polar-Polarizable Chromophores," *Journal of American Chemical Society*, vol. 125, pp. 5624–5625, 2003.

Watch your thoughts, for they become words. Watch your words, for they become actions. Watch your actions, for they become habits. Watch your habits, for they become character. Watch your character, for it becomes your destiny

Lao Tzu

2

Bistability phenomenon in Fc–PTM radical dyads: the role of the electron donor strength

2.1 Introduction

Multifunctional molecular materials have found an important development in modern materials science due to their extraordinary versatility. They offer the possibility to give high functionality (reduced weight, flexibility, and transparency) and easy processing allowing to cover large areas of manufacturing with low costs which has already been exploited in the field of organic electronic and optoelectronic devices[1,2].

The interesting properties of multifunctional molecular materials can have two different origins: molecular and/or supramolecular. The first one is related to the inherent molecular composition, like: the kind of atoms and functional groups, bridges, electron donor or acceptor units, etc.; while the second one depends on the structural composition like: the packing, weak interactions, cooperative forces, etc[3]. So, new properties can be obtained from the precise balance of these two origins. Playing with both, the chemical composition and the arrangement of the

molecules in one, two or three dimensions it is possible to tune the properties of the solid material or address new and desired electrical, optical, magnetic or biological properties[4,5].

2.1.1 Donor–Acceptor systems

Different molecular materials, whose electronic structure can change as a function of an external stimulus applied (light, temperature, pressure, potential, etc.) have been reported in the literature[6,7]. Dyads formed by donor (D) and acceptor (A) units covalently linked through an organic bridge are important systems that allow to study interesting phenomena related with their potential use as components of integrated molecular-sized devices[8].

D–A systems are interesting materials due to the possibility they offer to obtain different chemical and physical properties associated to the two degenerated electronic states of the molecules, which are induced by the intramolecular electron transfer (IET) between the redox-active units as a consequence of an external perturbation, such as photons, temperature or pressure. These molecular materials show high sensitivity to the environment, and the interconversion between the two localized electronic structures (neutral and zwitterionic) can be reversible[9] under specific conditions, as shown Figure 2.1.

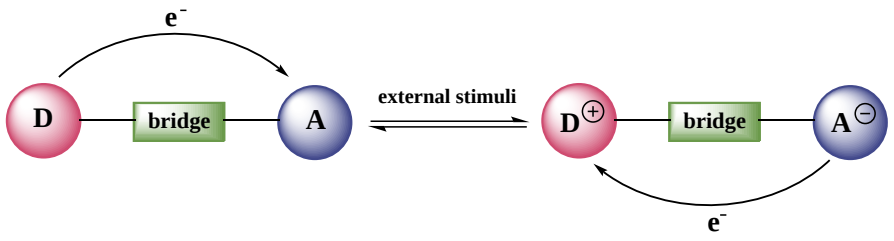

Figure 2.1: Schematic representation of D–A dyads in neutral and zwitterionic state.

The aforementioned electronic states: neutral and zwitterionic, can coexist if the difference in energy between them is small and when cooperative intermolecular interactions such as: electrostatic, $\pi-\pi$, hydrogen bonding, etc. are present. The equilibrate coexistence of these two different electronic states is defined by the bistability phenomenon in which the relative population of the states can be

tuned by changing the external conditions and is not easy to find in molecular materials[10,11].

Then, several molecules can be used as building blocks in D–A systems, which differ in both chemical nature and complexity but share common characteristics like the possibility to transfer one or more electrons from one unit to the other in a reversible way when an external stimulus is applied and the possibility to modulate their properties (electronic, optic or magnetic) according to the electronic state adopted (neutral or zwitterionic)[12].

2.1.2 Building Blocks

In the framework of this work, two building blocks will be used to form the D–A dyads; ferrocene derivatives as electron donors and the polychlorotriphenylmethyl radical as electron acceptor. The principal characteristics of each building block will be described hereafter.

Ferrocene is an organometallic compound that belongs to the metallocene family and it has been the first pure hydrocarbon derivative of iron prepared[13]. It is formed by two cyclopentadienyl rings bounded by strong covalent interactions, on opposite sides, to a central iron atom situated symmetrically between them with aromatic character[14]. Moreover, ferrocene (Fc) is stable to air, moisture and can be heated up to 470 °C. It can be exposed to strong conditions (boiling in concentrated hydrochloric acid or caustic soda) without decomposition; showing an extraordinary stability[13]. Due to its structure, Fc behaves like an aromatic electron-rich organic compound[15], and thanks to its redox capacity, it can be oxidized (loss one electron) at low potentials. The oxidized specie obtained, the ferricinium, which present an open-shell character, can be reduced back to ferrocene in a reversible way (Figure 2.2).

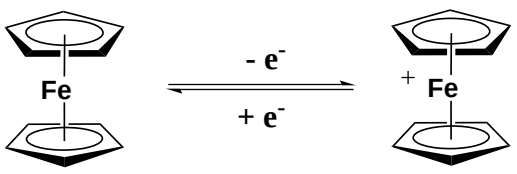

Figure 2.2: Reversible redox process of the Fc.

In this compound there are eighteen electrons available (but not necessary used) for iron to carbon binding, five π–electrons of each cyclopentadienyl unit, plus the eight electrons of the iron atom[16]. Thanks to the very versatile chemistry of this compound, numerous ferrocene derivatives have been synthesized through different reactions such as the Friedel-Craft reaction or lithiation processes followed by the introduction of several functional groups such as phosphines or silanes[11].

The redox potential of the ferrocene can be tuned playing with the type of substituents binding to the cyclopentadienyl rings and their electron-donor facility. Using electron withdrawing groups (e.g. carboxylic acids), the redox potential can be shifted towards the anodic direction (more positive values) while electron releasing groups (e.g. methyl) shift the potential in the opposite direction (more negative values). Thus, it will be easier to oxidize a methylated-ferrocene derivative than an unsubstituted one. Moreover, as ferrocene and ferricinium species present different magnetic moments, the magnetic property could be used as an output characteristic of an electrochemical switch with this compound opening the way to information storage applications.

On the other hand, a radical is an atom, ion or molecule that has a single unpaired valence electron and therefore presents an open-shell structure. Most of radicals are unstable exhibiting extremely short half-lives under normal laboratory conditions and are highly reactive towards other substances, or even towards themselves (dimerization or polymerization), which difficult their study. Then, obtaining persistent radical compounds is necessary to study their interesting properties and potential uses in order to develop new materials from molecules with a net electronic *spin* giving place to paramagnetic behavior[17]. In this sense, in order to build free radicals with thermal and chemical stabilities, resonance and steric hindrance have to be taken into account[18] along the design and synthesis. This steric hindering around the radical center, physically difficult the reactivity of the radical conferring it stability.

The perchlorotriphenylmethyl radical (PTM) was firstly described by Ballester *et al.*[18]. In a general way, the PTM radicals are neutral organic radicals composed by three partially or totally chlorinated benzene rings connected to a central car-

bon atom (α−carbon) with a sp^2 hybridization. The large persistence of the PTM radicals is conferred by the steric shield of the central trivalent carbon atom due to the presence of the bulky chlorine atoms in *ortho* positions. Such stability is reflected toward aggressive chemical species and typical radical reagents as well as thermally in solid state; withstanding temperatures up to 300 °C in air without significant decomposition. For all these reasons, the half-lives of these radicals are of the order of decades, being called *inert free radicals*[17,18]. Figure 2.3 shows the molecular structure of the PTM radical.

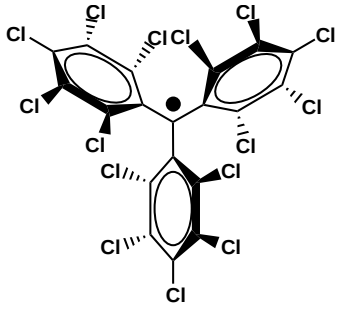

Figure 2.3: Molecular structure of the PTM radical.

PTM radicals are also electroactive species and can be oxidized to perchlorotriphenylcarbonium ion or reduced to perchlorotriphenylcarbanion[19]. The steric protection conferred by the chlorine atoms also confers stability to the cationic and anionic species which have good stability toward oxygen. Thus, the cyclic voltammetry of the perchlorotriphenylmethyl radical showed in Figure 2.4, presents one oxidation and one reduction processes from which two stable ionic species are formed in a easy and reversible way, the cation and the anion, respectively. The small formal potential observed for the reduction of the PTM radical indicates that this process is more favoured in comparison to the oxidation; being a good electron acceptor unit.

Different magnetic and optical properties characterize the PTM radical and its anionic specie; thus, while the PTM radical is a paramagnetic (S = 1/2) specie with its maximum absorbance centered at 385 nm and fluorescence emission at 688 nm; the anion is diamagnetic (S = 0), with maximum absorbance around 510 nm and does not emit fluorescence[20]. These different properties make this family of molecules excellent building blocks for applications in charge storage

memory devices where the optical and magnetic responses can be used as read-output signals[20–22].

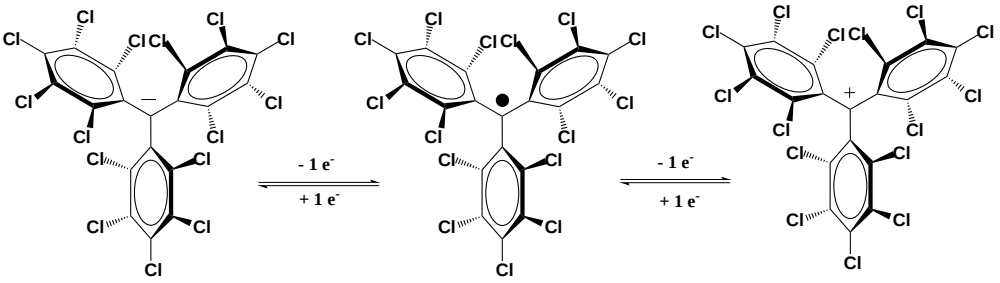

(a)

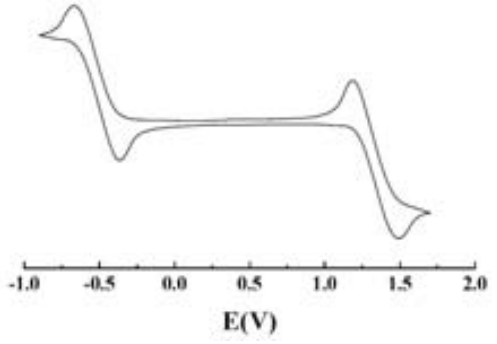

(b)

Figure 2.4: (a) Reversible redox processes of the PTM radical and its ionic species; and (b) cyclic voltammogram of the PTM in a CH_2Cl_2 solution of $Bu_4N^+PF_6^-$ [0.1 M] vs. Ag/AgCl.

The great stability, together with the interesting properties that show the Fc and the PTM radical as electron donor and electron acceptor unit, respectively, have made these building blocks to be considered in our group to develop new D–A systems giving place to promising molecular materials. However, before any real application can be visualized, a comprehensive and thorough knowledge of these systems is mandatory, together with the understanding of the influence of the environment and forces that are present at a supramolecular level to their properties.

2.1.3 Bistability phenomenon in Fc–PTM dyads

D–A systems based on a Fc moiety linked through a conjugated vinylene bridge to the PTM radical have been synthesized by Elsner *et al.*[23] few years ago.

The monoradical **2** is shown in Figure 2.5. These kind of dyads are interesting for both their magnetic properties and also their intramolecular electron transfer (IET) phenomena which can be studied from the charge transfer (CT) bands in the near-infrared (NIR) region of the absorption spectra.

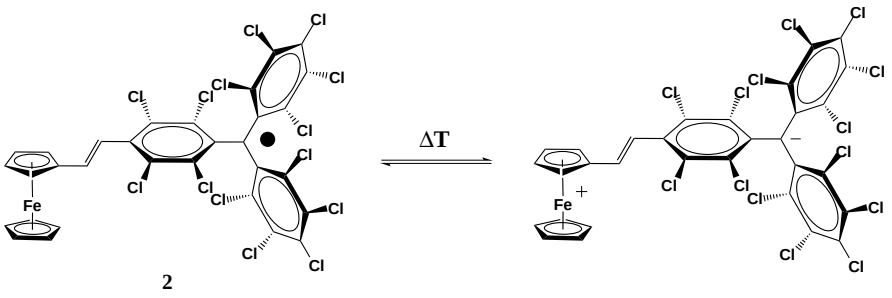

Figure 2.5: Dyad **2** in its neutral form (left) and zwitterionic state (right).

The optical absorption study of dyad **2** was performed by Ratera *et al.*[8]. Three main bands were observed at 387, 442 and 500 nm; the first intense band is characteristic of the PTM radical while the two following weak bands have been assigned to π–bridge–PTM acceptor CT band. Focusing in the NIR region (Figure 2.6), an intense broad band due to the IET process from the Fc unit to the radical was observed around 1000 nm.

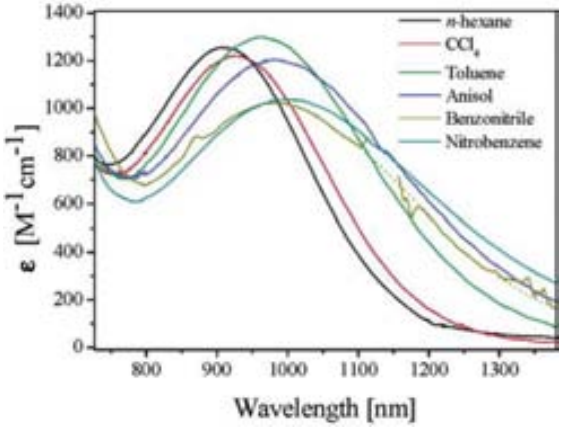

Figure 2.6: IET band of dyad **2** in solvents with different polarity.

This absorption band (shape and maximum position) is strongly solvent dependent and show positive solvtochromism (varying from 892 nm in n–hexane to 1003 nm in DMSO) with the charge-separated excited state more stabilized in polar solvents and thus showing less intense CT absorption bands.

The reversible interconversion between the two electronic isomers of dyad **2** (neutral and zwitterionic) in crystalline solid state was found to be thermally induced[24]. From Mössbauer spectroscopy performed in the temperature range of 293 to 4.2 K reported in Figure 2.7, it is possible to observe that the typical quadrupole doublet of Fc appears at the lowest temperature (4.2 K).

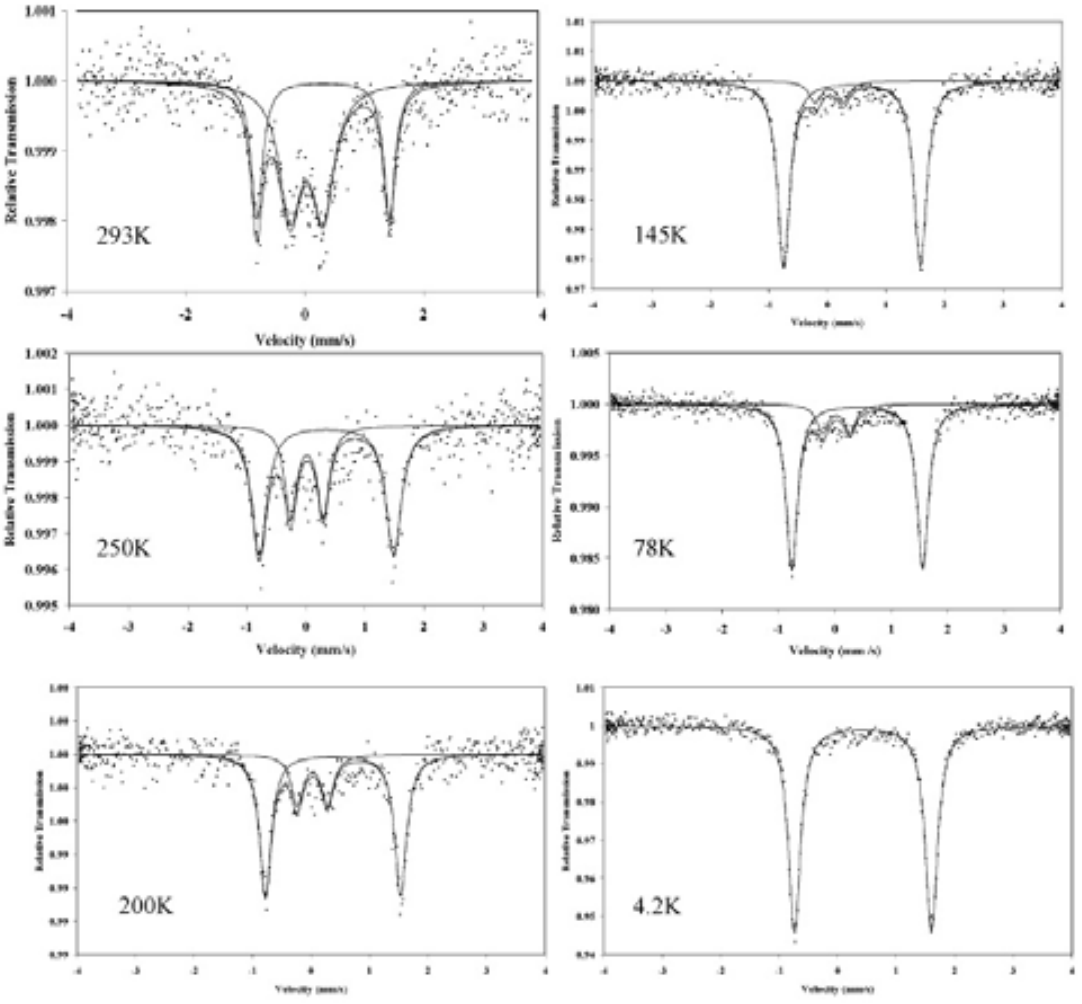

Figure 2.7: ^{57}Fe Mössbauer spectra of dyad **2** at different temperatures.

However a new quadrupole doublet characteristic of the ferricinium cation appears as the temperature increases; indicating that the electron transfer from the Fc to the PTM radical is induced. The critical temperature (T_C) at which there are almost equal amounts of both electronic isomers is found to be near to room-temperature (293 K) which is very interesting if we want to think about further applications of this molecular system.

2.1.4 The role of electrostatic intermolecular interactions

Since molecular materials are promising candidates for new and revolutionary applications, the possibility to handle interpretative tools that guide the synthetic routes from molecular to supramolecular level represents a great challenge to devise the relationships between the supramolecular structure and the properties of the material[25].

As result of intermolecular interactions like dispersion forces and intermolecular charge-transfer interactions, nonadditive-collective behavior appears in molecular materials. In fact, it was suggested by Krugler *et al.*[26] that electronic structures of the molecules can vary in a great manner when they are considered in the crystal lattice or as isolated molecules due to the presence of strong intermolecular electronic interactions[26].

Thus, important collective and cooperative effects are expected in polar and polarizable molecules. In this line, Terenziani and Painelli[25] presented a simple and very interesting model for clusters of polar and polarizable molecules where only classical electrostatic intermolecular interactions are taken into consideration[27]. In this model, each molecular unit is described in terms of a two-state model, which re- presents the simplest picture to describe polar molecules; and it is based on the Mulliken model which has been originally proposed to describe D–A CT complexes in solution[28].

To understand electrostatic interactions is necessary to take into account that each molecule in the material experiences the local electric field generated by the surrounding molecules in a significant feedback mechanism that is responsible for large collective and cooperative effects[25]. Moreover, the large dependence of the molecular polarity on supramolecular interactions give place to collective effects in the ground state. As a consequence of the large molecular polarizability of push-pull chromophores, the surrounding medium like the solvent can be used to tune the polarity of such molecules[29,30]. The authors extend this concept to supramolecular interactions in molecular materials and demonstrate that such interactions can widely tune the molecular polarity, and eventually lead it across the neutral-zwitterionic interface. Thus, molecular materials have the possibility to

support true phase transitions i.e. from the neutral to the zwitterionic state driven by cooperative interactions[25].

The essential "two- and three-states" model for Fc–PTM dyads

Few years ago a theoretical approach based on the "two-states" model was developed by Painelli *et al.*, in a joint work with our group. Such essential model tries to rationalize the bistability phenomenon observed for dyad **2** in the solid state[10].

Since, the $DA^{\bullet}$ $D^{+\bullet}A^{-}$ resonance (Figure 2.5) governs the low-energy states of dyad **2**; the minimal model that just accounts for the two basic electronic states that correspond to the following two resonating structures: $|DA^{\bullet}$ and $|D^{+\bullet}A^{-}$ use the relevant Hamiltonian[30,31]:

$$\hat{H} = 2z\hat{\rho} - \phi(\ DA^{\bullet} \quad D^{+\bullet}A^{-} + D^{+\bullet}A^{-} \quad DA^{\bullet}\ ) \tag{2.1}$$

where $\hat{\rho}$ is the ionicity operator, $2z$ is the ionization energy, meaning the energy gap between the two basis states, and ϕ is the hybridization energy that corresponds to the matrix element that mixes the two basis states. The ground and the excited state are given by the diagonalization of the two-state Hamiltonian. Such states are defined in terms of a single parameter ρ that measures the molecular ionicity, meaning the fraction of electron transferred in the ground state from D to $A^{\bullet}$. Depending on the sign of z, the ground state can be dominated by the neutral or zwitterionic state. Thus, positive z indicates that the ground state is neutral ($\rho < 0.5$) and on the contrary, it becomes zwitterionic for negative z ($\rho > 0.5$)[32]. At the neutral-zwitterionic interface, $z = 0$ and $\rho = 0.5$.

Additionally, for neutral systems, the electron transfer transition goes from the ground-state (small dipole-moment) toward the excited-state (large dipole moment). Due to the fact that polar solvents stabilize polar states, for neutral systems as increase the solvent polarity, a red-shift of the absorption band is observed. Further information about the molecular properties can be extracted from the high solvatochromism showed by these polar dyes. *Solvent-independent* molecular parameters can be extracted from the analysis of solution spectra based on the model

proposed by Painelli *et al.*[30,31]. An electric field, called the reaction field F_R is generated by the polarization of the solvent that surrounds a polar solute, and it is proportional to the dipole moment of the solute. This electric field decreases the energy of the zwitterionic ($|D^{+\bullet}A^{-}$) state and presents two main contributions. One due to the polarization of the electronic clouds of the solvent molecules and the other due to the reorientation of *polar* solvent molecules around the polar solute[30]. Treating the solvent as a continuum elastic medium, the solvent relaxation energy $_{or}$ is the parameter needed to define the polar solvation. It measures the decrease of the $|D^{+\bullet}A^{-}$ $-|DA^{\bullet}$ gap resulting of the reorientation of the solvent and depends on both, the refractive index and the dielectric constant of the solvent and also on the shape and the dimensions of the molecular solute.

The quantitatively rationalization of the bistability of dyad **2** in solid state at different temperatures combine both the molecular parameters extracted from the detailed analysis of the solution spectra and the model that account the cooperative electrostatic intermolecular interactions in crystals which is supported by quantum chemical calculations. The intermolecular electron transfer process was neglected since the intermolecular distances in dyad **2** are large enough to prevent such process which was supported by the crystal structure of this dyad[11]. For an extended description of the model, the lector is referred to ref.[10].

The "two-states" model previously described only accounts for the absorption band associated with the IET between the donor and the acceptor units of D–A dyads. An extension of such model to account for the electronic influence of the bridge was proposed by Grisanti *et al.*[33], through the analysis of the energy band related to the electron transfer between the π–electron of the vinylene bond and the acceptor (π–to–A). In this case the general resonating structures: $Fc-\pi-PTM$ $Fc-\pi^{+}-PTM^{-}$ $Fc^{+}-\pi-PTM^{-}$ need to be considered; where the two states described in the "two-states" model, the neutral ($Fc-\pi-PTM$) and the second zwitterionic ($Fc^{+}-\pi-PTM^{-}$), largely predominate over the first zwitterionic ($Fc-\pi^{+}-PTM^{-}$) state which presents a higher energy. In this model, some approximations were adopted since a detailed parametrization, results di cult and involve a considerable increase of the number of parameters. The "three-states"

model do not add much to the understanding of the IET process of Fc–PTM dyads, whose basic features were already well captured by the "two-states" model[10]. More details of the "three-states" model can be found in ref.[33].

2.2 Objectives

Along this chapter we will study the role of the electron donor strength on the bistability phenomenon in Fc–PTM radicals. Specifically, we will study the bistability phenomena of the Fc^8–PTM dyad **3**. This dyad contains eight methyl groups as substituents of the Fc moiety which will increase its donor ability. We will be interested in observing how such increase of donor ability favor the IET following the evolution of absorption spectrum in the UV-Vis-NIR region. We will also study the possibility to stabilize the neutral (N) or the zwitterionic (Z) state of dyad **3** in solution by playing with the polarity of the solvent used.

Finally, we will study the bistability phenomenon of this dyad by using solvents with an intermediate polarity to see if it is possible to observe the coexistence of both electronic stable states: N and Z claiming a true bistability for this molecular system in solution. Finally, we will be also interested to study the temperature induced bistability in solid state of the system with the methylated ferrocene to compare it with the one previously observed for the non-methylated unit.

2.3 Study of the bistability phenomena in Fc^8–PTM dyad 3*

The opportunity to play with the donor ability of the Fc subunit in these valence tautomeric systems can be used to favor the control of the observed bistability phenomenon. In this line, a new D–A system **3** was synthesized† with the Fc substituted by eight methyl groups. The study of dyad **3** both in solution and

*This study has been published as a part of the paper entitled "Bistability of Fc–PTM-based dyads. The role of the donor strenght"[34].

†Compound synthesized in the framework of the PhD Thesis of Dr. Judith Guasch at Institut de Ciència de Materials de Barcelona

in solid is interesting. In fact, remarkable differences in the electron transport mechanism of a molecule only induced by its environment have been previously observed for similar systems[8]. Additionally, this study is supported by the expected higher donor capacity of the Fc obtained by its chemical modification and also by the previous results (positive solvatochromism) obtained for the non-methylated dyad **2**.

On the other hand, the addition of methyl substituents to the Fc will decrease its redox potential thanks to the electron-donating ability of the methyl groups. This modification, will also provide more solubility and stability to the ferrocenium cations due, in part, to the steric hindrance around the iron atom which is increased by the presence of the methyl groups[35–37].

2.3.1 Synthesis of dyad 3

The radical dyad **3** was synthesized in three main steps with a good yield, from the protonated phosphonate PTM derivative (**20**) and the octamethylferrocene-carboxaldehyde (**19**)[34]. Details about the synthesis is given in Chapter 7 which corresponds to the Experimental Part of this thesis.

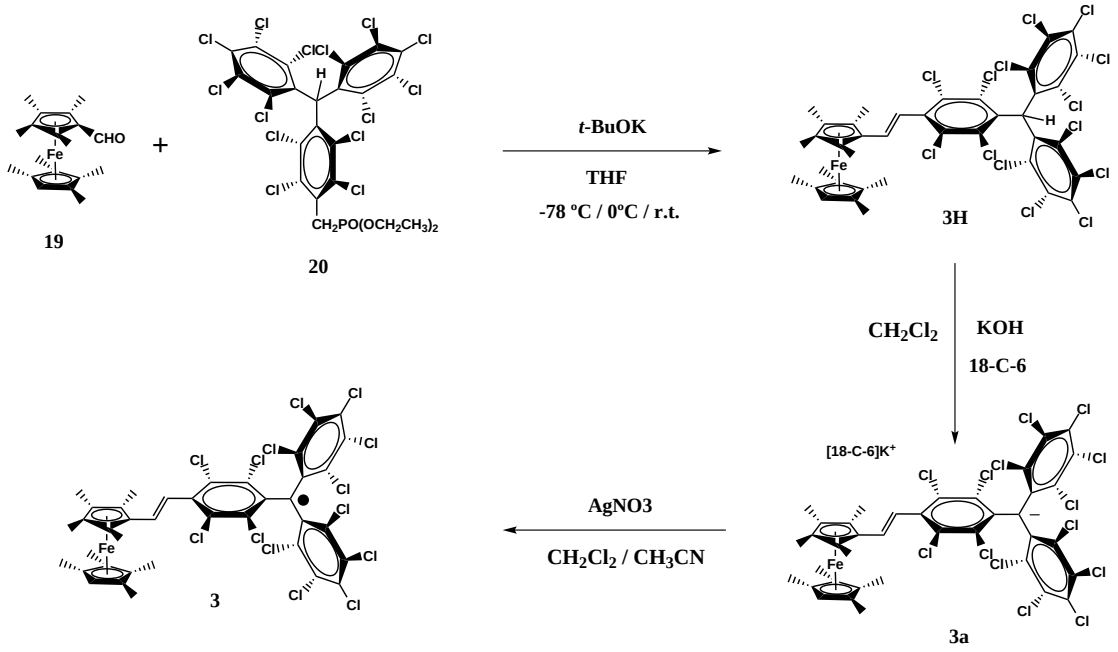

Scheme 2.1: Synthesis of dyad **3**.

First, a Wittig-Horner-Emmons reaction between precursors **19** and **20** yields the π-conjugated hydrocarbon derivative **3H**, which was deprotonated, under red light conditions, by using potassium hydroxide giving place to the anionic derivative **3a**. The anionic derivative **3a** was oxidized with silver nitrate resulting in the desired dyad **3** (Scheme 2.1) as dark brown microcrystals with a high stability under atmospheric conditions.

2.3.2 UV-Vis-NIR and CV characterization of dyad 3

Dyad **3** was studied in solution through UV/Vis/NIR spectroscopy. Solvents with different polarity from *n*-hexane to dimethylformamide (DMF) covering acetone and tetrahydrofuran (THF) were used to evaluate the dependence of this D–A system on the surrounding media. A concentration of 5E-5 M was used for all measurements and in order to avoid any decomposition of the radical the experimental part was made in a dark room. The spectra obtained from solvents with different polarity are shown in Figure 2.8.

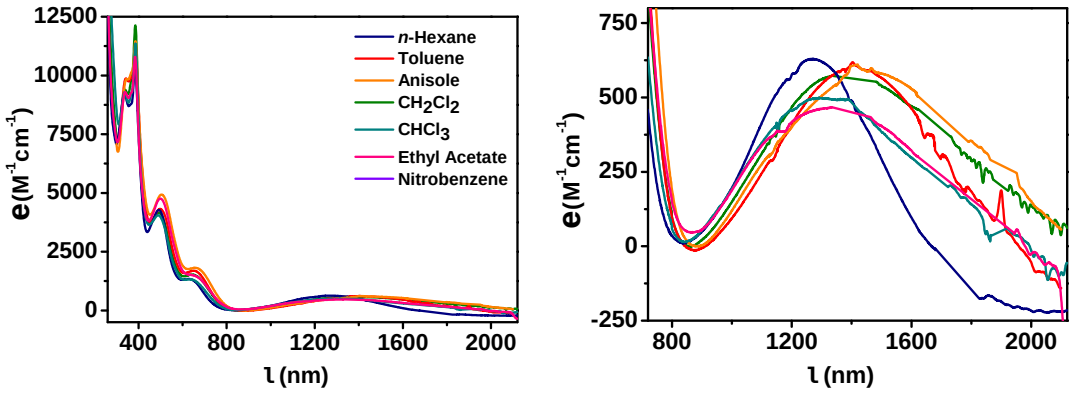

(a) (b)

Figure 2.8: (a) UV-Vis-NIR spectra of dyad **3** obtained in different solvents and (b) a zoom of its IET band in the NIR region.

Like the non-methylated dyad **2**; dyad **3** shows the typical intense radical absorption band around 385 nm accompanied by two weaker bands located around 490 and 645 nm which have been ascribed to the electronic conjugation of the unpaired electrons into the π-framework of the unsaturated substituents at the

para position; specifically these bands are related with a CT from the π-bridge to the PTM acceptor[8].

Further information was obtained from the broad band observed in the NIR region. Since this band appears at lower energy, it has been associated with the electron transfer process involved from the donor (Fc) to the acceptor (PTM) part of the dyad. This band follows the Lambert-Beer Law confirming the intramolecular character of the electron transfer process as it has been described for dyad **2**[8]. From Figure 2.8(b), it is possible to appreciate that both the shape and the maxima position of the IET band show a direct relation with the nature of the solvent used. Moreover, a positive solvatochromism was identified due to the shift to lower energies observed at the maxima position of the IET ($\Delta\lambda$ = 174 nm; $\Delta\nu$ = 940 cm^{-1}) when the polarity of the solvent changes. Thus, this band varied from 1276 nm (7837 cm^{-1}) in *n*-hexane to 1450 nm (6897 cm^{-1}) in anisole.

Comparing the octamethylated dyad **3** with respect to the previously described non-methylated dyad **2**, a sizeable red-shift of the IET band was observed. For instance, in *n*-hexane dyad **2** shows the maxima position of the IET band at 891 nm[8] while dyad **3** shows it at 1276 nm. This displacement towards lower energies is in agreement with the enhancement of the donor ability of the Fc in dyad **3** thanks to the presence of the eight methyl substituents groups; which means that less energy is required to achieve the electron movement inside the molecule.

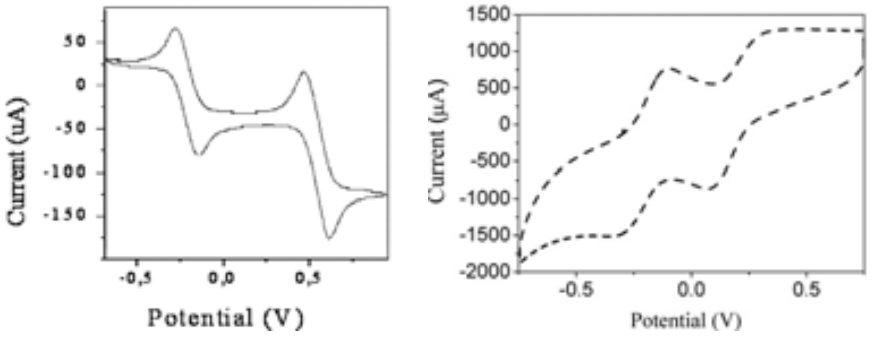

(a) (b)

Figure 2.9: Cyclic voltammetries of a solution of (a) dyad **2**[8] and (a) dyad **3**[11] in CH_2Cl_2 using *n*-Bu_4NPF_6.

This was also confirmed by cyclic voltammetry (CV)(Figure 2.9) measurements where for dyad **3** the two reversible processes of the redox centers appear at +216 mV and -212 mV corresponding to the oxidation of the Fc unit and the reduction of the PTM radical, respectively (ΔE_{redox} = 428 mV). While the same processes in dyad **2** appear at +587 mV and −177 mV with a ΔE_{redox} = 764 mV. The lower difference between the first reduction and oxidation is also indicative of the easiest IET taking place in dyad **3**.

2.3.3 Solvent-induced bistability of dyad 3

The behavior of dyad **3** in solvents with intermediate polarity (i.e. acetone, THF) and high polarity like DMF was also studied. The spectra collected from the optical absorption measurements are shown in Figure 2.10. The absorption spectrum performed in CH_2Cl_2 (green line) clearly exhibit the characteristic bands of the neutral ground state of dyad **3**, namely an intense band at 387 nm (25840 cm^{-1}) of the PTM together with the two weaker bands of the π-conjugated bridge and the broad IET band localized at lower energy.

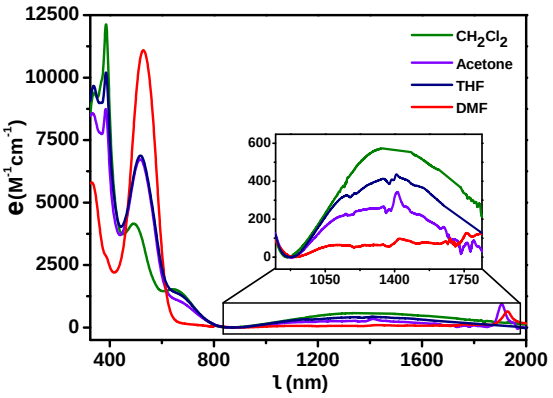

Figure 2.10: UV-Vis-NIR spectra of dyad **3** in solvents with different polarities. Inset: zoom of the NIR region.

On the opposite, a unique intense band located at 530 nm (18868 cm^{-1}) was distinguished when a high polar solvent like DFM (red line) was used. This very intense band corresponds to the anionic form of the PTM[22,38,39]; which is a clear indication that in this media only the charge-separated state of dyad **3** is stabilized due to the charge/spin transfer from the Fc to the PTM unit. In this case, the

IET band practically fades out. Interestingly, the absorption spectrum of dyad **3** performed in solvents with an intermediate polarity like acetone or THF, shares characteristic bands of the neutral and the zwitterionic state showing bands of the PTM and PTM anion at the same time. Then, it was demonstrated that just playing with the nature (polarity) of the solvent one can switch the equilibrium between the two electronic isomers (N and Z) of dyad **3**, and eventually force the coexistence of both states being possible to observe the bistability phenomenon in solution which it has not been possible for the non-methylated system **2**.

Since the energy gap between the two involved low-energy distinct states in solution usually has large values that difficult the overcoming of this energy barrier, the bistability is a non-common phenomenon observed in dyads like the ones studied along this chapter. The behavior observed for dyad **3** in solution certainly involves many factors. The bistability phenomenon probably has its origin in the low ΔE_{redox} value presented by this system thanks to the methylation of the ferrocene, which increase the electron donor strength of this moiety comparing with dyad **2** and therefore achieve a lower energy gap between the neutral and the zwitterionic basis states. Additionally, the interactions of dyad **3** with the molecules of solvent with an intermediate polarity are probably so strong that stabilize the two electronic isomers (N and Z). Hence, the influence of the nature of the solvent over the bistability phenomenon is probed.

In the effort to understand the bistability phenomena observed in dyad **3**, Prof. Anna Painelli *et al.*[34] have modeled this system using the two-state model previously mentioned. Through this model, it was probed that in low polarity solvents dyad **3** is in a largely neutral ground state while in DMF, the most polar solvent considered along this study, dyad **3** is zwitterionic. A good representation of this conclusion can be seen in Figure 2.11. Here, the black continuous lines show the ground state energy as a function of the solvent reaction field, F_{or}, calculated for dyad **3** (for details see ref.[34]).

In low polarity solvents like chloroform (panel a) and dichloromethane (panel b) the energy of the neutral basis state (violet line) is much lower than the energy of the zwitterionic basis state (orange line), then the ground state potential energy

surface (black line) is similar to the potential energy surface of the neutral (DA) state (violet line) and the system is in a largely neutral state. However, in strongly polar solvents like DMF (panel d) the zwitterionic state is greatly stabilized by the interaction with the polar solvent and the ground state potential energy surface (black line) shows a deep minimum corresponding to the zwitterionic state (orange line). At room temperature, only the zwitterionic state is populated (black dashed line).

Interesting, in the intermediate regime (acetone - panel c), the potential energy surfaces corresponding to the two neutral and zwitterionic states (violet and orange lines, respectively) have similar energies and, the ground state potential energy surface (black line) shows two minima corresponding to largely neutral and zwitterionic states. Boltzmann distribution (black dashed line) shows that both states are populated at ambient temperature, in agreement with experimental results for acetone solutions[34].

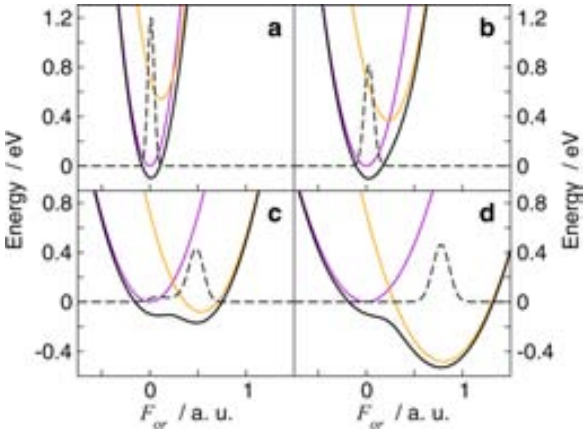

Figure 2.11: Black continuous curves: ground state energy calculated for dyad **3** as a function of the solvent reaction field, F_{or}, for (a) $CHCl_3$, (b) CH_2Cl_2, (c) acetone and (d) DMF. Violet and orange lines show the energies of neutral (DA) and zwitterionic (D^+A^-) state, respectively. Black dashed line shows the r.t. Boltzmann probability distribution calculated based on the ground state energy[34].

In conclusion, the evolution from a neutral to a zwitterionic ground state with increasing solvent polarity and the coexistence of the two states in intermediate polarity solvents is well captured by the two-state model.

2.3.4 Temperature induced bistability of dyad 3 in solid state

As it has been mentioned, the possibility of tuning the molecular properties by modifying the chemical structure is one of the most promising tools in molecular materials.

Mössbauer measurements of dyad **3** and its protonated analogous **3H** were recorded at different temperatures by Guasch *et al.*[34], and the spectra are shown in Figure 2.12.

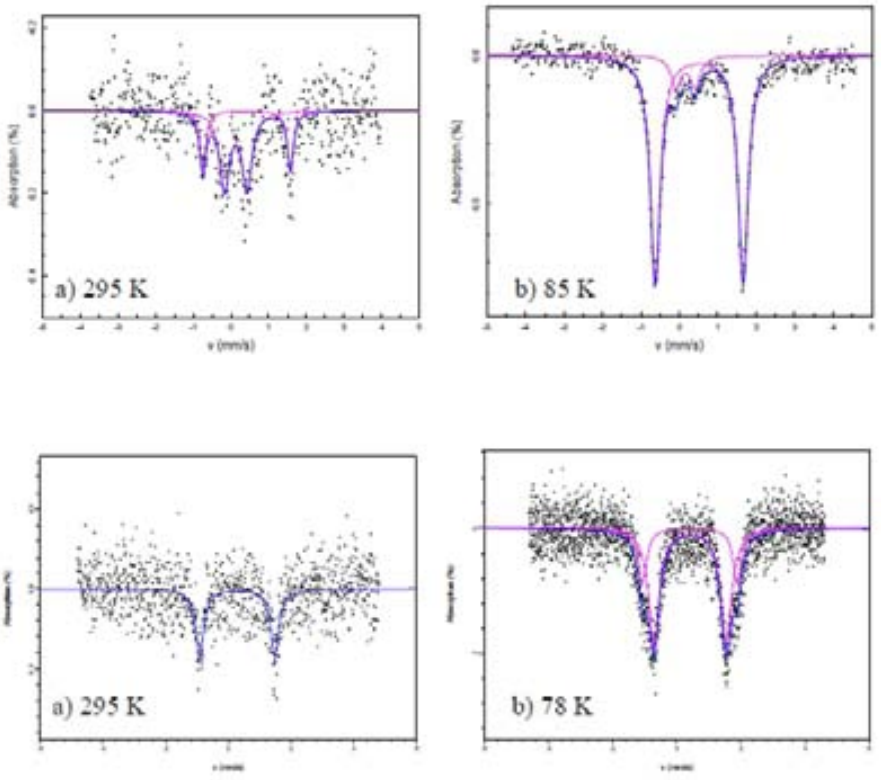

Figure 2.12: Mössbauer spectra of a crystalline sample of dyad **3** (up) and its protonated precursor **3H** (bottom) at different temperatures.

As it can be appreciated, at 295 K two doublets are distinguished which correspond to the Fe (II) (32%) and Fe (III) (68%) ions of the Fc and ferrocenium cation, respectively. However, the proportion of the zwitterionic (D^+A^-) form of dyad **3** with respect to the neutral (D–A) form at this temperature is higher than the one observed for **2** (Fe (III) $\sim$ 60%) without methylene substituents. On the other hand, Mössbauer spectra of the protonated precursor **3H**, taken at different temperature (295 and 78 K) only show the Fe (II) doublet, which is in agreement

with the fact that in this compound the IET is prevented by the protonation of the PTM unit[34] (Figure 2.12 bottom).

Through these measurements it was demonstrated that the enhancement of the donor ability of the Fc by the incorporation of eight methyl groups act favouring the zwitterionic state of these kind of D–A systems at room temperature which result of special interest for possible applications in which small energy is required (light, temperature, pressure) to achieve the switch between these two electronic isomers. As it has been previously observed for dyad **2**, in solid state, the intermolecular interactions play a decisive role on the stabilization of the two stable electronic states of dyad **3** favoring the simultaneously existence of both of them and thus allowing the bistability phenomena to take place.

Once again, with the aim to support with a theoretic model the bistability phenomena observed in crystals of dyad **3**, Prof. Anna Painelli *et al.*[34] have used the bottom-up modeling strategy, where electrostatic intermolecular interactions are introduced in the mean-field approximation. Molecular model parameters obtained from the analysis of solution spectra of dyad **3** were used and important information about the crystal was given by M, the electrostatic (Madelung) energy of a lattice of molecules in the zwitterionic D^+A^- state. In this sense, for attractive intermolecular interactions, M is negative and the energy required to create a zwitterionic molecule is reduced in the crystal.

The curve observed in the left panel of Figure 2.13, describes a crystal of largely neutral molecules ($\rho \approx 0$) for relatively weak electrostatic interactions and a crystal of zwitterions ($\rho \approx 1$) for strong interactions. In the intermediate region, the two stable solutions for the Hamiltonian present in Equation 2.2 corresponds to a crystal of largely neutral or largely ionic molecules. Then, the model for dyad **3** crystal supports bistability, in the case that the strength of electrostatic interactions falls in the region -0.87 eV < M < 0.67 eV .

$$H_{cry}(z_{cry}\ \phi) = h_{el}(z_{cry}\,\phi) + \frac{1}{2}\ \ {}_{\nu}q^2 - M\rho^2 \tag{2.2}$$

To confirm the model for bistability in dyad **3** crystals, M was calculated using another expression. Data observed in the black scale in the right panel of Figure 2.13 confirm that increasing the applied field, the molecules are driven from a largely

neutral ground state (no field) to a zwitterionic state (large applied field). Closed and open symbols refer to results obtained for the molecular geometry at room and low temperature, respectively. At low fields a smooth and almost linear $\mu_z(F)$ dependence is observed (molecule in a largely neutral state). With increasing field an abrupt jump in the calculated dipole is observed, toward another region of smooth and almost linear behavior (largely zwitterionic state). The threshold field estimated for dyad **3** is lower than the value previously obtained for dyad **2**, which is in agreement with the stronger donor character of the methylated Fc group. On the other hand, the red squares show the Madelung energy calculated. Madelung energies estimated in the neutral regime are negligible with respect to the values obtained in the F-range (region comprised between the two vertical dashed lines) relevant to the zwitterionic regime. Important is the fact that the estimated interval of M values largely overlaps with the bistability window predicted for dyad **3**. Thus, the proposed model really supports the hypothesis that the bistability observed in crystals of dyad **3** is induced by cooperative intermolecular electrostatic interactions[34].

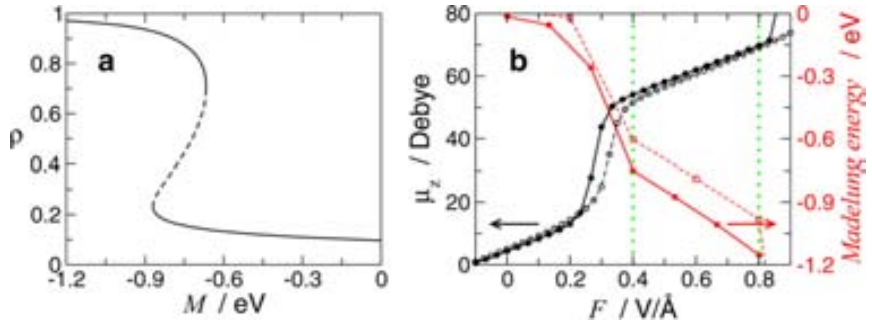

Figure 2.13: a) Graph of the molecular ionicity (ρ) calculated as a function of M and b) graph of the calculated component of the dipole moment along the D–A direction (black points) and calculated Madelung energy (red squares) as a function of the applied electric eld .

2.4 Summary and Perspectives: moving forward to a new dimension

After introducing that dyad **2** present bistability in solid state (3D) thanks to the cooperative intermolecular electrostatic forces that drive the coexistence of the

neutral and zwitterionic states at different temperatures, in this chapter we have seen that enhancing the donor ability of the Fc unit by the methylation of the two cyclopentadienyl rings, it was possible to reduce the energy gap between these two stable electronic states and thus favor the stabilization of the charge-separated state at room temperature. This observation was reflected in the higher proportion of the zwitterionic state observed in the corresponding Mössbauer spectrum, comparing with that observed for dyad **2** at the same temperature.

In solution, it has been demonstrated that just by playing with the nature (polarity) of the solvent one can also switch the equilibrium between the two electronic states (N or Z) of dyad **3**, and eventually force the coexistence of both state being possible to observe the bistability phenomenon in solution which it has not been possible for the non-methylated dyad **2**. Once we have deeply studied these D–A systems in bulk (solution and crystal), in order to exploit its possible use as multifunctional molecular materials for advanced applications we need to support them on a metallic substrate which at the same time will allow to easily integrate them into devices. To specifically evaluate the possible applications, a deep understanding of their properties at the nanoscale once supported and structured on a metallic surface will be of fundamental interest.

In fact, the possibility to stabilize one or the other electronic state applying an external stimulus such as temperature (in solid) or solvent and light (in solution) give a great motivation to think that these two systems will show interesting properties at the nanoscale. Thus, an interesting framework of opportunities are opened to work with these kinds of D–A systems as self-assembled structures in two dimensions (2D) where the different intermolecular interactions as a collective behavior are predicted to have a strong influence in the final property obtained in comparison with the 3D.

Thus, in the next chapters we will focus our attention into the study of the electronic properties of Fc–PTM based D–A systems deposited on surfaces as self-assembled monolayers (SAMs). In this regard, not only the bistability phenomena will be pursued at the nanoscale but also the use of this systems to modify the work function of electrodes or its use as molecular rectifiers. In general, a deep study

of how moving from 3D to 2D at the nanoscale could influence the properties of a molecular system will be perform.

Bibliography

[1] L. Bogani and W. Wernsdorfer, "Molecular spintronics using single-molecule magnets.," *Nature materials*, vol. 7, no. 3, pp. 179–86, 2008.

[2] T. Mori, "Molecular materials for organic field-effect transistors," *Journal of Physics: Condensed Matter*, vol. 20, no. 18, p. 184010, 2008.

[3] B. Albinsson, M. P. Eng, K. Pettersson, and M. U. Winters, "Electron and energy transfer in donor-acceptor systems with conjugated molecular bridges.," *Physical chemistry chemical physics*, vol. 9, no. 44, pp. 5847–64, 2007.

[4] I. Ratera and J. Veciana, "Playing with organic radicals as building blocks for functional molecular materials.," *Chemical Society reviews*, vol. 41, no. 1, pp. 303–49, 2012.

[5] J. Fraxedas, *Molecular Organic Materials. From Molecules to Crystalline Solids*. New York: Cambridge University Press, first ed., 2006.

[6] C. W. Chu, J. Ouyang, J.-H. Tseng, and Y. Yang, "Organic Donor-Acceptor System Exhibiting Electrical Bistability for Use in Memory Devices," *Advanced Materials*, vol. 17, no. 11, pp. 1440–1443, 2005.

[7] A. M. Oliver, D. C. Craig, M. N. Paddon-Row, J. Kroon, and J. W. Verhoeven, "Strong effects of the bridge configuration on photoinduced charge separation in rigidly linked donor-acceptor systems," *Chemical Physics Letters*, vol. 150, no. 5, pp. 366–373, 1988.

[8] I. Ratera, C. Sporer, D. Ruiz-Molina, N. Ventosa, J. Baggerman, A. M. Brouwer, C. Rovira, and J. Veciana, "Solvent tuning from normal to inverted marcus region of intramolecular electron transfer in ferrocene-based organic radicals.," *Journal of the American Chemical Society*, vol. 129, no. 19, pp. 6117–29, 2007.

[9] E. Evangelio and D. Ruiz-Molina, "Valence tautomerism: More actors than just electroactive ligands and metal ions," *Comptes Rendus Chimie*, vol. 11, no. 10, pp. 1137–1154, 2008.

[10] G. D'Avino, L. Grisanti, J. Guasch, I. Ratera, J. Veciana, and A. Painelli, "Bistability in Fc-PTM crystals: the role of intermolecular electrostatic interactions.," *Journal of the American Chemical Society*, vol. 130, no. 36, pp. 12064–72, 2008.

[11] J. Guasch, *Multifunctional Molecular Materials based on Donor-Acceptor Systems.* PhD thesis, Universitat Autònoma de Barcelona, 2011.

[12] M. Souto, D. C. Morales, J. Guasch, I. Ratera, C. Rovira, A. Painelli, and J. Veciana, "Intramolecular electron transfer and charge delocalization in bistable donor-acceptor systems based on perchlorotriphenylmethyl radicals linked to ferrocene and tetrathiafulvalene units," *Journal of Physical Organic Chemistry*, vol. 27, no. 6, pp. 465–469, 2014.

[13] A. Haaland, "Molecular structure and bonding in the 3d metallocenes," *Accounts of Chemical Research*, vol. 12, no. 11, pp. 415–422, 1979.

[14] A. Cotton and G. Wilkinson, "The Heat of Formation of Ferrocene," vol. 74, pp. 5764 – 5766, 1952.

[15] A. Togni and T. Hayashi, eds., *Ferrocenes.* New York: VCH Verlagsgesellschaft, 1995.

[16] G. Wilkinson, M. Rosenblum, M. C. Whiting, and R. B. Woodward, "The structure of iron bis-cyclopentadienyl," *Journal of the American Chemical Society*, vol. 74, no. 8, pp. 2125–2126, 1952.

[17] M. Ballester, "Inert Free Radicals (IFR): A Unique Trivalent Carbon Species," *Accounts of Chemical Research*, vol. 18, pp. 380–387, 1985.

[18] M. Ballester, J. Riera, J. Castatier, C. Badía, and J. M. Monsó, "Inert Carbon Free Radicals. I. Perchlorodiphenylmethyl and Perchlorotriphenylmethyl Rad-

ical Series,” *Journal of the American Chemical Society*, vol. 93:9, pp. 2215–2225, 1971.

[19] M. Ballester, J. Riera, J. Castañer, and M. Casulleras, “The reduction of inert free radicals with ascorbic acid. The reaction with perchlorotriphenylmethyl radical,” *Tetrahedron Letters*, vol. 19, no. 7, pp. 643–644, 1978.

[20] C. Simao, M. Mas-Torrent, N. Crivillers, V. Lloveras, J. M. Artés, P. Gorostiza, J. Veciana, and C. Rovira, “A robust molecular platform for non-volatile memory devices with optical and magnetic responses,” *Nature chemistry*, vol. 3, pp. 359–364, 2011.

[21] N. Crivillers, M. Mas-Torrent, S. Perruchas, N. Roques, J. Vidal-Gancedo, J. Veciana, C. Rovira, L. Basabe-Desmonts, B. J. Ravoo, M. Crego-Calama, and D. N. Reinhoudt, “Self-assembled monolayers of a multifunctional organic radical.,” *Angewandte Chemie*, vol. 46, no. 13, pp. 2215–9, 2007.

[22] C. Sporer, I. Ratera, D. Ruiz-Molina, Y. Zhao, J. Vidal-Gancedo, K. Wurst, P. Jaitner, K. Clays, A. Persoons, C. Rovira, and J. Veciana, “A molecular multiproperty switching array based on the redox behavior of a ferrocenyl polychlorotriphenylmethyl radical.,” *Angewandte Chemie*, vol. 43, no. 39, pp. 5266–8, 2004.

[23] O. Elsner, D. Ruiz-Molina, J. Vidal-Gancedo, C. Rovira, and J. Veciana, “Ferromagnetic interactions between triphenylmethyl radicals through an organometallic coupler,” *Chemical Communications*, no. 7, pp. 579–580, 1999.

[24] I. Ratera, D. Ruiz-Molina, F. Renz, J. Ensling, K. Wurst, C. Rovira, P. Gütlich, and J. Veciana, “A new valence tautomerism example in an electroactive ferrocene substituted triphenylmethyl radical.,” *Journal of the American Chemical Society*, vol. 125, no. 6, pp. 1462–3, 2003.

[25] F. Terenziani and A. Painelli, “Supramolecular interactions in clusters of polar and polarizable molecules,” *Physical Review B*, vol. 68, no. 16, p. 165405, 2003.

[26] J. I. Krugler, C. G. Montgomery, and H. M. McConnell, "Collective Electronic States in Molecular Crystals," *The Journal of Chemical Physics*, vol. 41, no. 8, p. 2421, 1964.

[27] E. Tsiper and Z. Soos, "Charge redistribution and polarization energy of organic molecular crystals," *Physical Review B*, vol. 64, no. 19, p. 195124, 2001.

[28] R. S. Mulliken, "Molecular Compounds and their Spectra. II," *Journal of American Chemical Society*, vol. 74, no. 3, pp. 811–824, 1952.

[29] C. Reichardt, "Solvatochromic Dyes as Solvent Polarity Indicators," *Chemical Reviews*, vol. 94, no. 8, pp. 2319–2358, 1994.

[30] A. Painelli, "Amplification of NLO responses: vibronic and solvent effects in push-pull polyenes," *Chemical Physics*, vol. 245, no. 1-3, pp. 185–197, 1999.

[31] A. Painelli, "Vibronic contribution to static NLO properties: exact results for the DA dimer," *Chemical Physics Letters*, vol. 285, no. 5-6, pp. 352–358, 1998.

[32] A. Painelli and F. Terenziani, "Multielectron Transfer in Clusters of Polar-Polarizable Chromophores," *Journal of American Chemical Society*, vol. 125, pp. 5624–5625, 2003.

[33] L. Grisanti, G. D'Avino, A. Painelli, J. Guasch, I. Ratera, and J. Veciana, "Essential state models for solvatochromism in donor-acceptor molecules: the role of the bridge.," *The journal of physical chemistry. B*, vol. 113, no. 14, pp. 4718–25, 2009.

[34] J. Guasch, L. Grisanti, S. Jung, D. Morales, G. D'Avino, M. Souto, X. Fontrodona, A. Painelli, F. Renz, I. Ratera, and J. Veciana, "Bistability of Fc-PTM-Based Dyads: The Role of the Donor Strength," *Chemistry of Materials*, vol. 25, pp. 808–814, 2013.

[35] L. Reynolds and G. Wilkinson, "Some methylcyclopentadienyl-metal compounds," *Journal of Inorganic and Nuclear Chemistry*, vol. 9, no. 1, pp. 86–92, 1959.

[36] M. T. Meredith, D. P. Hickey, J. P. Redemann, D. W. Schmidtke, and D. T. Glatzhofer, "Effects of ferrocene methylation on ferrocene-modified linear poly(ethylenimine) bioanodes," *Electrochimica Acta*, vol. 92, pp. 226–235, 2013.

[37] A. Hradsky, B. Bildstein, N. Schuler, H. Schottenberger, P. Jaitner, K.-H. Ongania, K. Wurst, and J.-P. Launay, "New Soluble Bis[nona-, octa-, and pentamethylferrocenes] as "Molecular Wires" with a Metal-to-Metal Distance of up to 40 A," *Organometallics*, vol. 16, pp. 392–402, 1997.

[38] V. Lloveras, J. Vidal-Gancedo, D. Ruiz-Molina, T. M. Figueira-Duarte, J.-F. Nierengarten, J. Veciana, and C. Rovira, "Influence of bridge topology and torsion on the intramolecular electron transfer," *Faraday Discussions*, vol. 131, p. 291, 2006.

[39] C. Sporer, I. Ratera, D. Ruiz-Molina, J. Vidal Gancedo, K. Wurst, P. Jaitner, C. Rovira, and J. Veciana, "Synthesis, X-ray structure, EPR and optical properties of a ferrocene substituted polychlorotriphenylmethyl radical," *Journal of Physics and Chemistry of Solids*, vol. 65, no. 4, pp. 753–758, 2004.

"In any moment of decision the best thing you can do is the right thing, the next best thing you can do is the wrong thing, and the worst thing you can do is nothing"

Theodore Roosevelt

3

Self-assembled monolayers of Fc–PTM radical dyads on surfaces

3.1 Introduction

Curiosity and need are two of the principal sources that promote discovery and development of fundamental knowledge and interesting technologies that have led us to a new era, where the relationship between efficiency, ultra-small sizes and new properties of the matter have attracted the attention of many research groups around the world. Physical and material properties of what around us at macroscopic scale are known, but new questions and challenges are faced when a "world of nanometer scale" is explored. At nanoscale, systems can show interesting and useful physical behaviors based on quantum or subdomain phenomena. Such nanosystems with sizes ranging from 1 to 100 nm, are obtained by chemical synthetic methods and can be applied in materials science, medicine, magnetic storage media or in electronic or optical devices[1]. The recent development of techniques with atomic resolution that reach the visualization and manipulation of nanoscale structures has meant a breakthrough in the field.

Unlike macroscopic materials, a high percentage of the constituent atoms of nanoscale structures are at the interface i.e. on a surface in case of SAMs. Then, such components experience a different environment from the bulk, giving place to different free energies, electronic states, reactivities, mobilities, and structures which are related to intermolecular forces. In fact, the properties of an interface can vary both along and perpendicular to it[2]. In this sense, self-assembly of molecules at the nanoscale offer a favorable way to study the properties of both the interface and the nanosystem which can be used as a component in molecular electronic.

3.1.1 Self-assembled monolayers as a way of nanofabrication

Self-assembled monolayers (SAMs), are organic organizations that through a spontaneous process of adsorption and self-assembly of molecular components form organized nanostructures. The molecular components can be transferred from a solution or a gas phase over a surface of solids. Since, the thickness of a SAM is normally between 1–3 nm, they are considered as the most elementary form of a nanometer-scale organic thin-film material[1].

Structure of the molecules for SAMs

The structure of the molecular components used to prepare SAMs is of crucial importance. Basically they have to contain three principal parts; *i)* a head group, which has a specific a nity for the substrate (e.g. thiol or disulfide groups are used to anchor molecules on gold surfaces), *ii)* a molecular spacer, which acts as insulating component between the substrate and the terminal functional group, and *iii)* a functional group or active part which will be used to tailor the properties of the surface. These three basic components are shown schematically in Figure 3.1.

Through chemical synthesis the different parts of the molecular components used for preparing SAMs can be modified taking into account that the organic interface, defined by the terminal functional group will determine the surface properties and the type of spacer chain will act over the molecular packing and could disturb the electronic properties (i.e. conductivity) of the monolayer. At the end, the de-

sired surface property will conduce any modification of the molecular components. The most widely studied SAMs are alkanethiols on metals, and more specifically on Au due to the strong strength of the S–Au bond (50 kcal mol^{-1}) [3].

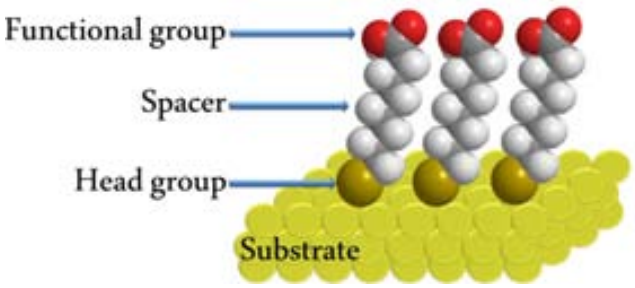

Figure 3.1: Schematic diagram of a SAM of alkanethiols on a gold surface with its principal parts.

General preparation of SAMs

Depending on the application of a SAM, both the substrate and the method of preparation can change. The most common substrates used are thin films (few nanometers) of metal supported on diverse substrates like: silicon wafers, glass, mica or plastics [1]. A general and basic procedure of SAMs preparation include the immersion of a freshly cleaned substrate into a solution of organic molecules during some hours at room temperature. The most common solvent used to prepared SAMs of thiol molecules is ethanol, however other organic solvents can be used in the process. In the same way, different concentrations can be used, which can be between $\approx$ 1–10 mM. Nevertheless, for each specific case all the experimental details need to be developed and optimized in order to achieve reproducible and organized molecular monolayers.

During the preparation of SAMs, several experimental factors can affect the final structure of the monolayer as well as the rate of formation. These factors are [1]: **a) Cleanness of the substrate**: a clean substrate, free of any dust will help to the adsorption of the molecules since in other case, the head group of the molecules (e.g. thiols) must displace any foreign material previously adsorbed onto the substrate (specially carbon and oxygen from the atmosphere) before forming any interaction with the substrate. In this sense, the adsorption of the molecules can be considered as an exchange process.

b) Solvent: the interactions of the solvent molecules with both the adsorbate (solvatation effects) and with the substrate can affect the dynamic equilibrium that governs the kinetics of formation of the monolayers and the mechanism of the assembly. Moreover, independently of the solvent used, a high purity is required as well as a low toxicity. Additionally, an inert atmosphere over the solution which has been previously degassed usually improves the reproducibility of the SAMs prepared and maintain their properties reducing possible oxidative processes during the formation of the SAM[4,5].

c) Purity of the adsorbate: impurities present on the molecules used to prepare SAMs can influence on the adsorption process and also can give place to important defects in the structure of the monolayers. Moreover, the structure of the adsorbate (chain length with odd or even carbon atoms, terminal groups, facility to form hydrogen bonds, etc.) can favor the weak interactions between adjacent molecules and thus improve the packing.

d) Concentration of adsorbate and immersion time: to achieve modified surfaces with high molecular coverage it is necessary to find the better commitment between these two factors. Long periods of immersion in diluted solutions of molecules or vice versa, do not guarantee the correct self-organization of the molecules on the surface and neither their properties.

e) Temperature: specially at the very beginning of the self-assembly process can have a strong influence on the structure of the SAMs, increasing the temperature usually favours the kinetics of formation and reduce the number of defects[6,7].

Molecular orientation and process of formation of SAMs

The formation process of SAMs can be considered as a two general steps process, the first one is characterized by a fast disordered adsorption of the molecules over the clean substrate, while the second slow step entails the self-organization of the adsorbed molecules to form a well-defined structure. Each of these processes is carried out in different times, while the adsorption of the molecules can happen in few minutes, the reorganization of the dynamic systems over the surface can take from a few to many hours in order to obtain the maximum density of molecules.

The adsorption of the molecules on a surface, implies *i)* the formation of a S–Au bond, which is associated with a certain tilt angle according to the position acquired by the sulfur head groups; together with other factors like *ii)* the inherent intermolecular forces that drive the average direction of the molecular packing within the monolayer. More specifically, three parameters can define the order and orientation of molecules adsorbed on a substrate: the angle of the tilt of the molecular axis with respect to the substrate normal (α_m), the angle of rotation (twist) of the hydrocarbon chain plane around the molecular axis (β_t), and the angle of precession (ν_p) around the surface normal which determines the tilt direction and is given by the projection of molecule on the substrate plane[8,9]. These angles are represented in Figure 3.2.

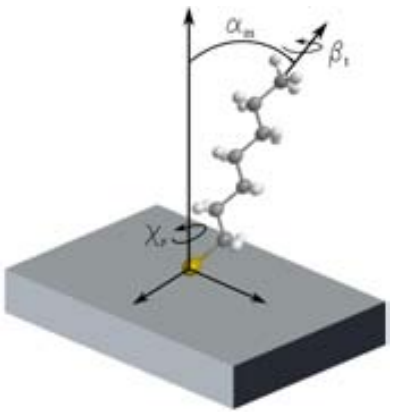

Figure 3.2: Schematic representation of an alkanethiolate molecule adsorbed on a surface in a standing up con guration.

Defects in SAMs

Since the quality of the monolayer depends strongly on the nature of the surface used, any defect on it (e.g. vacancy islands, step edges or intergrain boundaries) will affect the final structure of the monolayers[10]. However, not only the imperfections of the substrate affect the monolayer but also the interactions between molecules. Typical defects of SAMs of alkanethiols on Au(111) are missing rows specially when short molecules are used; vacancy Au islands produced during the self-assembly process; molecular defects induced by the absence of molecules or a disorder of them; domains boundaries characterized by a strong disorder of the

molecules[3], etc. Minimizing such defects is one of the key points to be considered during the optimization process for their preparation.

3.1.2 General characterization and applications of SAMs

Several techniques for surface analysis and physical characterization are used to study SAMs. Within spectroscopy-based techniques one can find the polarization-modulation infrared reflection adsorption spectroscopy (PM-IRRAS) used to study the transition dipoles associated with vibrational modes which allows to know the average molecular orientation and also the chemical composition of nanostructured systems. PM-IRRAS shows great advantages over the conventional IRRAS because different absorption of p- and s-polarized light at large angles of incidence are simultaneously obtained. Then the disturbing atmospheric absorptions caused by water vapour and CO_2 are eliminated since the molecules on metal surfaces only interact with the p-polarized fraction of light, then the reference of a clean substrate is not required. X-ray photoelectron spectroscopy (XPS) is another surface analysis technique employed to study the binding state of the atoms constituents of the molecules as well as their electronic structure and the mass coverage. Near-edge X-ray absorption fine structure spectroscopy (NEXAFS) gives information about the average orientation and the contribution of selected atoms on the unoccupied molecular orbitals. Surface-enhanced raman scattering (SERS) allows to determine chemical information of molecules on metallic substrates based on their vibrational modes. Microscopy-based techniques such as scanning tunneling microscopy (STM) and atomic force microscopy (AFM) provides direct images of the structure of the monolayers. Other SAM characterization techniques include contact angle measurements used to determine the wetting behavior of the surface and surface energies; surface plasmon resonance (SPR), ellipsometry and quartz crystal microbalance (QCM) used to provide information related to the thickness or surface coverage. Time-of-flight secondary ion mass spectrometry (ToF-SIMS) used to study the mass and get information about the structural composition of the monolayers. This technique uses a pulsed primary ion beam to desorb and ionize species from a surface. The resulting secondary ions are accelerated into

the mass spectrometer, where they are analyzed by measuring their time-of-flight from the surface to the detector which is directly related with the mass of the flying ions. Electron spin resonance (ESR) allows the analysis of the magnetic character of the monolayer[9]. In case SAMs contain electroactive molecules, cyclic voltammetry (CV) can be used to study the redox process of the molecular monolayer. This technique is also useful to analyse the stability of the SAM and to probe the chemisorption of the molecules on the surface.

The applications of SAMs include: the modification of surface properties (e.g. tuning of the wettability), the immobilization of different species or functional groups to be used in sensors and biosensors, and also the development of devices at the nanoscale for electronics and their use as nano-templates, among others[3]. The easy of preparation as well as the versatility of the molecular components used in SAMs give an important tool to explore a world that it has only started to be discovered.

3.1.3 Motivation for using D–A systems as functional molecules to functionalize surfaces

Different molecules can be used as building blocks in the molecular self-assembly processes; these molecules carry themselves the necessary information to construct defined supramolecular structures like SAMs.

In the last decades a large number of studies of SAMs on different substrates have been done[3,11–14]. In this context, donor-acceptor (D–A) SAMs have attracted special attention for rectification studies[15,16]. Moreover D–A SAMs that show high stability and desirable electronic properties are important for applications in molecular electronics[17] like: design of molecular switches, modification of the work function of electrodes to control the charge-injection barriers or for the investigation of photovoltaic charge-carrier generation[18], etc.

In the framework of this work, D–A SAMs based on Fc–PTM derivatives have been chosen to take advantage of the possibility to obtain oriented dipoles on surface which allows the modification of its effective work function and also as a good platform to perform studies of current rectification.

SAMs containing Fc or PTM building blocks separately, have been prepared and studied. SAMs of Fc have been widely reported in the literature[19–21] due to the redox-active character of this moiety which allows the study of electric and surface properties since Fc may act as a local molecular switch because the conduction through the two cyclopentadienyl ligand is poor in the reduced state but effective in the ferricinium cations[22]. In addition, conjugated bridges are desirable because π-delocalisation increases the coupling between two redox moieties and if there is also a conjugated π-system acting as spacer chain then could be possible to achieve the coupling between the nearest redox unit and the electrode (substrate)[23,24] favoring at the end the electron transport through the molecule.

SAMs of electroactive PTM radicals have been reported in our group on different substrates such as gold[25–27], silicon oxide[28] and ITO[29] demonstrating that it is possible to switch the electronic state of the molecule in a reversible way; with the advantage that the electrical input can be transduced not only into optical but also magnetic output depending on the stable redox state (radical or anion) of the molecule. Changing the electronic state of the system it is possible to obtain different surface wetting properties which can lead to future potential applications of this material in the industry.

Therefore, taking advantages of the good characteristics of these building blocks (Fc and PTM) as individual components as well as D–A systems (Fc–PTM) that show bistability in solid and in solution (Chapter 2), the functionalization of a substrate with such oriented dipolar molecules involves important expectations from a fundamental (i.e. charge transport study, surface potential modification, etc.) and practical (i.e. molecular switches or molecular rectifiers) point of view.

Additionally, the possibility to control the stabilization of the neutral or the zwitterionic state by applying an external stimulus such as temperature (in solid) or solvent and light (in solution) observed in 3-dimensional (3D) structures offers a great motivation to study if such control still can take place when moving from 3D D–A systems to the bidimensional (2D) nanoscale of SAMs of oriented D–A systems based on the Fc unit and the PTM moiety linked trough a vinylene bridge. Thus, an interesting framework of opportunities are opened to work with these kind

of D−A systems as self-assembled nanostructures where intermolecular interactions as a collective behavior are predicted to have a strong influence in the final property obtained.

Two principal D−A systems will be used along this work: Fc−PTM radical and its protonated closed-shell form Fc−HPTM. Additionally, octamethylated derivatives of the previously mentioned D−A systems will be used because increasing the donor ability of Fc−PTM systems by the methylation of the ferrocene moiety, favors the intramolecular electron transfer (IET) in solid state inducing a higher proportion of the zwitterionic electronic state of the molecule with respect to the neutral one at room temperature and also playing with the polarity of the solvents is possible to stabilize either (neutral or zwitterionic) state of the molecule, as it was previously study in Chapter 2. With these molecular systems we want to study the influence of the open-shell structure over the electronic characteristics and properties once they are nanostrutured on a surface.

3.1.4 General approaches used to functionalize Au surfaces with D−A systems

As it was mentioned, in the framework of this thesis we will be interested to prepare SAMs of D−A systems based on Fc−PTM molecules. Two different strategies can be employed to functionalize gold surfaces with functional molecular units like D−A systems: a one-step or a two-steps approach.

The two-steps approach consists in the prefunctionalization of the substrate with a base anchoring molecule which has two terminal reactive groups localized in opposite way, one of them is bonded to the substrate leaving the other one exposed at molecule/air interface. Then, in a second step a functional molecule with a complementary terminal reactive group is immobilized over the prefunctionalized substrate by the specific recognition of the free reactive group and the formation of a new covalent bond. A schematic representation of this approach is shown in Figure 3.3.

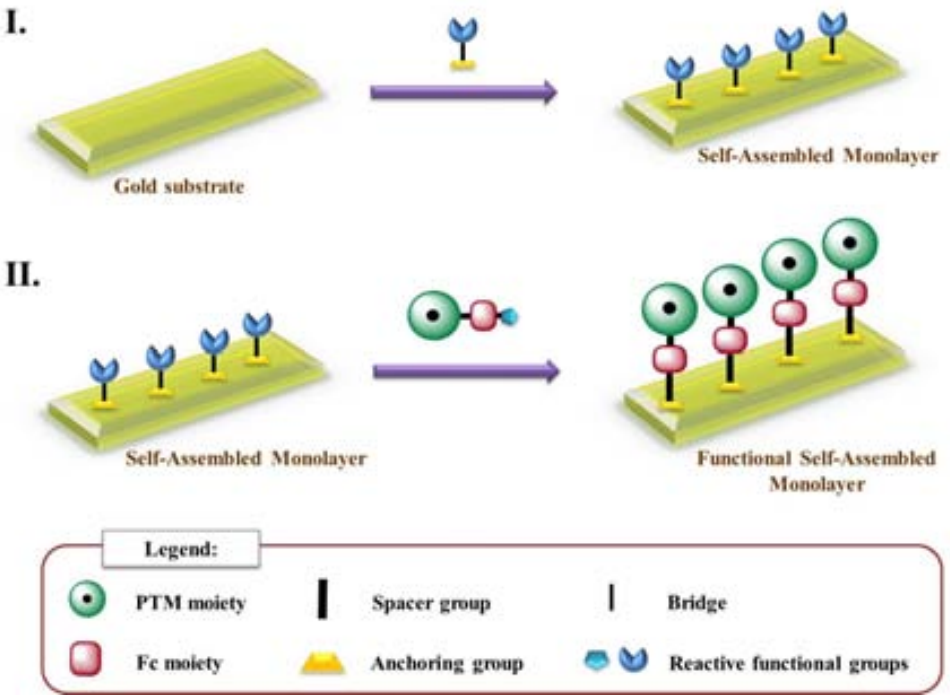

Figure 3.3: Scheme of the two-steps approach used for the Fc–PTM functionalization of Au substrates.

This approach has been previously used to functionalize SiO_2 surfaces with big size units. Crivillers *et al.*[28] have reported the formation of SAMs of multifunctional organic radicals by using the two-step approach. First, SiO_2 substrates were functionalized with a monolayer of silane molecules and subsequently a PTM radical derivative was immobilized by a covalent amide bond as shown Figure 3.4.

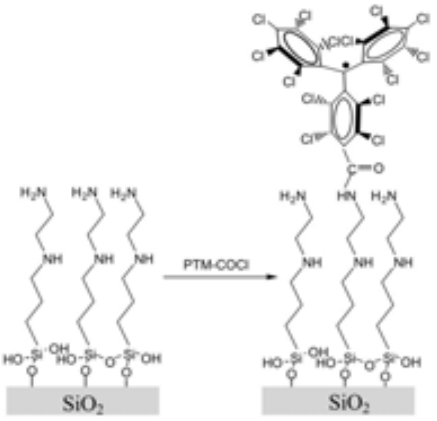

Figure 3.4: Schematic representation of PTM SAMs formed by two-steps approach[28].

In the one-step approach, a unique molecule that bears both the functional D–A system and the anchor group is directly self-assembled on the bare gold. A schematic representation of this approach is shown in Figure 3.5.

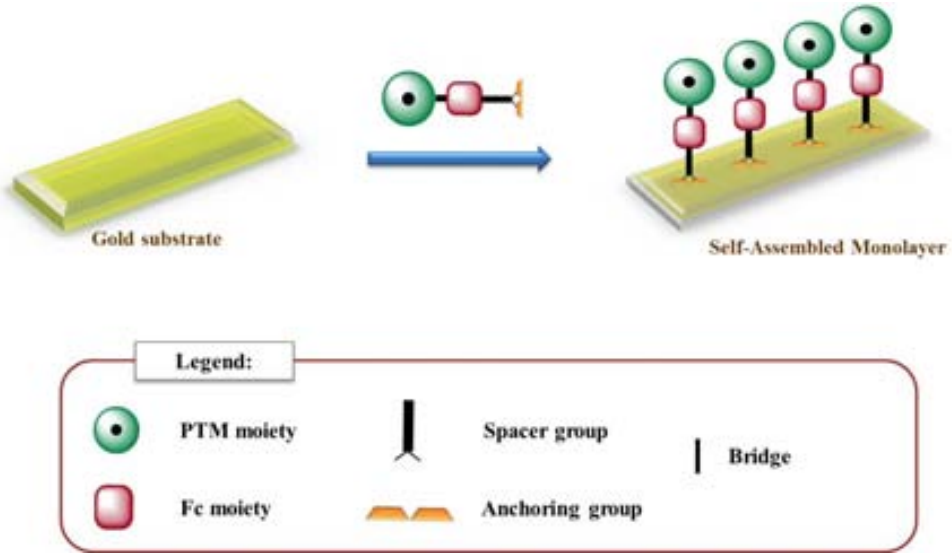

Figure 3.5: Scheme of the one-step approach used for the Fc–PTM functionalization of Au substrates.

The one-step approach has also been reported to be used for the formation of PTM SAMs over gold surfaces[25].

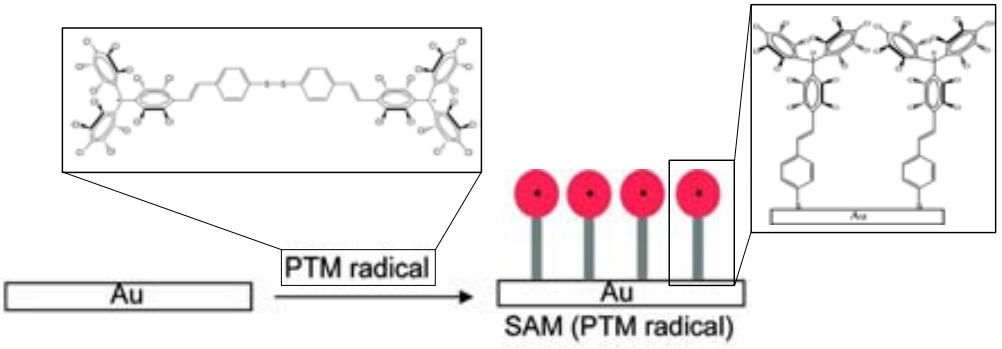

Figure 3.6: Schematic representation of PTM SAMs formed by one-steps approach[25].

In this work, both approaches will be used to prepared SAMs of D–A Fc–PTM systems. First, we will start using the two-steps approach to prepared SAMs of the octamethylated Fc^{8}–PTM and of the non-methylated Fc–PTM system and then, the one-step approach will be used to obtain SAMs of the non-methylated Fc–PTM.

Each SAM will be fully characterized by different surface techniques in order to probe the chemisorption process and a good coverage of the molecules over the substrate.

3.2 Objectives

In this chapter two different approaches will be used to functionalize gold surfaces with D–A electroactive systems. We will start with the so called two-step approach where molecules of 4-aminothiophenol (4–ATP) will be used to prefunctionalize freshly cleaned gold substrates and the chemical coupling between these molecules and Fc–PTM derivatives will take place by means an imine condensation reaction, as it is shown in Figure 3.7.

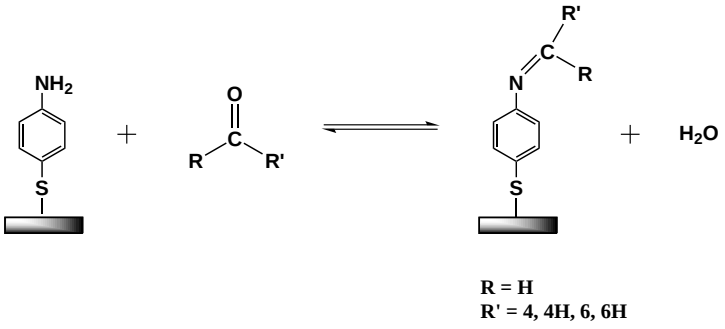

Figure 3.7: Schematic representation of the imine condensation reaction.

Four different Fc–PTM derivatives will be synthesized for the preparation of D–A monolayers using the two-step approach. They are shown in Figure 3.8. The principal characteristic of these Fc–PTM derivatives is the presence of a carbonyl (–CHO) functional group which will react with the amine ($-NH_2$) group of the 4–ATP molecules previously bonded on the gold substrate.

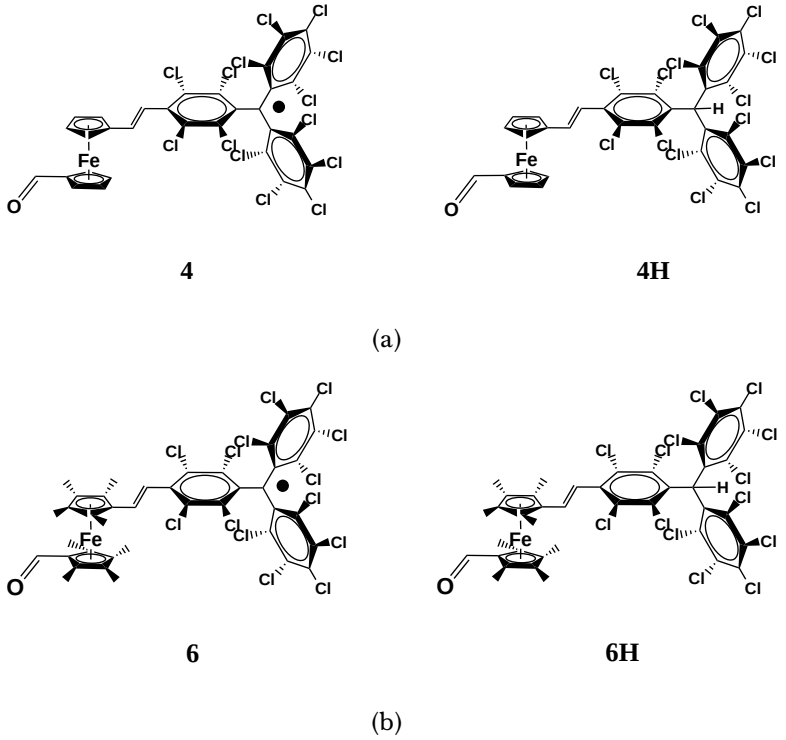

Figure 3.8: D–A derivatives used for the functionalization of surfaces based on (a) the non-methylated Fc–PTM and on (b) the octamethylated Fc^{8}–PTM.

To used the one-step approach, two new D–A molecules that incorporate an appropriate binding group (disulfide) and a spacer chain to isolate the D–A system from the gold substrate will be synthesized. They are showed in Figure 3.9.

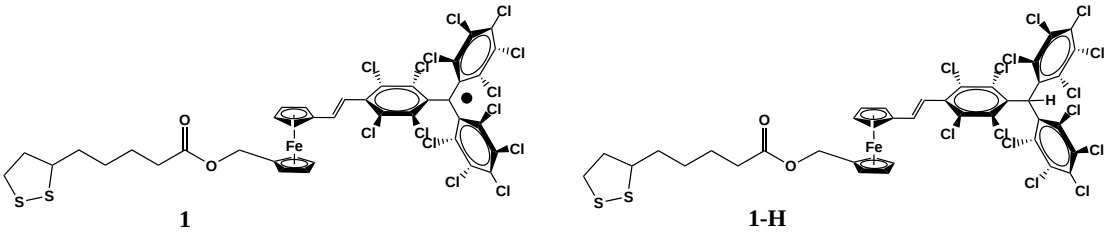

Figure 3.9: D–A Fc–PTM derivatives using in the one-step approach.

Then, different D–A SAMs will be fabricated and characterized using several surface analysis techniques.

3.3 Synthesis of Fc–PTM derivatives to be used in the two-step approach

3.3.1 Synthesis of the non-methylated Fc–PTM derivative 4

The synthesis of the Fc–PTM derivatives **4H** and **4** was made following a similar synthetic route like one previously described in Chapter 2 but using a ferrocene biscarboxaldehyde instead of a monoaldehyde.

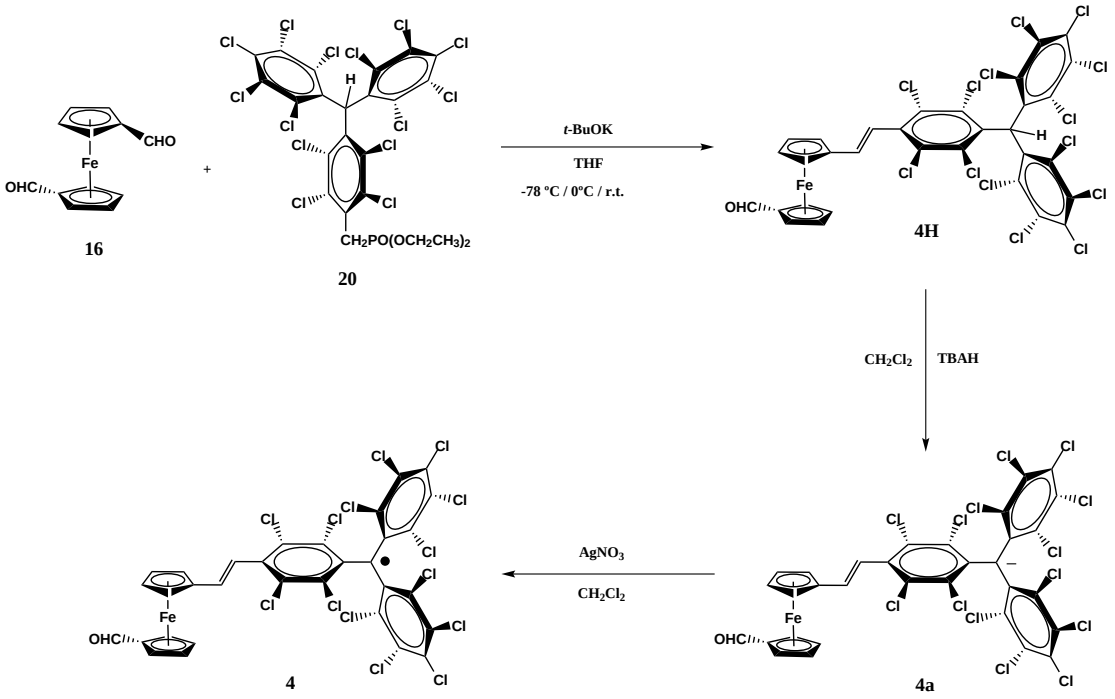

Scheme 3.1: Synthesis of the aldehyde derivatives **4H** and **4**.

So, **4H** was obtained after the purification of a mixture of mono and bi-substituted molecules obtained from a Wittig-Horner-Emmons reaction taken place between the ferrocene biscarboxaldehyde **(16)** and the phosphonate PTM derivative **(20)**. Then, the radical **4** was obtained by the deprotonation of **4H** and the subsequent oxidation of the anionic specie; as is shown in Scheme 3.1. This procedure was made under red light conditions.

3.3.2 Synthesis of the octamethylated Fc[8]–PTM derivative 6

The synthesis of the Fc[8]–PTM derivatives **6H** and **6** was made following the same synthetic route previously described for the non-methylated Fc–PTM derivatives using an octamethylated ferrocene biscarboxaldehyde. Thus, **6H** was obtained after the purification of a mixture of mono and bi-substituted molecules obtained from a Wittig-Horner-Emmons reaction taken place between the octamethylferrocene biscarboxaldehyde **(18)** and the phosphonate PTM derivative **(20)**. Then, the radical **6** was obtained by the deprotonation of **6H** and the subsequent oxidation of the anionic specie, working in absent of light; as is shown in Scheme 3.2.

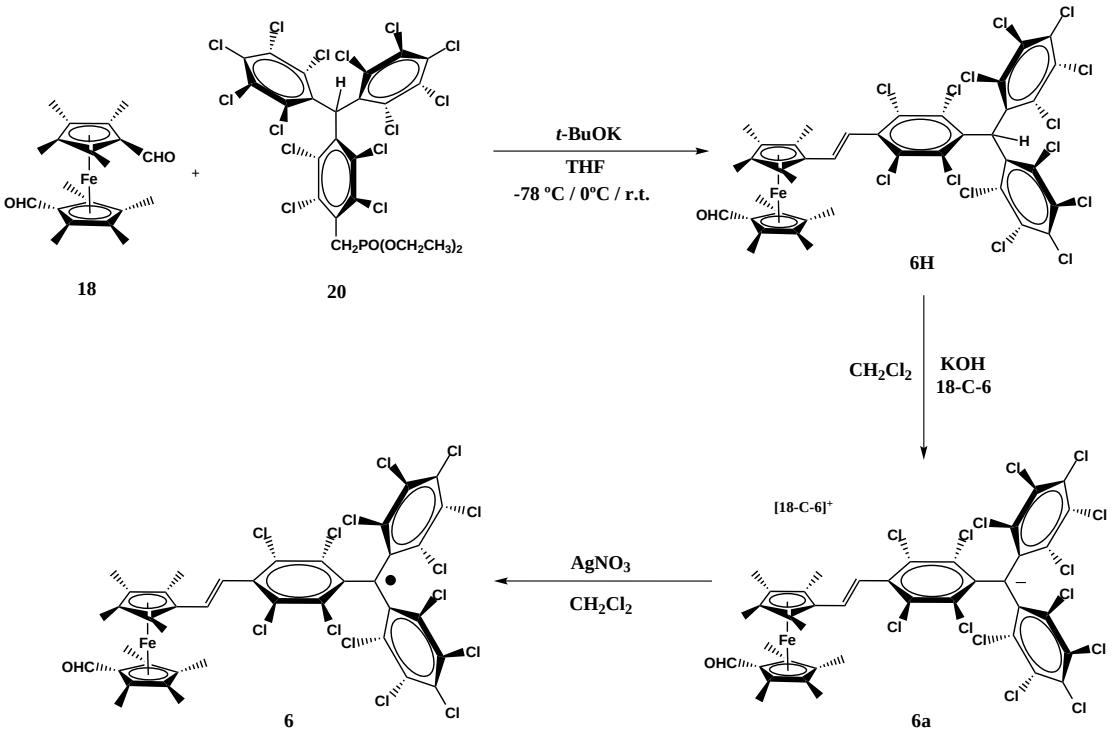

Scheme 3.2: Synthesis of the aldehyde derivatives **6H** and **6**.

3.4 SAMs of Fc–PTM derivatives using the two-step approach

To prepared SAMs by the two-step approach, two different molecules were used. In the first step, a freshly clean gold substrate was prefunctionalized with

4–ATP molecules which structure is shown in Figure 3.10. This molecule has on one side a thiol group (–SH) to anchor the molecule on a surface and on the opposite side the functional amine group ($-NH_2$) which will create a good platform to immobilize in a second step the D–A derivatives conferring interesting and new properties to the surface.

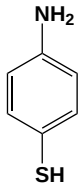

Figure 3.10: 4-aminothiophenol.

The second step will consist in the surface condensation of an amino group with an aldehyde group giving place to an imine covalent bond. For the second step we will use the non-methylated CHO-Fc–PTM radical (**4**) and its protonated form

CHO-Fc–HPTM (**4H**); and the octamethylated CHO-Fc^8–PTM radical (**6**) and its protonated form CHO-Fc^8–HPTM (**6H**) which are represented in Figure 3.8.

3.4.1 Preparation and characterization of the SAM S0

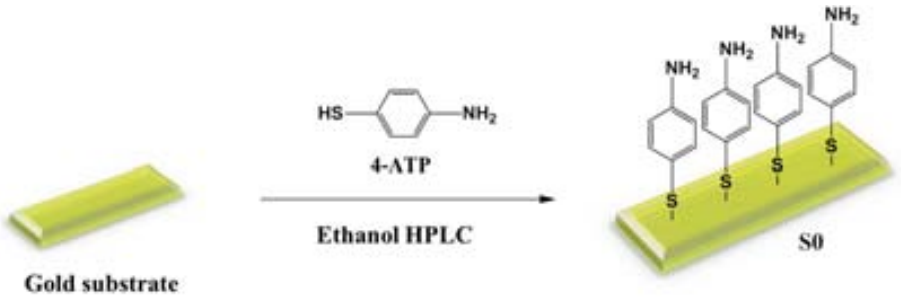

Figure 3.11: Schematic representation of the process of formation of the amino-terminated SAM **S0**.

To prepare SAM **S0**, a gold substrate was cleaned using four different solvents and an UV-ozone clean process (as it is reported in the experimental section) in order to remove any organic soil over the substrate. Then, the freshly clean gold

(Au 111 over mica or policrystalline Au over glass) was immersed in an ethanolic solution 10 mM of 4–ATP for 24 h, under inert conditions (argon atmosphere) according to what is reported in the literature[30,31]. Then, the amino-terminated monolayer **S0** was rinsed with enough ethanol to remove the physisorbed material and finally was dried under an argon stream. Figure 3.11 shows a schematic representation of the process. SAM **S0** was characterized by different surfaces techniques like: XPS, PM-IRRAS, AFM and contact angle; to guarantee the correct formation of the monolayer.

The elemental composition of **S0** monolayer was investigated by XPS focusing on the core-levels of sulfur, carbon and nitrogen atoms. The spectra obtained for these elements are shown in Figure 3.12 and give relevant information on the chemical nature of SAM **S0**. The C1s high-resolution spectrum has been fitted into two main components. The highest peak observed at 284.6 eV was attribute to the contribution of aromatic C–C and C–S bonds, while the peak shifted upwards in energy (286.2 eV) corresponds to C_{arom}–N bonds[30,32].

The N1s high-resolution spectrum curve fitting shows two peaks close in energy; the more intense peak observed at 399.4 eV was assigned to the free amino group $-NH_2$ (~75%) and the peak attributed to the protonated amine $-NH_3^+$ (~25%) was observed at 401 eV[30,32,33] as it has already been reported. Regarding to the S2p high-resolution spectrum, different peaks for the S $2p_{3\,2}$ and S $2p_{1\,2}$ species were observed. The first doublet observed at 161.9 eV, 163.2 eV is assigned to a covalent bond between the gold substrate and the sulfur of the 4–ATP monolayer **S0**. The next doublet around 163.9 eV, 164.9 eV was attributed to unbounded thiols according to values reported in the literature. Free thiols (~ 23%) probably are the results of the adsorption of some molecules through an interaction between N atoms and the Au in the 4–ATP assembly[30,34] as it has been also previously described. Additionally, a broad S2p peak observed at 168.3 eV is assigned to oxidized sulfur species, possibly in the form of sulfonates[35–39]. Oxidized sulfur species (~ 17%) could come from molecules interacting with gold through the nitrogen atom and also from 4–ATP molecules physisorbed on top of the SAM caused by the interplane hydrogen bonds formed between the terminal

functionality ($-NH_2$) of bounded 4–ATP thiolates and free 4–ATP molecules of the bulk solution[40].

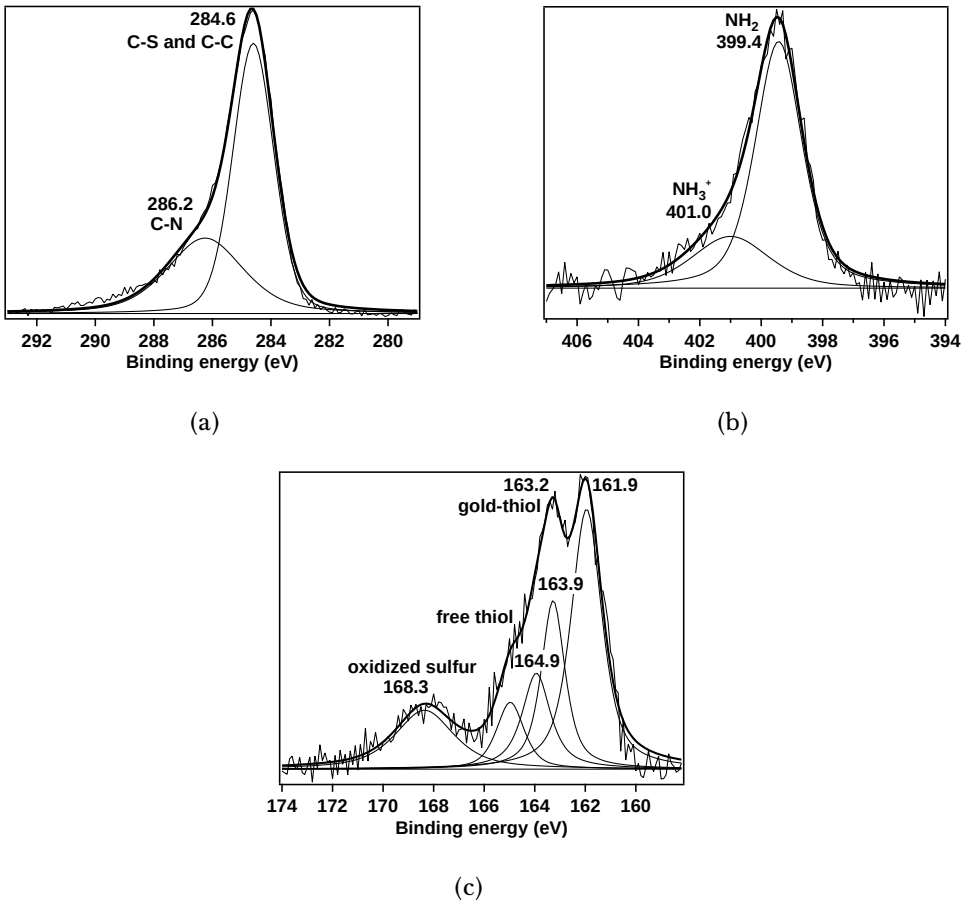

Figure 3.12: High-resolution spectra of (a) C1s, (b) N1s, and (c) S2p of amino-terminated monolayer **S0**.

The characterization of the molecular monolayer **S0** looking into its composition and chemical structure was made by PM-IRRAS. Figure 3.13 shows the comparison between the infrared (IR) spectrum of the 4–ATP in bulk and the PM-IRRAS spectrum of the amino-terminated SAM **S0** on gold. The relative intensity of the bulk spectrum with respect to the monolayer was chosen to give an easy visual comparison. It has to be taken into account because really meaningful comparisons of the intensities of the two types of spectra would require quantitative consideration of the optical and orientation effects at a metal interface[41] and for that they are not considering in this discussion.

Three principal bands maintain a good correlation between the molecule in 3D phase (bulk) and organized as 2D structure (SAM). The band observed around 1620 cm^{-1} is assigned to NH_2 in-plane deformation; while the band at 1492 cm^{-1} is related with C=C ring vibrations in-plane[42]. The intense band around 1593 cm^{-1} is assigned to C–C stretching vibration of benzene rings according to the literature[43].

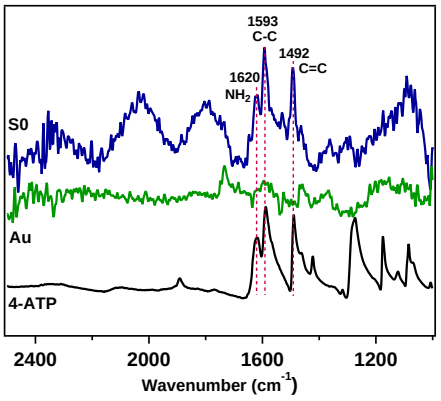

Figure 3.13: PM-IRRAS spectra of SAM **S0** compared with that of a bare substrate and the IR-spectrum of the molecule in bulk.

Both analysis XPS and PM-IRRAS of SAM **S0** confirm the presence of the molecule in a chemisorbed form on the gold substrate.

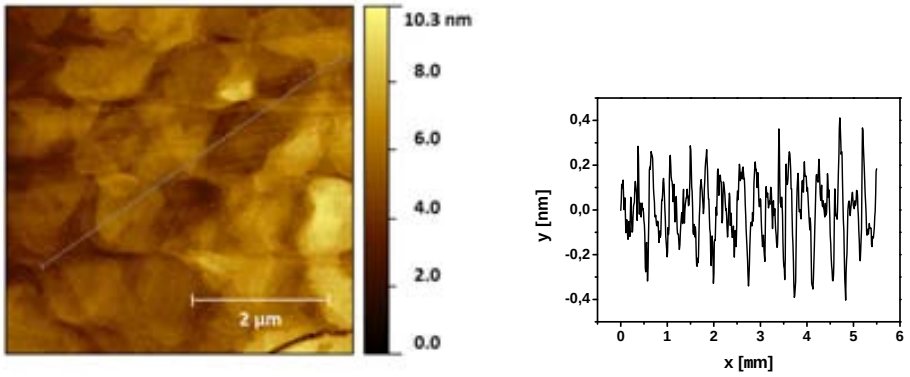

(a) (b)

Figure 3.14: (a) 5 μm x 5 μm AFM image and (b) roughness pro le of the amino-terminated SAM **S0**.

Additionally, AFM was used to analyze the homogeneity of the amino-terminated SAM **S0**. Figure 3.14 shows the topography of the surface as well as the roughness

profile in a random selected line across the AFM image. The topography follows exactly the same corrugation of the gold which is indicative of the complete monolayer formation without defects.

The contact angle of a surface gives important information regarding its wettability which is an intrinsic property of each system. Here contact angle measurements of a 3 μL Millipore water drop dispensed over the bare and functionalized gold (SAM **S0**) were performed and mean values obtained from at least three replicas were calculated. SAM **S0** shows a lower contact angle (79°±1.6) in comparison with the bare gold (83°±1.5) which indicates increased hydrophilicity due to the presence of the amino-terminated groups (NH_2) which can form hydrogen bonds with the water molecules.

Once it has been characterized the amino-terminated SAM **S0** and confirmed its chemisorbed nature. It is possible to continue with the preparation of the D–A monolayers, the main interest of this work.

3.4.2 Preparation and characterization of the octamethylated Fc^8–PTM SAM S6 and S6-H

The coupling between the amino-terminated monolayer **S0** and the aldehyde derivatives of the octamethylated Fc^8–PTM (**6H** and **6**) will be done through the formation of an imine bond[44]. Such bond will allow to maintain a π-conjugated structure along the whole system which will favour the study of charge transport through these well-defined 2D structures. It is import to take into account that in this imine condensation reaction two factors are essential: the availability of the reactive groups for the nucleophilic attack from the amine to the aldehyde, and the elimination of water molecules which at the end will determine the equilibrium of the reaction.

For a good surface coverage (homogeneity), a proper packing of the 4–ATP molecules and availability of the NH_2 groups at the top of the monolayer are essential features in order to achieve a high yield of the imine condensation reaction. Moreover, to displace the equilibrium of the reaction towards the imine formation is important to use a dehydrating agent. Under these considerations, different con-

ditions were tested in order to optimize the preparation of well-defined D–A SAMs using the two-step methodology.

Thus, after the preparation of **S0**, in the second step the freshly amino-terminated SAM **S0** was immediately immersed in a solution [1 mM] of the corresponding octamethylated Fc^8–PTM derivative (**6** and **6H**) under inert conditions. Two different solvents were tried for each SAM, dry toluene and trimethyl orthoformate (TMOF). It has been reported that TMOF can be used as solvent and dehydrated agent[45] which it is expected to favour the imine condensation reaction. The reaction was left for 48 hours under an argon atmosphere and finally the new SAMs **S6** and **S6-H** were rinsed with the same solvent used for their preparation in order to avoid breaking the imine bond. Finally, the SAMs were dried under an argon stream. All the preparation process was made under red light conditions since the PTM radicals are not stable under light in solution. Figure 3.15 shows a schematic representation of the preparation process of SAMs **S6** and **S6-H** on Au substrates, using the two-step methodology.

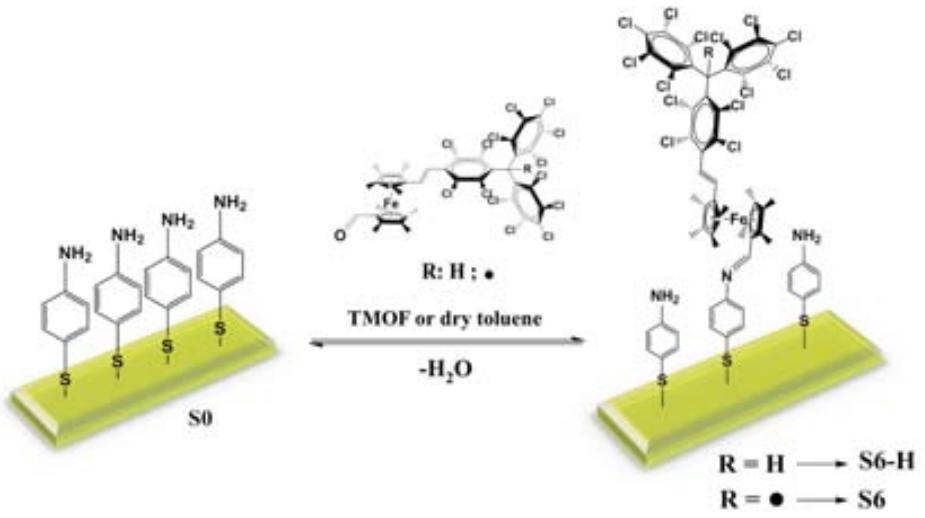

Figure 3.15: Schematic representation of the process of formation of the D–A SAM **S6** and its protonated form **S6-H**.

SAMs **S6** and **S6-H** were characterized using different surfaces science techniques. The chemical composition of SAM **S6-H** was analyzed through PM-IRRAS. The PM-IRRAS spectrum of **S6-H** is shown in Figure 3.16 and it is compared with the spectra obtained for **S0**. A drop-casted sample of **6H** in CH_2Cl_2 [1mM] di-

rectly on a gold substrate was also used to compare. As it can be seen, a new band appears around 1647 cm^{-1} which is attributed to the formation of the imine bond[46]. The peak corresponding to the aldehyde group observed at 1668 cm^{-1} in the drop-casted **6H** is not present in SAM **S6-H**. However, the broadness of the imine band could indicate that some contribution of the in-plane deformation band of free NH_2 ($\sim$ 1620 cm^{-1}) is overlapped.

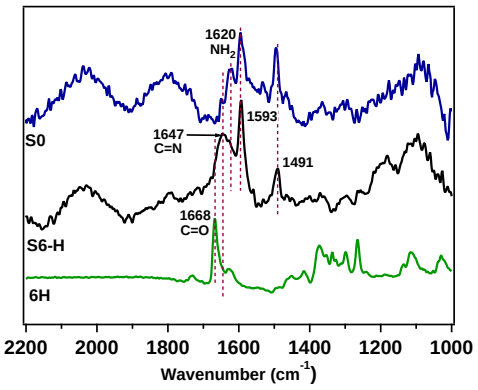

Figure 3.16: PM-IRRAS spectrum of SAM **S6-H** prepared with Tmof as solvent and comparison with the amino-terminated SAM **S0** and a sample of **6H** drop-casted on gold.

Moreover, two additional bands were clearly observed at 1594 and 1492 cm^{-1} which were attributed to C–C stretching vibrations and C=C ring vibrations in-plane[47] of the benzene rings, respectively. These bands have also been observed for SAM **S0**. Then, it seems that we have several NH_2 groups in free state which could be related with the big size of the PTM moieties in comparison with the size of the 4–ATP molecules which is not allowing a total coverage of the surface with the D–A systems due to a steric hindrance.

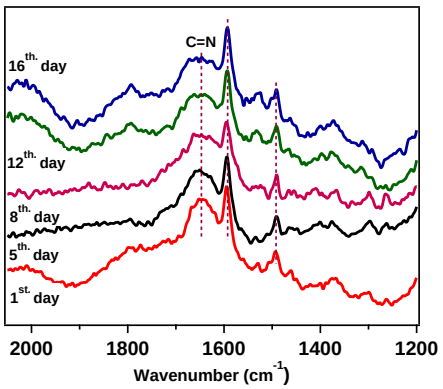

Figure 3.17: PM-IRRAS spectra of SAM **S6-H** taken at different days along two weeks.

In order to investigate the stability of the SAM **S6-H**, different measurements along two weeks were performed and they are shown in Figure 3.17. Even though the band observed around 1647 cm^{-1} assigned to the imine condensation formation, is maintained along the time, its broadness changes. After one week it starts to decay which is a clear indication of the sensitivity of this SAM. This band completely disappears after contact angle measurements which indicates the complete hydrolysis of the imine bond, as shown Figure 3.18.

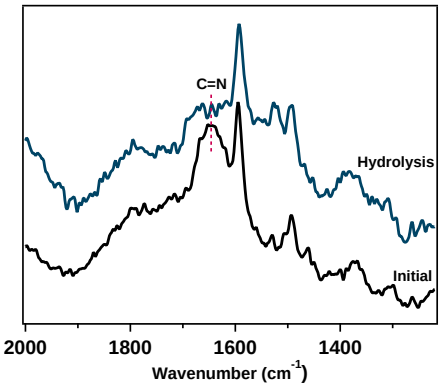

Figure 3.18: PM-IRRAS spectra of a freshly prepared SAM **S6-H** before and after hydrolysis.

Figure 3.19 shows the PM-IRRAS of **S6** in comparison with the spectra of SAMs **S6-H** and **S0**. The resolution of the spectra obtained for **S6** is lower than the others.

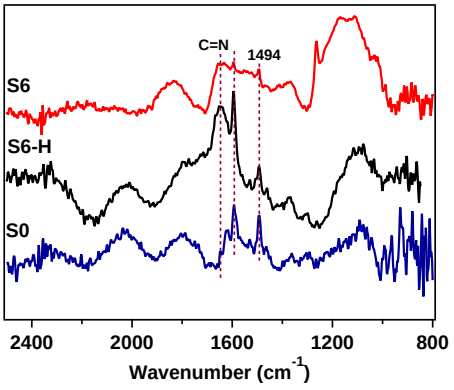

Figure 3.19: Comparison of PM-IRRAS spectra of SAM **S6** with respect to the protonated SAM **S6-H** and the amino-terminated SAM **S0**.

The band around 1648 cm^{-1} even with lower resolution still can be observed and was assigned to the imine formation (C=N), while the bands localized at 1594

and 1494 cm^{-1} could be related with the presence of unreacted 4–ATP molecules. As it was also been observed for **S6-H**. This is an indication that we do not have the surface complete functionalized with the D–A system, but we have a mixed monolayer of **S0** and **S6**.

As mentioned before the presence of bands corresponding to the SAM **S0** is an indication that the PTM is bigger building block than the 4–ATP leaving unreacted molecules but it can also be an indication that the imine formation has a low yield.

Following with the analysis of the chemical structure of SAMs **S6** and **S6-H**, XPS measurements were performed focusing on the core level of S2p, C1s, N1s, Fe2p and Cl2p. The high-resolution spectrum of each element was fitted and the graphs obtained are shown in Figure 3.20 and 3.21. The binding energy values are collected in Table 3.1.

The fitting of the high-resolution XPS spectrum for the S2p binding energy region was similar for both monolayers **S6** and **S6-H**. Three different species were observed: gold bound thiolates (S $2p_{3\,2}$ = 162.0 eV), unbound thiols (S $2p_{3\,2}$ ~ 164.0 eV) and oxidized sulfur species (168.3 eV). Such peaks are quite similar to that observed in the amino-terminated SAM **S0**.

The curve fitting performed in the C1s region showed three bands. The bigger one is localized at 284.6 eV and was attributed to both C–C and C_{arom}–S bond[30]. The band observed at 286.3 eV was assigned to the contribution of C_{arom}–N and sp^2 carbon atoms present in the chlorinated phenyl groups of the PTM moiety[48]. Finally, the band at 288.0 eV was related with C–Cl bonds[49].

The common organic nitrogen functionalities give N1s binding energies in the narrow region 399–401 eV[32]. N1s XPS spectra for both monolayers (**S6** and **S6-H**) were fitted to two bands, one band at 399.8 eV which is characteristic of a free amino group $-NH_2$[33] and other at lower energy (398.9 eV). Since the increase on the basicity of a nitrogen atom induces a shift towards lower binding energies[38,50], this new band clearly reflects the imine formation (C=N) in both SAMs **S6** and **S6-H**, as imine is a stronger base than amine. However, only a few percentage (~ 15%) of the N1s found in these SAMs corresponds to the imine

formation which corroborates that we have mixed monolayers, as it has been previously suggested from the PM-IRRAS analysis.

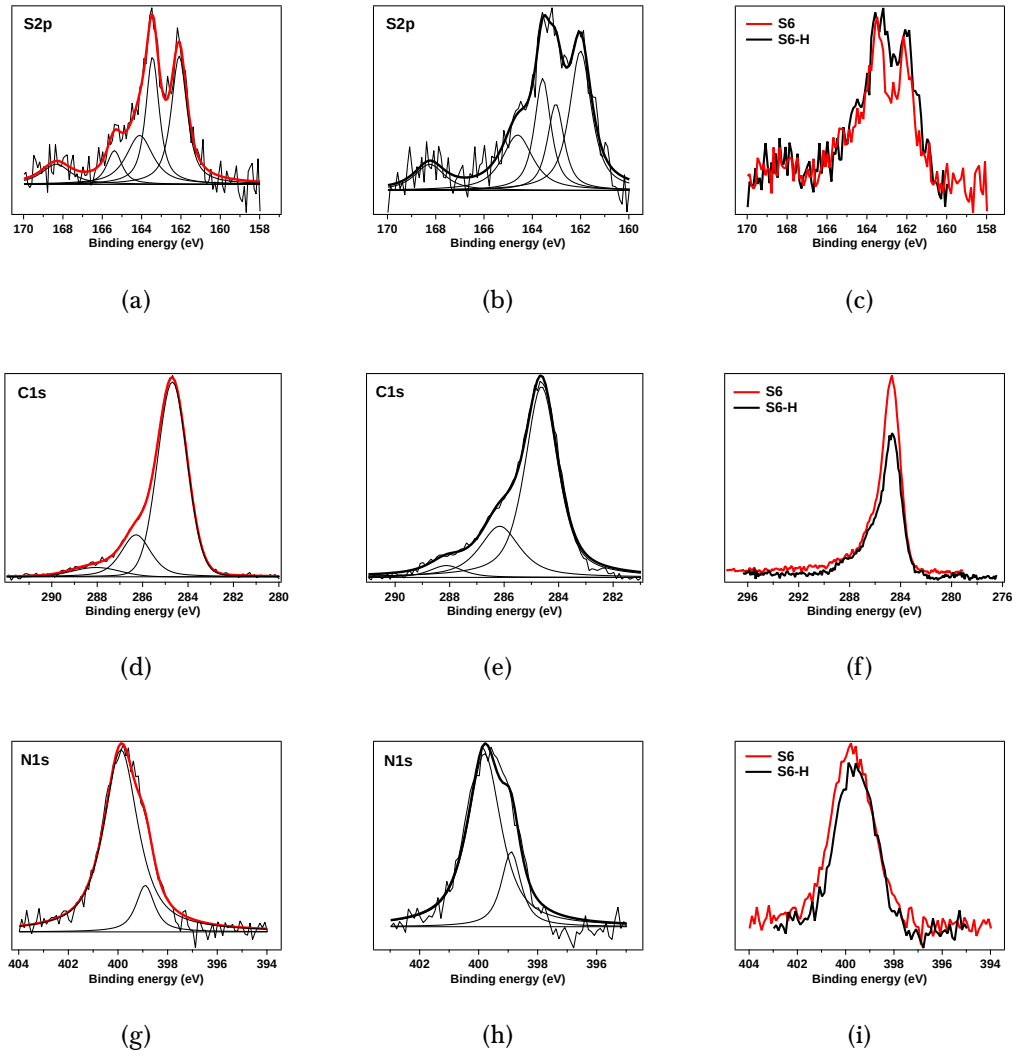

Figure 3.20: High resolution spectra of S2p of (a) **S6**, (b) **S6-H**, and (c) a comparison of both, C1s of (d) **S6**, (e) **S6-H** and (f) a comparison of both, N1s of (g) **S6**, (h) **S6-H** and (i) a comparison of both.

Regarding to the iron element, it is known that the peak positions of Fe $2p_{1\ 2}$ and Fe $2p_{3\ 2}$ depends on the ionic state of the atom; so special attention was put in the deconvolution of the spectrum of this element which has been obtained with very low resolution for both monolayers **S6** and **S6-H** even the accumulation of many scans. Such low resolution can be due to the fact that there is only one iron atom per molecule but also to the low yield of the imine condensation reaction in

the second step.

The poor signal-to-noise ratio of these spectra does not allow a clear identification of the iron species. However it seems that the reduce state of iron is present in **S6-H** while in **S6** peaks at binding energies associated with both reduced and oxidized state according to that reported in the literature[51], seems to be observed. But the low resolution obtained for these spectra and the high noise level do not allow to extract more conclusions from these data. Nevertheless it seems that we only have few active molecules on the surface.

Finally, the Cl2p spectra for **S6** and **S6-H** showed a common doublet around 200.6 – 202.5 eV which corresponds to Cl $2p_{3\ 2}$ and Cl $2p_{1\ 2}$, respectively. Such bands are characteristics of C–Cl bonds present in the PTM moiety[48]. Regarding to the Cl2p spectrum of **S6**, other doublet at lower energy (197.5 - 199.3 eV) was clearly identified. This doublet could be related with *meta* position of the chlorine atoms of the PTM.

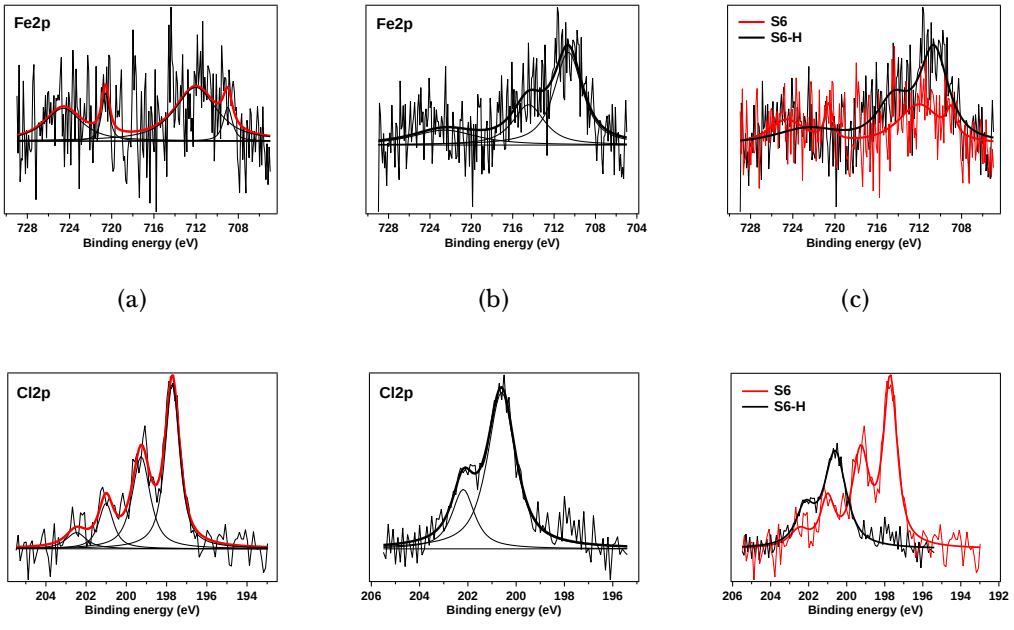

Figure 3.21: High resolution spectra of Fe2p of (a) **S6**, (b) **S6-H** and (c) a comparison of both, and Cl2p of (d) **S6**, (e) **S6-H** and (f) a comparison of both.

Table 3.1: High-resolution photoemission spectra data for **S6** and **S6-H** monolayers.

Atom	Binding energy (eV)		Type of bond
	S6	**S6-H**	
$Cl2p_{3\ 2}$	197.7		*meta* position of chlorine
$Cl2p_{1\ 2}$	199.3		
$Cl2p_{3\ 2}$	201.0	200.6	C–Cl bond, characteristic feature
$Cl2p_{1\ 2}$	202.5	202.2	of the PTM moiety.
$Fe2p_{3\ 2}$	709.0	710.6	Reduced state of the Fc moiety.
$Fe2p_{1\ 2}$	720.6	722.6	
$Fe2p_{3\ 2}$	712.0		Oxidized state of the Fc moiety.
$Fe2p_{1\ 2}$	724.6		
C1s	284.7	284.6	C–C and C_{arom}–S
	286.3	286.2	C_{arom}–N and sp^2 carbon atoms.
	288.0	288.1	C–Cl
N1s	398.9	398.9	N=C
	399.8	399.8	NH_2
$S2p_{3\ 2}$	162.0	162.0	Gold bound thiolate.
$S2p_{1\ 2}$	163.4	163.0	
$S2p_{3\ 2}$	164.1	163.6	Unbound thiols.
$S2p_{1\ 2}$	165.4	164.6	
S2p	168.4	168.3	Oxidized sulfur species.

SAMs **S6** and **S6-H** were also characterized by ToF-SIMS. Figure 3.22 shows the spectra obtained for both SAMs (**S6** and **S6-H**) in which is possible to observe the typical isotopic distribution for the 14 chlorine atoms belonging to the PTM moiety. Molecular fragments of different weights were observed for each monolayer. The peak at 750 m/z is attributed to the ionized specie $PTM^{\bullet}–CH_2=C^{+}$. Typical losses of chlorinated atoms of 35 are also observed as shown the peak identified at 1091 m/z which corresponds to [M]–3Cl.

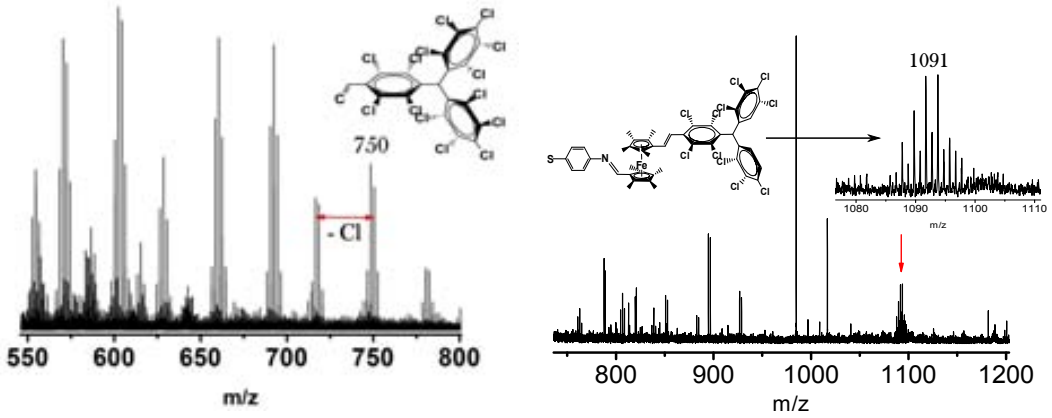

(a) (b)

Figure 3.22: ToF-SIMS spectra of (a) **S6** and (b) **S6-H** monolayers.

As we are dealing with an open-shell system **S6**, at this point it is also interesting to study if the magnetic character of the PTM is maintained once anchored on a surface. In fact, the characteristic signal of PTM radical immobilized on a surface was observed by electronic paramagnetic resonance (EPR) for SAM **S6** and it is shown in Figure 3.23 which is indicative of the conservation of the magnetic character of the PTM. This signal presents a g-factor = 2.00355 with a ΔH_{pp} = 8.5 G, values very close to that observed for other PTM radicals in solid state[28].

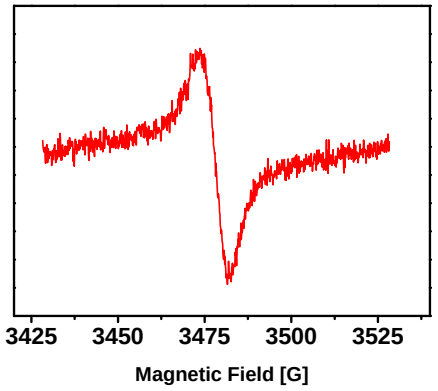

Figure 3.23: EPR of SAM **S6**

As it has been analyzed through the different surface techniques, D–A systems **6** and **6H** are chemical adsorbed on the top of prefunctionalized **S0** gold surfaces. However, from the data obtained we can say that it has not been possible

to obtain a complete molecular monolayer and instead, we have obtained mixed monolayers of **S0**/**S6** and **S0**/**S6-H**. The reason why no complete molecular monolayer coverage was achieved is essentially the second step of this approach. Then different factors can be considered to explain the poor yield of the imine formation: *1)* methylated Fc could be deactivating the imino condensation, *2)* imine is a labile bond very susceptible to ambient conditions, *3)* di cult to remove water from the reaction which is very important to displace the equilibrium of the reaction towards the formation of the desired product, *4)* the possible interaction of the 4–ATP molecules with gold through the nitrogen atom which prevent that imine condensation reaction takes place.

To study the electronic properties of D–A SAMs, which is the objective of this work we need very homogeneous and stable systems and thus mixed monolayers are not good candidates. At this point, it is necessary to improve the methodology used in order to obtain SAMs of D–A systems with high surface coverage. To do it, some experimental factors were taken into account for both steps used in the SAMs preparation. First, we will improve the quality of the amino-terminated monolayer **S0** in order to improve the molecular packing and avoid the formation of a second 4–ATP layer due to weak hydrogen bond interactions between the molecules anchored on the surface and molecules present in the solution. To do it we use 3% (v/v) of triethyl amine dissolved in the ethanolic solution of 4–ATP. The SAM obtained was rinsed with a solution of ethanol and 10% (v/v) of acetic acid, then with a solution of ethanol and 3% (v/v) of thiethyl amine and finally with pure ethanol[52]. SAM **S0** was dried under a nitrogen stream and immediately immersed in a solution of the corresponding Fc^{8}–PTM derivative (**6** or **6H**). Second, to obtain a better yield of the in-situ condensation reaction we tested the addition of 0.08% (v/v) of acetic acid in the solution of **6** or **6H** in the presence of activated molecular sieves (ca. 1g) to absorb water molecules, as it has been previously reported[44].

From all the different new methodologies used for the optimization of D–A SAMs, modifying different experimental factors, no clear success in our purpose of improving the coverage and homogeneity of these SAMs was achieved. In all

cases, low homogeneity and coverage as the previously mentioned or even worst were obtained. Since, as we have previously infer, one of the reasons of the low yield of the imine condensation reaction is the deactivation of the aldehyde **6** and **6H** due to the eight methylene groups that affecting negatively the imine formation. This is the reason why at this point we decided to try the same methodologies used until now for the preparation of SAMs in two-steps but using the non-methylated Fc–PTM derivatives **4** and **4H** in order to obtain more stable 2D structures.

3.4.3 Preparation and characterization of the non-methylated Fc–PTM SAM S4-H

Following the same two-step methodology, a new SAM **S4-H** was prepared using the non-methylated Fc–PTM derivative **4H**. To do it, a freshly amino-terminated SAM **S0** was immersed in a solution [1 mM] of **4H** under inert conditions. Here were also tested two different solvents: dry toluene and TMOF. The reaction was left for 48 hours under an argon atmosphere and finally SAM **S4-H** was rinsed with the same solvent used for its preparation (dry toluene or TMOF) and dried under an argon stream. Figure 3.24 shows a schematic representation of the preparation process of SAM **S4-H** on Au substrates, using the two-step methodology.

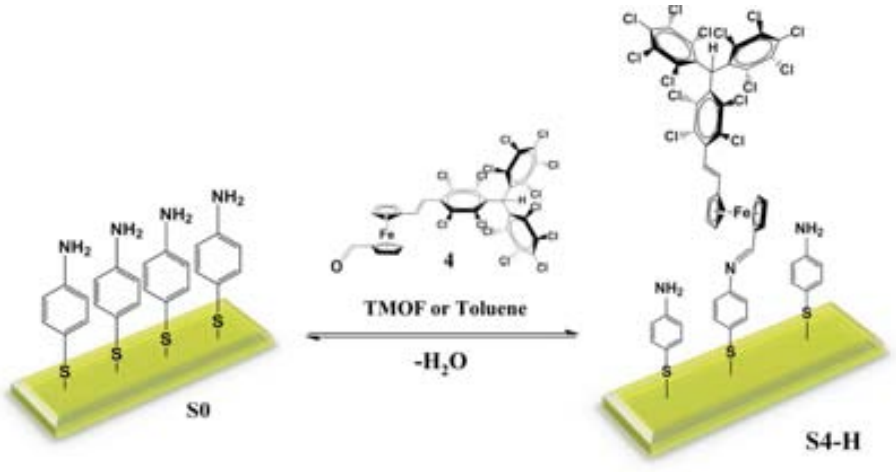

Figure 3.24: Schematic representation of the process of formation of the D–A SAM **S4-H**.

The elemental composition of SAM **S4-H** was studied by XPS and ToF-SIMs.

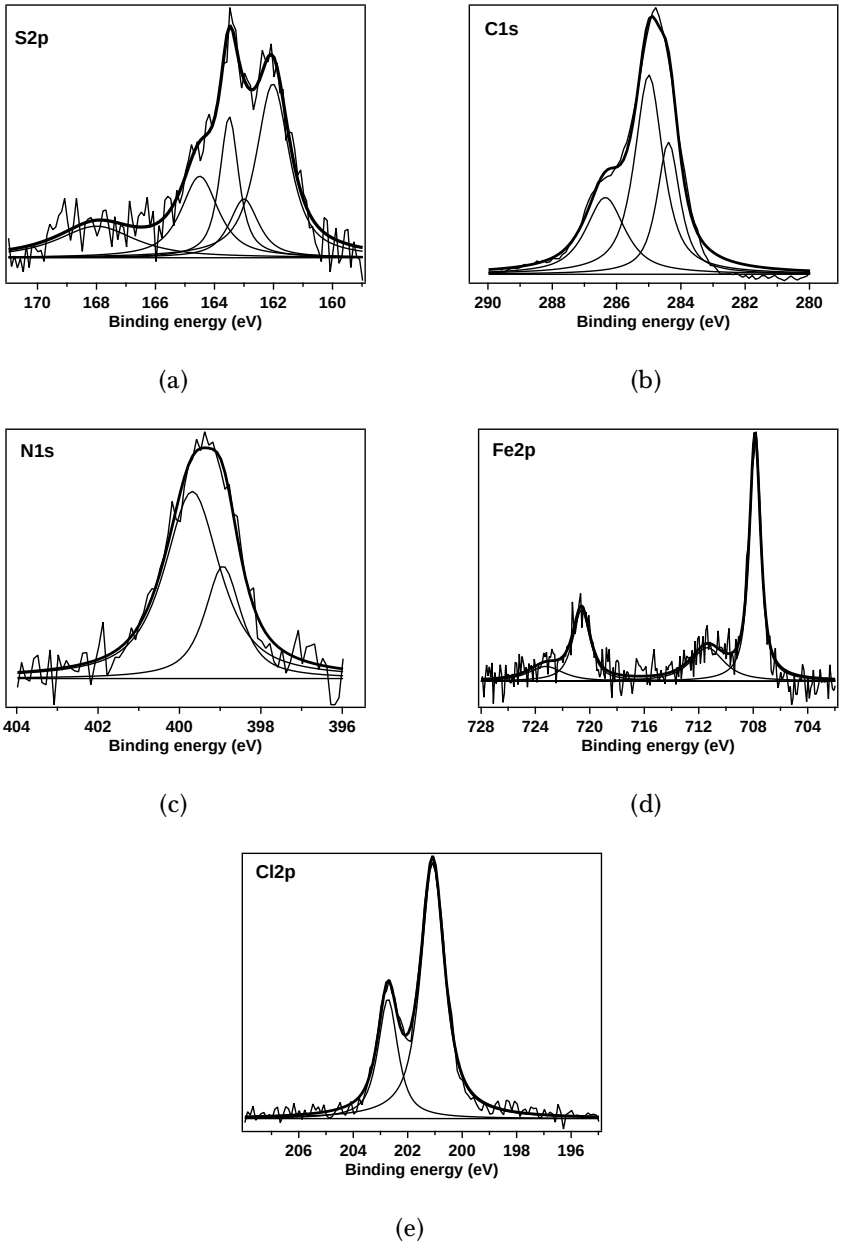

Figure 3.25: High resolution spectra of (a) S2p, (b) C1s, (c) N1s, (d) Fe2p and (e) Cl2p of SAM **S4-H**.

Figure 3.25 shows the spectra corresponding to the core level of S2p, C1s, N1s, Fe2p and Cl2p. Similar characteristics to that obtained for SAMs **S6** and **S6-H** were observed. From the S2p spectrum it was determined that both bonded (162 and 163 eV) and unbounded (163.5 and 164.5 eV) thiols are present on the monolayer. Oxidized species (~168 eV) were also observed.

C1s high-resolution spectrum shows the contribution of C–C and C_{arom}–S (284.4 eV), C_{arom}–$C_{central}$ of the PTM and cyclopentadienylcarbons (C_{Cp}) (285 eV)[53,54] and also C_{arom}–N and sp^2 carbon atoms (286.4 eV). In the N1s XPS spectrum both bands corresponding to neutral amino group (399.7 eV) and imine bonds (398.9 eV) were identified. Regarding to the Fe2p spectrum, four peaks at 707.8, 720.6, 711.4 and 723.2 eV were distinguished. Such peaks could be related with the presence of reduced and oxidized species. However, for the protonated **S4-H** monolayer it is not possible that the IET takes place generating the zwitterionic specie. The last two peaks located at 711.4 and 723.2 eV can be tentatively attributed to external effects caused by radiation or by impurities from solvents. Finally, the typical doublet of Cl2p (201 and 202.7 eV) was observed, confirming the integrity of the molecules over the surface.

The characteristic isotopic distribution of 14 chlorine atoms is observed in Figure 3.26. Three different molecular fragments were found and the lost of two chlorine atoms was also distinguished.

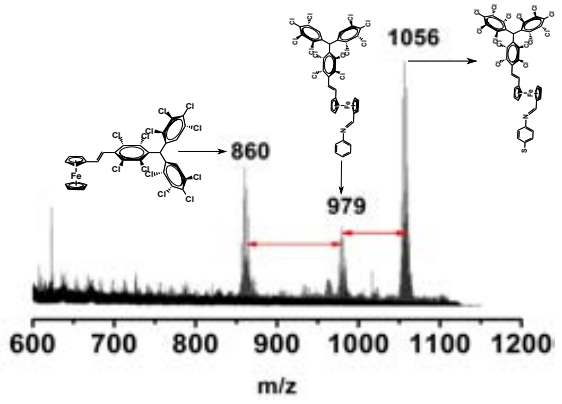

Figure 3.26: ToF-SIMS spectra of **S4-H** monolayer.

As we are dealing with electroactive building blocks we have also the possibility to study their redox processes once they are immobilized over a metallic surface. CV is a very useful technique to probe the presence of electroactive molecules attached to conductive surfaces. This technique also allows to study the stability of the monolayers and how easy the molecules desorb from the surface. The experiments were carried out with the standard setup using the functionalized substrate

(**S6**, **S6-H**, **S4** and **S4-H**) as working electrode (WE), solid silver and platinum wires as reference (RE) and counter-electrode (CE), respectively, and a solution of 0,1 M tetrabutylammonium hexafluorophosphate (TBAHFP) in acetonitrile as electrolyte. All measurements were referenced to Fc/Fc^{+} and the setup used is shown in Figure 3.27.

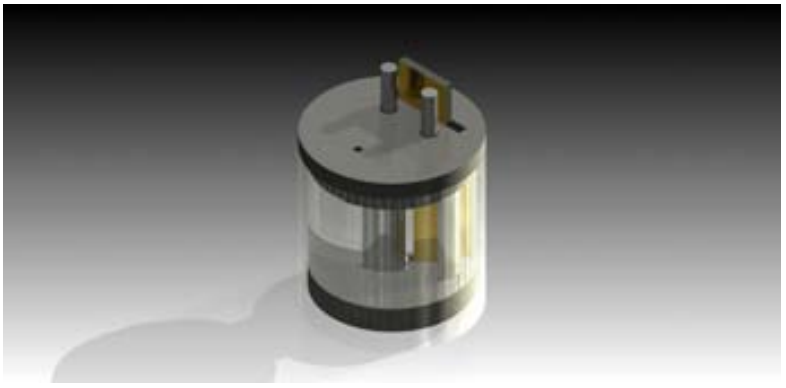

Figure 3.27: Schematic representation of the CV setup used. The three electrodes were: Au functionalized surface (WE), silver wire (RE) and platinum wire (CE).

Figure 3.28 shows the cyclic voltammograms at two scan rates (0.1 and 1 V/s) of the different SAMs prepared from the octamethylated Fc^{8}–PTM and non-methylated Fc–PTM derivatives (**6**, **6H** and **4**, **4H** respectively) using TMOF and dry toluene as solvent for the SAMs preparation.

As can be seen, at 0.1 V/s scan rate it was not possible to distinguish any redox peak. However increasing the scan rate (1 V/s) it was observed with some di culty the peaks corresponding to the oxidation of the ferrocene moiety and the reduction of the PTM unit. After some scans the low signal observed diminished even more until disappears which is an indication once again that these SAMs are not stable. The small peaks observed are also an indication that only few electroactive molecules are bonded to the gold and the low homogeneity and coverage of the SAMs.

All the challenges faced out during the fabrication of D–A monolayers using the two-step methodology like: *i)* possible bonding of the 4–ATP molecules on gold through the amino group, *ii)* low yield of the imine formation due to a possible steric impediment produced by the bulky PTM units, *iii)* deactivation of the

aldehyde D–A building block that possible difficult the nucleophilic attack of the nitrogen, *iv)* low stability of the imine bond, among other; have been not possible to overcome. For this reason we move to the one-step approach.

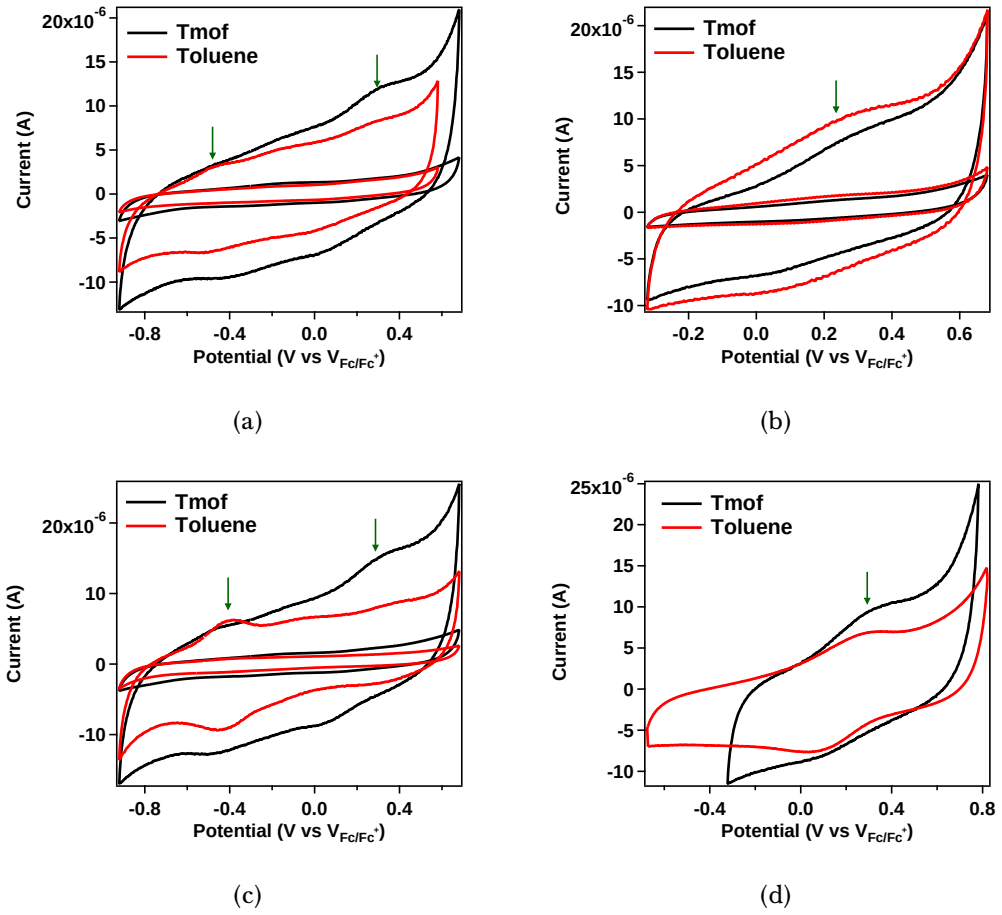

Figure 3.28: Cyclic voltammograms of (a) **S6**, (b) **S6-H**, (c) **S4**, and (d) **S4H** monolayers in acetonitrile, with 0.1 M $n-BuNPF_6$ at two different scan rates: 100 and 1000 mV/s. Comparison of SAMs obtained from two different solvents: TMOF and dry toluene.

3.5 Synthesis of Fc–PTM derivatives to be used in the one-step approach

Due to the difficulties faced to obtain D–A SAMs using the two-step approach we decided to functionalize the gold substrates using the one-step approach. In this line, three different molecular systems have been used. On one side, and in the effort of maintaining the π-conjugated structure along the whole molecule a new

Fc–PTM derivative **8H** was synthesized. On the other side, to accomplish this strategy, other two new molecules **1** and **1H** were synthesized. Since the thiol group has been widely used to anchor molecules on gold[3,55] and the relative big size of the Fc–PTM dyad, disulfide binding group was chosen to confer a better stability to the entire system. Fc–PTM derivatives, the radical and its protonated counterpart used to the functionalization of gold substrates has been previously shown in Figure 3.9.

The synthesis of Fc–PTM derivatives used for the modification of gold surfaces is summarized below. However all the details concerning the synthesis are full described in the experimental section (Chapter 7). It is import to mention that the synthetic rout to obtain compound **1**, the radical derivative, was made under red light conditions because the radical specie in solution is unstable under light.

3.5.1 Synthesis and characterization of 8H

In order to better control the reaction of imine condensation we have synthesized in solution the entire molecule to be used for the SAM formation in one-step. Thus, the Fc–PTM derivative **8H** was synthesized by a condensation reaction between the 4–ATP and the **4H** using toluene as solvent at 120 °C in a dean-stark system that allows to eliminate the water formed on the solution, as it is shown in Scheme 3.3. Molecules with disulfide bonds were formed due to the oxidation of thiols groups belonging to the 4–ATP assuming caused by the atmospheric molecular oxygen, giving place to molecules of the form R–S–S–R and R⊠-S–S–R.

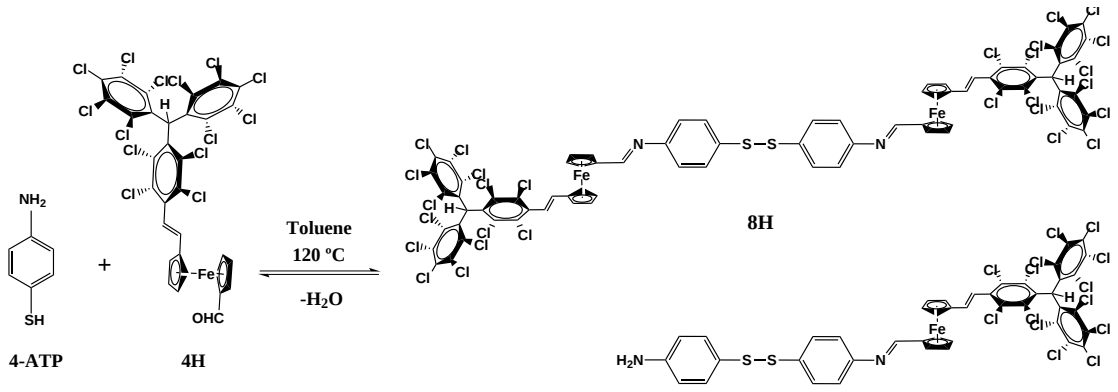

Scheme 3.3: Synthesis of **8H**.

The IR spectrum of **8H** is shown in Figure 3.29. More than one important band, like the corresponding to the vynilene bridge (CH=CH), free amino groups (NH_2) and the imine bond (C=N), appears at similar wavenumber (around 1615 – 1640 cm^{-1}). Important is the fact that the band corresponding to free carbonyl group (–CHO) localized around 1680 cm^{-1} in **4H** was not observed.

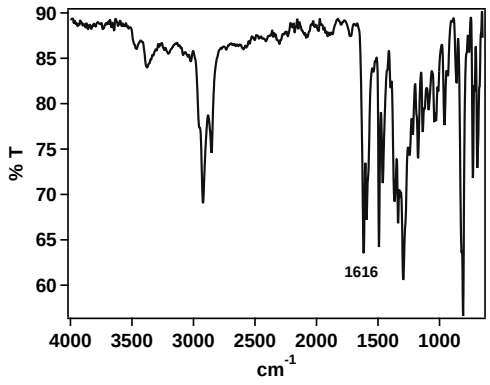

Figure 3.29: IR spectrum of **8H** derivative.

According to the NMR spectrum of **8H** it was possible to identify that we have a mixture of mono and bi-substituted molecules (like it is shown in Scheme 3.3) and also some unreacted 4–ATP dimers. The mixture was tried to purify using different strategies but any of them give good results, for this reason we decided to used the crude product for preparation of SAM **S8-H** in order to probe the one-step approach as a first attempt. The radical derivative **8** was not synthesized due to the sensitivity of the imine bond and the difficulties faced out during the purification of **8H**.

3.5.2 Synthesis and characterization of *5*

In order to obtain a complete study of the effect of D–A systems organized as 2D structures (SAMs with oriented dipoles), a new molecule containing the disulfide-alkyl chain and the Fc moiety was synthesized. Compound ***5*** was obtained through the esterification reaction between the ferrocenemethanol and the (±)-α-lipoic acid, according to the synthetic route showed in Scheme 3.4.

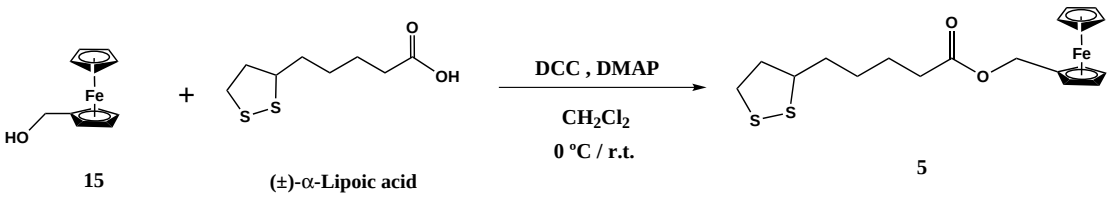

Scheme 3.4: Synthesis of **5**.

Formation of the ester was probed by the IR spectrum of **5** showed in Figure 3.30 where clearly is observed a strong band at 1728 cm^{-1}.

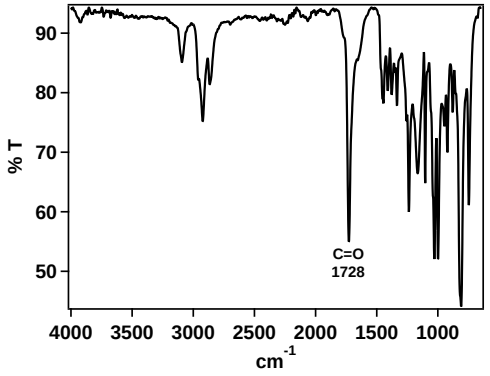

Figure 3.30: IR spectrum of **5** derivative.

3.5.3 Synthesis and characterization of 1H

In order to synthesized compound **1H** it was necessary to obtain the precursors **20** and **4H**. The protonated PTM phosphonate derivative **20** was synthesized following the procedure reported in the literature[56–58]. The multi-step synthetic route starts with a Grignard reaction between benzophenone and *p*-toluenemagnesium bromide to produce the corresponding alcohol **28**. Following, the reduction of **28** is made with formic acid to give compound **29**. Then, the three phenyl rings of **29** are chlorinated using the BMC reagent to obtain compound **30**. The methyl group of the resulting chlorinated hydrocarbon **30** is brominated to give the bromomethyl derivative **31**. Finally, compound **31** is phosphorylated by means of the Arbuzov reaction to produce the precursor **20** (Scheme 3.5).

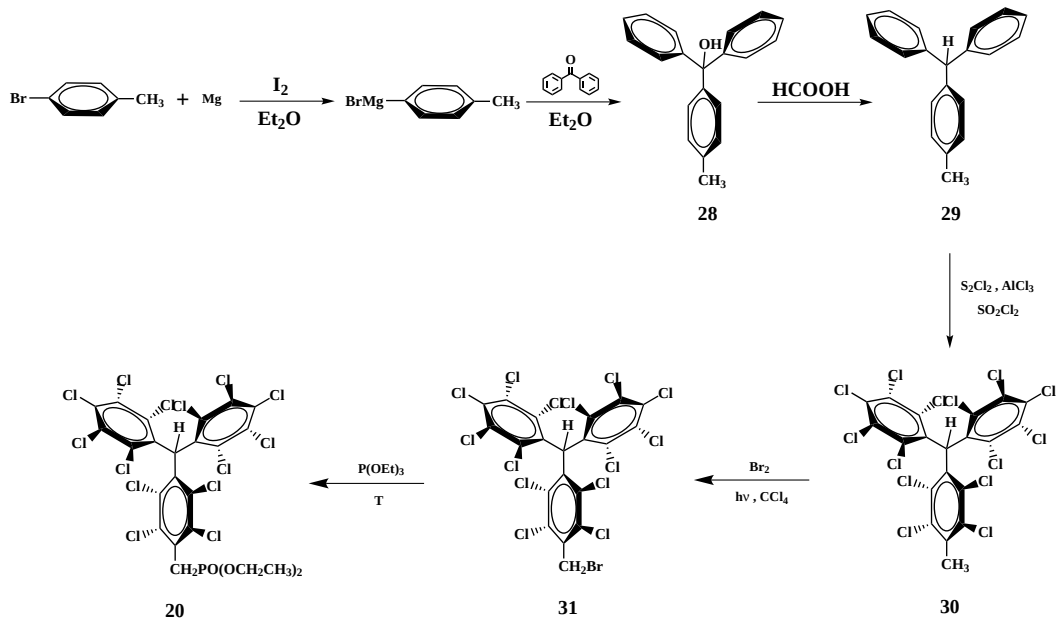

Scheme 3.5: Synthesis of the protonated phosphonate PTM derivate **20**.

The aldehyde Fc–PTM derivative **4H** was obtained through a Witting-Horner-Emmons reaction of the protonated PTM phosphonate derivative **20** and the 1,1′-ferrocenedicarboxaldehyde **16**. The strong stereoselectivity of this reaction gave place exclusively to the *trans* isomer[59] **4H** as shown Scheme 3.6. The crude of the reaction formed by the mixture of mono and bi-substituted molecules was purified by column chromatography in order to obtain only the monosubstituted compound **4H**.

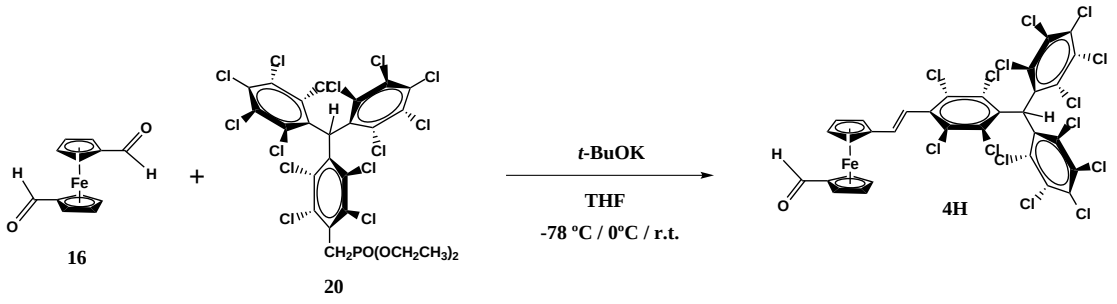

Scheme 3.6: Synthesis of **4H**.

The synthesis of **1H** is based on an esterification reaction between the (±)-α-lipoic acid and a methyl alcohol derivative of the desired Fc–PTM system. **1H** was synthesized in only three steps starting from the protonated aldehyde Fc–PTM derivative **4H**, which was reduced with sodium borohydride to give the

methyl alcohol derivative **7H** . This last compound was used in an esterification reaction together with the (±)-α-lipoic acid to give finally **1H**. Scheme 3.7 shows the synthetic route used.

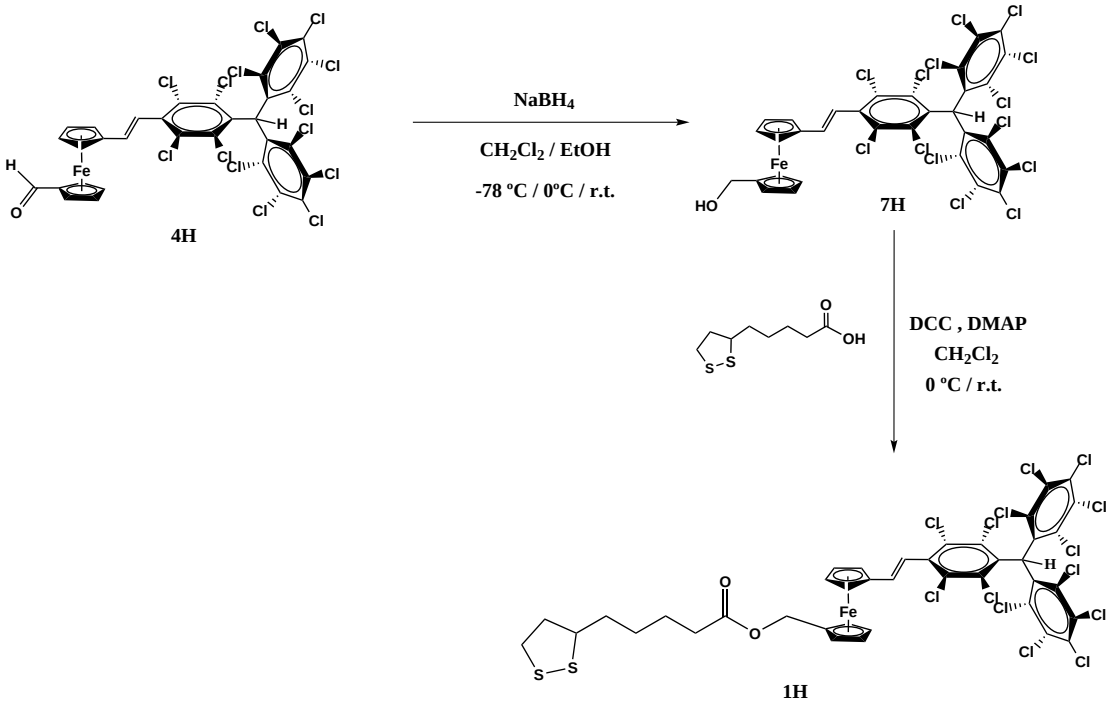

Scheme 3.7: Synthesis of **1-H**.

IR, ^{1}H NMR, MALDI-ToF, and CV techniques have been used for its fully characterization and the results are detailed in the experimental section. However, here we will discuss some of the important features observed in the characterization of compound **1H**. Additionally to all IR peaks that represent the typical fingerprint of PTM derivatives, compound **1H** IR spectrum shows a strong peak around 1730 cm^{-1} confirming the formation of the ester group which put together the Fc–PTM central core to the disulfide-alkyl chain.

Regarding the characterization by CV, only the reversible redox process corresponding to the oxidation of the Fc subunit is expected in **1H**. This redox wave was observed at $E_{1\ 2}$ = 206 mV ($vs\ Fc\ \ Fc^{+}$) and it is represented in Figure 3.31. The protonated PTM moiety does not give any signal in the voltammogram due to its non electroacitve character.

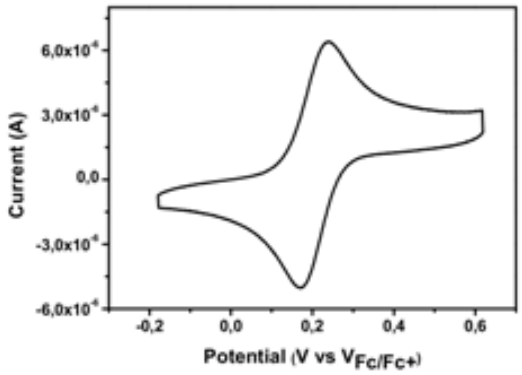

Figure 3.31: Cyclic voltammetry of **1H** in CH_2Cl_2 using $n\text{-}Bu_4NPF_6$ as electrolyte (0.1mM) at 0.1 $V.s^{-1}$

3.5.4 Synthesis and characterization of 1

The synthesis of compound **1** was optimized in four steps starting from the aldehyde Fc–PTM derivative in its protonated form **4H**.

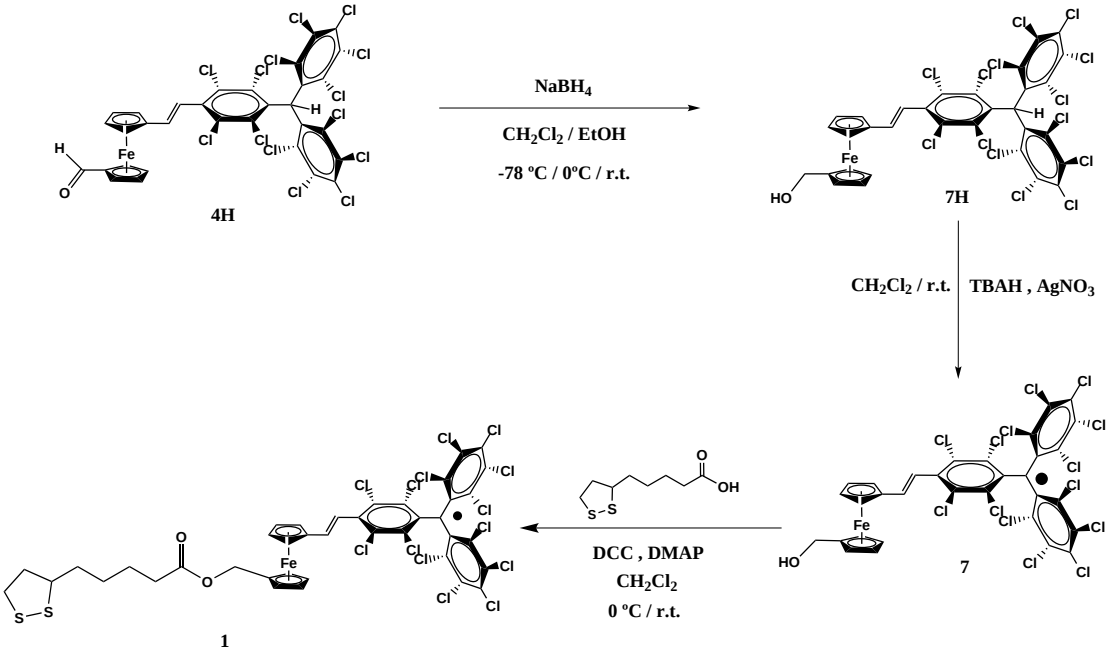

Scheme 3.8: Synthesis of **1**.

The aldehyde derivative **4H** was reduced with sodium borohydride to give the methyl alcohol derivative **7H** as it has been done for **1H**. The generation of the radical character of the PTM moiety was tried at different steps of the synthetic route. However no good results were obtained for most of them. Finally,

the deprotonation with tetrabutylammonium hydroxide (TBAH) solution and the oxidation with silver nitrate of the anionic to form the PTM was done for **7H**, under red light conditions, successfully giving the radical **7**. From **7**, the radical **1** was obtained through an esterification reaction between the methyl alcohol Fc–PTM radical **7** and the (±)-α-lipoic acid. Scheme 3.8 shows the synthetic route used.

The novel compound **1** was deeply characterized by means of IR, MALDI-ToF, UV-Vis-NIR, CV and EPR in a similar way that for **1H**. The IR spectrum shows the strong C=O stretching absorption at frequency around 1730 cm^{-1} [60]. The presence of this peak confirms the formation of the esther bond expected in the last step of the synthetic route of compound **1**. The characteristics bands of the chlorinated aromatic rings between 1400 and 800 cm^{-1} were also observed (Figure 3.32).

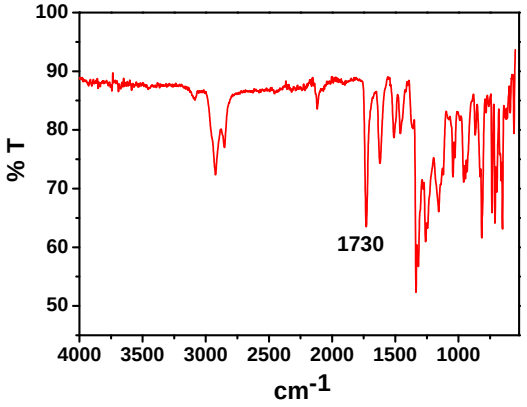

Figure 3.32: IR-ATR spectrum of **1**.

Figure 3.33 shows the UV-Vis-NIR spectrum of **1** in which is observed an intense absorption band of the PTM radical at 387 nm (25840 cm^{-1}) together with two weaker bands located around 440 nm (22727 cm^{-1}) and 573 (17452 cm^{-1}). These two lower absorption bands are ascribed to the electronic conjugation of the unpaired electron into the π-conjugated system, specifically to a π-bridge-to-PTM acceptor charge transfer (CT) band [59,61,62]. This assignment has been done based on the no observation of this band in nonconjugated PTM radicals. Comparing **1** with its non-methylated analogous **2** almost no difference was observed in the UV-Vis-NIR spectrum. However with respect to dyad **3** it was observed that the intensity of the radical band was higher while the π-bridge-to-PTM acceptor CT

band was lower. This is an indication of the lower degree of charge delocalization in **1** than in **3** due to the low electron donor ability of its non-methylated Fc unit as it was discussed in Chapter 2. The broad absorption band observed at 907 nm (11025 cm^{-1}) has been assigned to an IET process from the Fc moiety to the low lying singly-unoccupied molecular orbital of the PTM radical moiety. The energy of this band is in a good agreement with the ones reported for the Fc–PTM central core **2** (λ_{max} = 940 nm)[61], which is an indication that the IET process in **1** is not too much affected by the presence of the disulfide-alkyl chain.

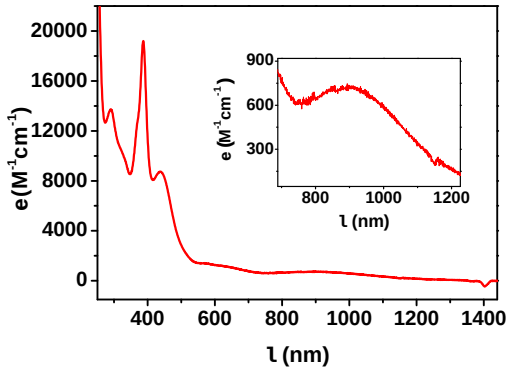

Figure 3.33: UV-Vis-NIR spectrum of **1** in CH_2Cl_2.

Information of the redox processes of **1** were extracted from the CV shown in Figure 3.34. The reversible process observed at positive potential ($E_{1\ 2}$ = +135 mV *vs Fc* Fc^+) corresponds to the oxidation of the Fc subunit to the ferrocenium cation $[\mathbf{1}]^+$ while the reversible redox wave at negative potential ($E_{1\ 2}$ = −708 mV *vs Fc* Fc^+) indicates the reduction of the PTM radical subunit to the corresponding carbanion $[\mathbf{1}]^-$. The redox difference between the first oxidation and the first reduction ($\Delta E_{red\ ox}$) gave a value of 843 mV, 79 mV higher that the redox difference reported for the Fc–PTM dyad **2** ($\Delta E_{red\ ox}$ = 764 mV)[63]. This small difference could be related with the presence of the ester group near to the Fc moiety.

The electrochemical reversibility of both redox processes was confirmed by the separation found for the cationic and anionic voltammetric peaks of the reversible oxidation and reduction waves (66 and 54 mV respectively), which in both cases were really close to the expected theoretical separation of 59 mV. Re-

markably is the fact that the oxidation of the Fc subunit to the ferrocenium radical cation $[\mathbf{1}]^+$ occurs at lower potential in comparison to **1H** (Δ = 71 mV), which is indicative of the modification of the electronic properties due to the presence (**1**) or not (**1H**) of the radical specie. The main difference will be the possibility to transfer one electron through an IET in the case of the radical **1** but no possibility of IET is possible for the protonated derivative **1H** which have no low lying unoccupied molecular orbital accessible.

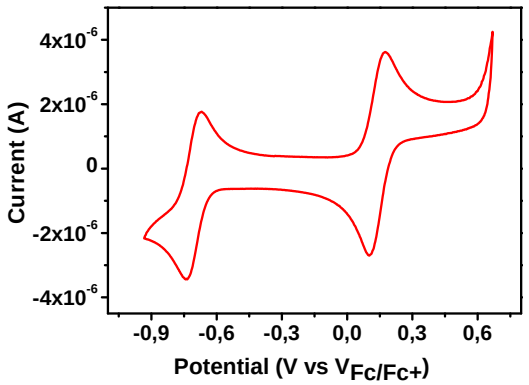

Figure 3.34: Cyclic voltammetry of **1** in CH_2Cl_2 using *n*-Bu_4NPF_6 as electrolyte (0.1mM) at 0.1 $V.s^{-1}$

More details of the characterization of **1** are given in the experimental section.

3.6 SAMs of Fc–PTM derivatives using the one-step approach

3.6.1 Preparation and characterization of the SAM S8-H

For the preparation of SAM **S8-H**, a freshly cleaned gold substrate was immersed in a 1 mM solution of **8H** in toluene for 24 hours under inert conditions. After that the SAM was rinsed with dry toluene and dried under an argon current.

SAM **S8-H** was characterized by PM-IRRAS, AFM and ToF-SIMS. In the PM-IRRAS spectrum showed in Figure 3.35 it is possible to observed the peak corresponding to C=N around 1639 cm^{-1}. The shape and the intensity of this

peak is different compared to that observed previously in SAMs prepared using the two-step approach. As it happened in the two-step approach it seems that here we also have a mixed monolayer due to the presence of the band at 1618 cm^{-1} which has been previously assigned to the NH_2 in-plane deformation of the 4–ATP molecule.

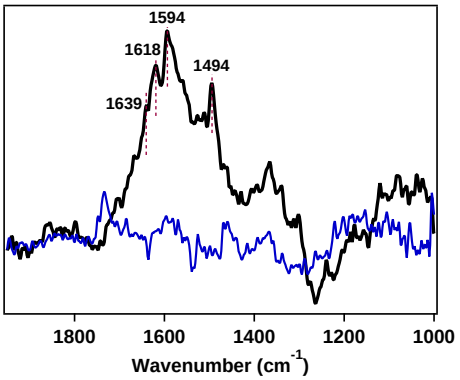

Figure 3.35: PM-IRRAS spectrum of SAM **S8-H** (black line) and the corresponding to bare Au (blue line).

Figure 3.36 shows the AFM image of SAM **S8-H**. The roughness profile follows exactly the same corrugation of the gold substrate with an *rms* roughness of 1.16 nm.

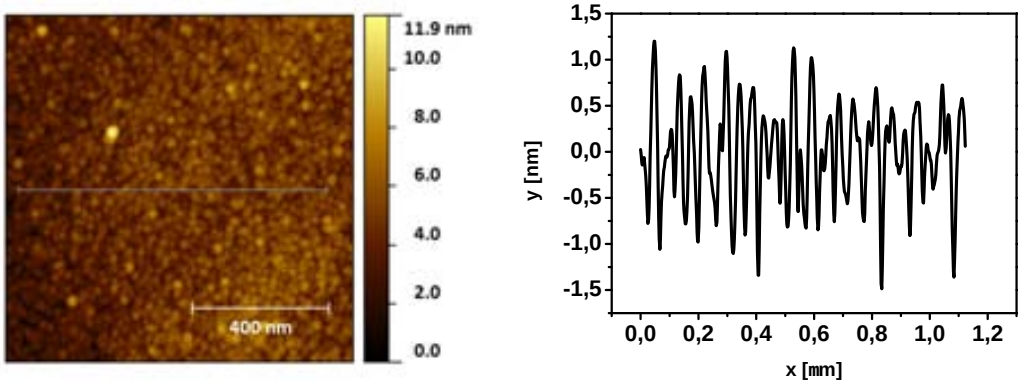

(a) (b)

Figure 3.36: (a) 1 μm x 1 μm AFM image and (b) roughness pro le of the SAM **S8-H**.

Figure 3.37 shows the ToF-SIMS spectra of **S8-H** monolayer where the expected isotopic distribution of the fourteen chlorine atoms of the PTM together with typical looses of chlorine atoms were observed.

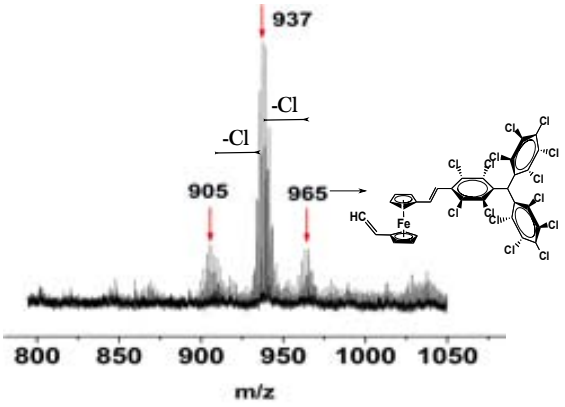

Figure 3.37: ToF-SIMS spectra of **S8-H** monolayer.

The cyclic voltammogram obtained of SAM **S8-H** shows the expected oxidation of the Fc unit with low difference between the anodic and cathodic peak which is an indication of the covalent binding of **8H** to the gold substrate. However, after ten redox cycles the intensity of the signal diminishes which is an indication of the desorption of molecules from the gold substrate indicative of low stability of **S8-H** (Figure 3.38).

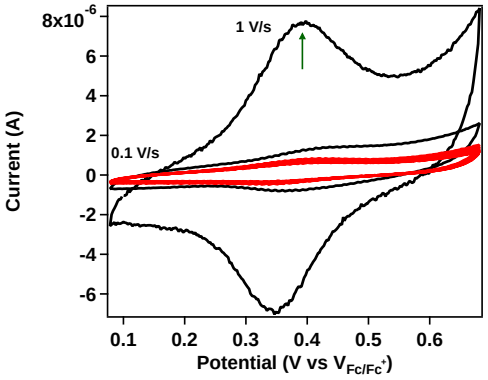

Figure 3.38: Cyclic voltammograms of **S8-H** monolayer in acetonitrile, with 0.1 M $n-BuNPF_6$ at two different scan rates: 100 and 1000 mV/s. The red voltammogram was taken at 100 mV/s for ten redox cycles.

SAMs with such low stability can not be use for any further study of electronic properties neither for applications. Therefore, we move to use the new and more robust molecules designed and synthesized to obtain SAMs with them.

3.6.2 Preparation and characterization of the SAM S5

SAM **S5** was prepared in order to have a good reference of an electron-donor SAM containing the same donor group that our D–A systems. The functionalization of gold substrates with ***5*** was carried out following the procedure shown in Figure 3.39.

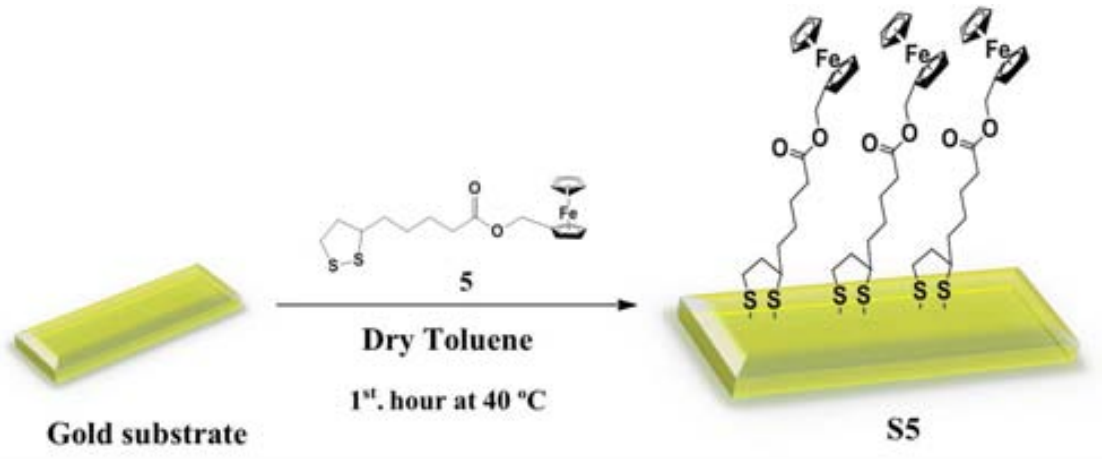

Figure 3.39: Schematic representation of the fabrication of SAM **S5** on Au using the one-step strategy.

The cleaning of the gold substrates was made using a combination of four different solvents (CH_2Cl_2, acetone, ethanol and isopropanol) together with an UV-ozone clean process. Then, the freshly cleaned gold was immersed in a dry toluene solution 1 mM of ***5*** for a total of around 50 hours, maintaining the solution at 40 °C for the first hour. The functionalized gold surface was rinsed with dry toluene and dried under an argon current.

SAM **S5** was characterized by cyclic voltammetry and it is shown in Figure 3.40. The experiments were carried out with the standard setup using the functionalized substrate (S5) as working electrode, solid silver and platinum wires as RE and CE, respectively and all the measurements were referenced to Fc/Fc^+. The reversible redox process of the ferrocene unit was observed at positive potential ($E_{1\ 2}$ = +0.115 V *vs* $Fc\ Fc^+$) as expected. And by means of the linear relation between the scan rate and the current was probed the chemical adsorption of ***5*** on the gold substrate.

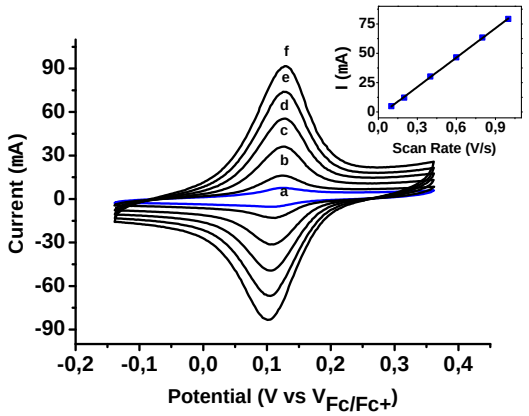

Figure 3.40: Cyclic voltammograms of **S5** monolayer in acetonitrile, with 0.1 M $n-BuNPF_6$ at different scan rates: a) 100; b) 200; c) 400; d) 600; e) 800; f)1000 mV/s. Inset: Plot showing the linear dependence of the current with scan rate.

3.6.3 Preparation and characterization of the SAMs S1 and S1-H

The functionalization of gold substrates with compounds **1** and **1-H** was carried out following the procedure shown in Figure 3.41.

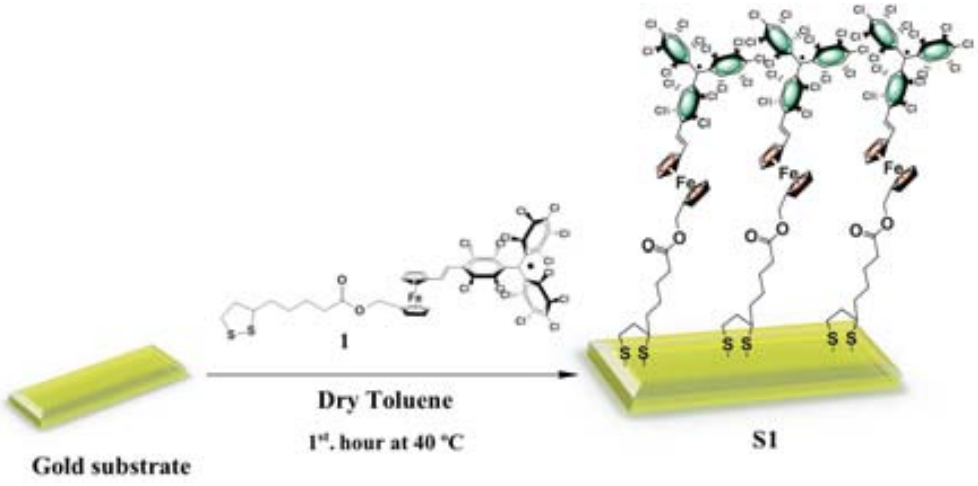

Figure 3.41: Schematic representation of the one-step strategy used for the fabrication of SAMs **S1** and **S1-H** on Au.

It is important to emphasize that the functionalization of gold with **1-H** is of crucial importance to compare with **1** and thus be able to understand the influence of the open-shell character of **1** on the electronic properties that these systems with

a very similar chemical structure but with different electronic structure show once they are covalently attached to a metal surface. To achieve a good functionalization of gold substrates with **1** and **1H** several parameters were optimized.

The cleaning of the gold substrates was made following the protocol described in the experimental section. Combination of four different solvents together with an UV-ozone clean process were used to remove any organic soil over the gold. Then, the freshly cleaned gold was immersed in a dry toluene solution 1 mM of **1** for **S1** or **1H** for **S1-H** for a total of around 50 hours. A critical step of the protocol is that during the first anchoring hour some energy as heat (40 °C) must be applied to the solution. When the process was finished, the functionalized surfaces were rinsed thoroughly with dry toluene to remove any physisorbed material. The custom-made glass container used for preparing SAMs with this procedure is shown in Figure 3.42.

Figure 3.42: Custom-made glass container used for the fabrication of **S1** and **S1-H** monolayers.

Characterization

Structural information of SAMs **S1** and **S1-H** was obtained from the PM-IRRAS, XPS and ToF-SIMs measurements. More surface information was determined by contact angle and AFM while the magnetic character of **S1** was evaluated through EPR. Finally the redox processes of both SAMs were studied by CV.

PM-IRRAS spectra of **S1** and **S1-H** are shown in Figure 3.43(a) and 3.43(b), respectively. A comparison with the IR spectrum of bulky compounds **1** and **1H** from which the monolayers were formed, is include in each figure. The relative intensities of the spectra of bulky compounds with respect to the spectra of the

monolayers were chosen to give an easy visual comparison. Quantitative comparisons of the intensities of the two types of spectra were not extracted from these data since in that case quantitative consideration of the optical and orientation effects at a metal interface is required[41].

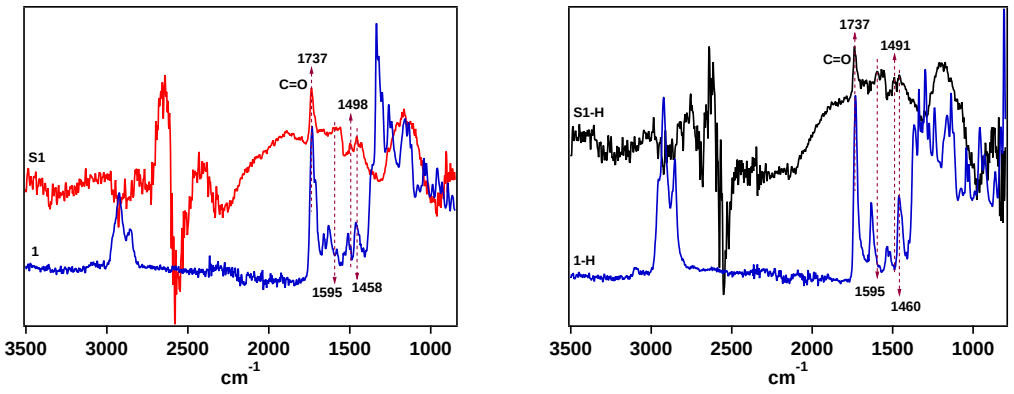

Figure 3.43: (a) IR spectra of **1** (blue line) and PM-IRRAS of **S1** (red line); and (b) IR of **1-H** (blue line) and PM-IRRAS of **S1-H** (black line).

The peak observed around 1595 cm^{-1} for both SAMs has been correlated with the in-plane stretching mode of the benzene ring and a net dipole vector change parallel to the molecular axis. The relative orientation of molecules anchored on a surface can be extracted from the intensity showed by the in-plane mode with respect to the out-of-plane mode of the same group. Thus, taking into account the surface selection rules; if the molecules are oriented normal to the Au surface it is expected that these in-plane modes have a strong intensity while the out-of-plane modes (~ 1106 cm^{-1}) have a weak intensity in the PM-IRRAS spectrum[64] as we observe. Moreover, it was observed a peak around 1495 cm^{-1} for both SAMs which results from the combination of C–C stretching and C–H bending vibration[43]. According to this analysis, it can be stated that the molecules of both SAMs **S1** and **S1-H** might be standing up on the substrate. However, they can not be completely normal oriented to the surface due to the intrinsic angle formed between the sulfur and gold atoms which is around 30° as it has already been reported for other disulfide SAMs. The thickness of the monolayer together with an approximation of the average tilted angle which confirm the orientation of the

molecules will be discussed in Chapter 4.

An other band observed in the PM-IRRAS spectra of **S1** and **S1-H** was localized around ~1460 cm^{-1}. This band can be attributed to the methylene groups CH_2 (scissor vibration band δ_s ~1470 cm^{-1}) of the aliphatic tail[65,66]. More interesting results the strong absorption band observed around 1737 cm^{-1} for **S1** and **S1-H** which corresponds to the stretch mode of the carbonyl group $\nu_{C=O}$[67] present in the ester, group that holds the Fc–PTM central core with the disulfide-alkyl chain and thus confirms the integrity of the molecule on the surface. This peak shows a small red shift when compared with the $\nu_{C=O}$ (1730 cm^{-1}) of the IR spectra of the bulky compounds **1** and **1H**.

The elemental composition of SAMs **S1** and **S1-H** was studied by XPS which gives information about the local bonding environment around specific atoms and hence their chemical state. In both cases a survey spectrum was performed in order to obtain a general view of the elements present on the functionalized Au substrate. Comparing the survey XPS spectra of SAMs **S1** and **S1-H** (Figure 3.44) no difference was observed regarding the expected elements. In addition, high resolution spectra for each element present were also performed.

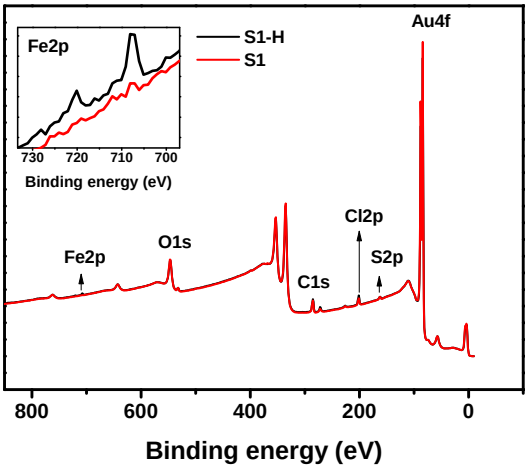

Figure 3.44: XPS survey spectra of **S1** (red) and **S1-H** (black). Inset: zoom in the binding energy region of Fe2p.

Deconvolution of the high resolution XPS (HR–XPS) spectra allows the assignment of different bonding modes of specific elements following either values reported in literature or through comparison between similar systems. Figure 3.45

and 3.46 shows all the HR–XPS spectra taken from **S1** and **S1-H** and their corresponding deconvolution, shown in the first and second raw, respectively. In the third raw a comparison between **S1** and **S1-H** is performed for S2p, Cl2p, C1s, O1s and Fe2p.

Regarding to sulfur atom (S2p), two components of a doublet were deconvoluted at 161.9 and 163.1 eV corresponding to S $2p_{3\ 2}$ and S $2p_{1\ 2}$, respectively[66,68]. The energy of these peaks was related to the thiolate bound to the Au surface. From these data there was no observation of the peaks attributed to unbound thiol groups neither to oxidized sulfur species. For Cl2p, a single doublet with components at 200.9 and 202.5 eV was observed for **S1** and **S1-H** which corresponds to Cl $2p_{3\ 2}$ and Cl $2p_{1\ 2}$, respectively[69,70].

From the fitted C1s HR-spectra of SAMs **S1** and **S1-H**, it was identified a sharp intense peak at 284.6 eV which could be assigned to the contribution of carbons of the alkane chains as well as some carbons present in the PTM subunits[71,72]. The contribution of the cyclopentadienyl carbons, C_{cp}, has been reported to be at 284.9 eV[53,54]. The peak localized at 286.3 eV has been ascribed to the C sp^2 in the chlorinated phenyl groups of the PTM moiety and the smaller peak observed at higher binding energy (289 eV) corresponds unequivocally to the carboxyl group (C=O)[48,71] present in both SAMs. The wide range of values found in the literature for the assignment of different bonding modes of C1s atoms give an idea of how tricky is the process of assignment.

Following with the analysis of the chemical structure of SAMs **S1** and **S1-H**, the HR-spectra of Fe2p shows two sharp photoelectron peaks at 707.8 and 720.2 eV. These peaks can be assigned to the Fe $2p_{3\ 2}$ and Fe $2p_{1\ 2}$, respectively[54,69,73] of the reduced iron atom. Moreover two additional weaker broad bands were observed at 711.2 (Fe $2p_{3\ 2}$) and 723.5 (Fe $2p_{1\ 2}$) eV corresponding to a higher oxidation state of the iron atom (Fe III) according to the literature[53]. The reduced specie only could make sense for SAM **S1** in which an electron transfer from the Fc subunit to the radical moiety can occurs giving place to the corresponding oxidized iron and the anionic specie of the PTM as it has been observed in solid state (crystal) and in solution for dyad **2**[74–76]; but not for **S1-H**. Then, such bands observed for

both SAMs (**S1** and **S1-H**) could come from the interaction between the sample and the incident light or maybe it is an effect of the deconvolution process. This observation will be contrasted in Chapter 4. No further information was obtained from the O1s spectra due to the high probability of contamination with oxygen from the atmosphere.

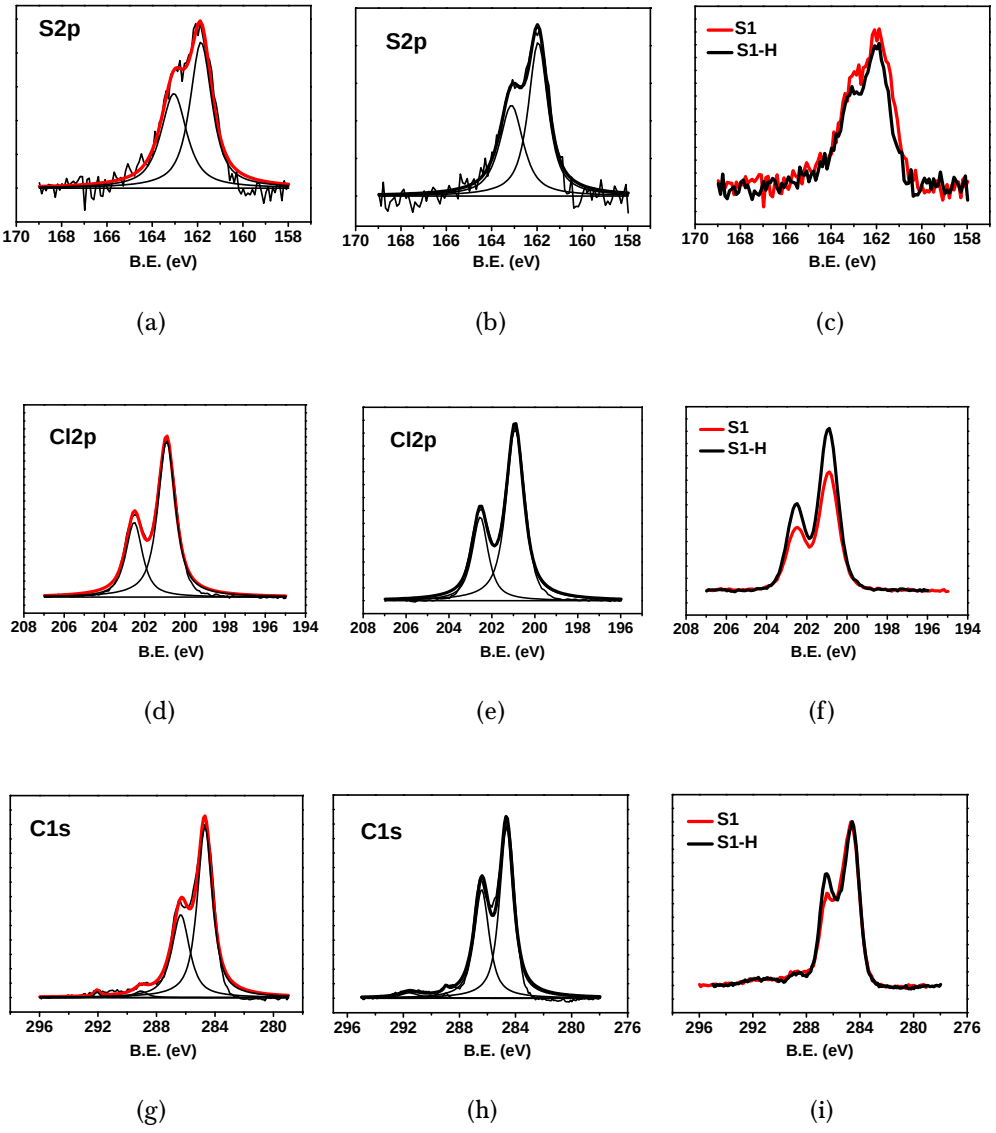

Figure 3.45: High resolution spectra of S2p of (a) **S1**,(b) **S1-H**, and (c) a comparison of both, Cl2p of (d) **S1**, (e) **S1-H** and (f) a comparison of both, C1s of (g) **S1**, (h) **S1-H** and (i) a comparison of both.

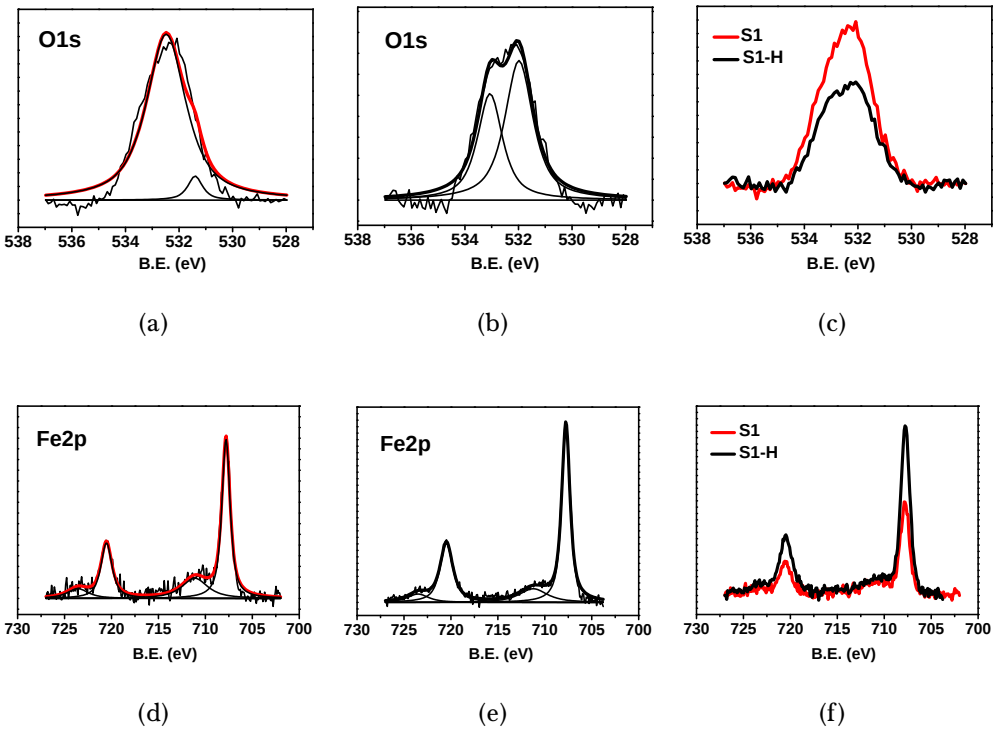

Figure 3.46: High resolution spectra of O1s of (a) **S1**, (b) **S1-H** and (c) a comparison of both, Fe2p of (d) **S1**, (e) **S1-H** and (f) a comparison of both.

One more proof of the anchoring of compounds **1** and **1-H** to the Au surface was given by ToF-SIMS measurements. The mass spectra obtained are shown in Figure 3.47 and 3.48. The highest $m\ z$ fragment detected for both SAMs **S1** and **S1-H** was the corresponding to the entire molecule (MW = 1154 g/mol) even though its intensity in the total spectrum was almost no perceptible. A fraction with a really high intensity was found at $m\ z = 948$ which corresponds to the fragment of the molecule broken at the ester bond region [M–tail]. A third important fragment was detected at $m\ z = 913$ corresponding to the fragment [M–tail] with loss of one chlorine atom.

Finally, at lower $m\ z$, three fragments of the PTM subunit namely [PTM–1Cl], [PTM–2Cl] and [PTM–3Cl] were identified at $m\ z = 707$, $m\ z = 672$ and $m\ z = 636$, respectively. This loss of chlorine atoms in the *orto* position of the PTM phenyl rings has been commonly observed[48,77]. The fragment at $m\ z = 707$ was the only one which was not detected in SAM **S1-H**. Moreover, all of the peaks mentioned before show the corresponding isotopic distribution of chlorine atoms present in

these ions.

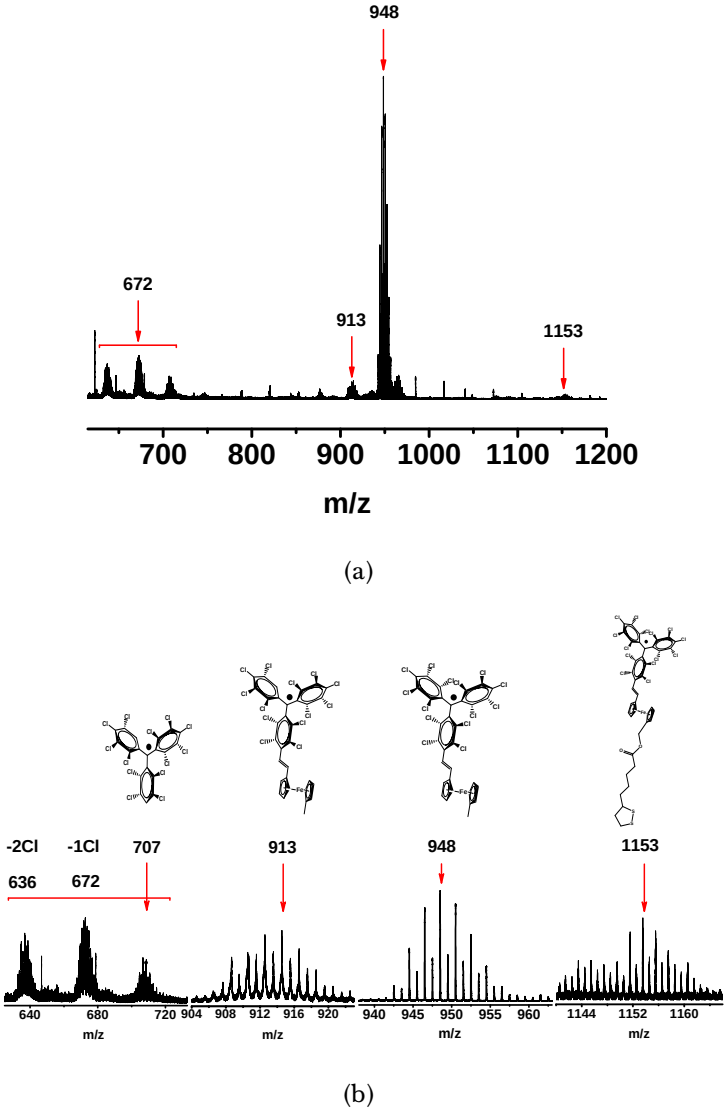

Figure 3.47: Positive mode ToF-SIMS mass spectrum of **S1**, (a) general spectrum and (b) zoom of four speci c regions with their corresponding molecular fractions.

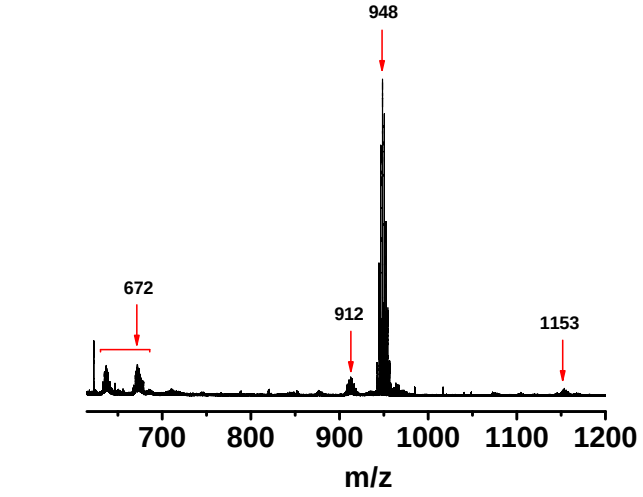

(a)

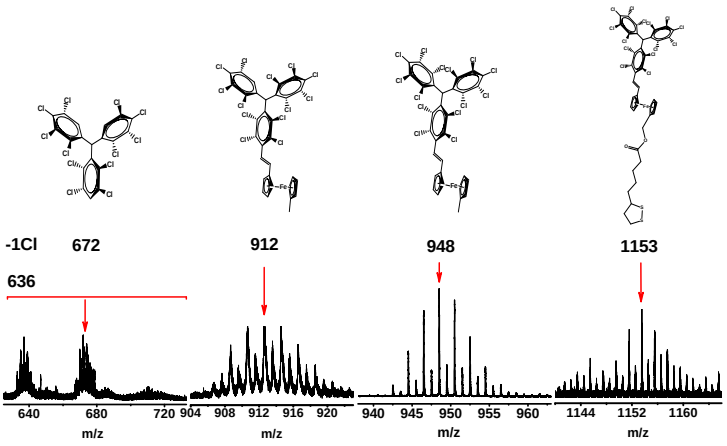

(b)

Figure 3.48: Positive mode ToF-SIMS mass spectrum of **S1-H**, (a) general spectrum and (b) zoom of four speci c regions with their corresponding molecular fractions.

In order to know the wettability of SAMs **S1** and **S1-H**, which is a characteristic of each system, contact angle measurements were performed using Millipore water as solvent. A drop of 3 μL was dispensed with an automated syringe over the functionalized surfaces as well as over a bare gold used as reference. Mean values of at least three measurements for each SAM are reported in Table 3.2 and representative images are shown in Figure 3.49 and 3.50.

Table 3.2: Contact angle values for **S1**, **S1-H** monolayers and bare Au.

Type	Surface	Contact Angle
Au/mica	**S1**	80.4±0.5
	S1-H	85.8±0.7
Au/glass	**S1**	90.0±0.5
	S1-H	93.1±0.3
	Au	83.9±0.1

Since the roughness of the substrate can affect the packing of the molecules and therefore the wettability showed by the monolayers, gold evaporated over two different materials (mica and glass) were used as substrates to prepare the SAMs. For both cases (Au/mica and Au/glass) the value of the contact angle of **S1** was smaller than that obtained for **S1-H** suggesting a slightly higher hidrophobicity for the protonated monolayer.

Comparing these values with respect to the contact angle of bare gold, variations of 6.1 and 9.2° for **S1** and **S1-H**, respectively were observed. This is a clear indication of the surface modification of the substrate. However, the results obtained for **S1** and **S1-H** monolayers do not follow the same tendency of wettability reported previously for SAMs of PTM derivatives on gold[26,27] in which the radical PTM monolayer present a higher contact angle than the protonated PTM monolayer. This observation should be related with the D–A character that present SAMs **S1** and **S1-H**.

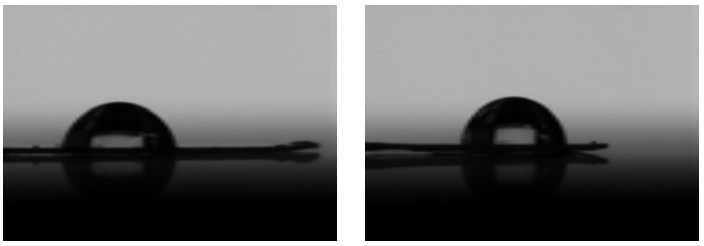

(a) (b)

Figure 3.49: Contact Angle of (a) **S1** and (b) **S1-H** on Au/mica.

(a) (b) (c)

Figure 3.50: Contact Angle of (a) **S1**, (b) **S1-H** on Au/glas and (c) bare gold.

Variations in the contact angle to a more hydrophilic one has been associated with either an increase in disorder at the monolayer–air interface or to an increase of polar interactions between monolayer and the liquid droplet[78]. At this point and according to the contact angle reported in Table 3.2 it is only possible to conclude that SAM **S1** presents more polar interaction with water molecules than SAM **S1-H**.

The homogeneity of the monolayers was studied by AFM. AFM images taken on **S1** and **S1-H** samples and their associated roughness profile (Figure 3.51) show that both surfaces are very flat over large (5μm x 5μm) areas. The corresponding *rms* roughness were calculated using the Gwyddion software and values of 1.045 nm and 0.895 nm for **S1** and **S1-H**, respectively were obtained. The homogeneity of the monolayers is reflected on the gold terraces that can be seen in the AFM images.

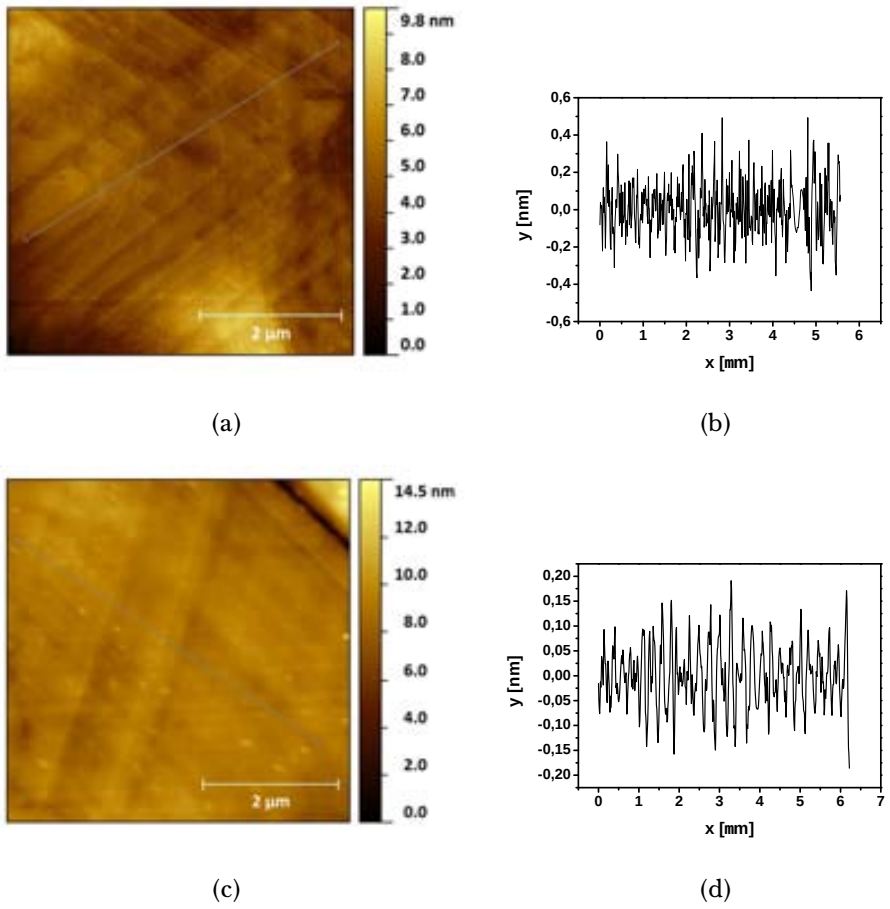

Figure 3.51: 5 μm x 5 μm AFM images and roughness pro les of **S1** (a), (b) and **S1-H** (c), (d), respectively.

The magnetic character of the radical SAM **S1** was tested by EPR.

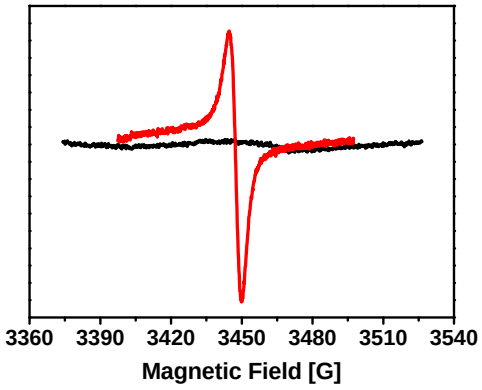

Figure 3.52: EPR spectra of SAMs **S1** (red line) and **S1-H** (black line).

The EPR spectrum (Figure 3.52) shows a signal at g = 2.00323, with a linewidth (δH) of 5.2 Gauss which is in a good agreement with that reported in lit-

erature for other PTM radicals[28,29,48] confirming the immobilization of an organic radical unit with paramagnetism (S = 1/2) thanks to the presence of the unpaired electron in **S1**. **S1-H** monolayer does not present any EPR signal because in this SAM the PTM moiety is a closed-shell specie and therefore, diamagnetic (S = 0).

Finally, the electroactive character of the SAMs was evaluated by CV. The experiments were carried out with the standard setup using the functionalized substrate (**S1** and **S1-H**) as working electrode, solid silver and platinum wires as RE and CE, respectively, and a solution of 0,1 M tetrabutylammonium hexafluorophosphate (TBAHFP) in acetonitrile as electrolyte using the setup showed in Figure 3.27. All measurements were referenced to Fc/Fc^+.

Figure 3.53 shows the CV of **S1** monolayer in which two reversible redox waves are observed, one corresponding to the oxidation of the Fc moiety and the other related with the reduction of the PTM radical. On the other hand, the voltammograms registered for SAM **S1-H** (Figure 3.54) exhibit only the one reversible redox wave of the Fc subunit, which was expected since the molecules in this SAM contain the protonated PTM moieties which are not electroactive species and therefore can not participate in the redox process.

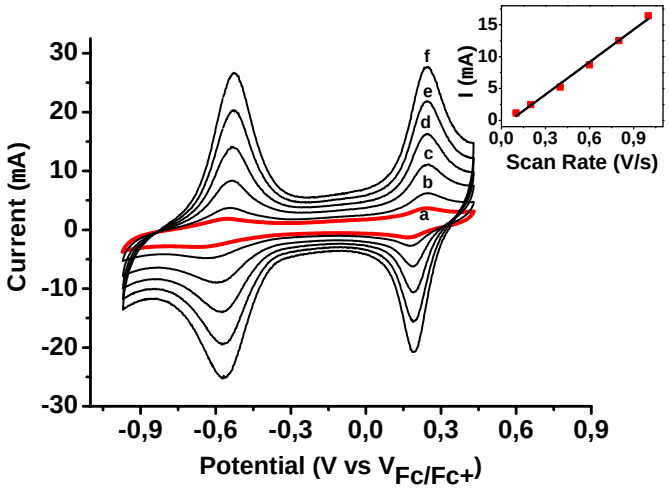

Figure 3.53: Cyclic voltammograms of **S1** monolayer in acetonitrile, with 0.1 M $n-BuNPF_6$ at different scan rates: a) 100; b) 200; c) 400; d) 600; e) 800; f)1000 mV/s. Inset: Plot showing the linear dependence of the current with scan rate.

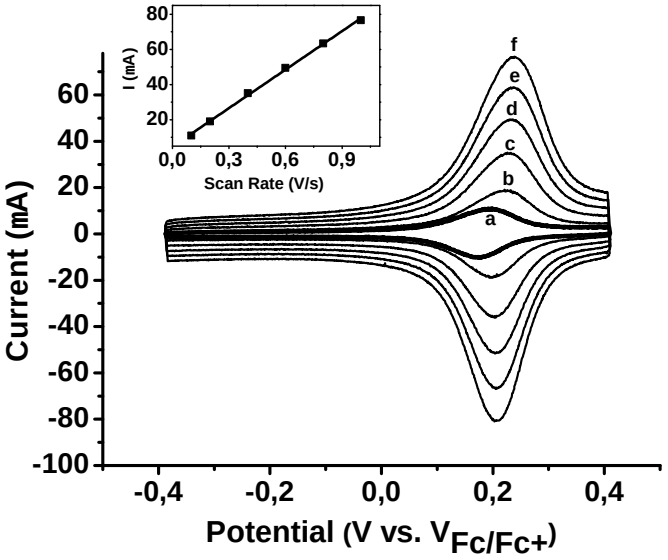

Figure 3.54: Cyclic voltammograms of **S1-H** monolayer in acetonitrile, with 0.1 M $n-BuNPF_6$ at different scan rates: a) 100; b) 200; c) 400; d) 600; e) 800; f)1000 mV/s. Inset: Plot showing the linear dependence of the current with scan rate.

SAM **S1** showed a higher stability after 10 cycles than SAM **S1-H** in which a small decreasing in the current intensity of the peaks was observed. Moreover in both SAMs a lineal relation between the increasing of the scan rate and the current peak intensities was observed which are typical voltammetric responses of molecules that have been covalently immobilized on a surface[79]. The shape of the peaks in the cyclic voltammograms are independent of the scan rate in the range used (from 100 to 1000 mV/s).

From the CV data several parameters such as: formal potential (E^0), electron transfer rate (ΔE_p), full-width at half maximum (ΔE_{fwhm}) and surface coverage (Γ) can be calculated allowing a further characterization of the SAMs. They are collected in Table 3.3.

Table 3.3: Electrochemical Data for **S1** and **S1-H** monolayers ($vs\ Fc\ Fc^+$).

Monolayer	E^0 **(mV)**	ΔE_p **(mV)**	ΔE_{fwhm} **(mV)**	Γ **(mol cm^{-2})**	θ **(nm^2/molec)**
S1	207	56.1	128.0	1.28E-10	1.3
	-598	80.6	188.0		
S1-H	240	58.6	100.1	3.26E-10	0.5

Theoretical values expected for covalently bonded electroactive molecules are: ΔE_p = 0 mV. ΔE_{fwhm} = 90.3 mV. Typical Γ = 4.5E-10 mol cm^{-2} for a well packed Fc monolayer.

Formal potential, (E^0)

The Fc and PTM formal potentials in the nanostructured SAMs **S1** and **S1-H** were determined from the average between the corresponding anodic (E_{pa}) and cathodic (E_{pc}) peak potential, as shown Equation 3.1.

$$E^0 = \frac{E_{pc} + E_{pa}}{2} \tag{3.1}$$

Comparing the Fc formal potential of both SAMs it was observed that **S1-H** monolayer exhibits a higher value for this parameter (E^0 = 240 mV) being the Fc formal potential of **S1** monolayer 33 mV lower (E^0 = 207 mV) which is indicative of a more favorable oxidation process of the Fc moiety for the open-shell monolayer. This observation is in good agreement with the values observed for compounds **1** and **1-H** in solution which is an indicative that ones the molecules are bonded to the gold substrate as SAMs, an electronic structure and interaction between the Fc and PTM moiety similar to the one observed in solution is obtained (Figure 3.31, 3.34 and Table 3.4).

Table 3.4: Electrochemical Data for compounds **1** and **1-H**.

Compounds	E^0 **(mV)**	ΔE_p **(mV)**
1	135	65.9
	-708	53.7
1-H	198	71.5

Although compounds **1** and **1-H** have a very similar chemical structure, they present very different electronic structure with very different energy levels due to the presence of an open-shell electronic structure in **1** but a closed-shell in **1H**. Then, the lower Fc formal oxidation potential of **1** and **S1** can be justified in terms of the presence of the PTM radical which allows the energy of the highest occupied molecular orbital (HOMO) localized in the Fc-donor subunit to be more accessible

than the corresponding one in the PTM protonated species **1H** and **S1-H**, being easier the extraction of one electron from the ferrocene in the radical forms.

Electron-transfer rate (ΔE_p)

The electron transfer rate between the forward and return potential scan of the redox centers that are covalently bonded to the gold in a SAM can be estimated from the anodic (E_{pa}) and cathodic (E_{pc}) peak separation ΔE_p, which is expected to be 0 mV for surface-confined electroactive species which participate in a reversible electron transfer process under ideal conditions[80]. This parameter can be calculated following Equation 3.2.

$$\Delta E_p = E_{pa} - E_{pc} \tag{3.2}$$

The experimental peak separation (ΔE_p) values obtained for **S1** and **S1-H** monolayers (Table 3.3) were different that the theoretically expected for an ideal Nernstian redox species adsorbed on a surface. In such ideal situation, it is expected the close proximity of all electroactive centers to the electrode surface in order to avoid any influence of the diffusion over the electron transfer process. As well as, it is expected that the surface-attached electroactive groups do not interact each other and to be in rapid equilibrium with the electrode. In our case, we have a disulfide-alkyl chain that separates the electroactive units from the substrate and also acts as an electronic insulator since it does not show conjugation. Then, nonzero ΔE_p values for SAMs **S1** and **S1-H** are in a good agreement with the presence of a disulfide-alkyl chain and also with possible electrostatic interactions between the redox centers of the SAMs. Moreover, they are similar to the values that have been reported in the literature for SAMs of PTM (ΔE_p = 76 mV)[81] and for Fc SAMs (20 to 30 mV)[80].

Comparing the peak separation between the cathodic and anodic peak of the Fc wave for **S1** and **S1-H** with respect to that registered for **1** and **1-H** in solution, we noticed a slight reduction of 9.8 and 12.9 mV, respectively, which is an additional indication of the chemical anchoring of the molecules on the surface. On the other hand, the ΔE_p for PTM wave was higher (80.6 mV) than its analogous wave for

compounds in solution. This difference could be related with the distance at which the PTM moiety is located with respect to the surface. Such bigger distance in comparison with the distance of the Fc unit with respect to the surface, probably hinders the electron transfer and also the rapid equilibrium with the electrode which could make sense since the molecules are in a standing-up position over the surface.

Full-width at half maximum (ΔE_{fwhm})

Important information about the relative interaction that can take place between the redox centers of the adsorbates organized in a monolayer is given by the full-width at half maximum height of the anodic (or cathodic) voltammetric wave. According to Equation 3.3 where R is the universal gas constant, T is the absolute temperature, n is the number of exchanged electrons and F is the Faraday constant, for an ideal case where almost no interaction is found between the electroactive units present in a monolayer, a ΔE_{fwhm} = 90.3 mV (considering that only one electron participates in the process) is expected[82].

$$fwhm = 3\ 53\frac{RT}{nF} = \frac{90\ 6}{n}mV \tag{3.3}$$

At experimental level, values of ΔE_{fwhm} larger or smaller than the theoretical one are usually found. In this sense, the larger experimental values obtained for **S1** have been attributed to possible intermolecular electrostatic interactions produced by oriented molecular dipole species in close proximity. This situation is expected especially when there is a high concentration of electroactive centers in the monolayer. For SAM **S1** both ΔE_{fwhm} values, one corresponding to the Fc wave (128 mV) and the other corresponding to the PTM wave (188 mV) were found to be larger than the ideal one. Significant interactions between redox centers has been previously reported for SAMs of PTM radicals (ΔE_{fwhm} = 184 mV)[25]. The value of ΔE_{fwhm} = 128 mV for the Fc unit of **S1** was found to be close to the typical range (130 to 155 mV) of those for pure SAMs terminated with Fc redox centers[80]. For SAM **S1-H** it was also observed a larger value of ΔE_{fwhm} = 100.1 mV than the ideal one. The values obtained point toward significant interactions between the

redox centers of the D–A SAMs.

The fact **S1-H** present a value closer to the ideal one in comparison with that present for SAM **S1** could be an indication of the higher homogeneity of the molecules forming the SAM **S1-H**. This observation can be due to the higher intermolecular electrostatic interactions of the oriented dipoles of the D–A monolayer in **S1** which present two redox centers than in **S1-H** with only one.

Surface coverage (Γ_{Fc})

Surface coverage tell us the number of molecules per area and is an indication of the quality of the molecular packing in the SAM. This parameter can be estimated from Equation 3.4. Where Γ is the surface coverage (mol cm^{-2}), Q_{Fc} is the total charge (C) calculated from the integration of the area under the anodic peak, n is the number of electrons involved in the electron transfer process (n = 1 for the Fc/Fc^+ redox couple), F is the Faraday constant (96485.309 C mol^{-1}) and A is the experimental surface area of the electrode (WE).

$$\Gamma_{Fc} = \frac{Q_{Fc}}{nFA} \tag{3.4}$$

It must be taken into account that the quality of the packing in a SAM depends of a lot of experimental parameters, some of them difficult to control. For the best packing found for **S1** and **S1-H** monolayers, considering the anodic peak of the ferrocene taken at 100 mV/s and knowing that the experimental areas of the working electrodes were 0.5 cm^2 and 0.6 cm^2, respectively; values of Γ_{Fc} of 1.28E-10 and 3.26E-10 mol cm^{-2} respectively for **S1** and **S1-H** were obtained. These values are lower than the theoretical maximum coverage of 4.5E-10 mol cm^{-2} calculated for a densely packed monolayer based on an alkyl thiol terminated chain with a Fc group on flat gold[83], which it makes sense since molecules in **S1** and **S1-H** contain the bulkier PTM unit at the top of the monolayer. In fact, it will be the area occupied by the PTM subunit that will determine the packing of the molecules in **S1** and **S1-H**.

In summary, the surface coverage for **S1-H** monolayer was higher than that determined for **S1** which is in a good agreement with the lower contact angle found for **S1** (Table 3.49 and 3.50) and the previously mentioned intermolecular electrostatic interactions present in this SAM. From these data we have also calculated the average area, θ , occupied by each molecule using Equation 3.5. Values of 130 (1.3 nm^2) and 51 (0.51 nm^2) $Å^2$ for **S1** and **S1-H**, respectively, were obtained, which are close to the area estimated for one PTM unit[25], the most bulky part of the molecule.

$$\theta\,(Å^2) = \frac{10^{16}}{6\ 023x10^{23}\Gamma} \tag{3.5}$$

The area occupied by the PTM unit was also calculated from the optimized geometry of the molecules (**1** and **1H**) in gas phase and assuming a rectangular shape*. A value of 0.652 nm^2/molecule was obtained for both molecules. The difference of this value with respect to that obtained for SAM **S1-H** could be explained from an experimental error or from the geometric shape assumed for the PTM moiety.

Molecular Orbitals

Further information about the HOMO relative to vacuum can be extracted from cyclic voltammograms using Equation 3.6[84], where $E_{abs\,NHE}$ is the absolute potential energy of the normal hydrogen electrode (-4.5 eV), and $E_{1\,2\,NHE}$ is the formal half-wave potential vs normal hydrogen electrode (NHE). Since the reference electrode (Ag_s) was calibrated using the Fc/Fc^+ couple, the formal potential was referenced to NHE (0 mV) using a value of +0.447 V.

$$E_{HOMO} = E_{abs\,NHE} - eE_{1\,2\,NHE} \tag{3.6}$$

Table 3.5 recollects the HOMO values found for the three monolayers (**S1**, **S1-H** and **S5**) studied, as well as for the corresponding compounds used for the SAMs preparation (**1**, **1-H** and **5**) measured in solution. Comparing the radical and the protonated monolayer one can appreciate that the HOMO value of **S1-H** is slightly higher than the corresponding of **S1** which is in agreement with the fact that for the

*Theoretical calculations performed by Francesca Delchiaro, PhD student in Dipartimento di Chimica at Parma University (Italy) under supervision of Prof. Anna Painelli.

protonated PTM is more di cult to extract the electron from the Fc moiety than for the radical. This interpretation is supported by the HOMO value calculated for the Fc monolayer, which is the smallest one. In this case, the Fc unit is more accessible and there is no interference of any other part. The energy of the HOMO was found to be **S1-H** > **S1** > **S5**. Nevertheless, the three monolayers show a HOMO value slightly bigger that the corresponding bulky compounds, differences of 0.07, 0.03 and 0.08 eV were found for **S1**, **S1-H** and **S5**, respectively. This increment could be related with the alignment of the energy levels at the metal frontier.

Table 3.5: Highest Occupied Molecular Orbital (HOMO) calculated from CV experiments.

E **in V**	**S1**	**S1-H**	**S5**	**1**	**1-H**	***5***
E_{pa}	0.235	0.269	0.118	0.168	0.234	0.180
	-0.557			-0.681		
E_{pc}	0.179	0.210	0.111	0.102	0.163	-0.117
	-0.638			-0.734		
$E_{1\ 2}$	0.207	0.240	0.115	0.135	0.198	0.031
	-0.598			-0.708		
$E_{1\ 2\,NHE}$	0.654	0.687	0.562	0.582	0.645	0.478
	-0.151			-0.261		
E_{HOMO} (eV)	-5.15	-5.187	-5.06	-5.08	-5.15	-4.98
E_{LUMO} (eV)	-4.35			-4.24		

3.7 Summary

Two different approaches have been used to prepared SAMs of D–A systems. We start using a two-step approach for the preparation of SAMs **S6**, **S6-H**, **S4** and **S4-H**. Due to the instability of the imine bond it has been not possible to obtain homogeneous monolayers but mixed monolayers that do not allow to continue with the study of the electronic properties of these SAMs.

In order to obtain robust and homogeneous SAMs of electron D–A systems three novel molecules were synthesized to be anchored to the surface following a

one-step approach. Very successful results were obtained for SAMs **S*5***, **S1** and **S1-H**. With these new SAMs it will be possible to study in detail in the following chapters their electronic properties for their possible applications in molecular electronics.

Bibliography

[1] J. C. Love, L. a. Estroff, J. K. Kriebel, R. G. Nuzzo, and G. M. Whitesides, "Self-assembled monolayers of thiolates on metals as a form of nanotechnology.," *Chemical reviews*, vol. 105, pp. 1103–69, 2005.

[2] A. Adamson and A. Gast, *Physical Chemistry of Surfaces*. New York: Wiley-Interscience Publication John Wiley & Sons, Inc., sixth ed., 1997.

[3] C. Vericat, M. E. Vela, and R. C. Salvarezza, "Self-assembled monolayers of alkanethiols on Au(111): surface structures, defects and dynamics.," *Physical chemistry chemical physics*, vol. 7, no. 18, pp. 3258–68, 2005.

[4] P. E. Laibinis, G. M. Whitesides, D. L. Allara, Y.-T. Tao, A. N. Parikh, and R. G. Nuzzo, "Comparison of the Structures and Wetting Properties of Self-Assembled Monolayers of n-Alkanethiols on the Coinage Metal Surfaces, Cu, Ag, Au," *Journal of American Chemical Society*, vol. 113, pp. 7152–7167, 1991.

[5] J. C. Love, D. B. Wolfe, R. Haasch, M. L. Chabinyc, K. E. Paul, G. M. Whitesides, and R. G. Nuzzo, "Formation and structure of self-assembled monolayers of alkanethiolates on palladium," *Journal of the American Chemical Society*, vol. 125, pp. 2597–609, 2003.

[6] M. Kawasaki, T. Sato, T. Tanaka, and K. Takao, "Rapid Self-Assembly of Alkanethiol Monolayers on Sputter-Grown Au(111)," *Langmuir*, vol. 16, no. 4, pp. 1719–1728, 2000.

[7] R. Yamada, H. Wano, and K. Uosaki, "Effect of Temperature on Structure of the Self-Assembled Monolayer of Decanethiol on Au(111) Surface," *Langmuir*, vol. 16, no. 13, pp. 5523–5525, 2000.

[8] E. Delamarche, B. Michel, H. A. Biebuyck, and C. Gerber, "Golden Interfaces : The Surface of Self-Assembled Monolayers," *Advanced Materials*, vol. 8, no. 9, pp. 719–729, 1996.

[9] F. Schreiber, "Structure and growth of self-assembling monolayers," *Progress in Surface Science*, vol. 65, pp. 151–257, 2000.

[10] L. A. Adamczyk, *Understanding the Structure and Properties of Self-Assembled Monolayers for Interfacial Patterning.* PhD thesis, Virginia Polytechnic Institute and State University, 2009.

[11] S. G. J. Mathijssen, E. C. P. Smits, P. a. van Hal, H. J. Wondergem, S. a. Ponomarenko, A. Moser, R. Resel, P. a. Bobbert, M. Kemerink, R. a. J. Janssen, and D. M. de Leeuw, "Monolayer coverage and channel length set the mobility in self-assembled monolayer field-effect transistors.," *Nature nanotechnology*, vol. 4, no. 10, pp. 674–80, 2009.

[12] J. Stettner and A. Winkler, "Characterization of alkanethiol self-assembled monolayers on gold by thermal desorption spectroscopy.," *Langmuir*, vol. 26, no. 12, pp. 9659–65, 2010.

[13] G. Zotti, B. Vercelli, and A. Berlin, "Monolayers and multilayers of conjugated polymers as nanosized electronic components.," *Accounts of chemical research*, vol. 41, no. 9, pp. 1098–109, 2008.

[14] R. G. Chapman, E. Ostuni, L. Yan, and G. M. Whitesides, "Preparation of Mixed Self-Assembled Monolayers (SAMs) That Resist Adsorption of Proteins Using the Reaction of Amines with a SAM That Presents Interchain Carboxylic Anhydride Groups," *Langmuir*, vol. 16, pp. 6927–6936, 2000.

[15] G. J. Ashwell, A. Mohib, C. J. Collins, and A. Aref, "Molecular rectification: Confirmation of its molecular origin by chemical suppression of the electrical asymmetry," *Synthetic Metals*, vol. 159, pp. 2282–2285, 2009.

[16] R. M. Metzger, B. Chen, U. Höpfner, M. V. Lakshmikantham, D. Vuillaume, T. Kawai, X. Wu, H. Tachibana, T. V. Hughes, H. Sakurai, J. W. Baldwin,

C. Hosch, M. P. Cava, L. Brehmer, and G. J. Ashwell, “Unimolecular Electrical Rectification in Hexadecylquinolinium Tricyanoquinodimethanide,” *J. Am. Chem. Soc.*, vol. 119, pp. 10455–10466, 1997.

[17] M. Kondratenko, A. G. Moiseev, and D. F. Perepichka, “New stable donorâ “ acceptor dyads for molecular electronics,” *Journal of Materials Chemistry*, vol. 21, no. 5, p. 1470, 2011.

[18] F. Fuchs, M. Linares, C. de Vet, P. Leclère, R. Demadrille, and B. Grévin, “On the photo-induced charge-carrier generation within monolayers of self-assembled organic donor-acceptor dyads.,” *Advanced materials (Deer eld Beach, Fla.)*, vol. 26, no. 37, pp. 6416–22, 2014.

[19] G. Valincius, G. Niaura, B. Kazakeviciene, Z. Talaikyte, M. Kazemekaite, E. Butkus, and V. Razumas, “Anion effect on mediated electron transfer through ferrocene-terminated self-assembled monolayers.,” *Langmuir*, vol. 20, no. 16, pp. 6631–8, 2004.

[20] R. Sahli, C. Fave, N. Raouafi, K. Boujlel, B. Schöllhorn, and B. Limoges, “Switching on/off the chemisorption of thioctic-based self-assembled monolayers on gold by applying a moderate cathodic/anodic potential.,” *Langmuir*, vol. 29, no. 17, pp. 5360–8, 2013.

[21] P. a. Bertin, D. Georganopoulou, T. Liang, A. L. Eckermann, M. Wunder, M. J. Ahrens, G. F. Blackburn, and T. J. Meade, “Electroactive self-assembled monolayers on gold via bipodal dithiazepane anchoring groups.,” *Langmuir*, vol. 24, no. 16, pp. 9096–101, 2008.

[22] C. Amatore, S. Gazard, E. Maisonhaute, C. Pebay, B. Schöllhorn, J.-L. Syssa-Magalé, and J. Wadhawan, “Ferrocenyl Oligo(phenylene-vinylene) Thiols for the Construction of Self-Assembled Monolayers,” *European Journal of Inorganic Chemistry*, vol. 2007, no. 25, pp. 4035–4042, 2007.

[23] H. D. Sikes, “Rapid Electron Tunneling Through Oligophenylenevinylene Bridges,” *Science*, vol. 291, no. 5508, pp. 1519–1523, 2001.

[24] S. Creager, C. J. Yu, C. Bamdad, S. O□Connor, T. MacLean, E. Lam, Y. Chong, G. T. Olsen, J. Luo, M. Gozin, and J. F. Kayyem, "Electron Transfer at Electrodes through Conjugated "Molecular Wire" Bridges,□ *Journal of American Chemical Society*, vol. 121, pp. 1059–1064, 1999.

[25] N. Crivillers, M. Mas-Torrent, J. Vidal-Gancedo, J. Veciana, and C. Rovira, "Self-assembled monolayers of electroactive polychlorotriphenylmethyl radicals on Au(111).,□ *Journal of the American Chemical Society*, vol. 130, no. 16, pp. 5499–506, 2008.

[26] N. Crivillers, C. Munuera, M. Mas-Torrent, C. Simão, S. T. Bromley, C. Ocal, C. Rovira, and J. Veciana, "Dramatic Influence of the Electronic Structure on the Conductivity through Open- and Closed-Shell Molecules,□ *Advanced Materials*, vol. 21, no. 10-11, pp. 1177–1181, 2009.

[27] C. Simao, M. Mas-Torrent, J. Veciana, and C. Rovira, "Multichannel Molecular Switch with a Surface-Confined Electroactive Radical Exhibiting Tunable Wetting Properties,□ *Nano letters*, vol. 11, pp. 4382–4385, 2011.

[28] N. Crivillers, M. Mas-Torrent, S. Perruchas, N. Roques, J. Vidal-Gancedo, J. Veciana, C. Rovira, L. Basabe-Desmonts, B. J. Ravoo, M. Crego-Calama, and D. N. Reinhoudt, "Self-assembled monolayers of a multifunctional organic radical.,□ *Angewandte Chemie*, vol. 46, no. 13, pp. 2215–9, 2007.

[29] C. Simao, M. Mas-Torrent, N. Crivillers, V. Lloveras, J. M. Artés, P. Gorostiza, J. Veciana, and C. Rovira, "A robust molecular platform for non-volatile memory devices with optical and magnetic responses,□ *Nature chemistry*, vol. 3, pp. 359–364, 2011.

[30] B. I. Rosario-Castro, E. R. Fachini, J. Hernández, M. E. Pérez-Davis, and C. R. Cabrera, "Electrochemical and surface characterization of 4-aminothiophenol adsorption at polycrystalline platinum electrodes.,□ *Langmuir*, vol. 22, no. 14, pp. 6102–8, 2006.

[31] J. M. Brockman, A. G. Frutos, and R. M. Corn, "A Multistep Chemical Modification Procedure To Create DNA Arrays on Gold Surfaces for the Study of

Protein - DNA Interactions with Surface Plasmon Resonance Imaging,” *J. Am. Chem. Soc.*, vol. 121, pp. 8044–8051, 1999.

[32] S.-J. Xiao, M. Wieland, and S. Brunner, “Surface reactions of 4-aminothiophenol with heterobifunctional crosslinkers bearing both succinimidyl ester and maleimide for biomolecular immobilization.,” *Journal of colloid and interface science*, vol. 290, no. 1, pp. 172–83, 2005.

[33] J. Lukkari, K. Kleemola, M. Meretoja, T. Ollonqvist, and J. Kankare, “Electrochemical Post-Self-Assembly Transformation of 4-Aminothiophenol Monolayers on Gold Electrodes,” *Langmuir*, vol. 14, no. 7, pp. 1705–1715, 1998.

[34] G. J. Ashwell, A. T. Williams, S. A. Barnes, S. L. Chappell, L. J. Phillips, B. J. Robinson, B. Urasinska-Wojcik, P. Wierzchowiec, I. R. Gentle, and B. J. Wood, “Self-Assembly of Amino - Thiols via Gold - Nitrogen Links and Consequence for in situ Elongation of Molecular Wires on Surface-Modified Electrodes,” *The Journal of Physical Chemistry C*, vol. 115, pp. 4200–4208, 2011.

[35] D. G. Castner, K. Hinds, and D. W. Grainger, “X-ray Photoelectron Spectroscopy Sulfur 2p Study of Organic Thiol and Disulfide Binding Interactions with Gold Surfaces,” *Langmuir*, vol. 12, pp. 5083–5086, 1996.

[36] J. E. Hutchison, T. A. Postlethwaite, and R. W. Murray, “Molecular Films of Thiol-Derivatized Tetraphenylporphyrins on Gold: Film Formation and Electrocatalytic Dioxygen Reduction,” *Langmuir*, vol. 9, pp. 3277–3283, 1993.

[37] C. M. Whelan, M. R. Smyth, and C. J. Barnes, “HREELS, XPS, and Electrochemical Study of Benzenethiol Adsorption on Au(111),” *Langmuir*, vol. 15, no. 1, pp. 116–126, 1999.

[38] J. J. W. M. Rosink, M. A. Blauw, L. J. Geerligs, E. V. D. Drift, B. A. C. Rousseeuw, and S. Radelaar, “Self-Assembly of pi-Conjugated Azomethine Oligomers by Sequential Deposition of Monomers from Solution,” *Langmuir*, vol. 16, pp. 4547–4553, 2000.

[39] J. T. Young, F. J. Boerio, Z. Zhang, and T. L. Beck, "Molecular Structure of Monolayers from Thiol-Terminated Polyimide Model Compounds on Gold. 1. A Spectroscopic Investigation," *Langmuir*, vol. 12, no. 5, pp. 1219–1226, 1996.

[40] W.-H. Chuang and J.-C. Lin, "Surface characterization and platelet adhesion studies for the mixed self-assembled monolayers with amine and carboxylic acid terminated functionalities," *Journal of Biomedical Materials Research Part A*, vol. 82, no. 4, pp. 820–830, 2007.

[41] C. E. D. Chidsey and D. N. Loiacono, "Chemical Functionality in Self - Assembled Monolayers : Structural and Electrochemical Properties," *Langmuir*, vol. 6, pp. 682–691, 1990.

[42] Y. Luo, M. Piantek, J. Miguel, M. Bernien, W. Kuch, and R. Haag, "In-situ formation and detailed analysis of imine bonds forÂtheÂconstruction of conjugated aromatic monolayers onÂAu(111)," *Applied Physics A*, vol. 93, no. 2, pp. 293–301, 2008.

[43] L.-s. Jiao, Z. Wang, L. Niu, J. Shen, T.-y. You, S.-j. Dong, and A. Ivaska, "In situ electrochemical SERS studies on electrodeposition of aniline on 4-ATP/Au surface," *Journal of Solid State Electrochemistry*, vol. 10, no. 11, pp. 886–893, 2006.

[44] J. H. Moon, J. W. Shin, S. Y. Kim, and J. W. Park, "Formation of Uniform Aminosilane Thin Layers:Â An Imine Formation To Measure Relative Surface Density of the Amine Group," *Langmuir*, vol. 12, no. 20, pp. 4621–4624, 1996.

[45] G. C. Look, M. M. Murphy, D. a. Campbell, and M. a. Gallop, "Trimethylorthoformate: A mild and effective dehydrating reagent for solution and solid phase imine formation," *Tetrahedron Letters*, vol. 36, no. 17, pp. 2937–2940, 1995.

[46] A. K. Saini, C. M. Carlin, and H. H. Patterson, "Confirmation of the Presence of lmine Bonds in Thermally Cured Polyimides," *Journal of Polymer Science Part A: Polymer Chemistry*, vol. 31, no. 11, pp. 2751–2758, 1993.

[47] Y. Luo, M. Bernien, A. Krüger, C. F. Hermanns, J. Miguel, Y.-M. Chang, S. Jaekel, W. Kuch, and R. Haag, "In situ hydrolysis of imine derivatives on Au(111) for the formation of aromatic mixed self-assembled monolayers: multitechnique analysis of this tunable surface modification.," *Langmuir*, vol. 28, no. 1, pp. 358–66, 2012.

[48] O. Shekhah, N. Roques, V. Mugnaini, C. Munuera, C. Ocal, J. Veciana, and C. Wöll, "Grafting of monocarboxylic substituted polychlorotriphenylmethyl radicals onto a COOH-functionalized self-assembled monolayer through copper (II) metal ions.," *Langmuir*, vol. 24, no. 13, pp. 6640–8, 2008.

[49] N. Crivillers, *Organitzacions bi i tridimensionals de molècules electroactives per aplicacions en dispositius.* PhD thesis, Universidat Autònoma de Barcelona, 2008.

[50] P. Snauwaert, R. Lazzaroni, J. Riga, J. J. Verbist, and D. Gonbeau, "A photoelectron spectroscopic study of the electrochemical processes in polyaniline," *The Journal of Chemical Physics*, vol. 92, no. 4, p. 2187, 1990.

[51] T. Yamashita and P. Hayes, "Analysis of XPS spectra of Fe2+ and Fe3+ ions in oxide materials," *Applied Surface Science*, vol. 254, no. 8, pp. 2441–2449, 2008.

[52] H. Wang, S. Chen, L. Li, and S. Jiang, "Improved method for the preparation of carboxylic acid and amine terminated self-assembled monolayers of alkanethiolates.," *Langmuir*, vol. 21, no. 7, pp. 2633–6, 2005.

[53] A. W. Taylor and P. Licence, "X-ray photoelectron spectroscopy of ferrocenyl- and ferrocenium-based ionic liquids.," *Chemphyschem : a European journal of chemical physics and physical chemistry*, vol. 13, no. 7, pp. 1917–26, 2012.

[54] C. M. Woodbridge, D. L. Pugmire, R. C. Johnson, N. M. Boag, and M. a. Langell, "HREELS and XPS Studies of Ferrocene on Ag(100)," *The Journal of Physical Chemistry B*, vol. 104, no. 14, pp. 3085–3093, 2000.

[55] A. Ulman, "Formation and Structure of Self-Assembled Monolayers.," *Chemical reviews*, vol. 96, no. 4, pp. 1533–1554, 1996.

[56] M. Ballester, J. Castañer, J. Riera, A. Ibáñez, and J. Pujadas, "Inert Carbon Free Radicals 2. Monofunctionalized Tetradecachlorotriphenylmethyl Radicals and Related Compounds," *The Journal of organic chemistry*, vol. 47, no. 643, pp. 259–264, 1982.

[57] M. Ballester, J. Veciana, J. Riera, J. Castañer, R. Concepción, and O. Armet, "Inert Carbon Free Radicals. 7. "The (Kinetic) Reverse Effect" and Relevant Synthesis of New Monofunctionalized Triphenylmethyl Radicals and Their Nonradical Counterparts," *The Journal of organic chemistry*, vol. 51, pp. 2472–2480, 1986.

[58] C. Rovira, D. Ruiz-Molina, O. Elsner, J. Vidal-Gancedo, J. Bonvoisin, J. P. Launay, and J. Veciana, "Influence of topology on the long-range electron-transfer phenomenon.," *Chemistry - A European Journal*, vol. 7, no. 1, pp. 240–50, 2001.

[59] O. Elsner, D. Ruiz-Molina, I. Ratera, J. Vidal-Gancedo, C. Rovira, and J. Veciana, "Ferrocene as a ferromagnetic coupler. Synthesis and characterization of a ferrocene bridged polychlorotriphenylmethyl diradical," *Journal of Organometallic Chemistry*, vol. 637-639, pp. 251–257, 2001.

[60] M. A. Herranz, L. Yu, N. Martín, and L. Echegoyen, "Synthesis, electrochemistry and self-assembled monolayers of novel tetrathiafulvalene (TTF) and pi-extended TTF (exTTF) disulfides.," *The Journal of organic chemistry*, vol. 68, no. 22, pp. 8379–85, 2003.

[61] I. Ratera, C. Sporer, D. Ruiz-Molina, N. Ventosa, J. Baggerman, A. M. Brouwer, C. Rovira, and J. Veciana, "Solvent tuning from normal to inverted marcus region of intramolecular electron transfer in ferrocene-based organic radicals.," *Journal of the American Chemical Society*, vol. 129, no. 19, pp. 6117–29, 2007.

[62] O. Armet, J. Veciana, C. Rovira, J. Riera, J. Castañer, E. Molinas, J. Rius, C. Miravitlles, S. Olivella, and J. Brichfeus, "Inert Carbon Free Radicals. 8.

Polychlorotriphenylmethyl Radicals. Synthesis, Structure, and Spin-Density Distribution," *The Journal of Physical Chemistry*, vol. 91, pp. 5608–5616, 1987.

[63] O. Elsner, D. Ruiz-Molina, J. Vidal-Gancedo, C. Rovira, and J. Veciana, "Ferromagnetic interactions between triphenylmethyl radicals through an organometallic coupler," *Chemical Communications*, no. 7, pp. 579–580, 1999.

[64] H. McNally, D. Janes, B. Kasibhatla, and C. Kubiak, "Electrostatic investigation into the bonding of poly(phenylene) thiols to gold," *Superlattices and Microstructures*, vol. 31, no. 5, pp. 239–245, 2002.

[65] G. Fonder, F. Cecchet, a. Peremans, P. Thiry, J. Delhalle, and Z. Mekhalif, "Conformational order of n-dodecanethiol and n-dodecaneselenol monolayers on polycrystalline copper investigated by PM-IRRAS and SFG spectroscopy," *Surface Science*, vol. 603, no. 15, pp. 2276–2282, 2009.

[66] L. P. Méndez De Leo, E. de la Llave, D. Scherlis, and F. J. Williams, "Molecular and electronic structure of electroactive self-assembled monolayers.," *The Journal of chemical physics*, vol. 138, no. 11, p. 114707, 2013.

[67] F. Thery-Merland, C. Méthivier, E. Pasquinet, L. Hairault, and C. Pradier, "Adsorption of functionalised thiols on gold surfaces: How to build a sensitive and selective sensor for a nitroaromatic compound?," *Sensors and Actuators B: Chemical*, vol. 114, no. 1, pp. 223–228, 2006.

[68] J. E. Baio, T. Weidner, J. Brison, D. J. Graham, L. J. Gamble, and D. G. Castner, "Amine Terminated SAMs: Investigating Why Oxygen is Present in these Films.," *Journal of electron spectroscopy and related phenomena*, vol. 172, no. 1-3, pp. 2–8, 2009.

[69] J. F. Moulder, W. F. Stickle, P. E. Sobol, and K. D. Bomben, *Handbook of X-ray Photoelectron Spectroscopy. A Reference Book of Standard Spectra for Identification and Interpretation of XPS Data.* Minnesota: Perkin-Elmer Corporation Physical Electronic Division, 1992.

[70] C. Wagner, W. Riggs, L. Davis, and J. Moulder, *Handbook of X-ray photoelectron spectroscopy. A Reference Book of Standard Data For Use in X-Ray Photoelectron Spectroscopy*. Minnesota: Perkin-Elmer Corporation Physical Electronic Division, 1979.

[71] T. M. Willey, A. L. Vance, C. Bostedt, T. van Buuren, R. W. Meulenberg, L. J. Terminello, and C. S. Fadley, "Surface structure and chemical switching of thioctic acid adsorbed on Au(111) as observed using near-edge X-ray absorption fine structure.," *Langmuir*, vol. 20, no. 12, pp. 4939–44, 2004.

[72] S. Watcharinyanon, E. Moons, and L. S. O. Johansson, "Mixed Self-Assembled Monolayers of Ferrocene-Terminated and Unsubstituted Alkanethiols on Gold: Surface Structure and Work Function," *The Journal of Physical Chemistry C*, vol. 113, no. 5, pp. 1972–1979, 2009.

[73] A. B. Fischer, M. S. Wrighton, M. Umana, and R. Iurray, "An X-ray Photoelectron Spectroscopic Study of Multilayers of an Electroactive Ferrocene Derivative Attached to Platinum and Gold Electrodes," *Journal of American Chemical Society*, vol. 101:13, pp. 3442–3446, 1979.

[74] G. D□Avino, L. Grisanti, J. Guasch, I. Ratera, J. Veciana, and A. Painelli, "Bistability in Fc-PTM crystals: the role of intermolecular electrostatic interactions.," *Journal of the American Chemical Society*, vol. 130, no. 36, pp. 12064–72, 2008.

[75] L. Grisanti, G. D□Avino, A. Painelli, J. Guasch, I. Ratera, and J. Veciana, "Essential state models for solvatochromism in donor-acceptor molecules: the role of the bridge.," *The journal of physical chemistry. B*, vol. 113, no. 14, pp. 4718–25, 2009.

[76] J. Guasch, L. Grisanti, S. Jung, D. Morales, G. D□Avino, M. Souto, X. Fontrodona, A. Painelli, F. Renz, I. Ratera, and J. Veciana, "Bistability of Fc-PTM-Based Dyads: The Role of the Donor Strength," *Chemistry of Materials*, vol. 25, pp. 808–814, 2013.

[77] M. A. Fox, E. Gaillard, and C.-C. Chen, "Photochemistry of Stable Free Radicals: The Photolysis of Perchlorotriphenylmethyl Radicals," *Journal of American Chemical Society*, vol. 109, pp. 7088–7094, 1987.

[78] S. D. Evans, E. Urankar, A. Ulman, and N. Ferris, "Self-Assembled Monolayers of Alkanethiols Containing a Polar Aromatic Group: Effects of the Dipole Position on Molecular Packing, Orientation, and Surface Wetting Properties," *Journal of American Chemical Society*, vol. 113, pp. 4121–4131, 1991.

[79] M. Chahma, J. S. Lee, and H.-B. Kraatz, "Fc-ssDNA conjugate: electrochemical properties in a borate buffer and adsorption on gold electrode surfaces," *Journal of Electroanalytical Chemistry*, vol. 567, no. 2, pp. 283–287, 2004.

[80] R. C. Sabapathy, S. Bhattacharyya, M. C. Leavy, W. E. Cleland, and C. L. Hussey, "Electrochemical and Spectroscopic Characterization of Self-Assembled Monolayers of Ferrocenylalkyl Compounds with Amide Linkages," *Langmuir*, vol. 14, pp. 124–136, 1998.

[81] N. Crivillers, M. Mas-Torrent, J. Vidal-Gancedo, J. Veciana, and C. Rovira, "Self-assembled monolayers of electroactive polychlorotriphenylmethyl radicals on Au(111).," *Journal of the American Chemical Society*, vol. 130, no. 16, pp. 5499–506, 2008.

[82] A. L. Eckermann, D. J. Feld, J. a. Shaw, and T. J. Meade, "Electrochemistry of redox-active self-assembled monolayers.," *Coordination chemistry reviews*, vol. 254, no. 15-16, pp. 1769–1802, 2010.

[83] C. E. D. Chidsey, C. R. Bertozzi, T. M. Putvinski, and A. M. Mujsce, "Coadsorption of Ferrocene-Terminated and Unsubstituted Alkanethiols on Gold : Electroactive Self-Assembled Monolayers," *Journal of American Chemical Society*, vol. 112, no. 11, pp. 4301–4306, 1990.

[84] C. a. Nijhuis, W. F. Reus, J. R. Barber, M. D. Dickey, and G. M. Whitesides, "Charge transport and rectification in arrays of SAM-based tunneling junctions.," *Nano letters*, vol. 10, no. 9, pp. 3611–9, 2010.

I learned that courage was not the absence of fear, but the triumph over it. The brave man is not he who does not feel afraid, but he who conquers that fear

Nelson Mandela

4

Electronic structure characterization of Fc–PTM radical SAMs using Synchrotron radiation

4.1 Introduction

In the effort to make electronic devices (like computers, cellphones, televisions, cameras, storage memories, etc.) more powerful while their size is reduced and their cost more accessible, technological and physical limits are encountered. One of the reasons is based on the relevant physical laws that govern the matter, which change from the classical to the quantum-mechanical laws as sizes approach the atomic scale. In fact, conventional silicon and gallium arsenide, inorganic semiconductors, could face some flaws when changes from classical physics to nanophysics take place, as the nanometer scale is achieved[1].

In general, the components used as part of electronic devices with such nanometer scale are framed in nanoelectronics. In this field the study of the interatomic interactions and quantum mechanical properties (i.e. classical boundary effects[2] due to the presence of a surface or an interface; phonon confinement[3,4],

etc.) of the so small materials used results imperative[5]. In a more specific way, when the device dimensions reach smaller and smaller sizes like a few nanometers, the carriers (particles free to move like electrons, ions, holes) which have a particle-wave duality can no longer be treated as classical point-like particles, and effects originating from the quantum mechanical nature of propagation begin to determine transport[6]. So, searching for miniaturization have opened a wide spectrum of possibilities in an emerging technology to fabricate new devices with nanometer size[1].

Molecular electronics can be considered as a promising candidate for nanoelectronics, due to the possibility to built new devices and circuit architectures by the assembly of a large numbers of nanoscale (molecules) objects[7]; or even the use of a single molecule as an active component of electronic devices. The later is the most ambitious goal of both, industrial and scientific community since single molecules constitute the smallest stable structure imaginable. This thesis is framed in the use of self-assembled monolayers (SAMs) as a way of nanofabrication for the development of molecular electronics. However, before they can be used in real applications, an extensive knowledge of the internal electronic structure of the molecules, and the different interactions between them and also with the surrounding media and with other components (like contacts), etc; are of crucial importance because they will defined the final performance of these units as a component of a whole and its integration into devices. Then, in order to use molecules as electronic components, two general properties need to be studied: the internal electronic structure of the molecules and the charge transport through them.

To study the electronic properties of organic molecules as promising candidates to be integrated into nanoelectronic devices, it is necessary to graft and nanostructure them on a metallic substrate. One way to do it is by the self-assembly process which was addressed in Chapter 3. Once the molecules are bonded to a metallic substrate, their electronic structure vary in different ways due to: *i)* interface–related processes that take place upon the adsorption of the molecule[8]; *ii)* intermolecular interactions within the SAM; *iii)* dimensionality effects, and

among others. Therefore, the understanding of the electronic structure and its correlation with both the chemical structure and the intermolecular interactions and how they determine the electronic properties, the electronic function and the potential applications of molecules as component of devices is of great importance in the field of nanoelectronics. Moreover, the molecular charge state and also the charge distribution are important properties of molecular adsorbates that can be used for instance in single-electron devices[9].

In this regards, synchrotron-based spectroscopic techniques confer a really good opportunity to study and to understand the properties of these kind of systems at the atomic scale, using different spectroscopy techniques like Photoemission (PES) and Resonant Photoemission (RPES), or Near Edge X-ray Absorption Fine Structure (NEXAFS). The possibility to be able to choose the photon energy to characterize each component (atom) of the molecular monolayer provides great advantages with respect to the conventional XPS technique in which only one energy can be used, generally 1486.6 eV, due to the source (Al K_α) of the monochromatic radiation.

From the molecular electronic point of view, D–A dyads which are the scope of this thesis; are interesting systems to produce molecular elements suitable to be used in electronic devices. Such interest is centered in three main aspects. *i)* On one side, as the donor and acceptor units are electroactive they can be considered as molecular switches with 3 different electronic states. *ii)* D–A systems that induce a dipole in the metal/molecule interface can also be interesting to improve the performance of charge injection in electronic devices. This improvement takes place due to the modification of the work function of the metallic interface thanks to its chemical modification with D–A SAM which allows controlling the energy barrier at the metal/organic interface[10]. *iii)* Additionally, the higher delocalization of the highest occupied molecular orbital (HOMO) and lowest unoccupied molecular orbital (LUMO) in D–A systems due to the presence of the π–bridge compared with that expected in the Aviram-Ratner model[7] is expected to favor the charge transport across these systems giving place to rectification.

On the other hand, as we have already seen in Chapter 2 the D–A system Fc–PTM radical (**2**) presents bistability being able to exist in the neutral (N) or zwitterionic (Z) state either in solution and in solid state thanks to cooperative intermolecular electrostatic forces (Chapter 2). Thus, working with this system results of special interest due to the possibility to study the influence of the dimensionality of the system to the bistability phenomena previously observed in 3D. We will be specially interested to demonstrate experimentally, if the bistability phenomenon observed in 3D structures can also be noted when these molecules are organized as SAMs in 2D structures.

The study of the molecular switching does not belong to the principal aim of this thesis. However, such process has been studied in similar electroactive systems like PTM radicals[11,12] and TTF[13,14] monolayers. Regarding to the modification of the electronic properties of surfaces by using these D–A SAMs, and also the charge transport study through them will be addressed along Chapters 5 and 6, respectively. While, this chapter will be dedicated to the study of the electronic structure of D–A SAMs based on Fc–PTM derivatives by synchrotron radiation. Focusing on the core-level of the principal elements of the SAMs, as well as on the occupied and unoccupied molecular orbitals.

4.2 Synchrotron radiation*

Synchrotron radiation (SR) was observed visually for the first time in 1947 at General Electric 70-Mev synchrotron accelerator by a group of investigators[15]. Synchrotron radiation is the electromagnetic radiation emitted in the tangential direction by charged particles travelling close to the speed of light that have been accelerated through magnetic fields in circular orbits. Initially, it was considered as a nuisance in high-energy accelerators and particle storage rings because the significant energy loss that represents. However, in the 1950s and 1960s, synchrotron radiation was eventually discovered as a very useful X-ray source that can be used

*The measurements using synchrotron radiation were performed at BL24-CIRCE and Materials Science beamline at ALBA and Elettra facilities, respectively; with the support of Dr. Virginia Pérez, Dr. Carlos Escudero and Dr. Robert Acres beamline scientists.

as potential tool in several fields of science (i.e. material science, biology, medicine, etc.). The energy of the SR covers a broad spectrum, although the radiation used at experimental level is primarily in the ultraviolet and X-ray wavelengths and it is characterized by high brilliance and tunable energy[16,17].

SR facilities typically consist of an injection system, a storage ring and beam lines. In the injection system, electrons are generated, pre-accelerated, and sometimes a second accelerator further accelerates these electrons to more than 1 GeV before injection into the storage ring. In the ring, bunches of electrons periodically circulate at relativistic speed for periods of up to many hours and extremely bright light is created when electrons are deflected through magnetic fields. Basically, the storage ring consists of radio-frequency (RF) cavities, bending or other kind of magnets and insertion devices like wigglers or undulators[16] as shown in Figure 4.1. The classical SR source is made up by an electron gun, a linear accelerator, a booster synchrotron, a storage ring, beamlines, and experimental end-stations.

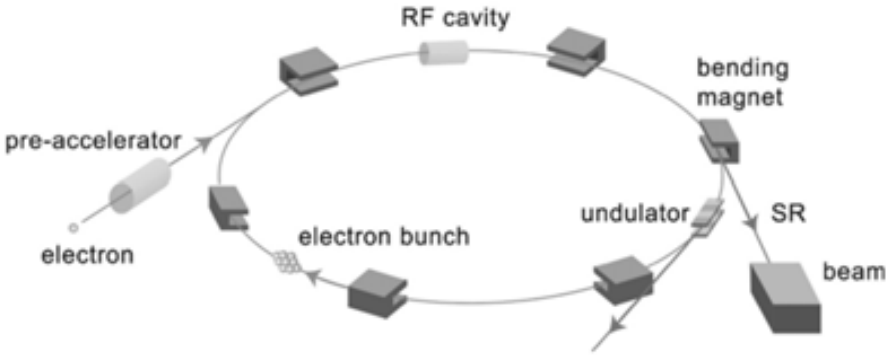

Figure 4.1: Schematic representation of the electron storage ring of a Sychrotron Radiation facility[16].

X-rays from a SR source enable non-destructive determination of the elemental analyses, distribution and chemical state (the electronic structure of the elements) and also imaging the elemental constituents of molecules, cells, etc; thanks to the very high brilliance and energy variability of the X-ray beam. The knowledge obtained in this way allows to gain new insights of the highly complex functions of materials, molecules, cells, etc.

Unique properties of the X-rays from a SR source like: *i)* tunability of the incident X-ray energy which makes possible to obtain the information of chemical

state of elements; *ii)* high photon flux, 10.000 times higher than conventional X-ray tubes which give high e cacy by reducing the measurement time; *iii)* high collimation which for example enables analysis of trace metallic elements contained in a biological specimen at a single cell level; *iv)* pulsed time structure which makes possible to perform time-resolved measurements; *v)* the selective distinct linear or circular polarization of the radiation[16], among others; make techniques based on SR very useful and widely employed in physical, chemical and biological fields.

4.3 Objectives

In this chapter we will use synchrotron radiation in order to characterize different aspects of the SAMs **S1** and **S1-H**. First we will be interested to study the internal electronic structure of molecules **1** and **1-H** once they are anchored to a gold substrate. Then, as we are dealing with an open-shell molecule, we will be also interested to corroborate that the magnetic character of the PTM radical is preserved once anchored to the metallic substrate as it was observed by EPR. We will also study the interaction between the gold substrate and the monolayer, and finally, we will take advantage of the possibility to study the electronic structure of a molecule in real time to try to use the synchrotron radiation to follow a possible switching behavior of SAM **1** under different external stimuli (water vapor and temperature) towards possible applications.

4.4 Photoemission spectroscopy (PES)

Photoemission spectroscopy (PES) is one of the most important techniques used to study the electronic structure of molecules, solids and interfaces. It is based on the photoexcitation of electrons localized at the core-level of an atom.

The process starts when a monochromatic electromagnetic radiation ($h\nu$) incidences over a surface in vacuum. The energy given by the photons is absorbed by core-level electrons and depending on the photon energy, they can be excited from this original state to an empty outer shell or they can escape from the material

as photoelectrons. The emitted photoelectrons are collected and their energy is analyzed. Thus, it is possible to plot the number of detected electrons per energy interval versus their kinetic energy giving place to the spectrum of the element. The kinetic energies of the emitted electrons is given by Equation 4.1.

$$KE = h\nu - BE - \pi_s \tag{4.1}$$

Where, KE is the kinetic enery, $h\nu$ is the energy of the photon, BE is the binding energy corresponding to the orbital from which the electron comes, and π_s is the spectrometer work function. In this process, the photon energy (hν) required to extract one electron from its core-level has to be equal or higher than the BE of the atomic orbital from which the electron originates. Thus, each element has a unique spectrum like a fingerprint that characterizes it. However, if the photon energy is higher, then the core-level electron absorbs the required energy to escape from the atom and the rest of the photon energy contributes to the electron kinetic energy as a free particle. Since the detected electrons can come only from the top few atomic layers because the mean free path of electrons is very small in solids, PES has been established as a very surface-sensitive technique[18].

Figure 4.2 shows the survey spectra of **S1** and **S1-H** monolayers at hν = 630 eV. In addition to the expected elements (Fe3p, S2p, Cl2p, C1s and O1s), it was observed the Si2p peak which comes from the substrate probably due to some imperfections of the evaporated gold layer.

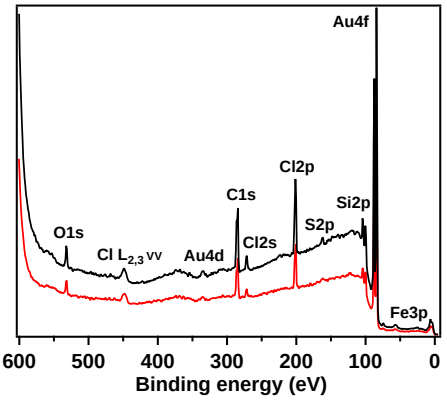

Figure 4.2: Survey PES spectra of **S1** (red line) and **S1-H** (black line) monolayers taken at 630 eV.

The peak observed at 448 eV (about 182 eV in KE) which is not common, corresponds to a chlorine Auger electron (Cl L_3VV) and the additional peak observed at 336 eV has been assigned to Au $4d_{5\ 2}$. Due to the photon energy used in these PES measurements it was not possible to see the Fe2p, but taking again the survey spectrum at higher energy (1486.6 eV) using an Al Kα X-ray source it has been possible to see it, at the expected energy (708 eV), as shown in Figure 4.3.

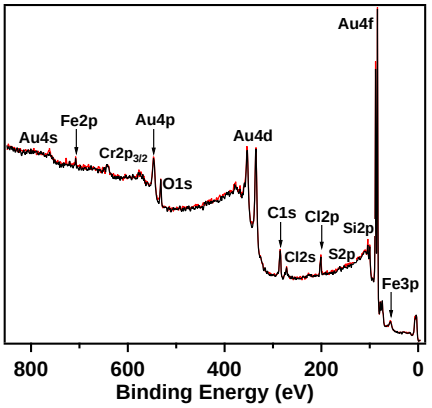

Figure 4.3: Survey XPS spectra of **S1** (red line) and **S1-H** (black line) monolayers taken at 1486.6 eV.

In order to compare XPS intensities of the two measured SAMs (**S1** and **S1-H**), the calculation of the relative atomic percentages (At.%) is required and not only a direct comparison of peak areas. Because the XPS spectrum is a combination of the number of electrons that leave the sample surface and the ability of the instrumentation to record such electrons. At.% is the representation of the intensities as a percentage; which guarantees that even though the experimental conditions change from measurement to measurement (or sample to sample), the relative peak intensities would remain constant[19].

More than one transition with suitable intensity can be used in quantification because each element has a range of electronic states open to excitation by the X-rays. However, transitions from different electronic states of the same element and also transitions from different elements vary in peak areas. Therefore, the peak areas calculated from the data must be scaled to ensure that the same quantity of the element is determined from either suitable transition and also from either element. Then, a set of relative sensitivity factors are necessary for transitions

within an element and also for all elements. The sensitivity factors are designed to scale the measured areas so the meaningful atomic concentrations can be obtained, regardless of the peak chosen[19].

Taking into account the relative sensitivity factors and once calculated the At.% for the different elements observed in the survey XPS spectra of both SAMs, it was possible to determine the XPS Cl:Fe ratio of the radical SAM **S1** and the protonated SAM **S1-H**, being 13:0.5 and 10.3:1.2, respectively. Such ratios were close to the stoichiometry of the molecule (14:1) demonstrating in this way that the integrity of the disulfide D–A systems **1** and **1H** is maintained once the monolayer has been formed.

Film thickness of SAMs **S1** and **S1-H** was obtained from the high resolution PE spectrum of Au taken at 630 eV shown in Figure 4.4 by evaluating the attenuation of the Au $4f_{7\ 2}$ peak of a sputtered substrate and for each functionalized substrate according to Equation 4.2[20,21].

$$I = I_o exp(-d\ \ \lambda cos\theta) \tag{4.2}$$

Where I and I_o correspond to the substrate intensity of the SAM covered and bare surface, respectively; d is the SAM thickness, and θ is the detection angle with respect to the surface normal. In this case, θ was zero since the analyser was normal to the sample surface obtaining a deviation of the emission angle from the surface normal of 0. λ is the photoelectron attenuation length and is characteristic of each system. λ depends on the kinetic energy of the photoelectrons and for these measurements it was assumed a value of 18.2 Å reported for adenine† as model organic system, supported by the fact that similar values have been reported for organic systems.

A thickness of 2.23 nm was estimated for **S1** and for **S1-H** monolayer a similar value of 2.27 nm was calculated. The values obtained reflects that molecules in both monolayers are standing up which is quite reasonable since both systems are almost identical in structure. Considering a total length of 2.6 nm for the molecule

†Lamont, C. and Wilkes, J. (1999) reported the expression $\lambda = 0\ 3E^{0.64}$ to claculate the attenuation length of photoelectrons of n-alkanethiols monolayers on gold in the range of 300-1000 eV of KE. Using this equation a value of λ = 16.94 Å is obtained, which is close to the value assumed.

(**1**, **1-H**) calculated in gas phase[‡], a tilt angle around 30° is expected which is in a good agreement with those reported in the literature[22,23] for complex systems with the same alkyl disulfide anchoring group.

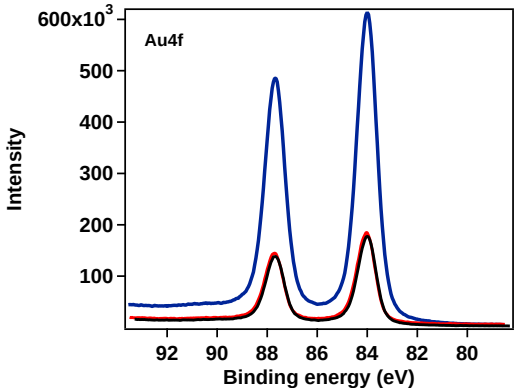

Figure 4.4: HR-PE spectra of **S1** (red line), **S1-H** (black line) monolayers and bare gold (blue line) taken at 630 eV.

The Au4f high resolution (HR) spectra of both monolayers (Figure 4.5(a)) show the expected doublet at 84 eV (Au $4f_{7\ 2}$) and 87.7 eV (Au $4f_{5\ 2}$). Another common doublet was found in the Cl2p spectra, with Cl $2p_{3\ 2}$ binding energy at 200.8 eV (C–Cl) and a spin orbit coupling between Cl $2p_{3\ 2}$ and Cl $2p_{1\ 2}$ equal to 1.7 eV. This feature is characteristic of the PTM moiety and it has been reported previously for other PTM radicals monolayers[24–26].

The Fe2p spectra for these systems is of great importance in order to determine the electronic structure (neutral or zwitterionic) of these Fc–PTM SAMs. The Fe2p HR X-ray photoemission spectra (Figure 4.5(c)) show two sharp photoelectron peaks at 707.9 (Fe $2p_{3\ 2}$) and 720.7 (Fe $2p_{1\ 2}$) eV. The binding energies of the doublet are in a good agreement with values reported in the literature[27,28] for Fc-compounds adsorbed on substrates and they have been assigned to the reduced (2+) state of Fc since the XPS Fe2p spectrum of the ferricinium cation (3+) is expected at 710.6 (Fe $2p_{3\ 2}$) and 723 eV (Fe $2p_{1\ 2}$)[29,30].

[‡]Value determined by Francesca Delchiaro, PhD student in the group of Prof. Anna Painelli at Parma University; using PM7 (RHF) calculations at optimized ground state (U)CAM-B3LYP/6-31G* level with modified dihedral angles.

O1s spectra (Figure 4.5(d)) show a broad band localized at 532.2 eV which corresponds to the oxygen atom present in the ester group.

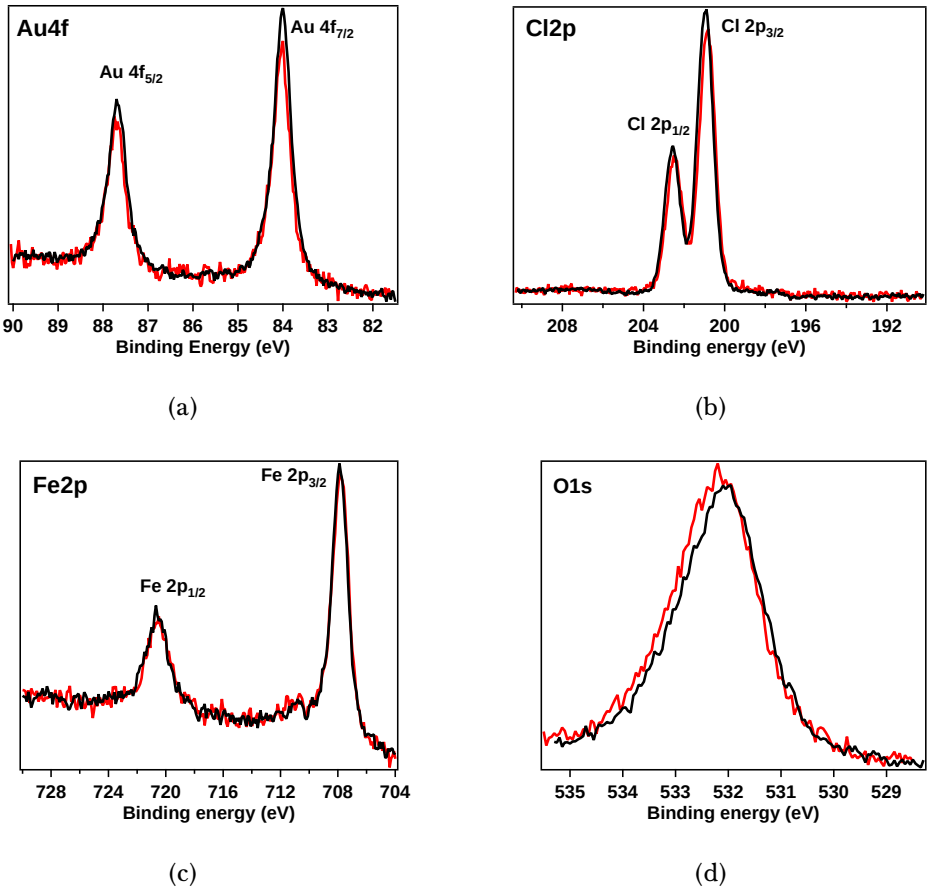

Figure 4.5: High Resolution Photoemission spectra of **S1** (red line) and **S1-H** (black line) for (a) Au 4f, (b) Cl2p, (c) Fe2p and (d) O1s.

The analysis of carbon 1s spectra (Figure 4.6) is more difficult that the aforementioned elements because the carbon atoms present in these systems contain different substituents and types of bonds. Additionally, the position of the photoelectron peak can be sensitive to different factors such as the charge density on the non-ionized atom or to the degree of shielding of the core hole generated by the loss of the electron, among others. As a result, chemical shifts to higher binding energies for carbons in higher oxidation states or with electronegative substituents can be expected[31]. Thus, in order to identified the different carbon atoms, the spectra obtained have been fitted using the XPS Peak software giving place to five well defined peaks which assignment has been suggested as follows. The peak at

284.4 eV corresponds to the aliphatic carbon atoms present in the thiotic acid-alkyl chain while the small peak at 288.6 was assigned to the carbonyl group (C=O) [31,32]. The peak at 284.8 eV in **S1** and shifted 0.2 eV in **S1-H** could have the contribution of the C_{arom}–$C_{central}$ atoms of the PTM moiety as well as the cyclopentadienyl carbons (C_{Cp}) [28,30]. Finally the peaks observed at 286.1 and 286.5 could corresponds to the sp^2 carbon atoms present in the chlorinated phenyl groups of the PTM [24].

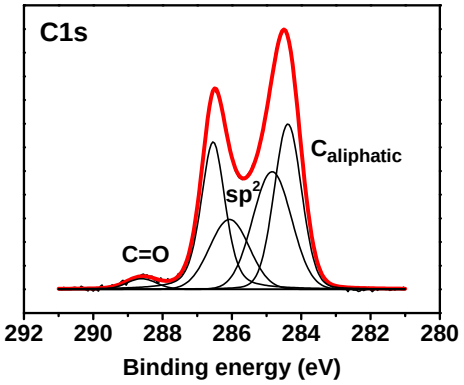

(a)

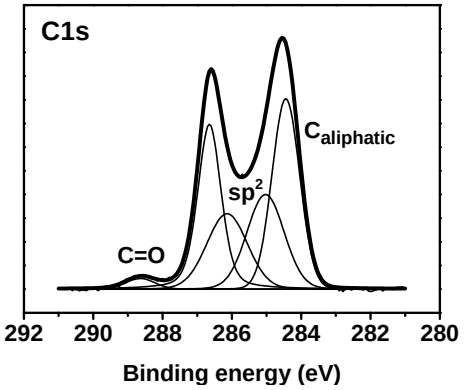

(b)

Figure 4.6: High Resolution Photoemission spectra of C1s of (a) **S1** and (b) **S1-H**

The degree of bonding between the molecules and the substrate can be evaluated from the S2p spectra. After deconvolution, four principal peaks were identified, two at lower binding energies which corresponds to the S2p doublet S $2p_{3\ 2}$ and S $2p_{1\ 2}$ with values of 161.8 and 163.1 eV, respectively. They are related to the gold bound thiolate species while the doublet observed at 163.7 (S $2p_{3\ 2}$) and

164.6 eV (S $2p_{1\ 2}$) was assigned to the unbound disulfide[20,33]. The percentage of unbounded sulfur is around 16% for both SAMs (**S1**, **S1-H**), which could be due to the fact that some molecules were attached only by one sulfur atom of the disulfidde anchoring unit.

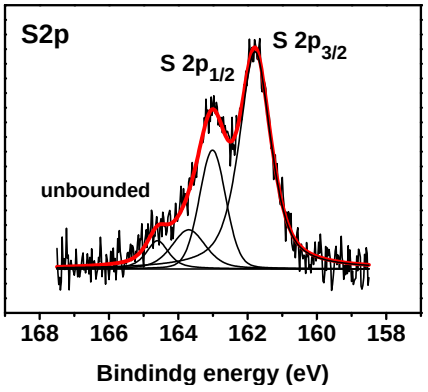

(a)

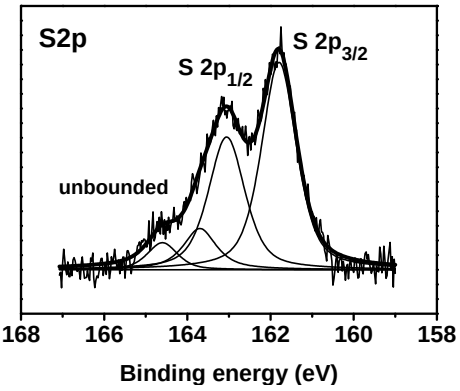

(b)

Figure 4.7: High Resolution Photoemission spectra of S2p of (a) **S1** and (b) **S1-H**

In Table 4.1 are summarized all the binding energies identified for each atom analyzed in the HR-spectra of **S1** and **S1-H** monolayers. Comparison with standards is mandatory to confirm these assignments, and thus, such assignments have been suggested based on what is reported in the literature for similar systems.

Table 4.1: High-resolution photoemission spectra data for **S1** and **S1-H** monolayers.

Atom	Binding energy (eV)		Type of bond
	S1	**S1-H**	
$Cl2p_{3\ 2}$	200.8	200.9	C–Cl bond, characteristic feature
$Cl2p_{1\ 2}$	202.5	202.55	of the PTM moiety.
$Fe2p_{3\ 2}$	707.9	707.9	Reduced state of the Fc moiety.
$Fe2p_{1\ 2}$	720.7	720.7	
C1s	284.4	284.4	Aliphatic carbon atoms.
	284.8	285.0	C_{arom}–$C_{central}$ (PTM) and cyclopentadienyl carbons (C_{Cp}).
	286.1	286.1	sp^2 carbon atoms and
	286.5	286.6	chlorinated phenyl groups of the PTM.
	288.6	288.6	Carboxyl group.
$S2p_{3\ 2}$	161.8	161.8	Gold bound thiolate.
$S2p_{1\ 2}$	163.0	163.1	
$S2p_{3\ 2}$	163.7	163.7	Unbound disulfide.
$S2p_{1\ 2}$	164.6	164.6	

4.5 Resonant photoemission spectroscopy (RPES)

Following with the study of the electronic structure of D–A systems self-assembled on gold, in order to investigate the interaction in terms of charge transfer at the metal/organic interface, resonant photoemission spectroscopy (RPES) was used. In RPES one excites the sample with photons of an energy ($h\nu$) very near to the adsorption threshold of a core level[34], achieving that some signals present in PE spectrum can be observed as more intense peaks in RPES due to the additional autoinization channels which open up in the resonance case[35]. Thus, the resonant process for comprehension purposes, could be visualized as a two-step process, the excitation of a core-electron and the deexcitation or decay of it. Due to the irradiation ($h\nu$) of the sample, a core-electron localized in the initial

state is photoexcited to an empty level (resonant bound state) forming an intermediate (excited) state where the system remains in the neutral electronic state, see Figure 4.8 (left). The intermediate state decays via an autoionization processes that annihilate the core-hole to yield a final state identical to that obtained by the direct photoemission process. After the decay process one electron is emitted and the system ends up with a single valence vacancy and a charge of +1.

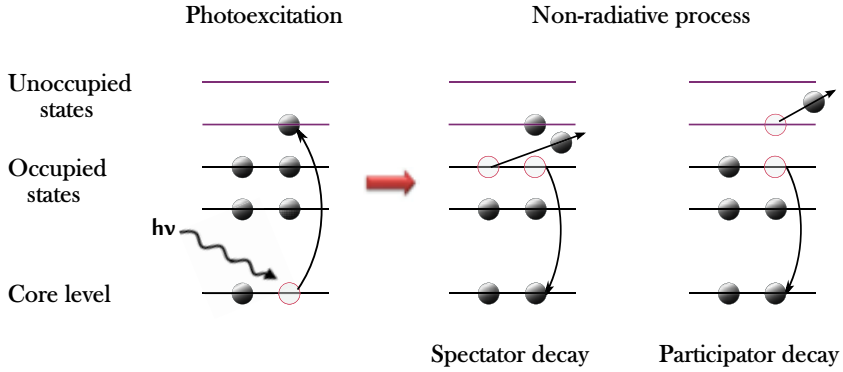

Figure 4.8: Schematic representation adapted from[36,37] of the X-ray absorption-induced transition from core level to lowest unoccupied level (left) and two possible core-hole decay paths: resonant Auger or spectator decay (middle) and resonant photoemission or participator decay (right).

The autoionization can take place via two different channels: *i)* one, often called *resonant Auger* or *spectator autoionization* because in the final state the excited electron stays localized on the unoccupied level, and instead of it, two valence electrons are removed in an Auger-like transition, one of them fills the core-hole and the other is emitted, see Figure 4.8 (middle); and *ii)* the other path, known as *participant channel* is the process where the excited electron takes part in the Auger process and is emitted while one valence-electron fills the core-hole, see Figure 4.8 (right), this final state is equivalent in energy to the valence photoemission spectra[36,38]. In both autoionization process the KE of the emitted electron is proportional to the exciting photon energy ($KE \propto h\nu$), and changing the photon energy the unoccupied orbital space of the sample is probed.

The photon energy (hν) can be chosen in a proper way to achieve selectively excitation and therefore the signal enhancement of particular elements present on the sample. Since disulfide D–A systems (**S1** and **S1-H**) in majority are formed by carbon atoms (40 atoms per molecule), carbon was chosen to perform RPES.

An energy sweep was made from 283 to 287 eV with increasing steps of 0.5 eV and very intense and clear resonance of carbon was found at 286.5 eV in both **S1** and **S1-H** monolayers (Figure 4.9) which is not commonly observed. At this energy a great increase of the intensity of four principal peaks was observed. The first two peaks observed in the different spectra showed in Figure 4.9, will not be considered in this analysis and that do not change in intensity. These two peaks have been interpreted as signals of the carbon of second order since their position is shifted twice the energy (1.0 eV) that is increased in each step (0.5 eV).

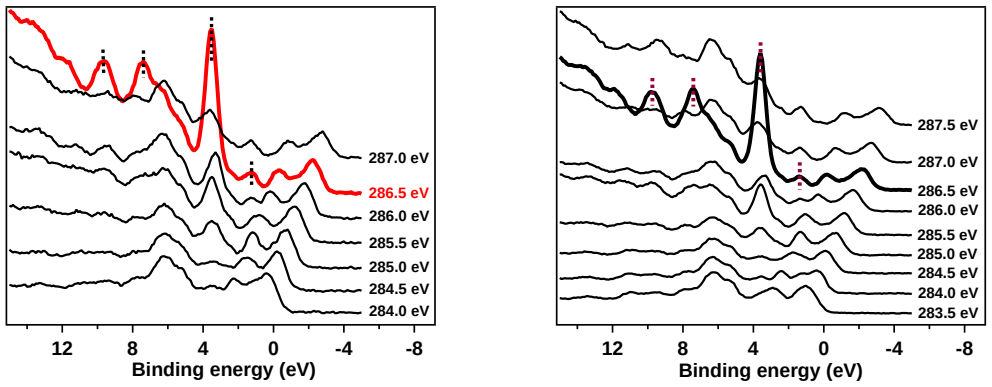

(a) (b)

Figure 4.9: Resonant photoemission (ResPES) spectra of **S1** taken at different binding energies (a). The corresponding spectra for **S1-H** monolayer are shown in (b).

The first peak observed for **S1** at 1.2 eV has been assigned to the contribution of carbon atoms belonging to the Fc moiety, on the HOMO of the system. Due to the electronic push-pull configuration of this system, the first occupied level accessible in energy has to be placed in the Fc-donor part. The remaining peaks observed at 3.5–3.6, 7.4 and 9.7 eV could belong to the delocalization of the different HOMO orbital on the carbon of the PTM moiety.

The high intensity showed by the resonance spectrum, specially by the peak around 3.5 eV is an indication of the weak metal-organic interactions. This is in agreement with the fact that if a molecule is placed on a metal substrate, there is a high probability for the excited electron to delocalize into the continuum electronic states of the metal if the LUMO of the molecule is strongly coupled with the metal substrate workfunction. In this case, both spectator and participator processes

are strongly quenched, yielding to low or almost no photoelectron intensity[37]. For **S1** and **S1-H** monolayers, the high intensity observed for the different peaks are a clear indication that the molecular orbitals are not delocalized in the substrate but they are localized in the molecule. It is important because it demonstrate that the molecule preserves its electronic structure which is very desirable for potential applications.

Regarding to the clear resonance peaks observed, the first two peaks are slightly shifted to higher BE in the **S1-H** monolayer (1.4 and 3.6 eV) with respect to that observed in the **S1** monolayer (1.2 and 3.5 eV). The difference of 0.2 eV for the first peak could be related with the presence of the PTM radical in **S1** with a singly-unoccupied molecular orbital (SUMO) at lower energy than the **S1-H** LUMO and close in energy to the HOMO of the Fc moiety. The small difference in energy between these two orbitals (SUMO and HOMO), probably allows a certain degree of coupling and then the energy required to extract one electron from the valence band is smaller in **S1** compared with **S1-H**.

4.6 Study of the occupied and unoccupied molecular orbitals of of Fc–PTM SAMs

4.6.1 Valence Band (VB) Spectra

The valence band (VB) of a sample is obtained when the surface is irradiated with a beamline of low photon energy. Then the outermost electron shell of atoms are ejected and recollected by the analyzer, given place to the band spectrum made up of the occupied molecular orbitals of the sample. The VB spectra for **S1** and **S1-H** monolayers were taken at 40 eV photon energy. Figure 4.10 shows a comparison between the VB spectrum of the monolayer and bare gold. Additionally, the resonance spectrum for carbon, previously mentioned was plot to compare the peaks observed.

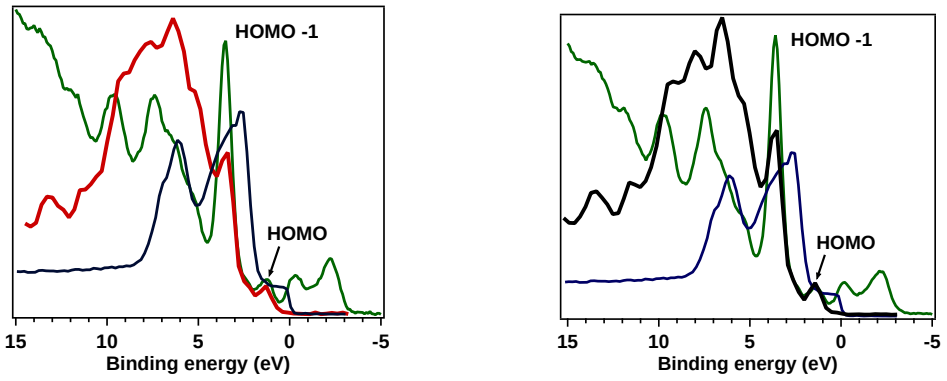

Figure 4.10: (a) Valence band spectrum of monolayer (red) and of bare gold (blue) measured at 40 eV photon energy for **S1**. Line pro le of C1s resonance at 286.5 eV (green) was added for comparison effects. The corresponding panels for **S1-H** monolayer are shown in (b). The intensities of both valence band spectra have been scaled for clarity.

The most remarkable feature observed in the VB spectra of both systems is the peak at 1.2 eV present in **S1** and 1.4 eV in **S1-H** with respect to the Fermi Level. Since the peaks observed in the VB spectrum corresponds to occupied molecular orbitals of the system, this peak could be related with the HOMO of the monolayers which should be more localized in the Fc-donor subunit.

A similar peak at ≈ 2.0 eV has been observed in the VB spectra of ferrocenyl-based salts but absent in their ferrocenium analogues[30], so it is possible to say that the Fc is in its reduced electronic state even though the lower BE at which was found this peak (1.2–1.4 eV) that can be due to the high electron acceptor ability of the PTM. The HR–XPS spectrum of the Fe2p confirms the reduced state of the Fc (Figure 4.5(c)).

Specifically, the observed peak has been assigned to photoemission from the HOMOs of the Fc (e_{2g} and a_{1g})[20,39]. In Fc, the valence orbitals aforementioned are filled by the six 3d electrons from iron giving an electron configuration of $(e_{2g})^4(a_{1g})^2$ while in ferrocenium compounds the configuration of the valence band electron corresponds to $(e_{2g})^3(a_{1g}^2)$[30]. At higher energy (3.6 eV for **S1** and 3.5 eV for **S1-H**) it was observed an intense peak, which also appears in the C1s resonance spectrum of both SAMs. Such peak corresponds to another occupied molecular

orbital higher in energy and named HOMO–1. This peak is more localized in the PTM unit since it was also observed in similar systems.

Summarizing, from the VB spectrum of **S1** the following bands that corresponds to the density of states (DOS) of the molecule **1** were observed at 1.2, 3.6, 5.1, 6.3, 7.5, 9.0, 11.4 and 13.2 eV while for **S1-H** monolayer the occupied molecular orbitals were distinguished at 1.4, 3.5, 5.3, 6.5, 8.0, 9.2, 11.6 and 13.4 eV.

In the Fermi Level region (Figure 4.11) it was possible to see in more detail the peak previously assigned to the HOMO of both systems (**S1** and **S1-H**) anchored to gold surface. The vanishment of the Au 5d band indicates the effective coverage of the surface with the disulfide D–A systems.

The shift observed in the HOMO peak between the **S1** and **S1-H** can be due to the presence of the higher electron acceptor ability of the radical in comparison with the closed shell structure of the **1H**.

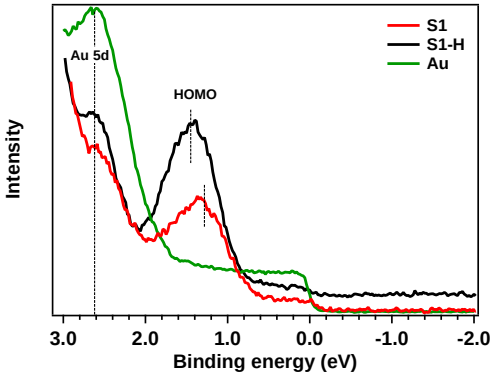

Figure 4.11: Spectra of the VB at the Fermi Level region for **S1**, **S1-H** and Au.

4.6.2 Near-Edge X-ray Absorption Fine Structure Spectroscopy (NEXAFS)

NEXAFS is a highly selective technique for studying the unoccupied molecular orbitals at selected atomic species being possible to observe optical transitions from a specific core level (usually K-edge) into the lowest unoccupied orbital.

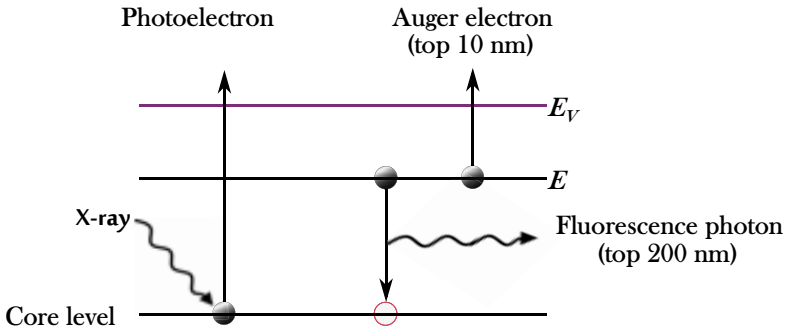

Figure 4.12: Energy diagram of the photoabsorption process and the subsequent electron decay by two different paths; taken from refs.[40,41]

This technique is based on the sample irradiation with monochromatic X-rays that induces the excitation of electrons from the core level to partially filled and empty states, which gives as result a photoelectron and a core hole. The subsequent decay of core-hole states ends in the emission of Auger electrons (from the top 10 nm) from the valence molecular orbitals or the emission of fluorescent photons (from the top 200 nm), resulting in a NEXAFS electron yield spectrum, where both the peak position and the spectral lineshape are directly related to the nature of these unoccupied electronic states[40,41] (see Figure 4.12) labeled as π^*- or σ^*- orbitals according to their symmetry.

NEXAFS is not limited to the knowledge of the electronic structure of molecules, moreover it is also useful to get information about the molecular orientation since bonds and molecular orbitals associated to them are highly directional and the angular dependence of the K-shell (electron closest shell to the nucleus) spectra is determined by the spatial orientation of the orbital on the excited atom. In this context, the polarization characteristics of synchrotron radiation plays an important role because the transition intensities observed in NEXAFS spectra depend on the orientation of the electric field vector of the incident X-rays with respect to the orientation of the molecule. Therefore, the intensity of a resonance is largest when the electric field vector **E** lies along the direction of the final state molecular orbital (**O**) and vanishes when **E** is perpendicular to it. Remind that π^*-orbitals have maximum amplitude normal to the bond direction while σ^*-orbitals have a maximum orbital amplitude along the bond axis, see Figure 4.13. Hence, the spatial orientation of an orbital can be determined by taking NEXAFS measurements

at two or more angles of incidence of the X-rays taking into account that all dipole transition moments contribute to the resonance[41].

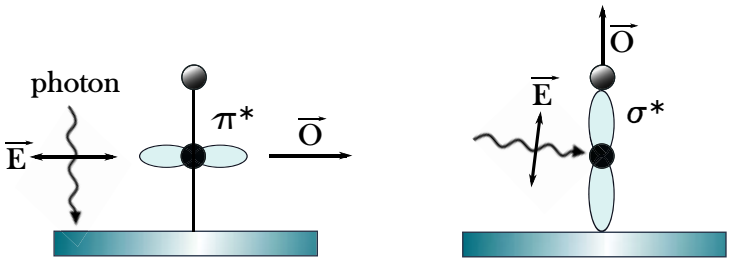

Figure 4.13: Schematic representation of the origin of the polarization angular dependence of NEXAFS resonances, where the $\pi*$–resonance is maximized at normal incidence (left), while the $\sigma*$–resonance is maximized at grazing incidence (right). Image adapted from refs.[40,41]

So, NEXFAS measurements of the C *K*-edge, Fe *L*-edge, Cl *K*-edge and O *K*-edge were performed for **S1** and **S1-H** monolayers. The carbon *K*-edge spectra of monolayers **S1** and **S1-H** recorded at normal (NI) and grazing (GI) incidence are shown in Figure 4.14. For the case of **S1** monolayer, it was observed that the intensity of the peaks corresponding to the π^* resonance is higher at normal incidence than at grazing incidence, which could be related with a certain degree of a preferential orientation of the molecules, situation that does not happen in **S1-H** monolayer. Such molecular orientation is expected since in normal incidence the **E** vector of the light results parallel to the surface, while in grazing is "almost" parallel to the normal and thus excites the orbitals along the molecular "axis".

On the other hand, comparing the spectra of both monolayers, the main difference between them was the small peak at 282.6 eV observed in the open-shell radical monolayer **S1** but not in its closed-shell protonated monolayer **S1-H**. This peak has been previously assigned to the SUMO[24] of the PTM; being a signature of this specie. At this point it is worth to emphasize that preserving the magnetic character (unpaired electron) of this system is really important with regard to possible applications in electronics. Such character has been previously seen by EPR at another scale (3D) but also in the SAM (see Figure 3.52). In the case of the monolayers (2D structures) the presence of an insulating chain keep the D–A central core far from the metal substrate preventing a possible hybridization.

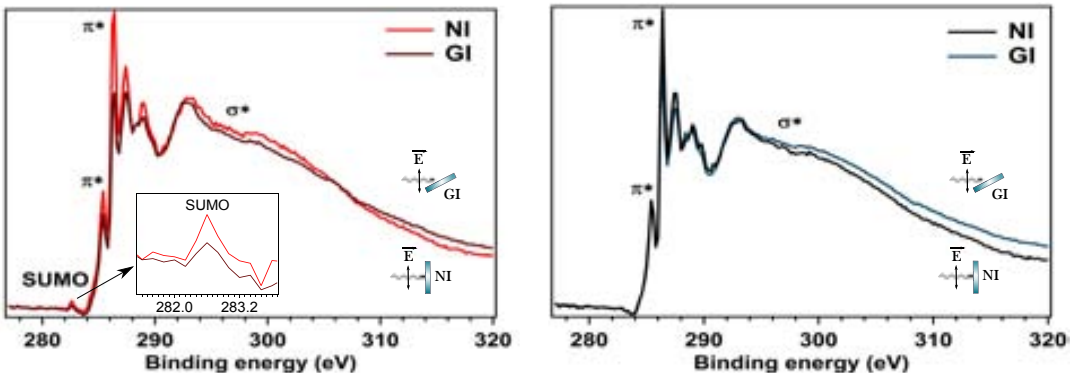

Figure 4.14: C K-edge NEXAFS of (a) **S1**, (b) **S1-H** monolayers at normal (NI) and grazing (GI) incidence.

The rest of the assignment has been performed taking as a base reference the previous work performed in our group[24] in which it has been studied substituted PTM radicals onto a COOH–functionalized SAM through copper (II) metal ions and also in accordance with refs[32,37,42–46].

The π^* resonance peak at 285.4 eV corresponds both to the transition of the C1s electrons into antibonging $4e_{1g}$ orbital of the Fc and C1s $\Rightarrow \pi^*$ transitions localized on carbon atoms on the perchlorinated benzene rings. The high intense peak observed at 286.4 eV was assigned as C(Ph) $\Rightarrow \pi^*$ resonance on the perchlorinated benzene rings. The peak at 287.4 eV essentially corresponds to the transition of the C1s electrons into antibonging $3e_{2u}$ orbital of the Fc and probably has a small contribution of the σ^* (C–S) resonance localized around 287 eV which resulted not distinguishable. At higher energy was observed a peak localized around 289 eV and a shoulder at 288.4 eV, these peaks can be related with C1s transitions into the π^* orbital of the carboxyl group. Finally the broad peaks at 292.8 and 299 eV corresponds to C–C σ^* resonance

In the Cl L-edge NEXAFS spectra of radical and non-radical monolayers (**S1**, **S1-H**) showed in Figure 4.15 a broad feature with two components was observed around 201 eV. This band could be related with the transition of Cl $2p_{1/2,3/2}$ electron to empty σ^* states. Another feature at 203.6 eV could be assigned to the 4s Rydberg excitation[47,48].

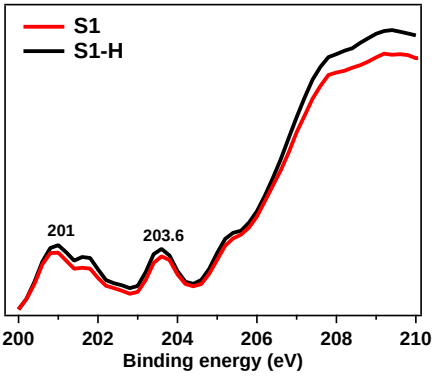

Figure 4.15: Cl L-edge NEXAFS spectra of **S1** and **S1-H** monolayers at normal incidence.

O K-edge NEXAFS spectra of **S1** and **S1-H** are shown in Figure 4.16. The intense feature observed at 531.8 eV can be attributed to transitions from O1s core level electrons to empty π^* C=O states while the broad band at higher photon energy range (537–540 eV) could have the contribution of several θ^* transitions (O–H, C–O and C=O)[49–53].

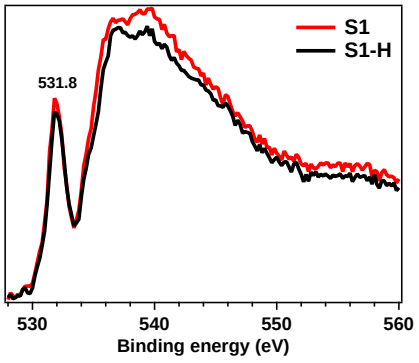

Figure 4.16: O K-edge NEXAFS spectra of **S1** and **S1-H** monolayers at normal incidence.

The Fe L-edge NEXAFS spectra of **S1** and **S1-H** monolayers (Figure 4.17) show the characteristic π^* resonances of Fc which correspond to the transition of the Fe 2p electron into the empty π^* ($4e_{1g}$) and π^* ($3e_{2u}$) orbitals[44,54].

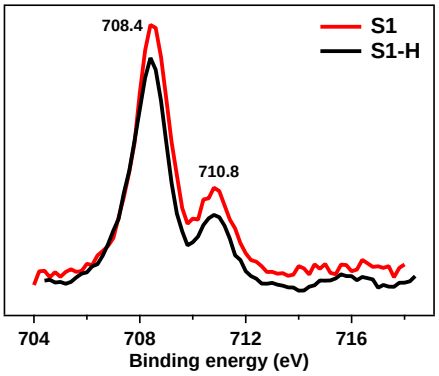

Figure 4.17: Fe L-edge NEXAFS spectra of **S1** and **S1-H** monolayers at normal incidence.

Moreover, analyzing the energy and the intensity at which appears the multiplet structure of the L_3 edge of Fe2p which is sensitive to the oxidation state of the metal[55]. It is possible to know the oxidation state of the Fc moiety. Specific energies and relative intensities have been observed for L_3 edge of Fe^{2+} and L_3 edge of Fe^{3+}, which are reported in the literature[56]. In both electronic states (reduced and oxidized) are clearly observed two peaks, one more intense than the other. In the reduced form the dominant peak is observed at lower energy while the weaker one is present at higher energy. However in the oxidized form the behaviour observed is the opposite, which means that the weaker peak appears at lower energy and the stronger peak at higher photon energy. Features in accordance with that reported by Zheng *et. al*[56] for Fc SAMs and by Hitchcock et al.[57] for isolated Fc have been observed in **S1** and **S1-H** monolayers. In the L_3 edge of Fe $2p_{3\,2}$ the dominant peak was observed at 708.4 eV and the weaker peak at 710.8 eV. The energies and the relative intensities observed correspond to Fe^{2+} which is in agreement with the reduced state observed previously in the HR–PES of iron atom (Figure 4.5(c)).

Since, modification of the electronic state of Fc-terminated monolayers has been observed by irradiation with soft X-rays[56]. It was really important to control such kind of modification along all these measurements. It was not any probe of the possible reduction of the Fc moiety due to the synchrotron radiation, neither in **S1** nor in **S1-H** . And to guarantee no decomposition of the sample, each spectrum was taken in different spots as it is explained in Appendix A.

4.7 Use of external stimuli to modify the electronic structure of Fc–PTM SAMs

As it has been mentioned in Chapter 2, D–A systems based on Fc–PTM have shown bistability in 3D structures between a wide range of temperatures. Also playing with the solvent polarity it has been possible to favour one state or another (neutral or zwitterionic, respectively) or the coexistence of both electronic states at the same time. Based on these studies, and on the fact that playing with the temperature or the solvent polarity, as external stimuli, it has been possible to modify the proportion of the two stable electronic states (neutral and zwitterionic) of these D–A systems; the possibility to observe the same phenomenon in 2D organized structures as SAMs constitutes a great scientist motivation for obtaining a molecular switch able to be modified by soft external factors.

From the previous characterization by synchrotron radiation, it has been demonstrated that all the molecules in **S1** monolayer are in their neutral state, and no signal of the charge-separated state was observed. However, in order to look for potential applications of these systems in molecular electronics it will be interesting the study of the molecular switching ability of these systems by applying an external stimuli.

4.7.1 Solvent effect

As it has already been studied in 3D (solution phase) modifying the polarity of the environment of the molecules it is possible to switch the system from the neutral to the zwitterionic state by using non-polar or polar solvents, respectively (see Chapter 2). Based on these observations it will be interesting to study if playing with the polarity of the environment it is possible to see some change of the electronic structure of the Fc–PTM SAMs in 2D. In order to perform such experiments we will take advantage of the recently built near ambient pressure (NAPP) end-station at CIRCE beamline inside ALBA synchrotron facilities in which it is possible to perform spectroscopic measurements at high pressures using vapors of different gases or solvents. Since water is a high polar solvent; vapors of this

solvent will be used to observe any differences in the charge transfer state due to a more or less solvation of the SAMs with polar water molecules.

Based on the work of Ketteler *et. al*, three different water vapor pressure were used to stimulate the intramolecular electron transfer of SAM **S1**, namely 10E-6 mbar, 10E-3 mbar and 1 mbar. **S1** monolayer was exposed for a total of 45 minutes in each water vapor pressure, and it was characterized by PES at the beginning and after 30 minutes. The principal atoms followed in this study were: C1s, Cl2p and Fe2p and are shown in Figures 4.18 and 4.19 at different water vapor pressures.

All the spectra for C1s and Cl2p taken at different water vapor pressures show exactly the same features that the reference spectrum and also the BE of the peaks corresponding to each atom are the same in each water vapor condition. As it can be seen in Figure 4.18 no shift of peak position is observed for C neither for Cl.

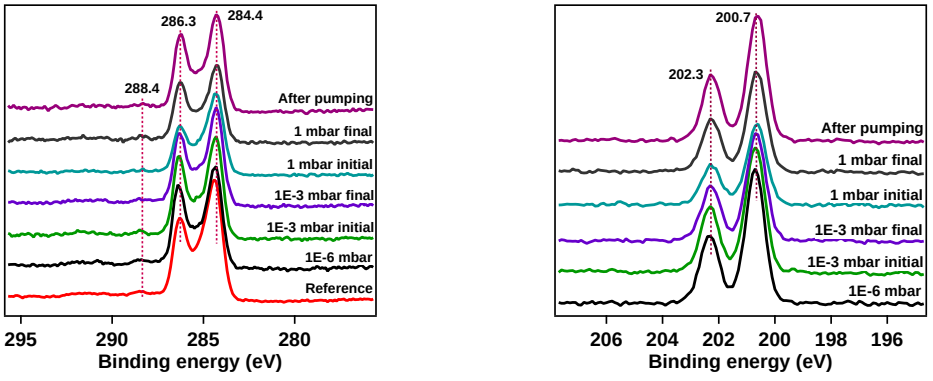

(a) (b)

Figure 4.18: High resolution photoemission of (a) C1s and (b) Cl2p under the effect of different pressure of water vapor.

On the other hand, since any change in the electronic structure of the molecule should be reflected mainly on the peak position of the iron atom; special interest was put in the analysis of this element. Figure 4.19 shows the Fe2p spectra taken under different pressures of water vapors.

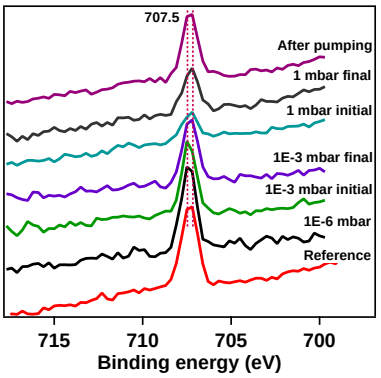

Figure 4.19: High resolution photoemission of Fe2p under the effect of different pressures of water vapors.

Contrary to that expected, when using vapors of polar solvent like water, there is no shift of the iron peak. This fact is an indication that the presence of water molecules on the top of the **S1** monolayer is not affecting the electronic structure of the Fc–PTM system. One reason for such lack of interaction could be related with the hydrophobicity of the system due to the presence of chlorine atoms at the top part of the SAM which will repeal the water molecules preventing a good solvation and therefore diminishing the possibility of any interaction between the Fc–PTM SAM and the water molecules. The small intensity change observed in the spectrum taken at 1 mbar during the first minutes could be related with the presence of a lot of water molecules on the top of the surface which di cult to obtain a good signal of the iron, element localized in the internal part of the SAM. Nevertheless the intensity of the iron peak was recovered after pumping the water vapor. Figure 4.20 shows the HR-PE spectrum of O1s taken at the water vapor phase and also on the top of the functionalized surface. As it can be seen the peak around 532 eV probe the presence of water molecules in contact with the SAM.

In the effort to induce any variation on the electronic structure of SAM **S1** by applying an external stimuli, and because it has not been possible to change the electronic state of the anchored molecules by using water as polar solvent. We will use temperature as another suitable option, since variation in the proportion of the neutral and zwitterionic state of the Fc–PTM system was previously achieved in bulk by effect of the temperature.

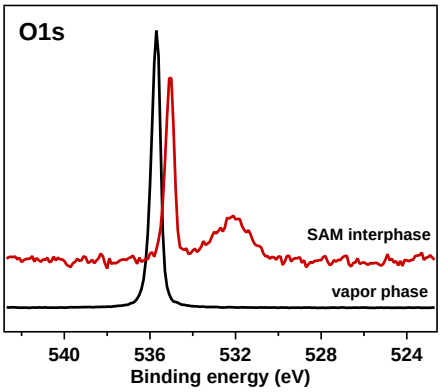

Figure 4.20: High resolution photoemission of O1s at the water vapor phase and on the top of the surface.

4.7.2 Temperature effect

Temperature is a relatively easy and handy stimulus to be used as external energy source to induce the intramolecular electron transfer (IET) from the donor to the acceptor part of the system. This electron movement can be checked by HR–PES of the iron atom because once the Fc part give one electron that is accepted by the PTM unit, the electronic structure of the iron atom changes and there are specific energies attributed to the oxidized specie formed. The experiments that allowed studying the effect of the temperature in **S1** monolayers were carried out in BL24–CIRCE beamline at ALBA facilities.

To heat the sample, a holder equipped with a filament for electron bombardment, a W:Re thermocouple, and two extra contacts was used; and the range of temperatures used was from room temperature up to 150 °C. Figure 4.21 shows the sample mounted in the holder used for temperature experiments.

Figure 4.21: Sample mounted on the holder used for temperature experiments.

To study the influence of the temperature over the electronic structure of the **S1** monolayer, the sample was heat from room temperature up to 120 °C, allowing the stabilization of the temperature before the corresponding measurement. Figure 4.22 shows the iron HR–PE spectra taken at different temperatures. Here, a small shift toward higher energies was observed, passing the maximum position of the peak from 707.7 eV at room temperature to 708.2 eV at 115 °C ($\Delta = 0.5\ eV$).

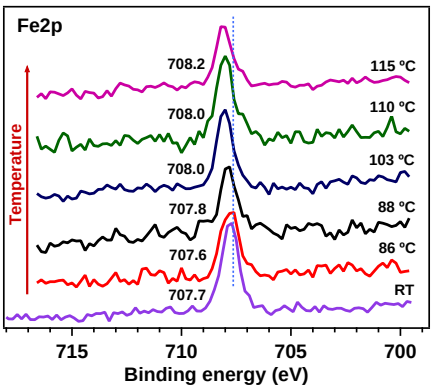

Figure 4.22: High resolution photoemission of Fe2p at different temperatures.

The range of the energy observed for the Fe2p peak can be interpreted in terms of the presence of the reduced specie and contrary to what was expected, no IET was induced by the temperature. However, the small shift in the energy was demonstrated to be reversible as it is shown in Figure 4.23, where it can be appreciated that once the sample is cooled again down to 50 °C the peak position returns to its initial point (707.8 eV).

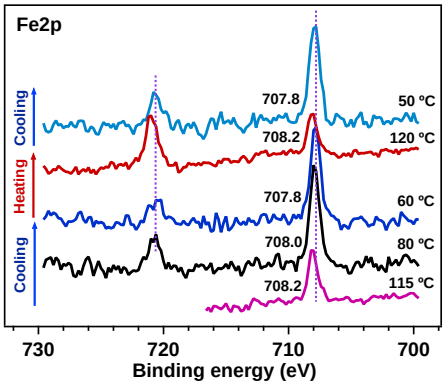

Figure 4.23: High resolution photoemission of Fe2p at different temperatures. Recovering the initial state.

In order to discard any artifact induced by the holder or by the heating system; the HR–PE spectra of two principal elements such as carbon and chlorine, were taken at different temperature and they are shown in Figure 4.24.

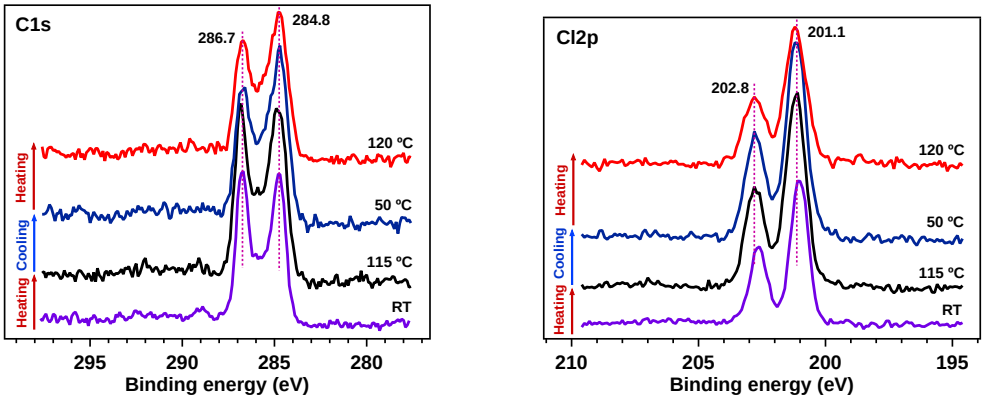

(a) (b)

Figure 4.24: High resolution photoemission spectra of (a) C1s, and (b) Cl2p of **S1** monolayers taken at different temperatures.

Regarding to the C1s, the maximum position of the peaks is practically the same both at room temperature and at 120 °C. The position of the Cl2p peaks present a shift of around 0.2 eV toward higher energies during the first heating but it is not reversible. Probably, such shift induced by the temperature is the result of some excitation in the electronic configuration of the system, as it has been previously observed for the iron environment (Figure 4.22).

After this analysis, the 0.5 eV variation observed in the case of Fe2p spectra should have an electronic structural nature. While it is true that no switch from the Fe^{2+} to the Fe^{3+} was achieved by applying temperature as it has been observed in 3D (bulk) it is clear, from the reversible shift observed in the Fe2p spectra taken at different temperatures (see Figure 4.25), that in 2D using the temperature as external stimuli, a partial charge transfer is promoted from the Fc donor to the PTM radical acceptor unit. Remember, that both reduced and oxidized states of the Fc are characterized for specific energies and that the peak of the Fe^{3+} appears at higher energy than the peak of Fe^{2+}, as it was previously analyzed. Probably, higher energy is required to induce the electron charge transfer in this case, but it was not possible to achieve it since at 150 °C the molecules showed a considerable

grade of degradation.

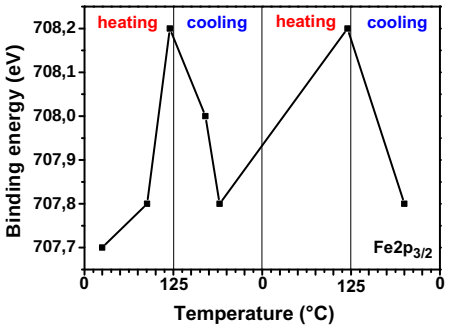

Figure 4.25: Binding energy of Fe $2p_{3/2}$ vs. temperature.

Two elements, C1s and Cl2p, were considered to study the degradation of the molecules with the temperature in **S1** monolayer, and big differences in the shape of the spectrum were observed for both elements. In the case of the C1s, the spectrum obtained after heating the sample to 150 °C, is very similar to that obtained for molecules degraded by the radiation (see Appendix A) where the main peak corresponding to sp^2 carbon atoms of the chlorinated phenyl groups of the PTM ($\approx$ 286–268.5 eV) is vanished (Figure 4.26(a)). Regarding to the spectrum of the Cl2p shown in Figure 4.26(b), a new additional peak was observed at lower energy (198.5 eV).

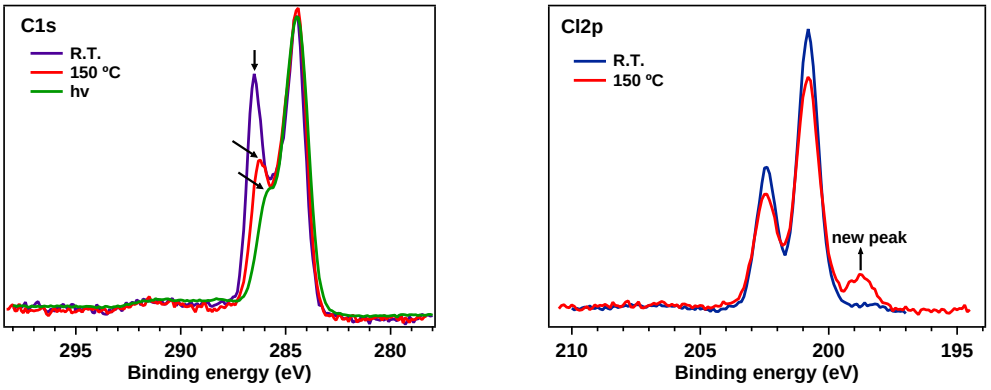

(a) (b)

Figure 4.26: High resolution photoemission spectra of (a) C1s and 4.26(b) Cl2p reflecting the degradation effect of the temperature.

As we have already mentioned, it is clear that once the Fc–PTM D–A system is organized as oriented dipoles in two dimensions, with the temperature (up to 120 °C) it is not possible to switch the system from the neutral to the zwitterionic state as it was possible to obtain in the 3D crystalline phase. However, in the 2D system with oriented dipoles, with the temperature it is possible to observe that some degree of electronic transfer is promoted from the donor to the acceptor (Figure 4.27). This observation elucidates the fact that the intermolecular electrostatic forces that in 3D structures work in a cooperative way to stabilize the neutral and zwitterionic states at room temperature; in 2D structures of oriented dipoles like in SAMs the dynamic equilibrium required to form such kind of structure seems to work in a oppositive way. That is to say, when molecules with permanent dipole moments are forced to be one close to the other an unstable situation is produced because the repulsion induced by charges of the same sign. Moreover, such oriented dipoles create an internal electric field that is contrary to the direction of the molecular dipole. Then, the no bistability observed in these D–A systems when they are organized as 2D structures is interesting from a fundamental point of view.

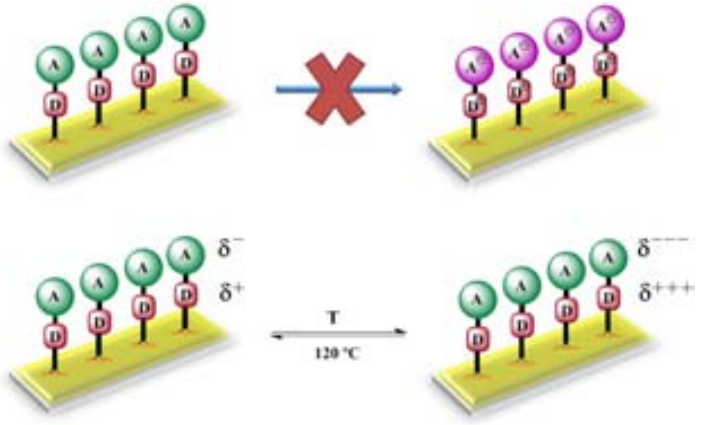

Figure 4.27: Electronic stimulation achieved by temperature.

Additionally, this kind of systems with probably a higher charge delocalization can show different dipole moment in a comparison with a neutral system which could be really interesting to modify metallic surfaces.

4.8 Summary

Along this chapter, a deep study of the correlation between the internal electronic structure and electronic performances of **1** and **1-H**, D−A systems anchored to gold surfaces (**S1** and **S1-H**, respectively) has been performed from a fundamental point of view as well as looking for possible applications.

The electronic characterization of **S1** and **S1-H** monolayers which have very similar molecular structure was studied by synchrotron radiation and through which it was determined the neutral character of the dyad **1** once it is attached to a gold surface as SAMs of oriented dipoles. From these measurements we have seen that the magnetic character was preserved in the SAM **S1** as the NEXAFS spectrum showed and compared with respect to the **S1-H** monolayer where the peak assigned to the SUMO localized on the α-carbon in the K-edge spectrum of the carbon atom, was not observed.

It has not been possible to switch completely the electronic state of the molecule, meaning to pass from the neutral to the zwitterionic state by applying external stimuli like temperature and water solvation. Interestingly, it has been possible to promote a partial charge transfer from the Fc to the PTM under the use of temperature as external stimuli which it has been probe to be reversible. These observations are the first proof that the intermolecular interactions that take place in these kind of structures considered as bi-dimensional are acting in an opposite way with respect to that observed in crystalline structures (3D).

Bibliography

[1] E. L. Wolf, *Nanophysics and Nanotechnology. An Introduction to Modern Concepts in Nanoscience.* New York: WILEY-VCH Verlag GmbH & Co. KGaA, second ed., 2006.

[2] W. R. Frensley, "Quantum transport modeling of resonant tunneling devices," *Solid-State Electronics*, vol. 31, no. 3-4, pp. 739–742, 1988.

[3] A. Forchel, M. Kamp, T. Happ, J. P. Reithmaier, M. Bayer, J. Koeth, and

R. Dietrich, “Photon confinement effects - from physics to applications,” *Microelectronic Engineering*, vol. 53, pp. 21–28, 2000.

[4] V. a. Fonoberov and A. a. Balandin, “Phonon confinement effects in hybrid virus-inorganic nanotubes for nanoelectronic applications.,” *Nano letters*, vol. 5, no. 10, pp. 1920–3, 2005.

[5] C. de Tomas, A. Cantarero, A. F. Lopeandia, and F. X. Alvarez, “From kinetic to collective behavior in thermal transport on semiconductors and semiconductor nanostructures,” *Journal of Applied Physics*, vol. 115, no. 16, p. 164314, 2014.

[6] M. Pourfath, V. Sverdlov, and S. Selberherr, “Transport modeling for nanoscale semiconductor devices,” *2010 10th IEEE International Conference on Solid-State and Integrated Circuit Technology*, pp. 1737–1740, 2010.

[7] D. Vuillaume, “Molecular-scale electronics,” *Comptes Rendus Physique*, vol. 9, no. 1, pp. 78–94, 2008.

[8] Y. Xue, S. Datta, and M. a. Ratner, “Charge transfer and "band lineup” in molecular electronic devices: A chemical and numerical interpretation,” *The Journal of Chemical Physics*, vol. 115, no. 9, p. 4292, 2001.

[9] L. Gross, F. Mohn, P. Liljeroth, J. Repp, F. J. Giessibl, and G. Meyer, “Measuring the charge state of an adatom with noncontact atomic force microscopy.,” *Science*, vol. 324, no. 5933, pp. 1428–31, 2009.

[10] D. M. Alloway, M. Hofmann, D. L. Smith, N. E. Gruhn, A. L. Graham, R. Colorado, V. H. Wysocki, T. R. Lee, P. A. Lee, and N. R. Armstrong, “Interface Dipoles Arising from Self-Assembled Monolayers on Gold : UV - Photoemission Studies of Alkanethiols and Partially Fluorinated Alkanethiols,” *The Journal of Physical Chemistry B*, vol. 107, pp. 11690–11699, 2003.

[11] N. Crivillers, M. Mas-Torrent, S. Perruchas, N. Roques, J. Vidal-Gancedo, J. Veciana, C. Rovira, L. Basabe-Desmonts, B. J. Ravoo, M. Crego-Calama,

and D. N. Reinhoudt, "Self-assembled monolayers of a multifunctional organic radical.," *Angewandte Chemie*, vol. 46, no. 13, pp. 2215–9, 2007.

[12] C. Simao, M. Mas-Torrent, N. Crivillers, V. Lloveras, J. M. Artés, P. Gorostiza, J. Veciana, and C. Rovira, "A robust molecular platform for non-volatile memory devices with optical and magnetic responses," *Nature chemistry*, vol. 3, pp. 359–364, 2011.

[13] J. Casado-Montenegro, M. Mas-Torrent, F. Otón, N. Crivillers, J. Veciana, and C. Rovira, "Electrochemical and chemical tuning of the surface wettability of tetrathiafulvalene self-assembled monolayers.," *Chemical communications (Cambridge, England)*, vol. 49, no. 73, pp. 8084–6, 2013.

[14] C. Simao, M. Mas-Torrent, J. Casado-Montenegro, F. Otón, J. Veciana, and C. Rovira, "A Three-State Surface-Confined Molecular Switch with Multiple Channel Outputs," *Journal of American Chemical Society*, vol. 133, pp. 13256–13259, 2011.

[15] F. R. Elder, M. Gurewitsch, R. V. Langmuir, and H. C. Pollock, "Radiation from Electrons in a Synchrotron," *Physical Review*, vol. 71, no. 11, pp. 829–830, 1947.

[16] A. Ide-Ektessabi, *Applications of Synchrotron Radiation: Micro Beams in Cell Micro Biiology and Medicine.* Kyoto: Springer-Verlag Berlin Heidelberg, 2007.

[17] F. R. Elder, R. V. Langmuir, and H. C. Pollock, "Radiation from Electrons Accelerated in a Synchrotron," *Physical Review*, vol. 74, no. 1, pp. 52–56, 1948.

[18] J. F. Moulder, W. F. Stickle, P. E. Sobol, and K. D. Bomben, *Handbook of X-ray Photoelectron Spectroscopy. A Reference Book of Standard Spectra for Identi cation and Interpretation of XPS Data.* Minnesota: Perkin-Elmer Corporation Physical Electronic Division, 1992.

[19] CasaXPS, "Basic Quantification of XPS Spectra," 2008.

[20] L. P. Méndez De Leo, E. de la Llave, D. Scherlis, and F. J. Williams, "Molecular and electronic structure of electroactive self-assembled monolayers.," *The Journal of chemical physics*, vol. 138, no. 11, p. 114707, 2013.

[21] P. E. Laibinis, C. D. Bain, and G. M. Whitesides, "Attenuation of photoelectrons in monolayers of n-alkanethiols adsorbed on copper, silver, and gold," *The Journal of Physical Chemistry*, vol. 95, no. 18, pp. 7017–7021, 1991.

[22] Y. Han, H. Noguchi, K. Sakaguchi, and K. Uosaki, "Formation process and solvent-dependent structure of a polyproline self-assembled monolayer on a gold surface.," *Langmuir*, vol. 27, no. 19, pp. 11951–7, 2011.

[23] Y. Miura, S. Kimura, Y. Imanishi, and J. Umemura, "Formation of Oriented Helical Peptide Layers on a Gold Surface Due to the Self-Assembling Properties of Peptides," *Langmuir*, vol. 14, no. 24, pp. 6935–6940, 1998.

[24] O. Shekhah, N. Roques, V. Mugnaini, C. Munuera, C. Ocal, J. Veciana, and C. Wöll, "Grafting of monocarboxylic substituted polychlorotriphenylmethyl radicals onto a COOH-functionalized self-assembled monolayer through copper (II) metal ions.," *Langmuir*, vol. 24, no. 13, pp. 6640–8, 2008.

[25] F. Grillo, V. Mugnaini, M. Oliveros, S. M. Francis, D.-J. Choi, M. V. Rastei, L. Limot, C. Cepek, M. Pedio, S. T. Bromley, N. V. Richardson, J.-P. Bucher, and J. Veciana, "Chiral Conformation at a Molecular Level of a Propeller-Like Open- Shell Molecule on Au(111)," *The Journal of Physical Chemistry Letters*, vol. 3, pp. 1559–1564, 2012.

[26] C. Simao, M. Mas-Torrent, J. Veciana, and C. Rovira, "Multichannel Molecular Switch with a Surface-Confined Electroactive Radical Exhibiting Tunable Wetting Properties," *Nano letters*, vol. 11, pp. 4382–4385, 2011.

[27] A. B. Fischer, M. S. Wrighton, M. Umana, and R. Iurray, "An X-ray Photoelectron Spectroscopic Study of Multilayers of an Electroactive Ferrocene Derivative Attached to Platinum and Gold Electrodes," *Journal of American Chemical Society*, vol. 101:13, pp. 3442–3446, 1979.

[28] C. M. Woodbridge, D. L. Pugmire, R. C. Johnson, N. M. Boag, and M. a. Langell, "HREELS and XPS Studies of Ferrocene on Ag(100)," *The Journal of Physical Chemistry B*, vol. 104, no. 14, pp. 3085–3093, 2000.

[29] M. Umaña, D. R. Rolison, R. Nowak, P. Daum, and R. W. Murray, "X-Ray Photoelectron Spectroscopy of metal, metal oxide, and carbon electrode surfaces chemically modified with ferrocene and ferricenium," *Surface Science*, vol. 101, pp. 295–309, 1980.

[30] A. Taylor and P. Licence, "X-Ray Photoelectron Spectroscopy of Ferrocenyl- and Ferrocenium-Based Ionic Liquids," *ChemPhysChem*, vol. 13, pp. 1917–1926, 2012.

[31] C. D. Bain, E. B. Troughton, Y.-T. Tao, J. Evall, G. M. Whitesides, and R. G. Nuzzo, "Formation of monolayer films by the spontaneous assembly of organic thiols from solution onto gold," *Journal of American Chemical Society*, vol. 111, pp. 321–335, 1989.

[32] T. M. Willey, A. L. Vance, C. Bostedt, T. van Buuren, R. W. Meulenberg, L. J. Terminello, and C. S. Fadley, "Surface structure and chemical switching of thioctic acid adsorbed on Au(111) as observed using near-edge X-ray absorption fine structure.," *Langmuir*, vol. 20, no. 12, pp. 4939–44, 2004.

[33] M.-C. Bourg, A. Badia, and R. B. Lennox, "Gold - Sulfur Bonding in 2D and 3D Self-Assembled Monolayers : XPS Characterization," *The Journal of Physical Chemistry B*, vol. 104, pp. 6562–6567, 2000.

[34] S. Hüfner, *Photoelectron Spectroscopy: Principles and Applications.* Gernamy: Springer-Verlag Berlin Heidelberg, third edit ed., 2003.

[35] C. Sauer, M. WieBner, A. Schöll, and F. Reinert, "Observation of a molecule-metal interface charge transfer state by resonant photoelectron spectroscopy," *Materials Science*, pp. 1–5, 2013.

[36] P. A. Brühwiler, O. Karis, and N. Martensson, "Charge-transfer dynamics

studied using resonant core spectroscopies," *Reviews of Modern Physics*, vol. 74, pp. 703–740, 2002.

[37] A. Batra, G. Kladnik, H. Vázquez, J. S. Meisner, L. Floreano, C. Nuckolls, D. Cvetko, A. Morgante, and L. Venkataraman, "Quantifying through-space charge transfer dynamics in π-coupled molecular systems.," *Nature communications*, vol. 3, p. 1086, 2012.

[38] O. Karis, A. Nilsson, M. Weinelt, T. Wiell, C. Puglia, N. Wassdahl, and N. Må rtensson, "One-Step and Two-Step Description of Deexcitation Processes in Weakly Interacting Systems," *Physical Review Letters*, vol. 76, no. 8, pp. 1380–1383, 1996.

[39] P. A. Dowben, C. Waldfied, T. Komesu, D. Welipitiya, T. McAvoy, and E. Vescovo, "The occupied and unoccupied electronic structure of adsorbed ferrocene," *Chemical Physics Letters*, vol. 283, pp. 44–50, 1998.

[40] T. Hemraj-Benny, S. Banerjee, S. Sambasivan, M. Balasubramanian, D. a. Fischer, G. Eres, A. a. Puretzky, D. B. Geohegan, D. H. Lowndes, W. Han, J. a. Misewich, and S. S. Wong, "Near-edge X-ray absorption fine structure spectroscopy as a tool for investigating nanomaterials," *Small*, vol. 2, no. 1, pp. 26–35, 2006.

[41] G. Hähner, "Near edge X-ray absorption fine structure spectroscopy as a tool to probe electronic and structural properties of thin organic films and liquids.," *Chemical Society reviews*, vol. 35, no. 12, pp. 1244–55, 2006.

[42] S. Watcharinyanon, E. Moons, and L. S. O. Johansson, "Mixed Self-Assembled Monolayers of Ferrocene-Terminated and Unsubstituted Alkanethiols on Gold: Surface Structure and Work Function," *The Journal of Physical Chemistry C*, vol. 113, no. 5, pp. 1972–1979, 2009.

[43] J. A. Horsley, J. Stöhr, A. P. Hitchcock, D. C. Newbury, a. L. Johnson, and F. Sette, "Resonances in the K shell excitation spectra of benzene and pyridine: Gas phase, solid, and chemisorbed states," *The Journal of Chemical Physics*, vol. 83, no. 12, p. 6099, 1985.

[44] A. Shaporenko, K. Rössler, H. Lang, and M. Zharnikov, "Self-assembled monolayers of ferrocene-substituted biphenyl ethynyl thiols on gold.," *The journal of physical chemistry. B*, vol. 110, pp. 24621–8, 2006.

[45] A. Orlov, D. J. Watson, F. J. Williams, M. Tikhov, and R. M. Lambert, "Interactions of 4-chlorophenol with TiO2 polycrystalline surfaces: a study of environmental interfaces by NEXAFS, XPS, and UPS.," *Langmuir*, vol. 23, no. 19, pp. 9551–4, 2007.

[46] T. Weidner, N. Ballav, M. Zharnikov, A. Priebe, N. J. Long, J. Maurer, R. Winter, A. Rothenberger, D. Fenske, D. Rother, C. Bruhn, H. Fink, and U. Siemeling, "Dipodal ferrocene-based adsorbate molecules for self-assembled monolayers on gold.," *Chemistry A European Journal*, vol. 14, no. 14, pp. 4346–60, 2008.

[47] P. Parent, J. Lasne, G. Marcotte, and C. Laffon, "HCl adsorption on ice at low temperature: a combined X-ray absorption, photoemission and infrared study.," *Physical chemistry chemical physics*, vol. 13, no. 15, pp. 7142–8, 2011.

[48] F. Bournel, C. Mangeney, M. Tronc, C. Laffon, and P. Parent, "Cl2p, O1s PSD-NEXAFS study of the adsorption of HCl on ice: a direct experimental evidence of the HCl ionization," *Surface Science*, vol. 528, no. 1-3, pp. 224–229, 2003.

[49] O. Plekan, V. Feyer, S. Ptasi□ska, N. Tsud, and K. C. Prince, "Cyclic dipeptide immobilization on Au(111) and Cu(110) surfaces.," *Physical Chemistry Chemical Physics*, vol. 16, no. 14, pp. 6657–65, 2014.

[50] B. J. Schultz, R. V. Dennis, J. P. Aldinger, C. Jaye, X. Wang, D. a. Fischer, A. N. Cartwright, and S. Banerjee, "X-ray absorption spectroscopy studies of electronic structure recovery and nitrogen local structure upon thermal reduction of graphene oxide in an ammonia environment," *RSC Advances*, vol. 4, no. 2, p. 634, 2014.

[51] H.-K. Jeong, H.-J. Noh, J.-Y. Kim, M. H. Jin, C. Y. Park, and Y. H. Lee, "X-ray

absorption spectroscopy of graphite oxide," *EPL (Europhysics Letters)*, vol. 82, no. 6, p. 67004, 2008.

[52] L. Cao, W. Zhang, Y. Han, T. Chen, Z. Zheng, L. Wan, F. Xu, K. Ibrahim, H. Qian, and J. Wang, "Angular dependent NEXAFS study of the molecular orientation of PTCDA multilayers on Au (111) surface," *Chinese Science Bulletin*, vol. 56, no. 33, pp. 3575–3577, 2011.

[53] V. Lee, R. V. Dennis, B. J. Schultz, C. Jaye, D. a. Fischer, and S. Banerjee, "Soft X-ray Absorption Spectroscopy Studies of the Electronic Structure Recovery of Graphene Oxide upon Chemical Defunctionalization," *The Journal of Physical Chemistry C*, vol. 116, no. 38, pp. 20591–20599, 2012.

[54] A. T. Wen, E. Rühl, and A. P. Hitchcock, "Inner-Shell Excitation of Organoiron Compounds by Electron Impact," *Organometallics*, vol. 11, pp. 2559–2569, 1992.

[55] L. A. J. Garvie and P. R. Buseck, "Ratios of ferrous to ferric iron from nanometre-sized areas in minerals," *Nature*, vol. 396, pp. 667–670, 1998.

[56] F. Zheng, V. Pérez-Dieste, J. McChesney, Y.-Y. Luk, N. L. Abbott, and F. Himpsel, "Detection and switching of the oxidation state of Fe in a self-assembled monolayer," *Surface Science*, vol. 587, no. 3, pp. L191–L196, 2005.

[57] A. P. Hitchcock, A. T. Wen, and E. Rühl, "Transition metal 2p excitation of organometallic compounds studied by electron energy loss spectroscopy," *Chemical Physics*, vol. 147, pp. 51–63, 1990.

You are always a student, never a master. You have to keep moving forward

Conrad Hall

5

Modification of surface potential with Fc–PTM radical SAMs: The effect of dipole moment and polarizability

5.1 Introduction

Surface engineering uses self-assembled monolayers (SAMs) for different applications where the control of surface structure and physico-chemical properties are the pivotal key. Small or big changes at the molecular level may result in control of macroscopic surface properties[1]. In this context, the spontaneous assembly of molecules on a supporting substrate forming densely packed and well-ordered two-dimensional phases can be used to modify macroscopic surface properties[2].

In the last years significant research effort has been directed towards understanding and controlling the interface energetics between metals (electrodes) and organic molecules. Such interfaces are a key for device function and e ciency. The rational design of highly functional organic electronic devices and the development of methods for controlling injection barriers will be only improved through a comprehensive understanding of phenomena at interfaces[3].

In this sense, diminishing the injection barrier between the charge transport channels (energy levels/bands of the organic semiconductors) and the Fermi energy of the contacts results of crucial importance for device performance. One of the often limitation in the energy level alignment at electrode/semiconductor interfaces is the small number of electrode materials compared with the large number of commercially available organic semiconductors[4]. To address this limitation, different ways have been probed to adjust the relative vacuum levels of metals and semiconductors[4]. For instance, depositing a thin film of a high/low work function materials on common metal electrodes[5,6]. Tuning the surface potential by the physisorption of organic molecules that form an interface dipole at the metal surface[7,8]. In some cases such tuning has allowed the reduction of the work function due to electron transfer from the adsorbate to the metal[9,10]. Other way for the injection barrier tuning is the use of SAMs[11] of molecules that exhibit a permanent dipole moment since dipolar organic monolayers covalently linked on metal surfaces induce a change in the work function (π) due to a shift of the relative vacuum levels[12]. Thus, the modification of the work function of a metal at will has special interest in organic and molecular electronics for the control of charge carrier injection[13]. Since in organic-based electronics, such as light-emitting diodes (LEDS), field-effect transistors (FETs) or bulk-heterojunction solar cells, device performance and lifetime depend critically on the properties of both the active materials and their interfaces[14].

As it has been mentioned, the adsorption process of organic molecules on metal surfaces involves a series of changes (phenomena) that take place specially at metal/surface interface. Changes that play a decisive role over the electronic properties of the molecules which will be reflected on the electrical properties of the molecular devices[15]. One of them is the change of surface potential produced by an adsorbate (molecules) which is reflected on the change of the work function of the adsorbent (surfaces). Almost any adsorbate on a surface as well as any change both in the state of the adsorbated or the adsorbent will produce a change in the work function of the surface[16].

In this context Lüben *et al.*[17] have been studied how two selected carboranethiol isomers modify flat silver surfaces. In such work, the authors proved that both isomers are oppositely oriented on the silver surfaces (Figure 5.1) and then modify in a different way the work function of the metal, while 1,2-$(HS)_2$-1,2-$C_2B_{10}H_{10}$ carboranethiol increases the work function, the 9,12-$(HS)_2$-1,2-$C_2B_{10}H_{10}$ carboranethiol decreases it.

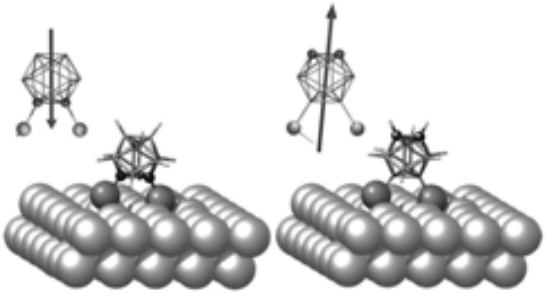

Figure 5.1: Schematic representation taken form ref.[17] of two carboranethiol isomers anchored on a silver surface and the dipole orientation of free molecules 1,2-$(HS)_2$-1,2-$C_2B_{10}H_{10}$ (left) and 9,12-$(HS)_2$-1,2-$C_2B_{10}H_{10}$ (right).

The study of the charge distribution in D−A systems which contain an intrinsic dipole moments once anchored on a surface is important from both a fundamental point of view and technologically interest. Regarding to the fundamental aspect, the oriented dipoles on the surface certainly will induce a change in the work function of the substrate used and the information extracted from this change will allow to understand the energetics of the interface formed during the self-assembly of the molecules. On the other hand, technological applications are found in organic electronic devices; where the optimization of the performance of devices is one of the challenges facing within this field; such optimization includes both reducing and balancing the charge-injection barriers. In organic electronic devices, holes are injected into the occupied states of the organic semiconductor once they have overcome the hole-injection barrier (HIB) at the anode, which means that below a certain onset voltage the device remains inactive (the same occurs for electrons at the cathode). In the effort to minimize this HIB, the selection of suitable materials for the electrodes has been a critical point and for that, materials with high work functions are usually chosen for the anode-hole injection

(low E_F) while low work function metals are ideal for the cathode-electron injection (high E_F). Additionally, for the optimization of the device performance, organic semiconductors that match their energy levels with the E_F of the electrodes[2] need to be used.

The great interest of these kind of devices, has promoted the use of SAMs of dipolar organic molecules to tune the effective work function of electrodes[12,18,19]. Thus, reducing the charge-injection barriers and minimizing the onset voltages, as it is represented in Figure 5.2.

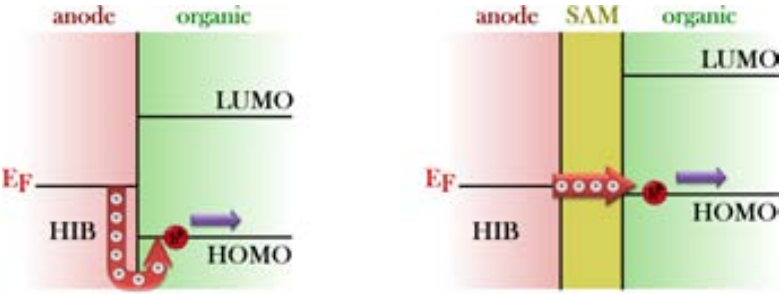

Figure 5.2: Schematic representation of the energy-level diagram at an electrode/organic semiconductor interface (left) and at a modi ed electrode/organic semiconductor interface (right) typically for organic electronic devices[2].

As can be seen in Figure 5.2, the modification of the anodic electrode with a suitable SAM can reduce the HIB. The position of both the highest and lowest occupied molecular orbitals (HOMO and LUMO, respectively) respect to the Fermi level (E_F) is changed due to the shift of the vacuum level of the metal. This occurs thanks to the presence of adsorbed molecules and therefore the injection of holes takes place in a favorable way.

As it has been mentioned, SAMs form highly ordered two-dimensional (2D) nanostructures which with a proper design allow having oriented dipoles with a desired direction on a substrae. This fact can be used for tuning the work function of electrodes. Thus, SAMs of alkanethiols and perfluorinated alkanethiols, due to their opposite dipoles have been used to decrease or increase the work function of metals, respectively[18].

Before to start, it is necessary to define to define the work function (π) of a surface. The work function is the minimum energy required to remove one electron

from the Fermi Level of a solid to a point in the vacuum. However, two vacuum levels can be identified: *i)* the *vacuum level of a finite-size sample* ($E_{vac(s)}$) which is defined as the energy of an electron at rest just outside the surface of the solid and *ii)* the *vacuum level at infinity* ($E_{vac(\infty)}$) which is defined as the energy of an electron at rest at infinite distance from the surface. Since the $E_{vac(\infty)}$ is experimentally inaccessible and remains unchanged, it is only used as reference level. Therefore, the vacuum level achieved when discussing about work function is $E_{vac(s)}$ which is characteristic of the surface and it is very sensitive to the electronic properties of the outer layers of the solid[20].

Different techniques can be used to determine the surface potential, measuring either the work function or the contact potential difference (CPD) which are correlated parameters. Thus, Ultraviolet Photoelectron Spectroscopy (UPS) and Kelvin Probe Force Microscopy (KPFM) can be used to measure the work function and the surface potential respectively. UPS is a very superficial technique that allows to measure directly the work function of a bare or modified substrate, while the KPFM is an indirect technique that measures the CPD. However, surface potential measurements can be performed with almost no change or disturbance of the surface during the measuring process, which makes it a relative simple method with high sensitivity (± 0.001 V) that allows to known the state of the surface[16]. In the KPFM the metal substrate and the metallic probe tip are acting as the two plates of a capacitor. The vibration of the probe tip induces an *ac* current which is nulled when the voltage applied to the tip is equal to the difference in surface potential between the tip and the substrate. For this reason, KPFM is used to determine the electrostatic effect of the dipole layer on the metallic substrates by measuring the change in the surface potential with respect to a reference[12].

As it was previously mentioned, many processes can take place when organic molecules interact with a substrate to form monolayers, specially at the moment of bond formation. Such bond formation usually involves some distribution of the electrical charges. In this sense, the surface dipole of SAMs of organic molecules containing thiols or disulfur groups, over gold surfaces can be considered as the contribution of two dipoles: the first one is related with the redistribution of the

electrical charge arising from a charge transfer between the metal surface and the molecule in the formation of the thiolate–Au bond ($Au^{\delta+}$–$S^{\delta-}$) and the second one corresponds to the intrinsic dipole moment of the molecule which is associated with the chemical structure, kind of atoms, type of bonds, among others. The polar nature of the metal–sulfur (M–S) interaction give place to a net dipole moment at the Au/monolayer interface with its permanent component perpendicular to the surface. The electrical double layer* formed at the metal surface constitutes a potential barrier (electrostatic) that electrons trying to move out of the metal, will feel[17,18,21–23]. This effect will be reflected in an *increasing of the work function* and hence a *decrease in the surface potential* measured.

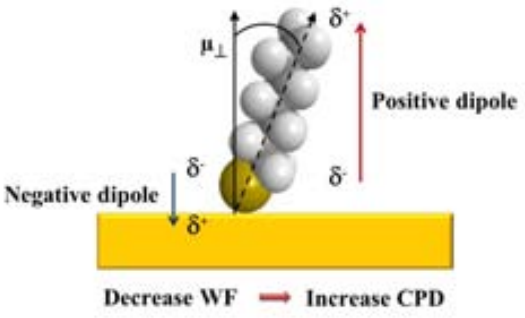

Figure 5.3: Schematic representation of an alkanethiol monolayer as an electrical double layer.

Previous studies of SAMs on gold have suggested that the dipole observed at M–S interface has a small contribution to the surface dipole and therefore the mayor contribution is given by the intrinsic molecular dipole moment[22,24]. The orientation of the surface dipole can be inferred from the sign of the CPD; a positive value of CPD respect to the bare Au would means that the effective R^+–S^- dipole must be larger than the Au^+–S^- dipole[25]. This positive change in the surface potential implies that the adsorbent is modifying the work function of the gold in such way that the escape of the electrons from the bulk metal is being favoured, then the π_{Au} decreases and hence the net surface dipole is oriented in opposite direction to the M–S dipole, with the negative charges residing close to the metal surface and the positive ones lying further away toward the monolayer/ambient interface[23,26] as it is shown in Figure 5.3. Additionally, the orientation of the molecules on

*Two parallel layers of charge that are formed at the metal/organic interface.

the monolayer has a determining function over the surface potential, since only the component of the molecular dipole which is perpendicular to the surface is affecting to the work function. Thus, the tilt of the molecule from the surface normal reduces the contribution of the molecular dipole to the work function[22,27] of the metal.

On the other hand, SAMs of molecules oriented with the negative pole at surface/air interface, increase the work function of the metal[17] as shown Figure 5.4. For instance perfluorinated monolayers give large negative changes in the surface potential with respect to bare gold (e.g. −750 mv) which has been justified with the strong electro-withdrawing properties of the fluorine atoms[27].

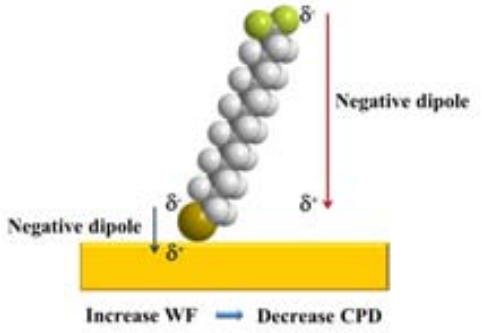

Figure 5.4: Schematic representation of a fluorinated alkanethiol monolayer on gold.

Even though, the amount of the work function change ($\Delta\pi$) is determined by the magnitude of the monolayer dipole moment and its sign by the dipole polarity, several effects like: a) chemical bonding of substrate−molecule, b) possible structural reorganizations of the molecules which can be associated with a depolarization effects due to the neighboring polar molecules, c) saturation of $\Delta\pi$ with the molecular dipole based on the dielectric breakdown of the layers or e) a significant charge transfer between the substrate and the SAM principally for large dipoles and SAMs of low polarizability[28], can disturb this correlation.

For all aforementioned, molecular materials are useful elements for examining the fundamental aspects of interfacial electronic structure since they are easy to characterize[7]. Therefore, studying the tuning of the work function of gold surfaces by two dipole organic molecules (**1** and **2**) very similar in molecular structure but different in electronic characteristics is of great interest. As well as the understand-

ing of the effect of dipole moment and polarizability of these molecules over the surface potential.

To obtain a complete study of the effect of the previous mentioned molecules organized as 2D structures (SAMs with oriented dipoles), it has been synthesized a new molecule containing the same disulfide-alkyl chain as in **1** and **1-H** but only with the Fc moiety, compound ***5*** (see Chapter 3).

5.2 Objectives

In this chapter we will be interested in studying the influence of the open-shell electronic structure of the Fc–PTM SAMs (**S1**) on the modification of the work function of a gold substrate. As a reference, we will use a SAM of molecules with very similar molecular structure but closed-shell electronic structure, **S1-H**. In this regard, we will be interested to understand not only the influence of the dipole moment which turns to be very similar for both systems but also their different polarizability. Thus we will perform UPS and KPFM measurements of SAMs **S1**, **S1-H** and **S*5***.

5.3 Ultraviolet-Photoelectron Spectroscopy (UPS)

Ultraviolet Photoelectron Spectroscopy (UPS), see Figure 5.5, was used to study the influence of the molecular dipole moment of the adsorbate over the work function of the gold. The low photon energy (i.e. He I, $h\nu$ = 21.2 eV) used in UPS does not allow deep core electron levels to be excited, and only photoelectrons emitted from the valence band (VB) are accessible. The high kinetic energy electrons will form the band structure spectrum of the material, while inelastically scattered electrons with still enough energy will escape into the vacuum and will be detected as secondary electrons providing a direct measure of the vacuum level of the sample because electrons with kinetic energy (KE) less than the substrate work function cannot escape from the solid[29].

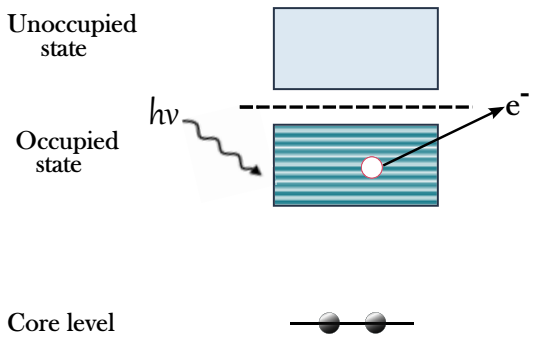

Figure 5.5: Schematic representation of the valence electrons emitted in Ultraviolet Photoemission Spectroscopy.

It is important to consider that when a film is used to functionalize a metal electrode, the change of the work function of the metal ($\Delta\phi_m$) observed as shifts in the low KE edge of the UPS spectrum is related to the net dipole moment (μ) of the film[30]. To performed UPS measurements, an He I (hν = 21.2 eV) ionization source was used and 3 V bias was added to enhance the detection of the low-KE electrons.

Figure 5.6 shows the UPS data in KE scale of **S1**, **S1-H** monolayers and a clean Au surface exposed to ambient conditions. Additionally, an spectrum of **S5** monolayer with only a donor Fc unit was taken as reference to study the influence of the PTM radical moiety.

The shape of the secondary electron cutoff (SECO) band observed in the spectra of the monolayers is very similar to that obtained for other systems anchored on a substrate. The work function (ϕ) in each case can be calculated from the spectrum, using Equation 5.1.

$$\phi = h\nu - W \tag{5.1}$$

Where hν is the photon energy (21.2 eV) and the width (W) is equal to:

$$W = KE_{\text{Fermi}} - KE_{\text{low-energy-cutoff}} \tag{5.2}$$

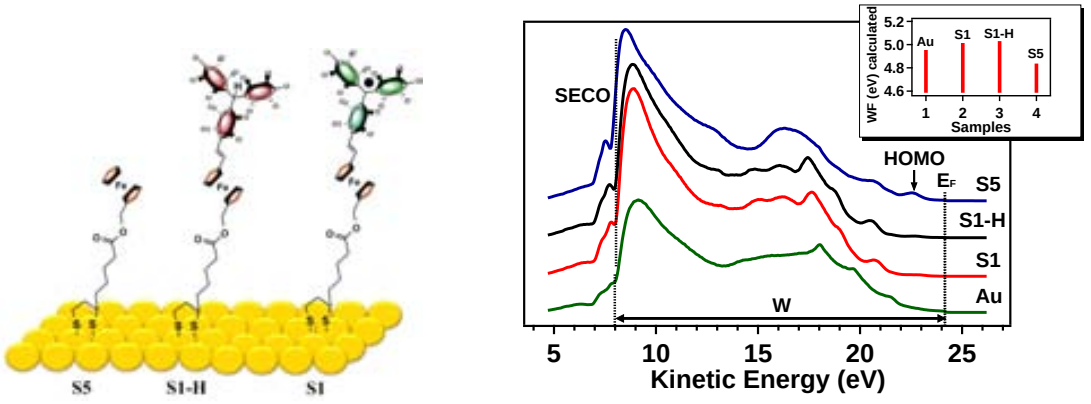

(a) (b)

Figure 5.6: (a) Schematic representation of the three monolayers studied, and (b) UV photoemission spectra for clean Au, **S1**, **S1-H** and **S5** monolayers. The inset shows the shifts of the effective work function (π_m) for each sample.

The $KE_{low-energy-cutoff}$ is determined at the very beginning of the slope of the SECO curve, point commonly known as onset; while the KE_{Fermi} for each monolayer take into account the Fermi level clearly observed for the bare gold at 0 eV in a BE plot. The work function of the gold substrate modified by three different monolayers are presented in Table 5.1 with a π_{Au} = 4.95 eV, value really close to that reported in the literature (π = 5.00 eV)[30]. In Table 5.1 are collected the data extracted from the spectra reported in Figure 5.6(b).

Table 5.1: Work Function (π) calculated from UV photoemission spectra.

Sample	low KE cuto (eV)	Fermi edge (eV)	π (eV)	$\Delta\pi$ (meV)
Au	7.954	24.2	4.954	
S1	8.018	24.2	5.018	64
S1-H	8.030	24.2	5.030	76
S-Fc	7.837	24.2	4.837	-117

Interesting, the protonated **S1-H** monolayer with $\Delta\pi$ = 76 meV presents a higher modification of the gold work function than the open shell **S1** with $\Delta\pi$ = 64 meV. Such higher value for **S1-H** in comparison with **S1** was not expected since the dipole moment of the closed-shell specie **1-H** is probably smaller

than the dipole moment of the open shell **1** due to the higher electron acceptor ability of PTM radical in comparison to the protonated PTM. The Fc monolayer **S5** containing the same disulfide-alkyl chain used in **S1** and **S1-H**, was also measured by UPS with $\Delta\pi = -117$ meV. The direction of the shift observed in the work function of the gold was opposite to the direction of **S1** and **S1-H**, indicative of the opposite direction of its dipole moment with respect to **S1** and **S1-H**.

Additional information can be extracted from Figure 5.6(b), the ionization potential (IP) of the molecules attached on the gold substrate, which can be estimated using Equation 5.3.

$$IP = h\nu - (E_{KE\,HOMO} - E_{KE\,low-energy-cutoff}) \tag{5.3}$$

Where the $E_{KE\,HOMO}$ was read directly from the UPS spectra focusing on the onset of the first peak observed after the Fermi level, which corresponds to the first occupied molecular orbital accessible in energy, see Figure 5.7.

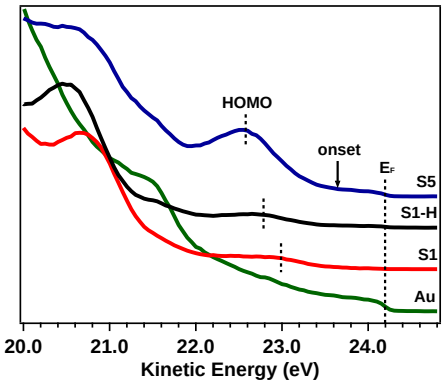

Figure 5.7: Zoom of the Fermi region of the UV photoemission spectra where the Highest Occupied Molecular Orbital (HOMO) of **S1**, **S1-H** and **S5** monolayers can be observed.

From Figure 5.7 and Equation 5.3 the values for the IP for the different studied SAMs are calculated and reported in Table 5.2.

Table 5.2: Ionization Potential Energy of SAMs, calculated from UPS spectra.

Sample	low KE cutoff (eV)	$E_{HOMO\,onset}$	IP (eV)
S1	8.018	23.689	5.529
S1-H	8.030	23.486	5.744
S-5	7.837	23.656	5.381

Figures 5.8, 5.9 and 5.10, show a schematic view of the band-edge offsets for **S1**, **S1-H** and **S5** monolayers on gold, respectively. To construct this figure data reported in Tables 5.1 and 5.2 containing information about the different values of work function as well as of the IP, were used. In Figures 5.8, 5.9 and 5.10 the scheme of the work function of a bare gold substrate is also presented, which corresponds to the energy between the Fermi level and the vacuum. After the functionalization of the substrate, the work function of the gold is shifted toward higher or lower energy values depending on the direction of the dipole moment of the adsorbate. Specifically for positive dipoles, the work function decreases while for negative dipoles the work function increases. Such variation in the work function has been drawn in the scheme as a shift in the vacuum energy. Additionally, it has been represented the IP of each SAM which corresponds to the energy difference between the HOMO and the new position of the vacuum level. To represent the position of the HOMO in these schemes, the values were took directly from the maximum position of the first peak observed in the UPS spectra, which represents the HOMO energy with respect to the Fermi level.

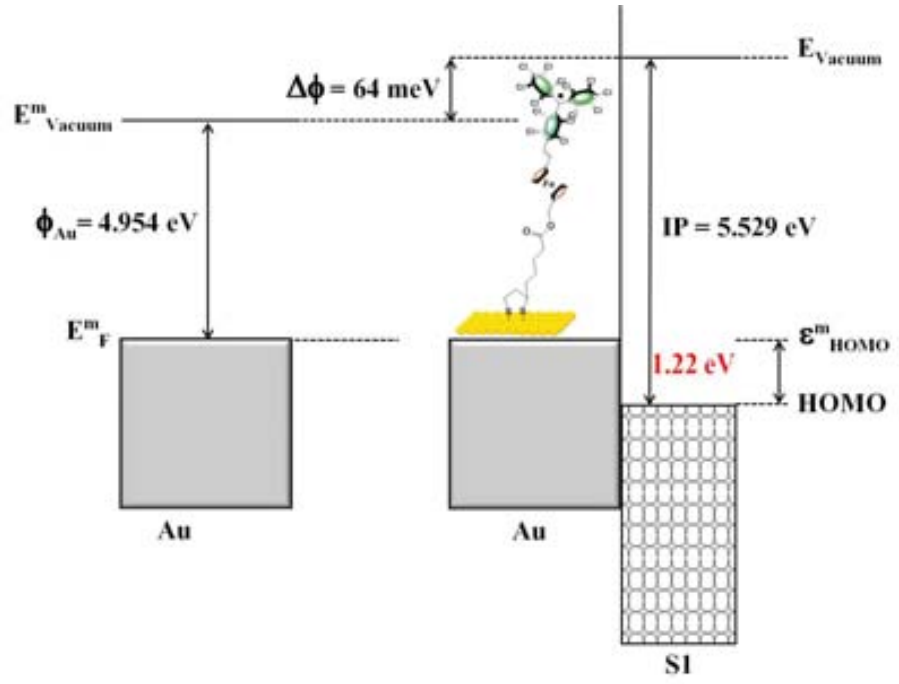

Figure 5.8: Schematic representation of the change of the work function of functionalized gold surfaces with **S1** monolayers, its IP and the HOMO.

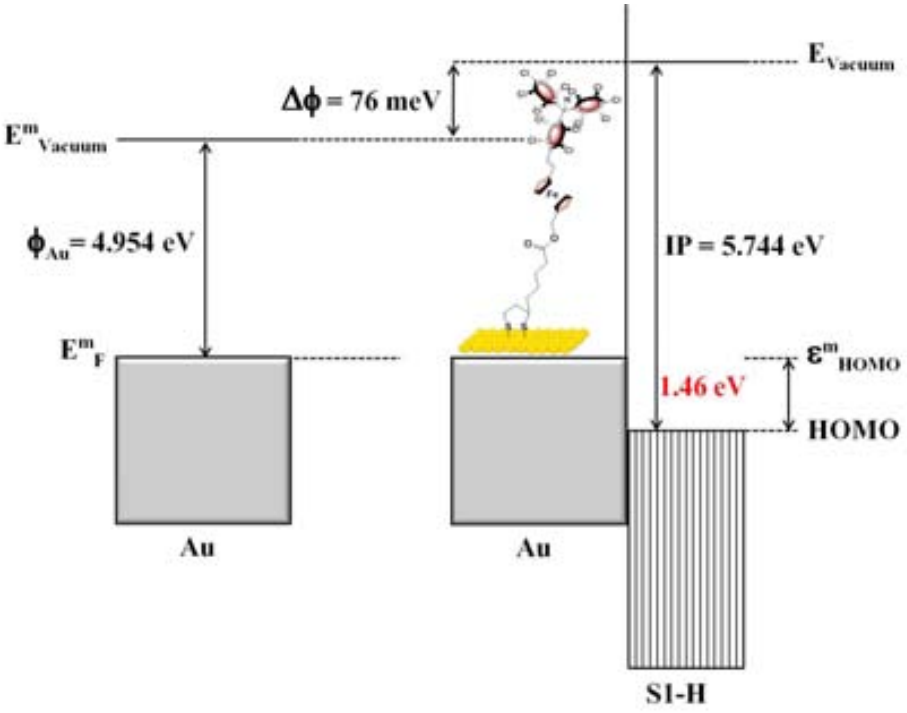

Figure 5.9: Schematic representation of the change of the work function of functionalized gold surfaces with **S1-H** monolayers and its IP.

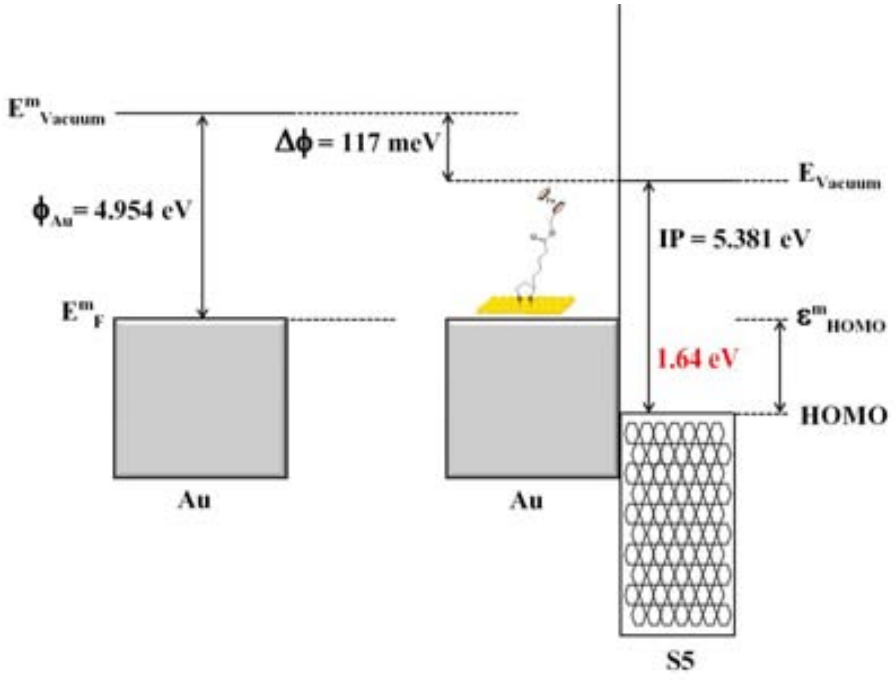

Figure 5.10: Schematic representation of the change of the work function of functionalized gold surfaces with **S5** monolayers and its IP.

To gain a better insight of these systems, the surface contact potential was also measured for these D–A systems by KPFM.

5.4 Kelvin Probe Force Microscopy (KPFM)

KPFM is a superficial technique that it is used to measure the local CPD between a scanning probe tip (reference electrode) and a sample (functionalized surface) as can be seen in Figure 5.11. The quantity obtained is closely related to the charge distribution on the surface and it is given by the difference of the work functions between the two materials (tip and sample) that have been put in electrical contact[21,31]. The CPD depends on the tip and the condition of the surface, which plays a crucial role since the adsorption of molecules with different dipole moments can change the work function of the substrate[21] and thus the CPD.

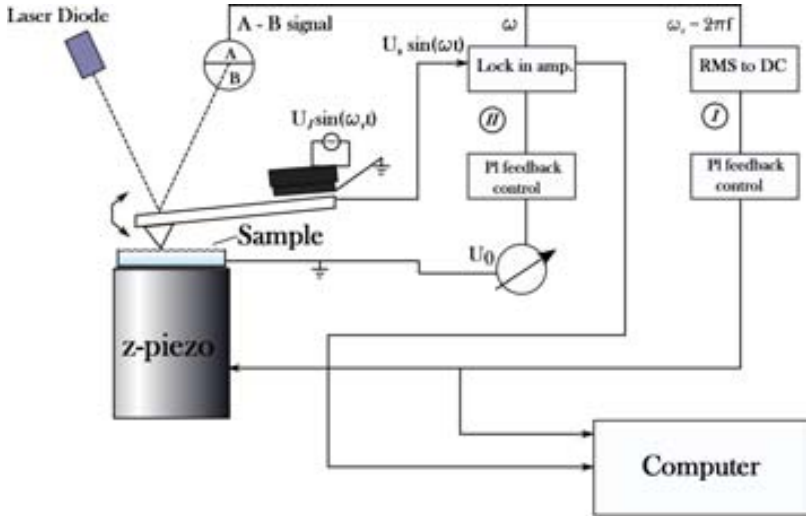

Figure 5.11: Experimental setup to perform KPFM measurements. Feedback I maintains a constant tip-sample distance and feedback II balances the electrostatic potential differences between the tip and the sample[25].

We will be interested in measuring the CPD of SAMs of D–A systems covalently linked to gold surfaces. For that, it is important to consider that the SAM properties that are related with the magnitude of the surface potential and therefore influence the changes of the work function of the metal are:

- Magnitude of the molecular dipole[16] μ (molecular dipole); θ (tilt angle of the molecule).
- Density of dipoles[16] A (area per molecule).
- Permittivity of the SAM ( ).
- Depolarization effects α (polarizability of the molecule) and molecular arrangement on the SAM

Then, the change in work function can be written as shown in Equation 5.4[18] since dipolar monolayers have been modeled as dielectric films with different components that contributes to the surface potential and the shift in local vacuum level[32].

$$\Delta\pi = -N\left[\frac{\mu_{SAM}}{{}_0\,{}_{SAM}} + \frac{\mu_{M-S}}{{}_0\,{}_{M-S}}\right] \tag{5.4}$$

In Equation 5.4, N is the areal density of the modifiers (typically ca. 3–5E14 cm^{-2}), μ_{SAM} is the dipole moment of the SAM projected along the normal axis, μ_{M-S} is the dipole moment of the metal-thiolate bond, ${}_0$ is the permittivity of vacuum, and ${}_{SAM}$ and ${}_{M-S}$ are the dielectric constants of the SAM and the metal-thiolate bond, respectively[32].

Since in KPFM we measure the difference in the local contact potential between the tip and the sample, a reference is necessary. A schematic representation of the different measurements that will be performed as well as of the substrate used are shown in Figure 5.12 which consists in a silicon wafer with gold electrodes (30 nm thickness) evaporated on it.

All the samples (clean gold, **S1**, **S1-H** and **S5**) were measured with respect to unmodified silicon oxide under a continuous current of nitrogen, at room temperature and at low humidity (less than 5%)[†]. Then the variation of the surface potential of the samples with respect to gold was calculated as follow:

$$CPD_{SAM-Au} = CPD_{SAM-SiO_2} - CPD_{Au-SiO_2} \tag{5.5}$$

[†]Measurements done in collaboration with Prof. Carmen Ocal group. The measurements were made by Dr. Marcos Paradinas, at Institut de Ciencia de Materials de Barcelona

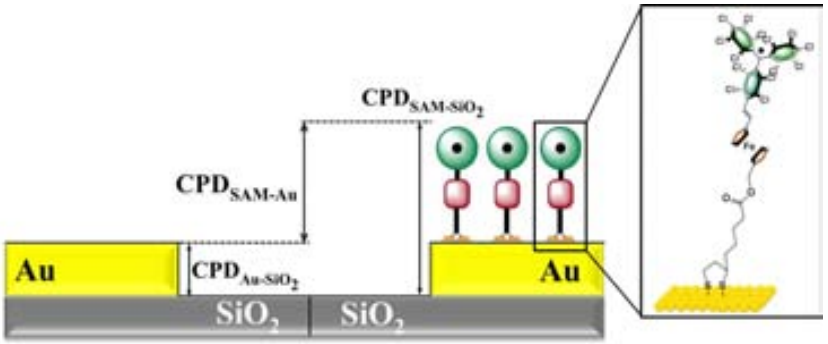

(a)

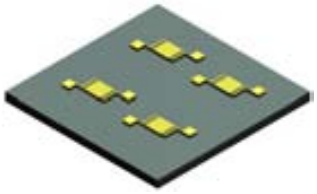

(b)

Figure 5.12: Representative scheme of (a) the measurements that will be performed by Kelvin Probe microscopy and (b) substrate used in the measurements.

The CPD of Au vs. SiO_2 was found to be 240 mV and thus following equation B.1 the CPD of the SAMs can be measured. The results obtained are summarized in Table 5.3 and the CPD data are collected in Figure 5.13.

Table 5.3: Contact Potential Difference of D-A monolayers.

Sample	$CPD_{SAM vs\ SiO_2}$ (mV)	$CPD_{SAM vs\ Au}$ (mV)
S1	220	-20
S1-H	185	-55
S5	640	400

Figure 5.13 shows histograms of the number of events measured in a region of the each sample. Such data have showed a normal distribution and each curve represent the local potential between the tip and the surface (monolayer or SiO_2). The CPD values reported in the second column of Table 5.3 corresponds to the difference between the maximum point in each gaussian curve.

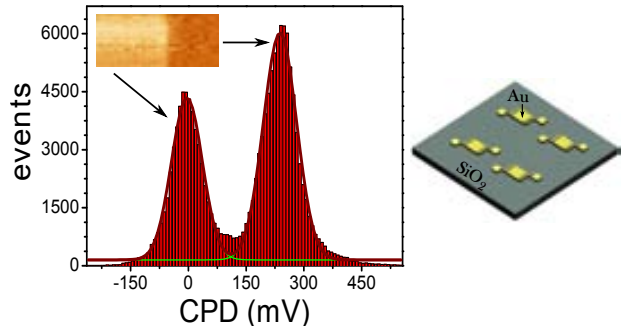

(a) **Au vs. SiO_2**

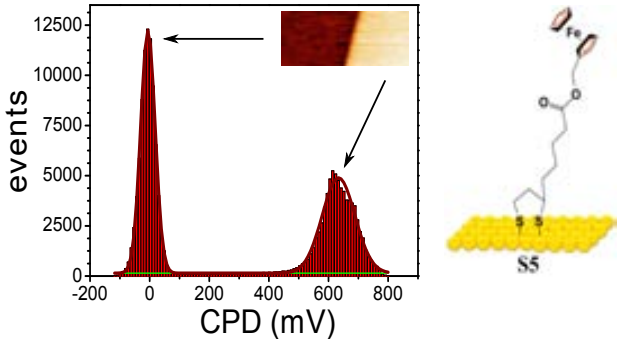

(b) **S5 monolayer vs. SiO_2**

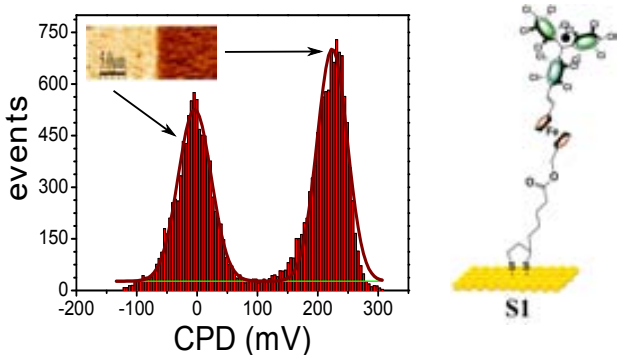

(c) **S1 monolayer vs. SiO_2**

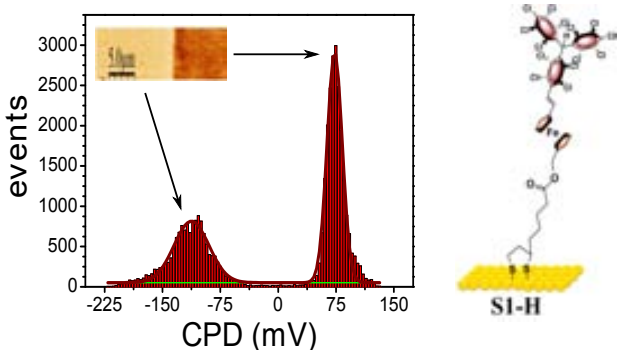

(d) **S1-H monolayer vs. SiO_2**

Figure 5.13: Surface potential data of (a) Au vs. SiO_2; (b) **S5** vs. SiO_2; (c) **S1** vs. SiO_2 and (d) **S1-H** vs. SiO_2. The corresponding distribution plot. Inset: CPD image of the analysed samples.

5.5 Discussion: UPS and KPFM

Since the physico-chemical properties of systems **1** and **1H**, both in solid state and in solution are different even though their similar chemical structure, it is expected to observed a big difference in the modification of the work function of gold surfaces containing SAMs **S1** and **S1-H**. Such differences are based fundamentally on the open- and closed-shell electronic structure of **1** and **1-H**, respectively.

From the UPS and KPFM measurements it was determined a real modification of the work function of gold substrates. The values obtained for each surface technique were of the same order. Contrary to what was expected, when comparing the modification of the work function of gold substrates by **S1** and **S1-H**, small differences were registered.

From all these data, it is possible to say that an opposite direction of the dipole is distinguished comparing the D−A SAMs **S1** and **S1-H** with respect to the Fc monolayer **S5**. The positive sign observed for CPD_{Fc-Au} implies that the work function of gold (π_{Au}) decreases and hence the surface dipole layer is oriented in such a way that the negative pole resides close to the metal surface and the positive one lies further away toward the monolayer/air interface.

The situation is inverted for the CPD_{S1-Au} and CPD_{S1H-Au}. The negative sign of the CPD shows an opposite effect of these monolayers over the work function of gold. Since the surface dipole layer is oriented with those positive charges residing close to the metal surface and negative charges lying further away toward the monolayer/ambient interface, an increase of the work function was obtained. The negative dipole observed is in accordance with previous results reported in the literature for fluorinated monolayers[23,33]. Then it is possible to think that the strong electron-withdrawing properties of the 14 chlorine atoms present in the PTM subunit induce the localization of the negative charges in this part of the molecule.

As the net dipole (μ) can be understood as composed of more than one component, one can think that the intrinsic dipole associated with the D−A group (Fc−PTM) is acting in the same direction that the M−S dipole. Even though, **1** and **1-H** systems contain an alkyl chain, the presence of the two oxygen atoms in the ester bond could give place to a negative dipole in this section. Then, it could

be expected a net negative surface dipole as shown Figure 5.14.

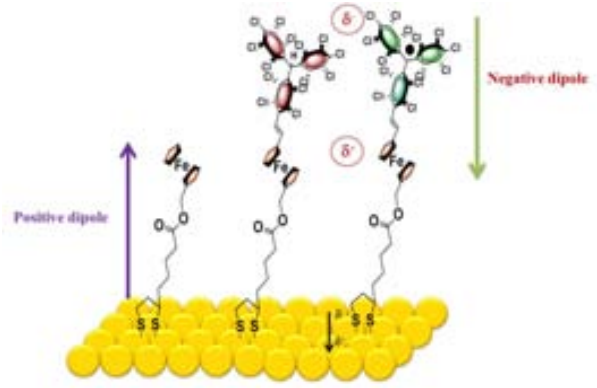

.

Figure 5.14: Schematic representation of the dipole direction of **S1**, **S1-H** and **S5** monolayers

For **S5** it is logic to think that a strong positive dipole can be formed thanks to the electron-withdrawing property of the ester group[34] and the electron-donating characteristic of the Fc unit.

More interesting is the comparison of CPD values obtained for **S1** and **S1-H** monolayers. Due to the presence of 14 chlorine atoms, a negative dipole is expected but not a higher effect of the protonated SAM instead of the radical one. The higher electron acceptor ability of the PTM radical moiety induced by the presence of a low energy singly-unoccupied molecular orbital (SUMO) is expected to lead a bigger dipole moment in Fc–PTM radical **1** than that observed in its protonated form Fc–HPTM **1H** where the PTM has a closed-shell structure. From these basis, it was expected to observe a higher modification of the work function due to the presence of **1** and a significant lower work function change for **S1-H** surface. On the contrary we have obtained a higher value for **S1-H** (−55 mV) than **S1** (−20 mV).

The first thing considered to explain these results was the molecular orientation within the monolayers. If the tilt angle of **S1** SAM from the surface normal, is higher than that corresponding to **S1-H** then it would be a good source for the lower effect observed for the radical monolayer, because only the component of the dipole perpendicular to the surface affects the work function of the substrate. In this way, only small changes in the orientation of the chromophore dipole could

have a significant effect on the observed surface potential[23]. The effect of the position of the D–A systems with respect to the surface was discarded since in both systems the same disulfide-alkyl chain was used. However, the thickness calculated for both monolayers through the high-resolution photoemission spectrum of Au4f (see Chapter 4) show that both molecules are standing up over the surface with a tilt angle of 30° approximately. Then, other should be the reason of these results.

Recently, Egger and Zojer using atomistic simulations have found an anticorrelation between the work function change respect to dipole of molecules assembled on a gold surface. Contrary to intuition, the authors showed that enhancing the dipoles leads to a reduction of the adsorption-induced change of the work function. An electronic localization and level shifts produced by large dipoles, drive the interface into a thermodynamically unstable situation which needs to be compensated somehow. A charge reorganizations takes place to compensate this unstable situation, which actually works against the molecular dipoles. As a result, increasing the molecular dipole moment can, in fact, reduce the work function change[28].

Regarding to **S1** and **S1-H** monolayers, two fundamental parameters need to be taken into account to explain in a comparative way the anticorrelation observed between **S1-H** and **S1**. The first one is the magnitude of the molecular dipole moment and the second one and equal in importance, the polarizability. A detailed discussion about them will be done in the next section.

In order to better understand the complex behavior of the system above described, theoretical calculations of the molecular dipole moment and the polarizability of the three systems under study were carried out[‡]. To optimize the molecular structure, some fixed parameters like the tilt angle (around 30 °) were assumed. The optimized molecular structure of **S1**, **S1-H** and **S5** are shown in Figure 5.15.

[‡]Theoretical calculations were performed by Francesca Delchiaro, PhD student in Dipartimento di Chimica at Parma University (Italy) under supervision of Prof. Anna Painelli.

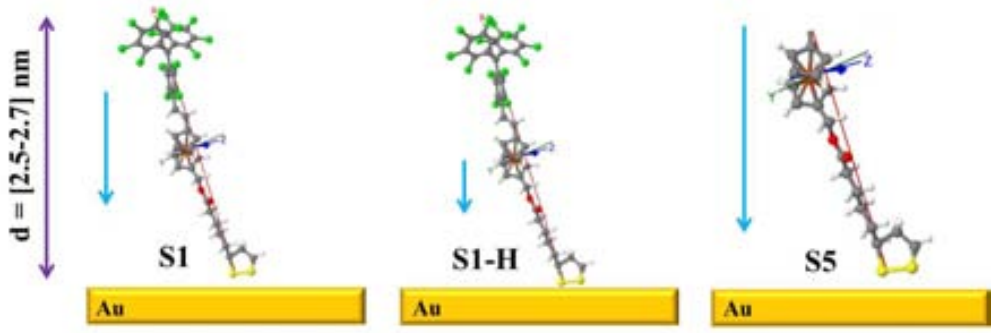

.

Figure 5.15: Optimized molecular structure of **S1**, **S1-H** and **S5** monolayers

The values of the molecular parameters (μ and α) as well as the molecular area considering the top of the molecules like a rectangle are collected in Table 5.4. They were obtained by PM7 (RHF) calculations at optimizing ground state (U)CAMB3LYP/6-31G* level with modified dihedral angles. Polarizability was determined considering the perpendicular component of the dipole moment.

Table 5.4: Molecular parameters.

Sample	$\overline{\mu}$ **(D)**	α	**(10^{-24} cm^{-3})**	A (nm^2/molecule)
S1	2.096	136		0.652
S1-H	2.160	13.8		0.652
S5	3.938	33.3		0.143

As can be seen, the molecular dipole moment of **S1** and **S1-H** are very similar but not their polarizability. Therefore, the minor modification of the work function of gold caused by **S1** could be directly related with its large polarizability. Specially as it relates to depolarization effects. Moreover the higher modification of the WF induced by SAM **S5** could be due to the relative large molecular dipole moment.

5.5.1 Anticorrelation between the net dipole moment and the induced work function modi□cations

In the effort to understand the unexpected small variation of the work function of gold substrates induced by dipolar **S1** and **S1-H** monolayers observed both

in UPS as well as in the surface potential measurements, it was necessary to consider a deep analysis of the energy of these systems based on similar theoretical calculations reported in the literature for dipolar systems[2,28,33,35,36].

From the data obtained from both UPS and KPFM it was observed that the three systems (**1**, **1-H** and **5**) used to functionalize gold surfaces, in effect, modify the work function of this metal. It was analyzed that both **S1** and **S1-H** monolayers increase the work function while **S5** decreases it. Therefore, the surface dipoles are opposite comparing the Fc–PTM systems with respect to the SAM of the Fc. A good agreement in the order of magnitude (relative values) of the data registered through UPS and KPFM was found, which confirms that our samples are quite homogeneous. Moreover, it was an indication that these monolayers are reproducible. Interesting, SAM **S1-H** showed a higher modification of the work function with respect to that observed for SAM **S1**.

As was mentioned in the previous section, dipolar molecules on a surface induce a change in the work function, this change has essentially two origins. First, the intrinsic dipole of the molecules and second, the dipole layer formed by the interfacial charge rearrangements due to the formation of the chemical bond between the linking group and the metal (Au–SAM bond formation). Both origins give rise to a shift of the electron potential energy designated as ΔE_{vac} and ΔE_{BD}, respectively. Then, the change in the work function ($\Delta\pi$) can be considered as follow:

$$\Delta\pi = \Delta E_{vac} + \Delta E_{BD} \tag{5.6}$$

However, the shift arising from the Metal–S bond has a marked influence not only over the work function of the metal but also on the alignment of the electronic levels within the SAM with respect to the metal Fermi energy.

In a general way, an intrinsic negative dipole pointing against the surface was observed for **1** and **1-H**. The acceptor subunit is located at the top of the molecule with 14 chlorine atoms, which concentrate the negative charges at this side; positive partial charges are expected on the the Fc part (see Figure 5.14).

For a better understanding of the surface energetics, the complex systems under consideration will be studied as the contribution of three fundamental parts:

i) the isolated monolayer, *ii)* the Metal/SAM interface and *iii)* the charge rearrangements that induce the change in the work function.

If one consider the potential energy diagram shown in Figure 5.16, two independent sides with respect to the molecule can be distinguished; one at which the molecule is bonded to the gold (left) and the other at the "vacuum" side (right). Then from a conceptual point of view, two distinct values of the potential energy of an electron can be assumed, E_{vac}^{left} in the vacuum on the thiol side and E_{vac}^{right} on the substituent side of the monolayer. The difference between these two values corresponds to ΔE_{vac} which is directly related to the molecular dipole moment and the area density of molecules in the SAM.

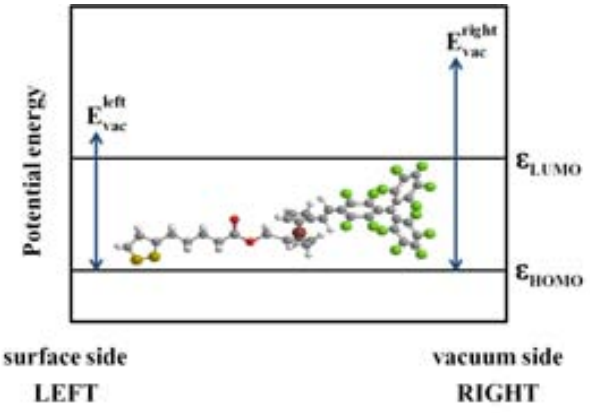

Figure 5.16: Schematic representation of the electron potential energy and the conceptually feature of E_{vac}.

The arrangement of molecules with an intrinsic dipole moment over a surface induces the formation of a dipole layer. However, before considering this effect is important to take into account the effects produced by the organization of the molecules without any interaction with the metal. In this sense, the molecular orientation, which means how is positioned one molecule with respect to the other in close proximity, has a strong effect over the collective dipole because the electrostatic interactions between neighboring polar molecules give place to depolarization effects. Thus, when dipole molecules are close one to the other, an electric field is created which acts in the opposite direction to the intrinsic dipole moment of the isolated individual species in vacuo. This effect will reduce the net surface dipole.

One parameter to keep in mind is that for isolated molecules, only one IP exists which is given by the energetic position of the HOMO relative to one unique vacuum level. However, the situation is different for the SAM, where two distinct IP exist (IP_{SAM}^{left} and IP_{SAM}^{rigth}) due to the presence of the two distinct vacuum levels (E_{vac}^{left} and E_{vac}^{right}) separated by ΔE_{vac}.

In a situation of no interaction between the monolayer and the substrate, the left vacuum level of the isolated monolayers aligns with the vacuum level above the Au surface. Nevertheless, this alignment becomes more complex when molecules interact with the substrate.

In the same way; when a metal does not have any molecule interacting with it, its intrinsic work function could be directly related with the energy difference between the Fermi Level and the potential energy of an electron in the vacuum. However, several processes take place when the chemical bond between the metal and the monolayer is formed. These process involves rearrangements of the charge density at the interface which come from the substitution of the thiol or disulfide bonds by sulfur-gold bonds and also due to the push-back effect, which cause the electron cloud that scaped out from the metal surface to be pushed back into the metal again.

The minimum energy state is the selected condition for dynamic systems. In this sense, SAMs as dynamic systems tend to be reorganized over the surface in order to find their equilibrium. In the process of self-assembly, charge rearrangements are inevitable due to the formation of the bond between the metal and the monolayer, electrostatic interactions between neighboring molecules, intrinsic molecular dipole moment, pinning effect, among others.

Atomistic simulations to demonstrate that under certain circumstances, increasing the molecular dipole moment can reduce the change of the work function, based on the maintenance of the thermodynamic equilibrium have recently been reported by Egger and Zojer[28].

In our case, where the molecules used to functionalize gold surfaces contain two well defined sides, one at the disulfide-alkyl chain and the other at the D–A part; it is important to consider that to achieve this equilibrium, the potential

energy in vacuum on the M–S side (E_{vac}^{left}) plays an important role because it affects not only to the change of the metal work function but also to the alignment of the molecular level at metal/monolayer frontier.

Considering the two assumed vacuum level (left and right) and depending on at which side is located the pinning level, the change in the work function will be different. For molecules with big dipole moment, if the pinning-level is spatially localized on the left side, its position (relative distance) with respect to the Fermi Level will not be strongly affected by a change in the ΔE_{vac}. Under this situation small charge rearrangements will be needed to maintain the equilibrium at the interface and therefore an increase of ΔE_{vac} will be directly reflected onto an increase of $\Delta\pi$ since ΔE_{BD} will remain almost constant. However, if the pinning-level is localized on the opposite side (right side) the effect of ΔE_{vac} would be higher over the relative position of this level with respect to the Fermi level. Then, in order to keep the correct alignment between the pinning-level and the E_F; bigger charge rearrangements will be needed which at the end would result in a larger ΔE_{BD}. In this case, $\Delta\pi$ would remain almost constant since an increase in ΔE_{vac} will be diminished by the larger ΔE_{BD} (see Equation 5.6).

So, the bigger effect over the gold work function induced by the protonated system (**1-H)** could be based on this theoretical work and then the smaller change of the work function observed in SAM **S1** could be justified by the reorganization of the energy levels of the molecules in order to guarantee a thermodynamic stable situation by preserving the occupied states lies below (or unoccupied above) the Fermi level.

Additionally, the higher polarizability present by molecules in **S1** could facilitated a bigger depolarization effect which in fact will reduce the net dipole of the molecules on the surface and consequently the ΔE_{vac}. Then it is possible that neighboring molecules can reorganize themselves as well as their energy levels in order to maintain a general equilibrium of the system on the surface. However in the case of the **S1-H** monolayers the lower polarizability could affecting such degree of freedom and the molecules probably are forced to maintain less relaxed. In conclusion, more than one effect could be related with the small modification

of the work function produced by the anchoring of D–A systems.

5.6 Summary

CPD and WF measurements of D–A open-shell SAMs on Au using KPFM and UPS techniques have been performed. Due to the D–A nature of the molecules negative dipoles moments have been found for these monolayers. The large dipole moment expected for **1** and **1-H** systems together with their standing up orientation over the gold and the good coverage of the monolayers, makes possible to think that probably these systems will modified in a great manner the work function of the gold. However, contrary to the expected a small variation of the work function of the gold was observed for both SAMs (**S1** and **S1-H**) and such variation was justified taken into consideration the following reasons:

- The magnitude of the molecular dipole moments is given not only by the intrinsic dipole moments of the substituents but also by the dipoles induced by the charge transfer from the backbones and the D–A part[36], in this process the local polarizability plays a decisive role. From the deep characterization of the SAMs; it was discarded any intramolecular electron transfer however the large polarizability expected for S1 could be affecting the total dipole moment observed for the SAM.

- The tilt angle of the molecules respect to the surface-normal has an important effect over the net dipole moment, since only the perpendicular component of the dipole respect to the surface is considered. With a tilt angle around 30° it is not expect a large decrease of the molecular dipole moment.

- Large dipole molecules with high polarizability can induce large depolarization effects in the monolayer and therefore the modification of the work function can be small.

- According to theoretical calculations, large dipole molecules in fact do not change the work function of the metal due to a reorganization of the energy level in order to maintain the thermodynamic equilibrium in the system.

Then large dipole moment of isolated molecules cannot be directly correlated with the shift of the work function.

Bibliography

[1] A. Ulman, “Formation and Structure of Self-Assembled Monolayers.,” *Chemical reviews*, vol. 96, no. 4, pp. 1533–1554, 1996.

[2] G. Heimel, L. Romaner, E. Zojer, and J.-L. Bredas, “The interface energetics of self-assembled monolayers on metals.,” *Accounts of chemical research*, vol. 41, no. 6, pp. 721–9, 2008.

[3] N. Koch, “Organic electronic devices and their functional interfaces.,” *Chemphyschem : a European journal of chemical physics and physical chemistry*, vol. 8, no. 10, pp. 1438–55, 2007.

[4] W. E. Ford, D. Gao, N. Knorr, R. Wirtz, F. Scholz, Z. Karipidou, K. Ogasawara, S. Rosselli, V. Rodin, G. Nelles, and F. V. Wrochem, “Organic Dipole Layers for Ultralow Work Function Electrodes,” *ACS nano*, vol. 8, no. 9, pp. 9173–9180, 2014.

[5] R. B. Pode, C. J. Lee, D. G. Moon, and J. I. Han, “Transparent conducting metal electrode for top emission organic light-emitting devices: Ca-Ag double layer,” *Applied Physics Letters*, vol. 84, no. 23, p. 4614, 2004.

[6] D. R. Baigent, R. N. Marks, N. C. Greenham, R. H. Friend, S. C. Moratti, and a. B. Holmes, “Conjugated polymer light-emitting diodes on silicon substrates,” *Applied Physics Letters*, vol. 65, no. 21, p. 2636, 1994.

[7] H. Ishii, K. Sugiyama, E. Ito, and K. Seki, “Energy Level Alignment and Interfacial Electronic Structures at Organic/Metal and Organic/Organic Interfaces,” *Advanced Materials*, vol. 11, no. 8, pp. 605–625, 1999.

[8] I. G. Hill, J. Schwartz, and A. Kahn, “Metal-dependent charge transfer and chemical interaction at interfaces between 3,4,9,10-perylenetetracarboxylic

bisimidazole and gold, silver and magnesium,” *Organic Electronics*, vol. 1, pp. 5–13, 2000.

[9] L. Lindell, M. Unge, W. Osikowicz, S. Stafström, W. R. Salaneck, X. Crispin, and M. P. de Jong, “Integer charge transfer at the tetrakis(dimethylamino)ethylene/Au interface,” *Applied Physics Letters*, vol. 92, no. 16, p. 163302, 2008.

[10] B. Bröker, R.-P. Blum, J. Frisch, a. Vollmer, O. T. Hofmann, R. Rieger, K. Müllen, J. P. Rabe, E. Zojer, and N. Koch, “Gold work function reduction by 2.2â eV with an air-stable molecular donor layer,” *Applied Physics Letters*, vol. 93, no. 24, p. 243303, 2008.

[11] J. C. Love, L. a. Estroff, J. K. Kriebel, R. G. Nuzzo, and G. M. Whitesides, “Self-assembled monolayers of thiolates on metals as a form of nanotechnology.,” *Chemical reviews*, vol. 105, pp. 1103–69, 2005.

[12] I. H. Campbell, S. Rubin, T. Zawodzinski, J. Kress, R. Martin, D. Smith, N. Barashkov, and J. Ferraris, “Controlling Schottky energy barriers in organic electronic devices using self-assembled monolayers.,” *Physical review. B*, vol. 54, no. 20, pp. R14321–R14324, 1996.

[13] M. Ratner, “Pushing electrons around,” *Nature*, vol. 404, no. 6774, pp. 137–8, 2000.

[14] S. Braun, W. R. Salaneck, and M. Fahlman, “Energy-Level Alignment at Organic/Metal and Organic/Organic Interfaces,” *Advanced Materials*, vol. 21, no. 14-15, pp. 1450–1472, 2009.

[15] D. Vuillaume, “Molecular-scale electronics,” *Comptes Rendus Physique*, vol. 9, no. 1, pp. 78–94, 2008.

[16] A. G. Knapp, “Surface Potentials and their measurement by the Diode Method,” *Surface Science*, vol. 34, pp. 289–316, 1973.

[17] J. F. Lübben, T. Ba□e, P. Rupper, T. Künniger, J. Machá□ek, and S. Guimond, "Tuning the surface potential of Ag surfaces by chemisorption of oppositely-oriented thiolated carborane dipoles.," *Journal of colloid and interface science*, vol. 354, no. 1, pp. 168–74, 2011.

[18] B. de Boer, a. Hadipour, M. M. Mandoc, T. van Woudenbergh, and P. W. M. Blom, "Tuning of Metal Work Functions with Self-Assembled Monolayers," *Advanced Materials*, vol. 17, no. 5, pp. 621–625, 2005.

[19] C. Ganzorig, K.-J. Kwak, K. Yagi, and M. Fujihira, "Fine tuning work function of indium tin oxide by surface molecular design: Enhanced hole injection in organic electroluminescent devices," *Applied Physics Letters*, vol. 79, no. 2, p. 272, 2001.

[20] D. Cahen and A. Kahn, "Electron Energetics at Surfaces and Interfaces : Concepts and Experiments," *Advanced Materials*, vol. 15, no. 4, pp. 271–277, 2003.

[21] M. Fujihira, "Kelvin Probe Force Microscopy of Molecular Surfaces," *Annual Review of Materials Science*, vol. 29, no. 1, pp. 353–380, 1999.

[22] S. Watcharinyanon, E. Moons, and L. S. O. Johansson, "Mixed Self-Assembled Monolayers of Ferrocene-Terminated and Unsubstituted Alkanethiols on Gold: Surface Structure and Work Function," *The Journal of Physical Chemistry C*, vol. 113, no. 5, pp. 1972–1979, 2009.

[23] S. D. Evans, E. Urankar, A. Ulman, and N. Ferris, "Self-Assembled Monolayers of Alkanethiols Containing a Polar Aromatic Group: Effects of the Dipole Position on Molecular Packing, Orientation, and Surface Wetting Properties," *Journal of American Chemical Society*, vol. 113, pp. 4121–4131, 1991.

[24] S. Howell, D. Kuila, B. Kasibhatla, C. P. Kubiak, D. Janes, and R. Reifenberger, "Molecular Electrostatics of Conjugated Self-Assembled Monolayers on Au(111) Using Electrostatic Force Microscopy," *Langmuir*, vol. 18, no. 13, pp. 5120–5125, 2002.

[25] J. Lu, E. Delamarche, L. Eng, R. Bennewitz, E. Meyer, and H. Güntherodt, "Kelvin Probe Force Microscopy on Surfaces : Investigation of the Surface Potential of Self-Assembled Monolayers on," *Langmuir*, vol. 15, pp. 8184–8188, 1999.

[26] R. W. Zehner, B. F. Parsons, and L. R. Sita, "Tuning the Work Function of Gold with Self-Assembled Monolayers Derived from X- n C6H4-SH (n= 0, 1, 2; X= H, F, CH3, CF3, and OCH3)," *Langmuir*, vol. 15, pp. 1121–1127, 1999.

[27] S. D. Evans and A. Ulman, "Surface potential studies of alkyl-thiol monolayers adsorbed on gold," *Chemical Physics Letters*, vol. 170, no. 5-6, pp. 462–466, 1990.

[28] D. A. Egger and E. Zojer, "Anticorrelation between the Evolution of Molecular Dipole Moments and Induced Work Function Modifications," *The Journal of Physical Chemistry Letters*, vol. 4, pp. 3521–3526, 2013.

[29] S. Zhong, J. Q. Zhong, H. Y. Mao, J. L. Zhang, J. D. Lin, and W. Chen, "The role of gap states in the energy level alignment at the organic-organic heterojunction interfaces.," *Physical chemistry chemical physics*, vol. 14, no. 41, pp. 14127–41, 2012.

[30] H.-J. Che, P.-J. Chia, L.-L. Chua, S. Sivaramakrishnan, J.-C. Tang, A. T. S. Wee, H. S. O. Chan, and P. K. H. Ho, "Robust reproducible large-area molecular rectifier junctions," *Applied Physics Letters*, vol. 92, no. 25, p. 253503, 2008.

[31] F. Mohn, L. Gross, N. Moll, and G. Meyer, "Imaging the charge distribution within a single molecule.," *Nature nanotechnology*, vol. 7, no. 4, pp. 227–31, 2012.

[32] D. M. Alloway, A. L. Graham, X. Yang, A. Mudalige, R. Colorado, Jr, V. H. Wysocki, J. E. Pemberton, T. R. Lee, R. J. Wysocki, and N. R. Armstrong, "Tuning the Effective Work Function of Gold and Silver Using -Functionalized Alkanethiols: Varying Surface Composition through Dilution and Choice of Terminal Groups," *J. Phys. Chem. C*, vol. 113, pp. 20328–20334, 2009.

[33] D. A. Egger, F. Rissner, G. M. Rangger, O. T. Hofmann, L. Wittwer, G. Heimel, and E. Zojer, "Self-assembled monolayers of polar molecules on Au(111) surfaces: distributing the dipoles," *Physical chemistry chemical physics*, vol. 12, pp. 4291–4294, 2010.

[34] C. E. D. Chidsey, C. R. Bertozzi, T. M. Putvinski, and A. M. Mujsce, "Coadsorption of Ferrocene-Terminated and Unsubstituted Alkanethiols on Gold : Electroactive Self-Assembled Monolayers," *Journal of American Chemical Society*, vol. 112, no. 11, pp. 4301–4306, 1990.

[35] L. Romaner, G. Heimel, and E. Zojer, "Electronic structure of thiol-bonded self-assembled monolayers: Impact of coverage," *Physical Review B*, vol. 77, no. 4, p. 045113, 2008.

[36] L. Wang, G. M. Rangger, L. Romaner, G. Heimel, T. Bu□ko, Z. Ma, Q. Li, Z. Shuai, and E. Zojer, "Electronic Structure of Self-Assembled Monolayers on Au(111) Surfaces: The Impact of Backbone Polarizability," *Advanced Functional Materials*, vol. 19, no. 23, pp. 3766–3775, 2009.

"Success is to be measured not so much by the position that one has reached in life as by the obstacles which he has overcome"

Booker T. Washington

6

Conductivity through Fc–PTM radical SAMs

6.1 Introduction

The understanding of the electronic transport through a single molecule is of crucial importance for both a fundamental and practical point of view in the field of molecular electronics opening potential applications in ultrasmall electronic devices[1]. However this complex process can not be studied as a whole because different contributions add to the overall effect of the charge transport. In this sense, contributions as: the mechanism of charge transfer from the electrodes to the molecules, the transport through the molecules and across them, the influence of the nature of molecule–electrode contact[2], need to be considered to get insight into the performance of the system.

The study of the charge transport through an organic molecular monolayer requires a simple test device which can be formed by a metal/molecular monolayer/metal junction[3], which give place to a structure composed by two metal/molecule interfaces. What happens at these interfaces will strongly determine the final properties of the system.

The self-assembly process constitutes one of the the most useful technique to graft and nanostructure functional molecules on a substrate that allows the study of the electronic properties of organic molecules as promising candidates to be integrated into nanoelectronic devices. In this sense, interface–related processes that take place, upon the adsorption of a molecule onto a metal surfaces, like: charge transfer between the molecule and the metals; the interaction of the molecular levels with the continuum of states in the metal (e.g. the lineup of the molecular orbitals (MOs) relative to the Fermi level of the electrodes); and intramolecular modification of the energy levels induced by the change of electrostatic potential within the molecule; determine important electronic parameters. Such parameters can be the energy and character of the molecular orbitals responsible for the electron transport through the molecules, the current-voltage characteristics and the magnitude of the current[4].

To investigate the properties that allow using molecules as electronic devices, a scheme of three fundamental steps can be considered which includes: *a)* fabrication of stable molecular junctions, *b)* characterization of their properties and *c)* control of such properties.

One of the important active elements in electronic devices are switches, memories or rectifiers. A switch is an electrical component with two electric states (ON state and OFF state). A memory is the element in which information can be written and read. A diode is a two-terminal electronic component that shows asymmetric conductance with high resistance to current in one direction and low resistance in the other. The typical scheme of a diode is represented in Figure 6.1.

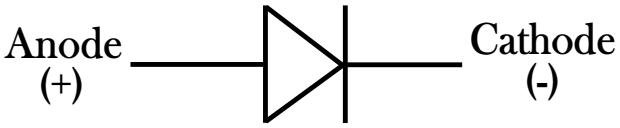

Figure 6.1: Typical scheme of a diode.

Thus, if we want to use all molecular based devices it is of fundamental interest to find new molecules and mechanism to obtain switching, memory and rectification behaviour.

6.1.1 Techniques employed for the fabrication of Metal/Molecule Junctions

Since the metal/molecule interface plays a decisive role on the stability and conductivity of single-molecule junctions, different techniques with different interfaces have been developed to study the electronic transport at nanoscale. Such techniques can be divided in two groups: *i)* the ones that allow measuring electrical transport through a single molecule and *ii)* techniques that measure the transport of a group of molecules using self-assembled monolayer (SAM) prepared on a metallic surface and measured with different kind of top electrodes.

In the single molecule measurement the molecule is connected to noble metal electrodes through specific linking groups (–SH, $-NH_2$, –COOH[5]) where the strong chemical bonds formed between the metal electrodes and the molecule confer stability to the junction.

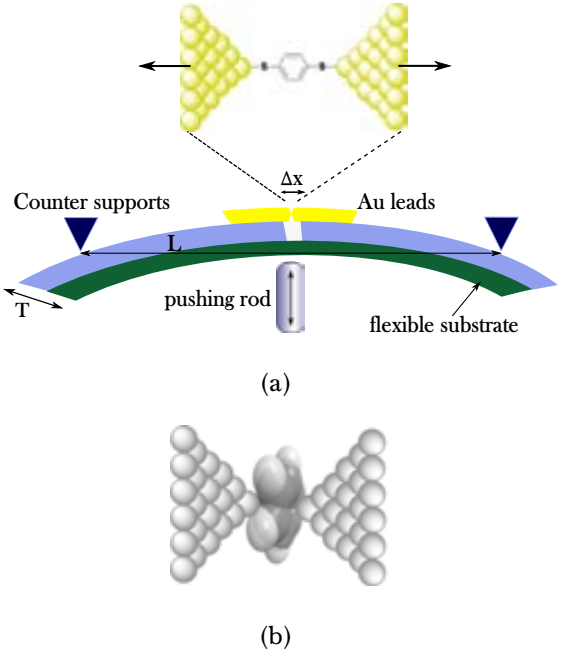

Figure 6.2: Scheme of two different single molecule junctions. (a) mechanically controllable break junction formed though chemical bond of anchoring groups with metallic electrodes and (b) molecular junctions formed directly with the electrodes.

This kind of single molecule junctions can be fabricated using the Mechanically Controllable Break Junction (MCBJ) technique which consists in the trapping

of molecules in the nanogap formed when a metal contact is broken after the adsorption of the functional molecules from solution and under an inert atmosphere. Just before the junction is broken by means of stretching, a single-molecule junctions is formed[6]. Another kind of molecular junction for single molecule measurement is formed by direct binding of π-conjugated organic molecules to metallic electrodes[7,8]. In this case, are no anchoring groups required because the delocalized π molecular orbital directly hybridizes with the metal orbital. Figure 6.2 shows a schematic representation of these kind of single molecule junctions.

Regarding to techniques that measure the electron transport through of a group of molecules, SAMs prepared on a metallic surface is the common denominator but different kind of top electrodes are used to perform the measurements. For instance, a scanning probe tip[2], a Hg drop, metal (Au) evaporated on the top of the SAMs, Au evaporated over a conducting interlayer of PEDOT:PSS, or an alloy of EGaIn. The last kind of top electrode will be used in the framework of this thesis and it will be addressed later. Figure 6.3 shows different molecular junctions.

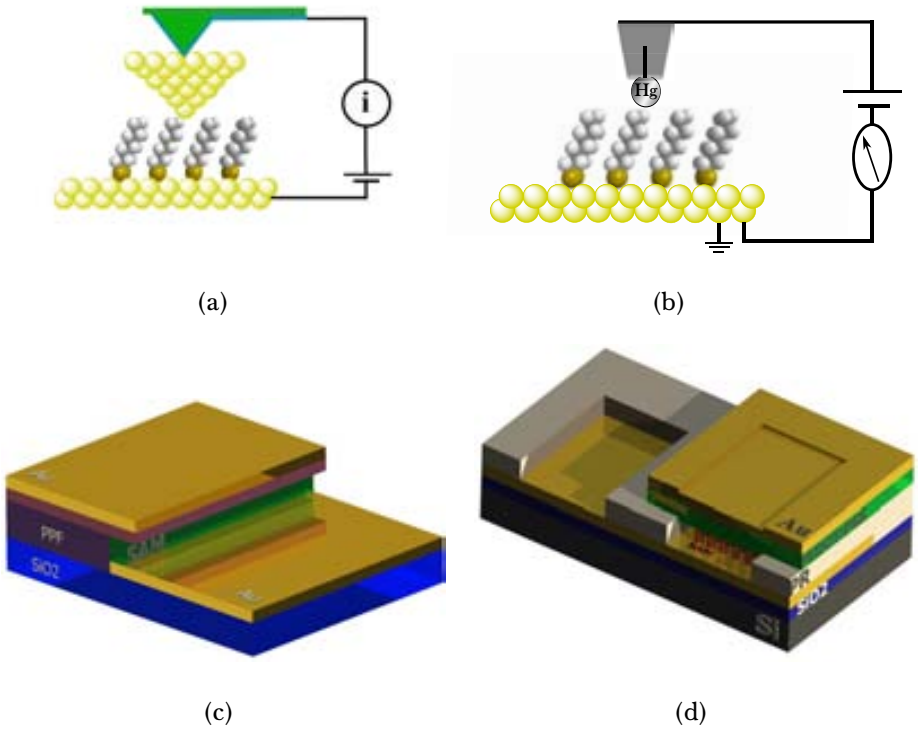

Figure 6.3: Scheme of different molecular junctions using as top electrode: (a) a scanning probe tip, (b) a Hg drop, (c) Au evaporated[9], and (d) Au evaporated over a PEDOT:PSS conducting layer.

However, the different fabrication techniques used to study the charge transport characteristics trough one or few molecules organized over a conductive substrate, have encountered several limitations like poor stability of the junctions, low reproducibility, low yields or some ambiguities that test the real origin of the current or rectification observed. For instance, *i)* junctions that involve directly evaporation of metallic top contacts onto the SAMs can lead to low yields due to the migration of the metal inside the monolayer forming metal filaments or due to the damage of the SAM[10]; *ii)* junctions that use STM or AFM tips to contact SAMs at metal surfaces always have a tunneling gap between the tip and the top of the SAM and the force applied to contact the SAMs, respectively, influence in different ways the charge transport measurements across the molecules[11,12]; *iii)* junctions that use a conductive polymer (PEDOT:PSS) to protect the SAM during the metal deposition show certain disadvantages due to the possible interactions occurring at the SAM/conductive polymer interface, or due to the intrinsic process used to prepared such junctions which can affect the integrity of the SAM and which seems to depend on the details of the molecular structure of the SAM[13]; *iv)* junctions that use Hg as a "soft" liquid-metal electrode also use a kind of protective layer between the SAM and the top electrode, protective layer that is commonly formed by a short-chain SAM and confers stability to the top electrode but adds a resistive component[14].

6.1.2 Electron Transport

Electrical conductance of a macroscopic object is described by the Ohm's law (Equation 6.1) which mentions that the conductance (G) of a rectangular conductor is proportional to its width (W) and inversely proportional to its length (L).

$$G = \frac{\theta\, W}{L} \tag{6.1}$$

Here θ is the conductivity of the conductor, which is decided mainly by the charge carrier density and the mean free path.

Several effects that are negligible in a macroscopic conductor become to be important as the conductor gets smaller. In fact, when the conductor reaches the

nanoscale, electron transport usually does not follow the Ohm's law. Several reasons can explain the failure of Ohm's law at such scale. First, the electron transport is not anymore a diffusive process as described by Ohm's law, because the size is smaller than the mean free path. Instead of that, the electron transport takes place in a ballistic conduction regime, where a charge carrier experiences no scattering in the transport within the conductor. Second, the contact between macroscopic electrodes and the nanoscale conductor strongly affects the overall conductance, so depending on the properties of the contact, the overall transport behavior can be very different. Third, a nanoscale object has a large charge addition energy and a quantized excitation spectrum. All these factors, strongly affect electron transport through molecules of nano-objects especially at low temperatures[15].

Therefore, the potential of using single molecules as active components of electronic circuitry[16] makes the study of charge transport at this level, an imperative need. As was mentioned in Chapter 5, subtle changes in the molecular properties arise when a molecule is connected to one or more electrodes. As a result of metal–molecule coupling, the molecular orbitals can hybridize with the states of the metal contacts causing that the original molecular levels broaden and shift compared to a free molecule in vacuum[17].

Several studies have been performed in the effort to clarify the interface metal- molecule process. Thus, it has been observed that the thiol binding site and the atomic environment in the junction can vary significantly the conductance[18]. A wide range of conductance values have been obtained depending on the adsorption site (atop, bridge[19], hollow[20]) at which the metal–sulfur bond takes place which is not favourable to develop of single molecular electronics where high and fixed conductance values are required. In general, linking groups acts as resistive spacers between the electrodes and the molecules which leads to a low conductivity and also sensitivity to different environmental effects (e.g. neighbor adsorbed species)[8]. On the other hand, poor contacts limit the junction transport which pushes the research to look for stable, reliable and reproducible molecular junctions.

When the metal electrodes and the molecule start to interacts, some charge flow inducing a charge rearrangement and also geometric reorganization from which the Fermi level of the electrodes ends lying in the halfway between the HOMO-LUMO gap of the molecule[21]. However, when a chemical interaction (surface bond formation) between the electrodes and the molecules takes place, these energy levels alignment start to depend on the interfacial electronic structure and of course on the interfacial dipole layer[22] as was discussed in Chapter 5.

Regarding to the charge transport process, two principal mechanism can be identified, tunneling or coherent mechanism and hopping or incoherent transport. The non-resonant tunneling transport predominates in short molecules, this mechanism is strongly distance-dependent but temperature independent. Experimentally, it has been observed an exponential molecular resistance variation with respect to the length of the molecules[23]. The hopping conduction or sequential charge transfer is common in long molecular wires[24], this mechanism, contrary to the tunneling is weakly distance-dependent but has temperature dependence.

The probability of an electron to be transmitted by tunneling is dictated by the *electronic superexchange coupling* quantity. Oppositely, sequential charge transfer (thermally activated hopping mechanism) involves real intermediate states that couple the internal nuclear motions of the bridge and the surrounding medium. These states are energetically accessible and occurs when there is near-resonant charge injection, vibronic overlap of the ion pair states formed as the charge moves from site to site in the molecule, and vibronic overlap of the ion pair state in which the charge is located[25].

Charge transport mechanism is affected by the molecular electronic structure which includes both the energy gap between the HOMO and LUMO, and the alignment of the two frontier molecular orbitals with respect to the metal Fermi Level as was discussed previously. Therefore, when the difference in energy between the molecular orbital and the metal Fermi level is large, charge transport occurs by tunneling. In contrast, if the Fermi level approaches the energy of the orbitals of the molecules, either hopping or resonant tunneling may take place[26], in this case the conduction of electrons will be through the molecular orbitals.

In a general way, two principal factors can be considered as determining in the charge transport mechanism: *i)* the electronic coupling between the system components and *ii)* the energy matching which is given by the energies of the molecular frontier orbitals with respect to the Fermi energy of the metallic contacts, which is related to the charge injection energy. Depending on the intrinsic properties of a system, charge transport can occurs via one or another mechanism. Nevertheless, for long-distance systems charge transport rate could be dictated by some combination of coherent transport and incoherent charge hopping[27]. In the literature it has been reported that choosing electroactive molecular components could drive the system toward incoherent behaviour at long distances or that in D–bridge–A systems the charge transport mechanism can changes from direct tunneling to hopping[24]. More related with our work, Crivillers *et al.*[28,29] have reported that the negative differential resistance (NDR) showed by SAMs based on polychlorotriphenylmethyl (PTM) is attributed to similar resonant tunneling with unoccupied molecular orbitals.

6.1.3 Molecular Devices: recti□ers, memories and switches

As it has been mentioned in the introduction one of the aims of molecular electronics is to use molecules as active electronic elements of electronic circuits devices. One important active element is the rectifier. The first molecular rectifying diode, see Figure 6.4, was proposed by Aviram and Ratner (AR-rectifier) in 1974. This theoretical model comprised an acceptor–bridge–donor (A–b–D) molecule which would imitate the properties of a p–n junction and could play the same role as it, in molecular electronics.

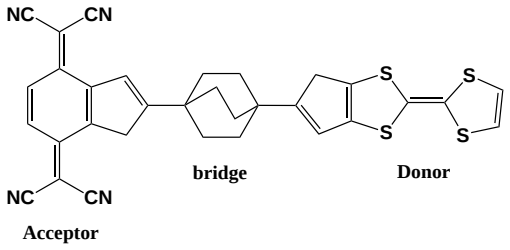

Figure 6.4: Donor–θ–Acceptor molecule (TTF–θ–TCNQ) proposed by Aviram and Ratner[16] as an example of a molecular recti er.

The presence of a bridge (θ –electron system) between the donor and the acceptor subunits cause that the π–levels of these two sites (D and A) do not interact each other on the time-scale of electronic motion to or from the electrodes. Then the electron current was expected to pass through the molecule only from left to right as a three-step process of equivalent resistance (cathode acceptor; acceptor donor; and donor anode) but not in the other sense, observing thus the rectifier property of the molecule[16].

It has been calculated that the electrical rectification results from the asymmetric profile of the electrostatic potential across the system produced e.g. by a stronger coupling of the molecule with one electrode than with the other. Moreover, the rectification current also strongly depends on the position where the HOMO and LUMO rest with respect to the Fermi levels of the two metal electrodes, before bias is applied and on the shift of such positions induced by the applied bias[30].

Molecular switches and memories are other components of great interest for molecular electronic devices. They can be grouped into different clusters depending on the kind of the internal modification that molecules experiment when an external stimuli is applied. Thus, one can find molecular memories which mechanism is based on the soft nature of organic molecules; more specifically on the conformational changes that molecules can suffer once they have been excited, changes that are associated with different conductivity levels of the molecule[31]. Other memories use the redox properties of active molecules, such operation is based on charging and discharging of electrons into and from energy levels in the molecules which induces the presence of different reversible chemical redox states (reduced or oxidized)[32,33]. Other molecular memories that show fast switching times and possible long retention times are characterized by a negative differential resistance (NDR) behavior in their current-voltage curves, being NDR the phenomenon of decreasing current with increasing voltage[29,34,35].

6.2 Objectives

In this chapter, molecules **1** and **1-H**, which have very similar molecular structure but different electronic structure will be used to understand the influence of an open or closed-shell structure over the electronic properties of organized monolayers (2D structures) on surfaces, taking into account that the intramolecular charge transport can only be feasible in the case of the open-shell **1** system where the singly-unoccupied molecular orbital (SUMO) can accept the electron coming from the ferrocene unit, obtaining in this way a charge-separated electronic state.

6.3 Charge transport measurements in Fc–PTM open-shell SAMs

Since the transport properties of a molecular system depends between other factors on the intrinsic structure of the molecules. Charge transport measurements on two SAMs containing similar molecular structure but very different electronic structure is interesting. Through these molecular junctions it is expected to know the dependence of the charge transport on the electronic structure of systems **S1** and **S1-H**, which contain important donor-acceptor groups.

As it has been mentioned, most of the techniques used to study charge transport through molecules organized on a conductive substrate have limitations. Such limitations make imperative to use an appropriate development methodology to study the charge transport in junctions. Thus, in the context of this thesis, a specific type of junctions reported by Nijhuis *et. al*[36] based on ultra-flat Au bottom electrodes and liquid metal (Ga_2O_3/EGaIn) top electrodes was used. This kind of junctions allows a systematic physical-organic study based on statistically large numbers of data[37], and shows great advantages over other fabrication techniques for junctions because the ultra flat bottom electrode avoid failures coming from possible defects or topographical irregularities of the electrode. The top electrode (Ga_2O_3/EGaIn) is less susceptible to alloying and short-circuiting than the previously mentioned Hg-drop and therefore allows to have higher yields of working

junctions, moreover it is nonvolatile, nontoxic and ease of manipulation. Even though the layer of Ga_2O_3 shows an important resistivity, it is several orders of magnitude less than the total resistance of the junction over the range of voltages applied as reported the authors[36].

The conductivity study through this kind of systems is also of interest to know the differences at electronic level of **1** and **1-H** once they are bonded to a gold surface. As we have mentioned, the charge transport across a molecule depends on the intrinsic nature of the molecules and how it is interacting with its environment. Moreover, the relative energy position of the molecular orbitals of the D–A systems with respect to the Fermi Level of the electrodes will determine the charge transport mechanism (tunneling or hopping) and also the energy barrier height that need to be overcome before the charge transfer takes place. Finally, the possibility to obtain current rectification in the case of the D–A open-shell system **1** give great expectations to these charge transport measurements. As well as studying which is the influence of the open-shell electronic structure on charge transport properties.

6.3.1 Conductivity measurements in Au-S1//Ga_2O_3/EGaIn and Au-S1H//Ga_2O_3/EGaIn junctions

Stable and reproducible molecular tunneling junctions based on SAMs of **1** and **1-H** were prepared on template-stripped gold (Au^{TS}) used as bottom electrode, and a eutectic indium-gallium (EGaIn) alloy with a surface layer of Ga_2O_3 as top contact. These measurements have been carried out in the group of Prof. Christian Nijhuis.*

The intrinsic chemical structure of the molecules (**1** and **1-H**) used for the fabrication of these junctions can essentially give place to two specific sections, one isolating (disulfide-alkyl chain) and another conducting (Fc–PTM system). The different materials of the two electrodes and the corresponding dissimilarity in

*Current measurements were performed by Li Yuan, Ph.D. student in The Nijhuis Group - Molecular Electronics and Nanofabrication (MEN) at the Department of Chemistry in the National University of Singapore, NUS.

the molecule–electrode contacts will produce two important interfaces, one at the bottom electrode where the molecule is covalently bonded to the gold and another at the top electrode where probably Van der Waals interactions take place between the molecules and the Ga_2O_3/EGaIn top electronde.

Charge transport study requires stable, reproducible and well formed molecular junctions. In an ideal case, junctions with no defects in either electrode and perfectly ordered SAMs are required however at experimental level such kind of precision is not possible due to the intrinsic dynamism of the molecular systems and the interactions of the molecules with the environment (electrodes). Then, different kinds of defects could be observed in the molecular junction, including: *a)* structural imperfections on the bottom contact (step edges and vacancy islands), *b)* different sites at which the bond between the molecule and the bottom electrode is formed which will have important influence over the tilt angle of the molecules with respect to the surface normal, *c)* physisorbed material on the bottom electrode and *d)* impurities (e.g. dust)[20,37,38]. All these defects could cause variations of the distance between the top and the bottom electrodes, strongly affecting the tunneling current which as discussed above, has a strong distance dependence. Another source of variations can be based on the dynamic behaviour of SAMs; where different orientations can be adopted by the molecules on the surface due to bulky units on the system, resulting in a small disorder.

As it has been mentioned, the contact of the molecules with the bottom and top electrodes plays an important role on the charge conduction. The asymmetrical conduction (i.e. rectification) is expected due to rectification in molecular junctions. However, it can also occurs as a consequence of non-molecular effects like: different materials of the electrodes, different type of the contact between molecules and the electrodes (bottom/top), formation of metal oxides at the electrodes[39,40], or any other asymmetry encountered in the structure of the junctions. This consideration will be discussed later.

S1 and **S1-H** monolayers based junctions with EGaIn top electrodes (Figure 6.5) were measured in a bias ranged from +2 to -2 V.

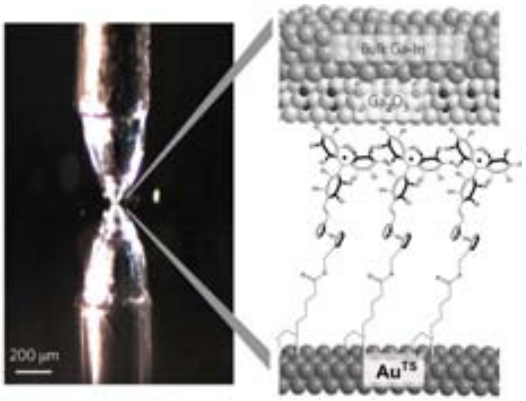

Figure 6.5: Scheme of the monolayers based junctions with EGaIn top electrode and Au bottom electrode.

Large number of data were acquired and a statistical analysis of them was made in order to discard any artifact from the real data. Table 6.1 collects the statistics of **S1** and **S1-H** monolayers based junctions. More than 400 traces were measured for each sample (**S1** and **S1-H**) and comparable yields of working junctions were obtained for these systems (95 and 88%, respectively). A big difference of the rectification ratio was observed, comparing the junction containing the radical D–A system **1** (5.57) with respect to their protonated analogous **1H** (98.98) (Figure 6.6) which is a clear evidence of the different electronic nature of these two molecular systems which have almost the same molecular structure.

Table 6.1: Statistics for the I-V measurements of Au-**S1**//Ga_2O_3/EGaIn and Au-**S1H**//Ga_2O_3/EGaIn Junctions.

Parameter	S1	S1-H
Number of junctions	20	25
Number of shorts	1	3
Number of traces	456	528
Nonshorting junctions (%)[a]	95	88
Recti□cation ratio (δlog)[b]	5.57 (0.55)	98.98 (0.65)

[a] Working junctions that gave stable J(V) characteristics.

[b] The rectification ratio has been defined as $R = J(-V)\ \ J(V)$

Through these measurements two principal quantities were evaluated, the current density and the rectification ratio (Figure 6.6). Junctions based on **S1** monolayers show higher current (~ 100 larger at −1.0 V) but smaller rectification ratio (R = 5.57) in comparison with junctions of **S1-H**. The small R found indicates that junctions based on **1** do not rectify current strongly, while **S1-H** junctions do it (R = 98.98).

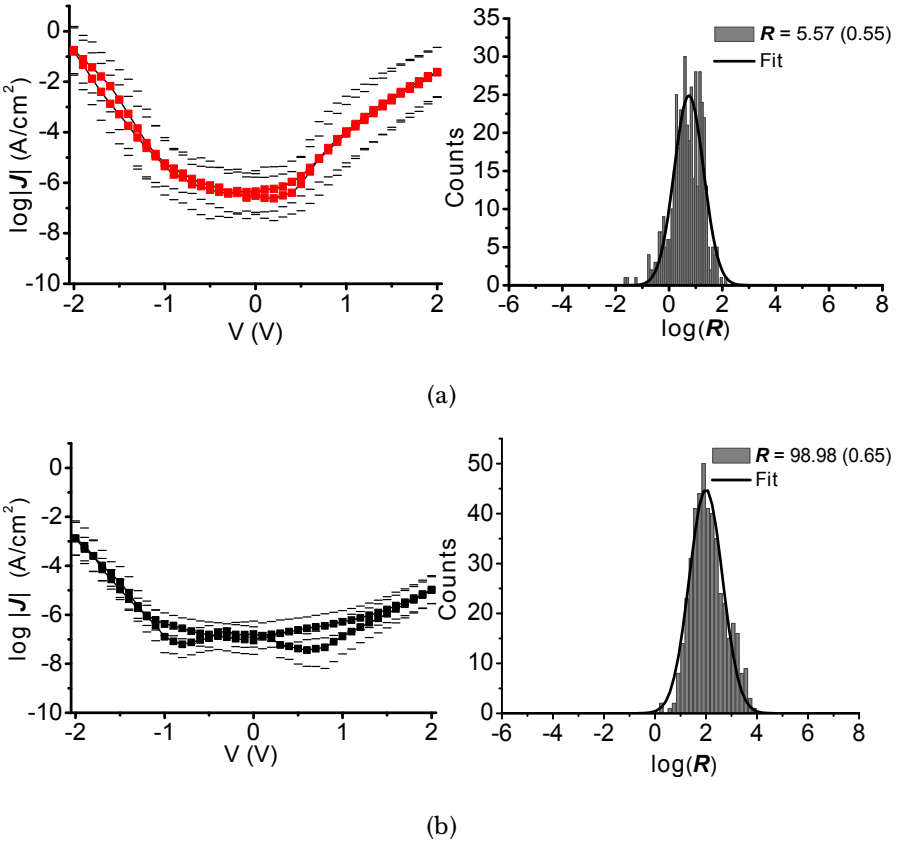

Figure 6.6: J(V) plot and histogram of recti cation ratio tted with Gaussian distribution in a range bias of ± 2.0 V of (a) **S1** and (b) **S1-H** monolayers based junctions.

As it has been already mentioned, in our group it has been observed that SAMs based only on the PTM unit in its radical and protonated form exhibit different transport behaviors which have been correlated with the distinct electronic structure of the two PTM-SAMs. In the work of Crivillers *et. al* it was demonstrated that the conductivity through the PTM radical SAM is much higher than the protonated PTM SAM[28] which is in agreement with the higher current density observed for **S1** junctions in front of **S1-H**. However, contrary to what it was

initially expected for junctions containing D–A molecular systems, compound **1** showed a small rectification effect which should be explained as consequence of the accessibility of molecular orbitals at both, forward and reverse bias.

Probably, the rectification phenomenon in these junctions do not obey only to a molecular origin but also could be a contribution of the several asymmetries that comes from the fabrication method of the junctions; asymmetries related with the different material used for the electrodes (Au-bottom and Ga_2O_3/EGaIn-top) and the different nature of the contact between the SAM and the electrodes. Moreover, focusing on the top electrode region, some uncertainty could be inserted in the measurements due to several factors like; the resistance of the layer of Ga_2O_3 which depends on the growth conditions[41]; the exact nature of the interface between the SAM and the layer of Ga_2O_3 which probably is driven by van der Waals forces; unpredictable organic material on the surface of the top electrode (Ga_2O_3/EGaIn) and the roughness of the layer of Ga_2O_3 which could affect the contact surface preventing a complete contact of the monolayer with the top electrode[37], among others.

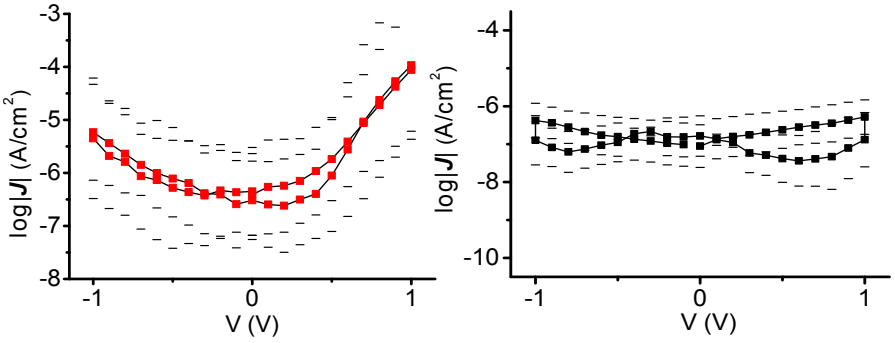

Figure 6.7: J(V) plot in a range bias of ± 1.0 V of **S1** (left) and **S1-H** (right) monolayers.

When we consider ±1.0 V (Figure 6.7) as voltage range in the ±2.0 V range, higher current is observed for the open-shell **S1** monolayers than for the **S1-H** closed-shell one. But, interesting results the behavior of junctions based on **S1** monolayers when ±1.0 V is considered as voltage range. In such case, it has been possible to observe a higher current density at positive bias (+1.0 V) than at negative one (-1.0 V), opposite to the behavior observed at ±2.0 V. The change in the direction of the bias at which higher current density is distinguished, could

be related with the higher polarizability of this molecule with respect to **S1-H**. The dipole moment of **1** can create an internal electrical field which probably is favouring the direction of charge transport at +1.0 V and not at -1.0 V.

On the other hand, at ±2.0 V bias range the high current density observed at forward and reverse bias for **S1** could be related with the alignment of the molecular orbitals of D–A system **1** with respect to the Fermi levels of the electrodes and additionally with a possible coupling of the singly-unoccupied molecular orbital (SUMO) with the nearest electrode (Ga_2O_3/EGaIn). A general analysis of the bands diagram based on the Nijhuis work[37] will be discussed in the following section.

The fact that the value of *R* for junctions based on **S1-H** monolayers, is a factor of $\approx 10^2$ larger than the one for the radical system, it should be directly related with the molecular energy asymmetry of the protonated system **1-H** incorporated in the junction and not due to other asymmetries in the junctions. However, this large rectification was not achieved before applying a bias of -2 V which could be an indication of some energy barrier caused probably by the LUMO of the **1H** system which need to be overcome before the HOMO of the Fc starts to participate in the process and allow an easier charge transport at forward bias and not at reverse bias. More details will be covered in the next section.

6.4 Analysis of the bands diagrams

Nijhuis and col.[37], proposed an interesting mechanism for the rectification of current observed in SAM-based tunneling junctions containing alkanethiols with Fc head groups. Taking into account this mechanism they found out that to get large rectification ratios it is necessary to have one energetically accessible molecular orbital, which has to be placed asymmetrically in the space inside the junction and to be lower in energy than the Fermi levels of both electrodes. Thus, in order to get rectification, the HOMO needs to follow the potential of the Fermi level of the nearest spatially electrode (Ga_2O_3/EGaIn) and overlap energetically with the Fermi levels of both bottom and top electrodes only in one direction of the bias[37].

Following this proposed mechanism and considering that **S1** and **S1-H** tunneling junctions were prepared using ultra-flat Au as bottom electrode and Ga_2O_3/EGaIn as top electrode, Figures 6.8 and 6.9 show a schematic representation of the energy level diagrams that try to explain the possible mechanism observed in these current measurements. In these diagrams the bottom electrode (Au) is represented at left side followed by the molecule with the disulfide group bonded to Au and the PTM moiety on the opposite side. Close to the PTM unit is the Ga_2O_3/EGaIn top electrode. Between both electrodes are drawn the molecular orbitals of **S1** and **S1-H** which will help us to understand the charge transport mechanism through the SAMs as well as the current rectification.

The work function for modified gold surfaces was taken from UPS measurements, since the work function (π) of a metal can change due to the presence of adsorbates on the surface. Then a reference mean value of ≈5.0 eV was assumed for Au-bottom electrode and a value of ≈4.3 eV[37] for Ga_2O_3/EGaIn-top electrode. The initial represented state is an open circuit (V = 0 V) where the Fermi levels of the bottom and top electrodes tend to be aligned with and intermediate value of 4.65 eV.

The molecular orbitals involved in the electron charge transport of the open-shell **S1** monolayers (HOMO and SUMO) were determined by wet cyclic voltammetry, previously described in Chapter 3 (Table 3.5). From these data it has been found that in energy the HOMO (5.15 eV) remains below the two electrodes (4.65 eV) but the SUMO is positioned slightly above them (4.35 eV).

When a bias of ±1.0 V is applied, the Fermi level of the Ga_2O_3/EGaIn top electrode is shifted up or down in 1.0 V and due to the close proximity of the SUMO, this level goes up or down together with the Fermi level but only in 0.7 V since a potential drop of 0.3 V across the SAM/Ga_2O_3 interface has been assumed[37] [†]. Additionally, it is assumed that the HOMO is electronically coupled with the SUMO due to both the small energy gap (0.8 eV) observed between them and the high delocalization of the electrons over the system (Fc−PTM) and therefore

[†]The 0.3 eV is a value assumed as potential drop considering that the potential drop across the SAM//Ga_2O_3 interface is less than that across an alkyl chain[37].

it follows to the SUMO (0.7 V) without any potential drop.

At forward bias (−1.0 V), the SUMO of **S1** achieves the same energy than the Fermi level of the top electrode while the HOMO falls within the energy window determined by the values of the Fermi level of the bottom and top electrode. However, when a reverse bias (+1.0 V) is applied the HOMO remains below in energy than the two electrodes but the SUMO falls within the energy window. In this case it is clear that the current transport through the open-shell **S1** molecules takes place with the participation of the SUMO at both bias and this is reason of the higher conductance observed for **S1**. According to Figure 6.7 (left), the current density is clearly observed to be higher at reverse bias (+1.0 V) which could be related with the fact that due to the dipole moment of the oriented D−A molecules an internal electric field is created which acts in opposite direction to the dipole of the SAM and maybe it is favoring the current transport at reverse bias. Moreover, since the SUMO at forward bias is not place within the energy window but it is at the same energy than the Fermi level of the top electrode probably allows to obtain a general high density current but not rectifies in this direction. Then, it seems that to obtain rectification is imperative that the molecular level is placed asymmetrically both in energy and spatially between the Fermi level of the bottom and top electrode.

When the bias applied is increased till ±2.0 V, the new alignment of the energy levels of **S1** follows the description aforementioned, which means that the Fermi level of the Ga_2O_3/EGaIn electrode shifts up or down in 2.0 V and the SUMO and HOMO do the same but only in 1.4 V, assuming a potential drop of 0.3 V per each volt applied[37]. In this case both the SUMO and the HOMO fall in the energy window at forward (−2.0 V) and reverse (+2.0V) bias. Due to the asymmetric position of the SUMO, physical and also in energy close to the Fermi level of the top electrode, these two energy levels could be coupled and thus the SUMO could participate in the charge transport across the molecule at both bias (forward and reverse), such assumption agrees with the fact that almost no rectification is observed but does a high current density.

The energy level diagram built for junctions based on closed-shell **S1-H** monolayers was made in the same way that the energy level diagram for junctions based on **S1** monolayers. The main difference is the non-presence of the SUMO in the PTM moiety which in this system has a closed-shell electronic structure. In this case, its analogous unoccupied energy level, LUMO, cannot be estimated by wet cyclic voltammetry due to the non-electroactive character of this moiety and thus, only the value for the HOMO has been calculated and will play a role. In **S1-H**, the first unoccupied orbital, LUMO, will lie much higher in energy as it has been previously reported[29].

The HOMO levels at negative and positive bias were qualitative estimated (0.4 eV) since the absent of quantitative data for the potential drops along the PTM moiety must be added to the previously mentioned 0.3 V of potential drop across the van der Waals interface. Under all these considerations, when ±1.0 V bias is applied only at forward bias (−1.0 V) the HOMO falls into the energy window, however the current density is very small as can be seen in Figure 6.7 (right). Probably, this is due to the fact that the LUMO localized in the PTM moiety is acting as an energy barrier. Moreover, at reverse bias (+1.0 V) together with the possible energy barrier given by the LUMO; the HOMO was found to be outside of the energy window, which will explain the almost zero current density observed. Nevertheless, when the bias applied increases until ±2.0 V, the HOMO falls within the energy window at both bias (forward and reverse) and the energy difference between the LUMO and the Fermi level of the Ga_2O_3/EGaIn or Au electrode becomes smaller.

It seems that at forward bias (−2.0 V) the energy is enough to overcome the barrier induced by the LUMO giving place to the possible participation of the HOMO in the charge transport thanks to some kind of coupling with the Fermi level of the Ga_2O_3/EGaIn electrode. On the other hand, at reverse bias (+2.0 V) the current density continues to be small even though the HOMO is placed inside the energy window and close in energy to the Fermi level of the top electrode. The LUMO is still much higher than the Fermi levels of both electrodes (bottom and top) for which it is probably that the system does not consider such level in the

current transport and thus it overlaps energetically with both Fermi levels of the electrodes only in one direction (forward) of bias showing rectification ($R = 98.98$).

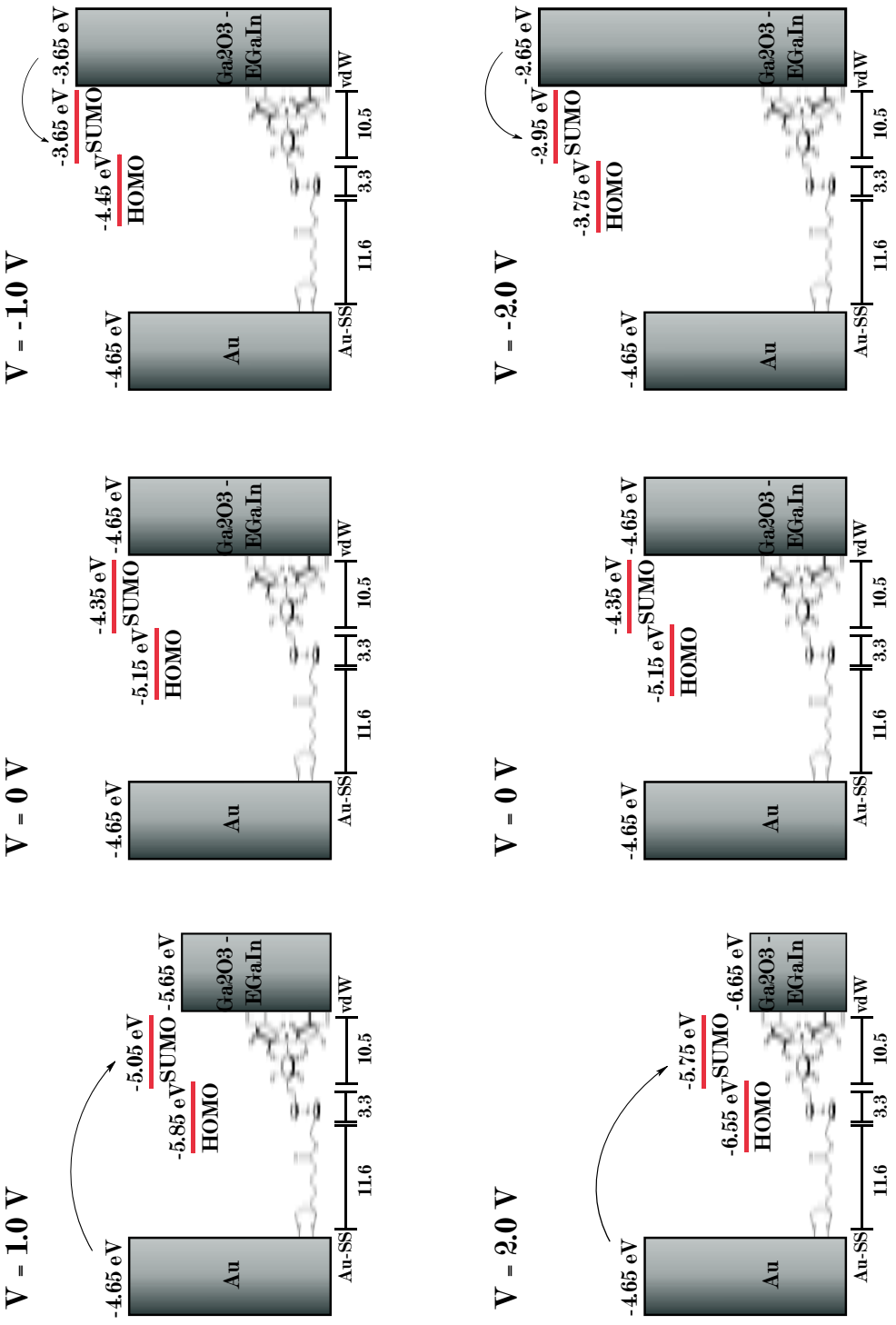

Figure 6.8: Schematic representation of the energy levels diagrams proposed for **S1** junction at ± 1 V and ± 2 V.

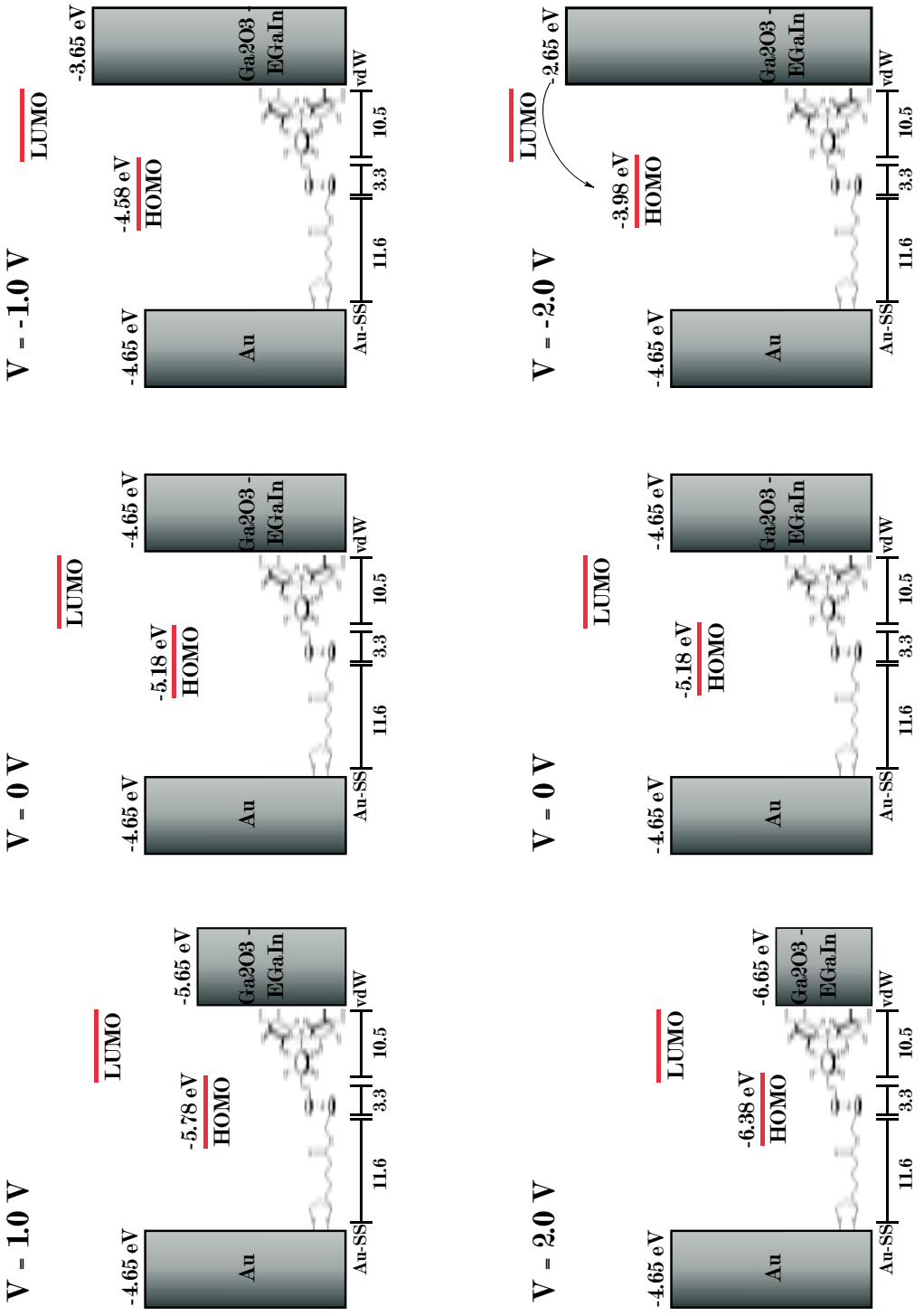

Figure 6.9: Schematic representation of the energy levels diagrams proposed for **S1-H** junction at ± 1 V and ± 2 V.

Even though, the rectification in junctions based on **S1-H** monolayers was observed at - 2.0 V, such rectification comes from the molecule and not from the external artifacts like the possible oxidation of the top electrode, which was probed by the no rectification observed for the junctions based on **S1** monolayers. Moreover, the substrate, SAM, and top contact remain the same across the range of biases applied incorporating the same defects. Additionally, the current in one direction serves as an internal standard through with the current in the opposite direction can be examined by comparison[37].

6.5 Summary

Even during the course of this thesis it has not been possible to perform transport measurement at different temperatures to know the mechanism of charge transport, the charge transport in both types of junctions seems to be by tunneling due to the small size of the molecule (~2.7 nm). Moreover, for other SAMs containing only the PTM unit with alkyl chains of different lengths it has been observed a distance-dependent behavior. The hopping mechanism is more considered to explain the charge transport across long molecules or wires. Moreover in **S1** and **S1-H** SAMs it seems that some contribution of the coupling between the molecular orbitals and the closest electrode Fermi level is present. Finally, it seems that the close proximity both in energy and spatially between an accessible molecular orbital and the Fermi level of the electrode only in one direction of bias is required to achieve rectified currents.

In summary, two structurally similar but electronically very different molecules have been bonded to gold surfaces and the charge transport across them has been studied, showing remarkable differences both in the current density and in the rectifiaction ratio. Such differences are based on the distinct electronic structure of **1** and **1-H** systems. For junctions based on open-shell **S1** monolayers there is a lost of the rectification but there is a high current density at both bias. On the other hand, for junctions based on **S1-H** monolayers it was observed a large rectification ratio once the energy barrier induced by the LUMO was almost overcome at

−2.0 V.

So, if we want to find molecules that can be active in electric devices like rectifiers it is very important first to choose correctly the technique to evaluate the current transport in order to know the influence of the electronic structure of the molecule on the wanted electronic activity and second to achieve an asymmetric placement of the accessible molecular orbital within the junction.

Bibliography

[1] M. Kiguchi and S. Kaneko, "Electron transport through single π-conjugated molecules bridging between metal electrodes.," *Chemphyschem : a European journal of chemical physics and physical chemistry*, vol. 13, no. 5, pp. 1116–26, 2012.

[2] Y. Qi, I. Ratera, J. Y. Park, P. D. Ashby, S. Y. Quek, J. B. Neaton, and M. Salmeron, "Mechanical and charge transport properties of alkanethiol self-assembled monolayers on a au(111) surface: the role of molecular tilt.," *Langmuir*, vol. 24, no. 5, pp. 2219–23, 2008.

[3] D. Vuillaume, "Molecular-scale electronics," *Comptes Rendus Physique*, vol. 9, no. 1, pp. 78–94, 2008.

[4] Y. Xue, S. Datta, and M. a. Ratner, "Charge transfer and "band lineup" in molecular electronic devices: A chemical and numerical interpretation," *The Journal of Chemical Physics*, vol. 115, no. 9, p. 4292, 2001.

[5] F. Chen, X. Li, J. Hihath, Z. Huang, and N. Tao, "Effect of anchoring groups on single-molecule conductance: comparative study of thiol-, amine-, and carboxylic-acid-terminated molecules.," *Journal of the American Chemical Society*, vol. 128, no. 49, pp. 15874–81, 2006.

[6] M. a. Reed, "Conductance of a Molecular Junction," *Science*, vol. 278, no. 5336, pp. 252–254, 1997.

[7] S. Kaneko, T. Nakazumi, and M. Kiguchi, "Fabrication of a Well-Defined Single Benzene Molecule Junction Using Ag Electrodes," *The Journal of Physical Chemistry Letters*, vol. 1, no. 24, pp. 3520–3523, 2010.

[8] M. Kiguchi, O. Tal, S. Wohlthat, F. Pauly, M. Krieger, D. Djukic, J. Cuevas, and J. van Ruitenbeek, "Highly Conductive Molecular Junctions Based on Direct Binding of Benzene to Platinum Electrodes," *Physical Review Letters*, vol. 101, no. 4, p. 046801, 2008.

[9] A. P. Bonifas and R. L. McCreery, "Soft Au, Pt and Cu contacts for molecular junctions through surface-diffusion-mediated deposition.," *Nature nanotechnology*, vol. 5, no. August, pp. 612–617, 2010.

[10] H. Haick and D. Cahen, "Contacting organic molecules by soft methods: towards molecule-based electronic devices.," *Accounts of chemical research*, vol. 41, no. 3, pp. 359–66, 2008.

[11] L. A. Bumm, J. J. Arnold, T. D. Dunbar, D. L. Allara, and P. S. Weiss, "Electron Transfer through Organic Molecules," *The Journal of Physical Chemistry B*, vol. 103, pp. 8122–8127, 1999.

[12] V. B. Engelkes, J. M. Beebe, and C. D. Frisbie, "Analysis of the Causes of Variance in Resistance Measurements on Metal - Molecule - Metal Junctions Formed by Conducting-Probe Atomic Force Microscopy," *The Journal of Physical Chemistry B*, vol. 109, pp. 16801–16810, 2005.

[13] H. B. Akkerman and B. de Boer, "Electrical conduction through single molecules and self-assembled monolayers," *Journal of Physics: Condensed Matter*, vol. 20, no. 1, p. 013001, 2008.

[14] R. Haag, M. A. Rampi, R. E. Holmlin, and G. M. Whitesides, "Electrical Breakdown of Aliphatic and Aromatic Self-Assembled Monolayers Used as Nanometer-Thick Organic Dielectrics," *Journal of the American Chemical Society*, vol. 121, no. 34, pp. 7895–7906, 1999.

[15] J. Park, *Electron Transport in Single Molecule Transistors.* PhD thesis, University of California, Berkeley, 2003.

[16] A. Aviram and M. A. Ratner, "Molecular Rectifiers," *Chemical Physics Letters*, vol. 29, no. 2, pp. 277–283, 1974.

[17] S. Jan van der Molen and P. Liljeroth, "Charge transport through molecular switches.," *Journal of physics. Condensed matter*, vol. 22, no. 13, p. 133001, 2010.

[18] K.-H. Müller, "Effect of the atomic configuration of gold electrodes on the electrical conduction of alkanedithiol molecules," *Physical Review B*, vol. 73, no. 4, p. 045403, 2006.

[19] C. Li, I. Pobelov, T. Wandlowski, A. Bagrets, A. Arnold, and F. Evers, "Charge transport in single Au / alkanedithiol / Au junctions: coordination geometries and conformational degrees of freedom.," *Journal of the American Chemical Society*, vol. 130, no. 1, pp. 318–26, 2008.

[20] J. C. Love, L. a. Estroff, J. K. Kriebel, R. G. Nuzzo, and G. M. Whitesides, "Self-assembled monolayers of thiolates on metals as a form of nanotechnology.," *Chemical reviews*, vol. 105, pp. 1103–69, 2005.

[21] A. Nitzan and M. a. Ratner, "Electron transport in molecular wire junctions.," *Science*, vol. 300, pp. 1384–9, 2003.

[22] L. Routaboul, P. Braunstein, J. Xiao, Z. Zhang, P. a. Dowben, G. Dalmas, V. Da Costa, O. Félix, G. Decher, L. G. Rosa, and B. Doudin, "Altering the static dipole on surfaces through chemistry: molecular films of zwitterionic quinonoids.," *Journal of the American Chemical Society*, vol. 134, no. 20, pp. 8494–506, 2012.

[23] D. J. Wold, R. Haag, M. A. Rampi, and C. D. Frisbie, "Distance Dependence of Electron Tunneling through Self-Assembled Monolayers Measured by Conducting Probe Atomic Force Microscopy: Unsaturated versus Saturated Molecular Junctions," *The Journal of Physical Chemistry B*, vol. 106, no. 11, pp. 2813–2816, 2002.

[24] S. H. Choi, B. Kim, and A. D. Frisbie, "Electrical Resistance of Long Conjugated Molecular Wires," *Science*, vol. 320, p. 1482, 2008.

[25] E. a. Weiss, M. R. Wasielewski, and M. a. Ratner, "Molecules as wires: molecule-assisted movement of charge and energy.," *Topics in current chemistry*, vol. 257, pp. 103–33, 2005.

[26] Q. Lu, K. Liu, H. Zhang, Z. Du, X. Wang, and F. Wang, "From Tunneling to Hopping : A Comprehensive Investigation of Charge Transport Mechanism in Molecular Junctions Based on Oligo(p-phenylene etlynylene)s," *ACS nano*, vol. 3, no. 12, pp. 3861–3868, 2009.

[27] E. A. Weiss, M. J. Ahrens, L. E. Sinks, A. V. Gusev, M. A. Ratner, and M. R. Wasielewski, "Making a Molecular Wire: Charge and Spin Transport through para-Phenylene Oligomers," *J. Am. Chem. Soc.*, vol. 126, pp. 5577–5584, 2004.

[28] N. Crivillers, C. Munuera, M. Mas-Torrent, C. Simão, S. T. Bromley, C. Ocal, C. Rovira, and J. Veciana, "Dramatic Influence of the Electronic Structure on the Conductivity through Open- and Closed-Shell Molecules," *Advanced Materials*, vol. 21, no. 10-11, pp. 1177–1181, 2009.

[29] N. Crivillers, M. Paradinas, M. Mas-Torrent, S. T. Bromley, C. Rovira, C. Ocal, and J. Veciana, "Negative differential resistance (NDR) in similar molecules with distinct redox behaviour.," *Chemical communications*, vol. 47, no. 16, pp. 4664–6, 2011.

[30] C. Krzeminski, C. Delerue, G. Allan, D. Vuillaume, and R. Metzger, "Theory of electrical rectification in a molecular monolayer," *Physical Review B*, vol. 64, no. 8, p. 085405, 2001.

[31] L. Venkataraman, J. E. Klare, C. Nuckolls, M. S. Hybertsen, and M. L. Steigerwald, "Dependence of single-molecule junction conductance on molecular conformation.," *Nature*, vol. 442, no. 7105, pp. 904–7, 2006.

[32] Q. Li, G. Mathur, M. Homsi, S. Surthi, V. Misra, V. Malinovskii, K.-H. Schweikart, L. Yu, J. S. Lindsey, Z. Liu, R. B. Dabke, A. Yasseri, D. F. Bocian,

and W. G. Kuhr, "Capacitance and conductance characterization of ferrocene-containing self-assembled monolayers on silicon surfaces for memory applications," *Applied Physics Letters*, vol. 81, no. 8, p. 1494, 2002.

[33] C. Simao, M. Mas-Torrent, N. Crivillers, V. Lloveras, J. M. Artés, P. Gorostiza, J. Veciana, and C. Rovira, "A robust molecular platform for non-volatile memory devices with optical and magnetic responses," *Nature chemistry*, vol. 3, pp. 359–364, 2011.

[34] I. W. Lyo and P. Avouris, "Negative differential resistance on the atomic scale: implications for atomic scale devices.," *Science*, vol. 245, no. 4924, pp. 1369–71, 1989.

[35] A. K. Chauhan, D. K. Aswal, S. P. Koiry, N. Padma, V. Saxena, S. K. Gupta, and J. V. Yakhmi, "Resistive memory effect in self-assembled 3-aminopropyltrimethoxysilane molecular multilayers," *Physica Status Solidi (a)*, vol. 205, no. 2, pp. 373–377, 2008.

[36] C. a. Nijhuis, W. F. Reus, and G. M. Whitesides, "Molecular rectification in metal-SAM-metal oxide-metal junctions.," *Journal of the American Chemical Society*, vol. 131, no. 49, pp. 17814–27, 2009.

[37] C. a. Nijhuis, W. F. Reus, and G. M. Whitesides, "Mechanism of rectification in tunneling junctions based on molecules with asymmetric potential drops.," *Journal of the American Chemical Society*, vol. 132, no. 51, pp. 18386–401, 2010.

[38] G. E. Poirier, "Characterization of Organosulfur Molecular Monolayers on Au(111) using Scanning Tunneling Microscopy.," *Chemical reviews*, vol. 97, no. 4, pp. 1117–1128, 1997.

[39] R. M. Metzger, "Electrical Rectification by a Molecule: The Advent of Unimolecular Electronic Devices," *Accounts of Chemical Research*, vol. 32, pp. 950–957, 1999.

[40] R. M. Metzger, "Unimolecular electrical rectifiers.," *Chemical reviews*, vol. 103, no. 9, pp. 3803–34, 2003.

[41] M. R. Lorenz, J. F. Woods, and R. J. Gambino, “Some electrical properties of the semiconductor B-Ga2O3,” *Journal of Physics and Chemistry of Solids*, vol. 28, pp. 403–404, 1967.

"Courage is not living without fear. Courage is being scared to death and doing the right thing anyway"

Chae Richardson

7

Experimental Section

In this chapter will be described in detail the experimental procedures used for both, synthesis of organic compounds and preparation of self-assembled monolayers. It will be divided in four main parts that cover: *i)* reagents, solvents and materials specifications; *ii)* analytic and surface techniques used to characterize the organic compounds and the SAMs, respectively; *iii)* synthetic procedures followed to obtain the different organic compounds used along this Thesis; and *iv)* methodologies used for SAMs preparation.

7.1 Reagents, solvents and materials

7.1.1 General reagents and solvents

The reagents and solvents employed for the synthesis of organic compounds were of synthesis grade, belonging to different chemical companies such as: *Sigma-Aldrich, Fluka, SDS S.A. and Merck.* The solvents used in optical spectroscopy, cyclic voltammetry experiments and surface chemistry were HPLC grade provided by *ROMIL–SpS* (Super Purity Solvent). The toluene of HPLC grade used for preparation of self-assembled monolayers was distilled under nitrogen using metallic

sodium as dehydrating agent.

7.1.2 Substrates and materials for the SAMs preparation

Au (111) surfaces were purchased from *Georg Albert* PVD–Beschichtungen (University of Heidelberg in Germany) with the follow characteristics: epitaxial gold on mica, size 25x25 mm^2 with 300 nm thickness (111)-layer of gold. These substrates were cut according to the necessity.

Bionano borosilicate glass slides (75 x 25 x 1.1 mm) with 50 nm gold thickness over a titanium adhesion layer were obtained from *Phasis* (Switzerland). To perform cyclic voltammetry experiments, specific sizes of these substrates were required that were laser-cut in Centro Nacional de Microelectrónica (CNM–CSIC) facilities into 2.5 x 0.5 cm pieces.

When specific conditions (gold thickness, dimensions, opacity, etc) were required; gold was evaporated on pieces of microscope glass. To prepare the substrates used for synchrotron experiments, small pieces of silicon test wafers with N/phosporus dopant and a resistivity of 2-5 Ohm.cm were employed. Gold was evaporated on both substrates using chromium as adhesion layer with an *Evaporation System Auto 306 from Boc Edwards* in the Nanoquim platform (Clean Room) at the Institut de Ciència de Materials de Barcelona (ICMAB–CSIC). Prior to evaporation, these substrates were hand-cut with a diamond-coated knife or in the Electron Microscopy Sample Preparation Service at Institut Catalá de Nanociència i Nanotecnologia (ICN2) into pieces with the required dimensions.

7.2 Instrumentation and Techniques

7.2.1 Analytic Techniques for the characterization of the organic compounds

Infrared spectroscopy (IR):

The IR spectra were performed on a Perkin Elmer Spectrum One Fourier Transform spectrometer using the attenuated total reflection (ATR) mode. In the spectra

collected the following abbreviations: weak band (w), medium band (m) and sharp band (s), were used to define the intensity of the peaks.

Nuclear Magnetic Resonance spectroscopy (NMR):

The NMR spectra were recorded at the Servei de Ressonància Magnètica Nuclear of Universitat Autònoma de Barcelona; using a Bruker Avance spectrometer 250 MHz. The solvent employed ($CDCl_3$ or $(CD_3)_2SO$) was at the same time the internal reference.

Ultraviolet-Visible Near-Infrared absorption spectroscopy (UV-Vis-NIR):

The UV-Vis-NIR spectra were recorded on a Cary 5000E Varian spectrometer.

Electron Paramagnetic Resonance spectroscopy (EPR):

The EPR spectra were collected by Dr. Vega Lloveras (ICMAB-CSIC) on a Bruker ESP 300E spectrometer operating in the X-band (9.5 GHz) with a T102 rectangular cavity.

Matrix-Assisted Laser Desorption Ionization Time-of-Flight mass spectrometry (MALDI/LDI TOF-MS):

The spectra were performed by Amable Bernabé on a Bruker Ultraflex LDI-TOF mass spectrometer operating with pulsed extraction of ions in positive or negative mode at high power.

Chromatography:

- **Thin layer chromatography (TLC)**: Both, the progress of the reactions and the chromatographic columns were controlled by means of aluminum sheets covered with silica gel 60 F_{254} provided by Merck. All aluminum sheets were revealed under an ultraviolet lamp ($\lambda = 254nm$).

- **Column chromatography**: Silica gel 60 A. C. C. with grain sizes between 35-70 μm was used to prepare column chromatography.

7.2.2 Surface Techniques for the characterization of the SAMs

Polarization modulation-infrared reflection-adsorption spectroscopy (PM-IRRAS):

PM-IRRAS measurements were performed at Nanostructuration Platfom of Institut de Ciència de Materials de Barcelona on a IR-spectrometer Vertex 70 from Bruker equiped with MTC and TGS detectors as well as with the PMA 50 accessory. All spectra were recorded at an incident angle of 80°.

X-ray Photoelectron spectroscopy (XPS):

XPS measurements were performed by Dr. Daniel Gamarra at the Servicios de Análisis y Caracterización de Sólidos y Superficies de los Servicios de Apoyo a la Investigación de la Universidad de Extremadura in a Thermo Scientific K-Alpha X-ray photoelectron spectrometer system with a monochromatic source (Al Kα line of 1486.68 eV energy). The radiation was perpendicular to the sample (90°) with a spot size of 30-400 μm in ellipsoidal arrangement. Voltage 12 KV. The properties of the depth profile source were: Ar^+ bombardment ion source (1, 2 or 3 KeV of energy) located at an angle of 30 degrees to the horizontal sample. Compensation device charging via ultra low energy flood gun. To recollect the high resolution spectra, it was used a pass energy of 50 eV, a dwell time of 50 ms, an energy step size of 0.1 eV and several scans were accumulated to obtain a better resolution (100 scan for C1s, O1s and Cl2p; 200 scans for S2p and Fe2p).

Time of Flight - Secondary Ion Mass spectroscopy (TOF-SIMs):

TOF-SIMs measurements of SAMs were recorded by Dr. Daniel Gamarra at the Servicios de Análisis y Caracterización de Sólidos y Superficies de los Servicios de Apoyo a la Investigación de la Universidad de Extremadura using a TOF-SIMS[5] (Time of Flight Secondary Ions Mass sppectrometer). The primary gun was bombardment with Bi ions with the following intensities: 1.2 pA (Bi^+), 0.3 pA (Bi_3^+, 0.2 pA (Bi_3^{++}). The primary gun energy was 25 KV, the extractor energy 8.5 KV, the current of emission 1.05 μA. The mass spectra were obtained with a spot size

of 200x200 μm, with a resolution of 128x128 pixel.

Electrochemical experiments (Cyclic voltammetry):

Cyclic voltammograms were collected on a potentiostat-galvanostat VersaSTAT from Princeton Applied Research and also in a 20V/400 mA potentiostat/galvanostat Autolab/PGSTAT204 from Metrohm; using a standard cell with three-electrodes setup. To characterize electroactive compounds in solution, the working and counter electrodes used were platinum wires while a silver wire was used as pseudo-reference electrode. The solvent used to prepare the electrolyte solution was dichloromethane HPLC grade.
However for surface electrochemistry, the gold functionalized surfaces were used as working electrode and acetonitrile as solvent. 0.1 M solution of TBAHFP in the corresponding solvent was used as electrolite and prior to the measurements, the solution was degassed with argon.

Contact Angle (CA):

Contact angle measurements were performed to analyze the wettability of the modified surfaces. A 3 μL of Mili-Q water was dispensed on the surfaces with an automatic syringe and the contact angle was measured with the Contact Angle Measuring System DSA 100 from KRÜSS, in the Nanoquim platform at ICMAB.

Atomic Force Microscopy (AFM):

The AFM measurements were performed under ambient conditions using an Agilent 5500 LS AFM/SPM Stage Microscope and using an intermittent contact mode.

Kelvin Probe Force Microscopy (KPFM):

KPFM measurements were performed at room temperature using conductive probes (Pt/Cr-coated Si tips) mounted in cantilevers with nominal force constant of ~2.8 N/m. These measurements were performed under N_2 atmosphere (relative humidity <5%) to reduce relative room humidity impact.

Ultraviolet Photoelectron Spectroscopy (UPS):

UPS experiments were performed with a PHOIBOS 150 analyzer (SPECS GmbH, Berlin, Germany)) in ultra-high vacuum conditions (base pressure 1E-10mbar) and with monochromatic HeI UV source (21,2eV). Work function determination was done by applying bias of -10V at the sample.

Synchrotron Radiation:

The electronic characterization of the D−A systems bonded on gold surfaces was performed in two different synchrotron radiation facilities. In Elettra synchrotron, the measurements were performed at Materials Science Beamline (MSB) which is a versatile beamline that allows the tunability of the photon energy over a wide range (22 - 1000 eV) with mainly linearly polarized light from a bending magnet source. Measures of XPS, UPS, resonant photoemission (RPES) and NEXAFS spectroscopies were made with high energy resolution and tunable excitation energy for the best photoionization cross sections.

In ALBA, it was used the NAPP (near ambient pressure photoemission) end-station at CIRCE beamline which is a variable polarization soft X-ray beamline. Contrary to the MSB, the source for the CIRCE beamline is a pure permanent magnet APPLE II helical undulator, inserted in the center of the 9th medium straight section of the ALBA storage ring. This device is capable of delivering linearly polarized light in any direction, as well as circularly-polarized light (left- or right-handed).

Two important characteristics of the NAPP end-station were exploited. In one side, the possibility to record data acquisition while the samples are heat up to 120 °C by using a sample holder with an encapsulated filament. On the other hand, the possibility to operate at a sample pressure range from UHV up to 1 mbar thanks to a differential pumping system which ensures a pressure difference of 10E-9 between detector and sample. Through these modes, two different external stimuli were applying to the SAMs in order to induce the intramolecular electron transfer.

Conductivity Measurements:

The "EGaIn-setup" is a home-built set-up that uses the eutectic metal alloy EGaIn with its surface layer of predominantly Ga_2O_3 to contact SAMs electrically and to measure the J(V) characteristics at room temperature. The micromanipulator used as component of the EGaIn-setup has a low drift (1 nm/h) and can move the top-electrode with 10 nm precision in the z-direction, and over a distance of 10 cm in the xy-direction. To ensure good electrical contact, a copper wire is soldered to the micro-needle of the Hamilton syringe which is connected to the instruments with alligator clips. A gold probe tip held by a micro-positioner (Crest innovation, S-725PLM) penetrated the SAMs to form direct electrical contact with the substrate. The Ga2O3/EGaIn top-electrode is biased and grounded the substrate using a sub-femtoamp source meter (Keithly 6430) and shielded cables. To operate the source meter and to record I(V) curve, a code written in LabView 2011 is used. The whole setup is placed in Faraday cage placed on vibration isolation table (9101 Series Vibraplane Workstation) to minimize vibrations[1].

7.3 Theoretical calculations

DFT calculations for **1**, **1H** and ***5*** compounds were performed at their optimized geometry. The level of theory used was (U)CAM-B3LYP 6-31G*. From the output files, parameters like: molecular orbitals, eigenvalues and dipole moment were analyzed. For all calculation, the Gaussian09 software packages were used.
PM7 (RHF) calculation at optimized ground state (gs) (U)CAM-B3LYP/6-31G* level with modified dihedral angles were performed. Polarizability was determined considering the module of the dipole moment and applying the electric field along the perpendicular axis.

7.4 Synthesis and characterization of PTM derivatives

7.4.1 Synthesis of αH-tetradecachloro-4-methyltriphenyl methane (30)*

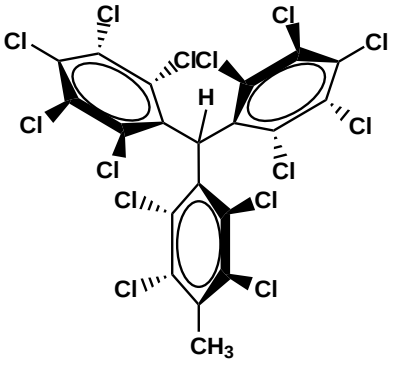

Procedure:

3.3 g (24.6 mmol) of aluminum chloride, 3.9 ml (48.2 mmol) of sulfur chloride, and 530 ml (6.6 mol) of sulfuryl chloride were suspended under an argon atmosphere, stirred, and refluxed. Then, 17.0 g (65.8 mmol) of 4-methyltriphenylmethane dissolved in 340 ml (4.2 mol) of sulfuryl chloride were added during a period of 2 hours, and the solution was refluxed for 10 hours. During this time, small quantities of sulfuryl chloride were added in order to keep the volume of the reaction constant. After that, the solution was concentrated by evaporation of half of the reaction volume and cooled down to r.t. A yellowish precipitate was formed when the mixture was poured over an ice bath (400 ml). The mixture was neutralized after the slow addition of sodium bicarbonate, obtaining a solid which was dissolved in chloroform and extracted with water. Finally, the organic phase was dried with magnesium sulfate, filtrated, and the solvent was evaporated under vacuum. The green solid produced was purified by a digestion with pentane and 33.4 g (69%) of the expected product were recovered.

Characterization: $C_{20}H_4Cl_{14}$ [740.59 g/mol]. **M.P.** (°C): 337-338 °C (lit. 336-339 °C). **^{1}H-RMN** (250MHz, $CDCl_3$, δ(ppm)): 6.99 (s, 1H, CH); 2.63 (s, 3H, CH_3). **FT-IR** (KBr, ν(cm^{-1})): 2927 (w), 1530 (w), 1439 (w), 1396 (w), 1367 (s), 1340 (s), 1321 (s), 1296 (s), 1240 (m), 1209 (w), 1191 (w), 1134 (s), 1119 (m), 1024 (m), 947 (w), 923 (w), 863 (w), 846 (m), 807 (s), 758 (w), 727 (w), 712 (m), 686 (s), 663 (s). **LDI-TOF** (negative mode, m/z): 738 $[M-2]^-$, 668 $[M-70]^-$.

*Synthesized by Dr. Judit Guasch.

7.4.2 Synthesis of αH-4-(bromomethyl)tetradecachloro-triphenylmethane (31)[2]

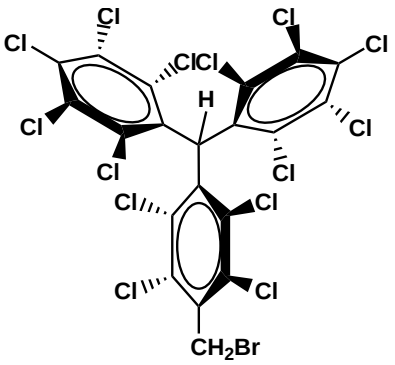

Procedure:

15.9 g (21.4 mmol) of αH-tetradecachloro-4-methyltriphenylmethane (**30**) were put into a three neck round flask and dissolved in 700 ml of anhydrous carbon tetrachloride (CCl_4) by constant stirring under argon atmosphere. Then, the solution was heated up to reflux with a white lamp and after 15 minutes, 10 ml (194.2 mmol) of bromine were added. The mixture was refluxed for 6 hours under a slow, steady argon stream. The unreacted bromine was pushed out bubbling the argon inside the reaction to three traps connected in series to the reaction flask. The first trap was empty, the second one contained a solution of sodium bisulfite and the third one with sodium bicarbonate in order to neutralize the rests of halogen. Since the reaction was not completed, a small amount of N-bromosuccinimide (99%) was added and the mixture was refluxed for 2.5 hours more. The reaction was cooled down to room temperature under inert conditions. The mixture was transferred to an Erlenmeyer flask and put into an ice bath, then 400 ml of sodium bisulfide solution (≈ 40 %) were added slowly while the solution was stirred until the observation of no rests of bromine. If the solution does not change its color from red to greenish yellow, a small amount of water (55 ml) can be added to facilitate the process. The pH of the solution was adjusted to ≈ 6 by adding slowly 26 g of sodium carbonate anhydrous. The organic phase was extracted with dichloromethane (CH_2Cl_2), dried with anhydrous magnesium sulfate ($MgSO_4$). After filtering it, the solvent was evaporated under vacuum and finally a dark beige solid was obtained which was purified by digestion with pentane. 12.9 g (74 %) of the final product were obtained.

Characterization: $C_{20}H_3BrCl_{14}$ [819.48 g/mol]. **^{1}H-RMN** (250MHz, $CDCl_3$, δ(ppm)): 7.00 (s, 1H, CH); 4.81 (s, 2H, CH_2Br). **FT-IR** (ATR, ν(cm^{-1})): 2953 (w), 2923 (w), 2853 (w), 1533 (w), 1463 (w), 1434 (w), 1368 (s), 1335 (s), 1298 (s), 1241 (m), 1217 (s), 1190 (w), 1138 (s), 1017 (w), 995 (w), 946 (w), 928 (w), 888 (m), 865 (w), 851 (w), 807 (s), 760 (w), 733 (w), 717 (m), 696 (w), 674 (s).

7.4.3 Synthesis of diethyl 4-[bis(2,3,4,5,6-pentachlorophenyl) methyl]-2,3,5,6-tetrachlorobenzyl phosphonate (20)[3]

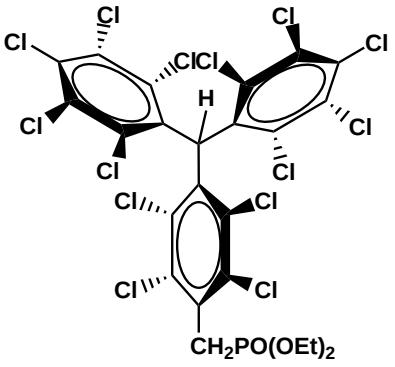

Procedure:

12.9 g (15.8 mmol) of αH-4-(bromomethyl)tetradecachlorotriphenylmethane (**31**) were dissolved in 27.0 ml (157.9 mmol) of triethyl phosphite ($P(OEt)_3$). The solution was refluxed at 150 °C for 3.5 hours. Then, 163 ml of Mili-Q water were added slowly and the mixture was refluxed for 40 minutes more. After that, the mixture was cooled down to room temperature and the oily precipitated was extracted with chloroform ($CHCl_3$). The organic phase was washed with Mili-Q water and dried with anhydrous magnesium sulfate ($MgSO_4$). The solvent was evaporated after filtering the solution. The oily product was precipitated with pentane overnight and purified by column chromatography of silica gel using mixtures of hexane/ethyl acetate as eluent. The oily purified product was precipitated with pentane overnight and the solvent evaporated under vacuum obtaining 9.49 g (68 %) of the desired product.

Characterization: $C_{24}H_{13}Cl_{14}O_3P$ [876.67 g/mol]. **^{1}H-RMN** (250MHz, $CDCl_3$, δ(ppm)): 7.00 (s, 1H, CH); 4.11 (q, 4H, CH_2, J=7.10 Hz); 3.81 (d, CH_2, CH, J=22.47 Hz); 1.29 (t, 6H, CH_3, J=7.07 Hz). **FT-IR** (ATR, ν(cm^{-1})): 2982 (w), 2936 (w), 2905 (w), 2867 (w), 1534 (w), 1479 (w), 1441 (w), 1415 (w), 1391 (w), 1365 (m), 1340 (m), 1294 (m), 1254 (s), 1161 (w), 1135 (m), 1099 (w), 1053 (m), 1020 (s), 972 (s), 856 (s), 806 (s), 784 (m), 739 (w), 707 (w), 688 (w), 668 (s). **LDI-TOF** (negative mode, m/z): 876.5 $[M]^-$, 806.8 $[M-70]^-$.

7.5 Synthesis and characterization of non-methylated Fc–PTM derivatives

7.5.1 Synthesis of (*E*)-4-ferrocenylvinylene-2,3,5,6-(tetrachlorophenyl)bis(pentachlorophenyl) methane (2H)

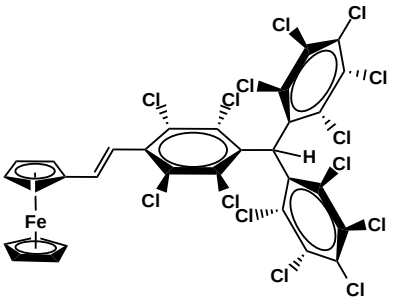

Procedure:

409.5 mg (467.1 μmol) of the protonated phosphonate PTM derivative (**20**) were put into a schlenk and dissolved in 60 ml of anhydrous tetrahydroduran (THF) under inert conditions. The solution was cooled down to −78 °C using an acetone/liquid nitrogen bath for 30 minutes and then 105.3 mg (0.94 mmols) of potassium *tert*-butoxide were added. The solution was stirred for 30 minutes maintaining the temperature at −78 °C to form an orange ylide. After that, the mixture was heat up to 0 °C by changing the dewar recipient for an ice bath which is maintained for 10 minutes at such temperature. The ice bath was removed and 100.3 mg (468.7 μmol) of ferrocenecarboxaldehyde were added. The mixture was left at continuous stirring and at room temperature for 66 hours under argon atmosphere. After that, the mixture was acidified with 5 ml of a 0.8 M solution of hydrochloric acid (HCl) and maintained stirring for 15 minutes. The organic phase was extracted with 2 portions of 20 ml of chloroform ($CHCl_3$), washed with Mili-Q water (3 x 10 ml), dried with anhydrous magnesium sulfate ($MgSO_4$) and filtered. The solvent was evaporated under vacuum and the product was purified by column chromatography of silica gel using as eluent a mixture of hexane/$CHCl_3$ (3:1). Finally, 322.8 mg (74 %) of the final product **2H** were obtained.

Characterization: $C_{31}H_{12}Cl_{14}Fe$ [936.61 g/mol]. **^{1}H-RMN** (250MHz, $CDCl_3$, δ(ppm)): 7.0 (s, 1H, CH); 6.92 (d, 1H, CH=CH, J = 16.23 Hz); 6.66 (d, 1H, CH=CH, J = 16.23 Hz); 4.51 (s, 2H, C_5H_4); 4.36 (s, 2H, C_5H_4); 4.20 (s, 5H, C_5H_4). **FT-IR** (KBr, ν(cm^{-1})): 2925 (m), 2851 (m), 1631 (m), 1534 (w), 1458 (w), 1362 (s), 1336 (s), 1297 (s), 1240 (m), 1187 (w), 1136 (m), 1106 (m), 1043 (w), 1027 (w), 1001 (m), 957 (m), 931 (w), 863 (w), 807 (s), 714 (w), 686 (m). **LDI-TOF** (positive mode, m/z): 935 $[M]^+$, 901 $[M-34]^+$, 865 $[M-70]^+$.

7.5.2 Synthesis of (*E*)-4-ferrocenylvinylene-2,3,5,6-(tetrachlorophenyl)bis(pentachlorophenyl) methyl radical (2)

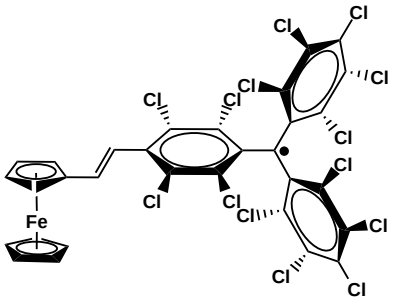

Procedure:

193.4 mg (206.5 μmol) of **2H** were dissolved in 20 ml of anhydrous dichloromethane previously passed through activated alumina in order to deactivate the acidic points of the solvent. Working under inert conditions (argon atmosphere), 120 μl (247.8 μmol) of tetrabutylammonium hydroxide solution dissolved in 0.5 ml of CH_2Cl_2 were added. The mixture was stirred at room temperature for 5 h and 25 minutes to form the anion derivative. Then, 45.3 mg (266.5 μmol) of silver nitrate previously dissolved in 0.5 ml of acetonitrile were added. The formation of the radical was followed by UV-Vis and after 45 minutes, the mixture was immediately filtered though a flash silica column using dichloromethane as solvent. The solvent was evaporated and 193.18 mg (72 %) of the desired product was obtained after purification by column chromatography of silica gel using a mixture of hexane/CH_2Cl_2 (1:1) as eluent.

Characterization: $C_{31}H_{11}Cl_{14}Fe^{\bullet}$ [935.61 g/mol]. **FT-IR** (KBr, ν(cm^{-1})): 2924 (m), 2853 (m), 1628 (m), 1512 (m), 1464 (w), 1362 (s), 1335 (s), 1300 (s), 1260 (s), 1187 (w), 1137 (m), 1107 (m), 1044 (w), 1028 (w), 1001 (w), 958 (m), 933 (w), 865 (w), 810 (s), 734 (m), 712 (m), 694 (m). **LDI-TOF** (positive mode, m/z): 935 $[M]^+$, 864 $[M-71]^+$.

7.5.3 Synthesis of (*E*)-4-[2-(1′-formyl-ferrocen)ethen-1-yl]-2,3,5,6-(tetrachlorophenyl)bis(pentachlorophenyl) methane (4H)

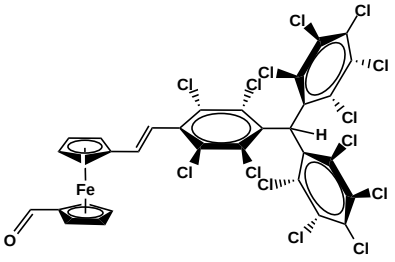

Procedure:

419.4 mg (876.9 μmol) of protonated phosphonate PTM derivative (**20**) were put into a schlenk and dissolved in 80 ml of anhydrous tetrahydroduran (THF) under inert conditions. The solution was cooling down to −78 °C using an acetone/liquid nitrogen bath for 25 minutes and then 128.7 mg (1.2 mmol) of potassium *tert*-butoxide were added. The solution was stirred for 25 minutes maintaining the temperature (−78 °C) to form an orange ylide. After that, the mixture was heat up to 0 °C by changing the dewar recipient for an ice bath and maintained for 10 minutes at such temperature. The ice bath was removed and 128.7 mg (531.7 μmol) of 1,1′-Ferrocenedicarboxaldehyde were added. The mixture was left at continuous stirring and at room temperature for 66 hours under argon atmosphere. After that, the mixture was acidified with 15 ml of a 0.8 M solution of hydrochloric acid (HCl) and maintained stirring for 15 minutes. The organic phase was extracted with 3 portions of 20 ml of chloroform ($CHCl_3$), washed with Mili-Q water (3 x 20 ml), dried with anhydrous magnesium sulfate ($MgSO_4$) and filtered. The solvent was evaporated under vacuum and the product was purified by column chromatography of silica gel using as eluent a mixture of hexane/$CHCl_3$ (2:1) and after that only with $CHCl_3$. Finally, 289.7 mg (63 %) of the final product (**4H**) were obtained.

Characterization: $C_{32}H_{12}Cl_{14}FeO$ [964.62 g/mol]. **^{1}H-RMN** (250MHz, $CDCl_3$, δ(ppm)): 10.0 (s, 1H, CHO); 7.01 (s, 1H, CH); 6.85 (d, 1H, CH=CH, J = 16.54 Hz); 6.73 (d, 1H, CH=CH, J = 16.54 Hz); 4.82 (s, 2H, Fc); 4.65 (d, 4H, J = 16.58 Hz, Fc); 4.48 (s, 2H, Fc). **FT-IR** (KBr, ν(cm^{-1})): 2922 (s), 2852 (m), 1728 (w), 1682 (s), 1635 (m), 1533 (w), 1455 (m), 1366 (s), 1336 (s), 1299 (s), 1276 (m), 1242 (s), 1189 (w), 1136 (m), 1032 (m), 961 (m), 931 (w), 864 (w), 831 (m), 808 (s), 778 (w), 742 (m), 715 (w), 687 (m). **LDI-TOF** (positive mode, m/z): 964.2 $[M]^+$.

7.5.4 Synthesis of (*E*)-4-[2-(1′-formyl-ferrocen)ethen-1-yl]-2,3,5,6-(tetrachlorophenyl)bis(pentachlorophenyl) methyl radical (4)

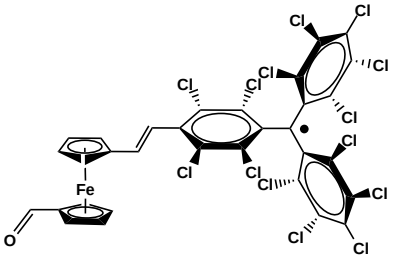

Procedure:

100 mg (103.6 μmol) of **4H** were dissolved in 60 ml of dry CH_2Cl_2 under inert conditions. Then 58 mg (219.6 μmol) of crown ether (18-C-6) and 120 mg (2138.8 μmol) of potassium hydroxide (KOH) were added to the solution. The mixture was maintained stirring for 24 hours in absence of light. After controlling by UV-Vis the total formation of the anion derivative, the mixture was immediately filtrated under vacuum and the solvent was evaporated. Then, few ml of hexane were added and the solvent was evaporated obtaining 112 mg (85%) of the anion derivative **4a**. This compound was used only as an intermediary reaction. To prepare radical **4**, 212 mg (167.31 μmol) of the anion derivative **4a** were dissolved under inert conditions (in absent of light) in 60 ml of dry CH_2Cl_2 previously passed through alumina in order to deactivated the acidic points of the solvent. Then, 40 mg (235.4 μmol) of silver nitrate were added. The mixture was stirred for 30 minutes and after that it was immediately filtrated and washed with a potassium hydroxide (KOH) solution to remove any residue of crown ether. The solvent was evaporated under vacuum and the product was purified by column chromatography of silica gel using CH_2Cl_2 as eluent obtaining 117.7 mg (73%) of the final product **4**.

Characterization: $C_{32}H_{11}Cl_{14}FeO^{\bullet}$ [963.62 g/mol]. **FT-IR** (KBr, ν(cm^{-1})): 2955 (m), 2924 (m), 2855 (m), 1683 (s), 1665 (m), 1627 (m), 1509 (w), 1455 (m), 1367 (m), 1335 (s), 1319 (s), 1260 (s), 1244 (s), 1188 (w), 1157 (w), 1138 (w), 1120 (w), 1043 (m), 1033 (m), 989 (w), 959 (m), 945 (m), 934 (m), 867 (w), 831 (m), 814 (s), 782 (w), 736 (s), 710 (m), 698 (m), 673 (w). **LDI-TOF** (positive mode, m/z): 964.5 $[M]^+$, 893.5 $[M-71]^+$.

7.5.5 Synthesis of (*E*)-4-[2-(1-metoxi-ferrocen)ethen-1-yl]-2,3,5,6-(tetrachlorophenyl)bis(pentachlorophenyl) methane (7H)

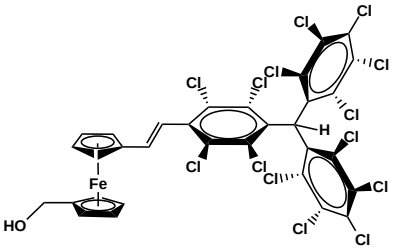

Procedure:

355 mg (368 μmol) of **4H** were dissolved in 12 ml of a mixture of anhydrous dichloromethane/ethanol (1:1) under inert conditions. The solution was cooled down to −78 °C using an acetone/liquid nitrogen bath for 25 minutes. After that, 14.13 mg (373.5 μmol) of sodium borohydride previously dissolved in 2 ml of a mixture (1:1) of anhydrous dichloromethane/ethanol and cooled, were added. The mixture was stirred and maintained at −78 °C for 30 minutes. Then the mixture was heated up to 0 °C for 30 minutes, changing the acetone/nitrogen bath for an ice bath. After that, the ice bath was removed and the reaction was stirred at room temperature for 2 hours and 40 minutes. The mixture was cooled again to 0 °C during 10 minutes and then acidified with 185 μL of a 2 M solution of hydrochloric acid (HCl) and maintained at 0 °C during 10 minutes more. The mixture was stirred for 15 minutes more at room temperature and immediately after it was filtered. The mixture was washed with distillated water (3 x 6 ml) and the organic phase was extracted with dichloromethane, dried with anhydrous magnesium sulfate ($MgSO_4$), filtered and the solvent evaporated under vacuum. The product was purified by column chromatography of silica gel using a mixture of hexane/CH_2Cl_2/AcOEt (1:3:0,2) as eluent. Finally, 266 mg (75 %) of the pure product (**7H**) were obtained.

Characterization: $C_{32}H_{14}Cl_{14}FeO$ [966.54 g/mol]. **^{1}H-RMN** (250MHz, DMSO, δ(ppm)): 6.93 (s, 1H, CH); 6.95 (d, 1H, CH=CH, J = 16.46 Hz); 6.73 (d, 1H, CH=CH, J = 16.46 Hz); 4.79 (t, 1H, OH); 4.58 (t, 2H, C_5H_4); 4.38 (t, 2H, C_5H_4); 4.23 (d, 2H, CH_2); 4.17 (t, 2H, C_5H_4); 4.14 (t, 2H, C_5H_4). **FT-IR** (KBr, ν(cm^{-1})): 3380 (w), 2953 (w), 2924 (w), 2852 (w), 1631 (m), 1535 (w), 1464 (w), 1365 (s), 1336 (s), 1298 (s), 1275 (m), 1238 (m), 1187 (w), 1137 (m), 1043 (m), 997 (m), 959 (m), 930 (w), 863 (w), 827 (m), 808 (s), 779 (w), 715 (w), 687 (m). **LDI-TOF** (positive mode, m/z): 965.7 $[M]^+$, 948.7 $[M-17]^+$.

7.5.6 Synthesis of (*E*)-4-[2-(1'-metoxi-ferrocen)ethen-1-yl]-2,3,5,6-(tetrachlorophenyl)bis(pentachlorophenyl) methyl radical (7)

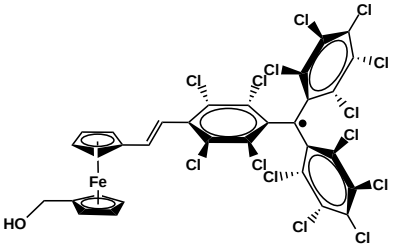

Procedure:

266 mg (275.2 μmol) of **7H** were dissolved in 15 ml of anhydrous dichloromethane previously passed through activated alumina in order to deactivate the acidic points of the solvent. Working under inert conditions (argon atmosphere), 200 μL (412.5 μmol) of tetrabutylammonium hydroxide solution dissolved in 0.5 ml of CH_2Cl_2 were added. The mixture was stirred at room temperature for 5 h and 20 minutes to form the anion derivative. Then, 87.5 mg (514.8 μmol) of silver nitrate previously dissolved in 0.5 ml of acetonitrile were added. The formation of the radical was followed by UV-Vis and after 50 minutes, the mixture was immediately filtered though a flash silica column using dichloromethane as solvent. The solvent was evaporated and 160 mg (60 %) of the desired product was obtained after purification by column chromatography of silica gel using a mixture of hexane/CH_2Cl_2/AcOEt (1:3:0,2) as eluent.

Characterization: $C_{32}H_{13}Cl_{14}FeO^{\bullet}$ [965.63 g/mol]. **FT-IR** (KBr, ν(cm^{-1})): 3373 (w), 2952 (w), 2925 (m), 2858 (w), 1660 (w), 1620 (m), 1510 (m), 1463 (w), 1334 (s), 1320 (s), 1259 (s), 1186 (w), 1156 (w), 1135 (w), 1119 (w), 1143 (m), 1026 (m), 960 (m), 946 (w), 932 (w), 865 (w), 816 (s), 765 (m), 734 (m), 710 (m), 699 (m). **LDI-TOF** (positive mode, m/z): 965.8 $[M]^+$, 948.8 $[M-17]^+$.

7.5.7 Synthesis of 5-(1,2-dithiolan-3-yl)pentanoate of (*E*)-4-[2-(1'-methyl-ferrocen)ethen-1-yl]-2,3,5,6-(tetrachlorophenyl)bis(pentachlorophenyl) methane (1-H)

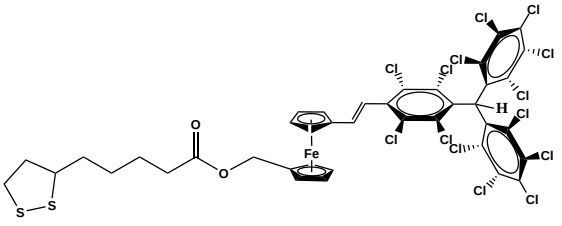

Procedure:

86 mg (88.9 μmol) of **7H** were dissolved in 10 ml of anhydrous dichloromethane under inert conditions. 23.1 mg (111.9 μmol) of (±)−α−Lipoic acid dissolved in 1 ml of anhydrous dichloromethane were added. The mixture was stirred and cooled to 0° for 15 minutes. At the same time 28 mg (135.7 μmol) of DCC and 3.5 mg (28.7 μmol) of DMAP each of one, previously dissolved in 1.5 ml of anhydrous dichloromethane were mixed in a small round flask and cooled to 0° for 15 minutes. After that, the second mixture was added in the first one and maintained at 0° for 15 minutes more. The ice bath was removed and the reaction was left at room temperature for 25 h. The mixture was washed with distilled water (3 x 10 ml), extracted with dichloromethane and dried with anhydrous magnesium sulfate ($MgSO_4$), filtered and the solvent evaporated under vacuum. The product was purified by a small-flash column chromatography of silica gel using a mixture of hexane/CH_2Cl_2/AcOEt (1:1:0,05) as eluent. Finally, 74.8 mg (73 %) of the pure product **1-H** were obtained.

Characterization: $C_{40}H_{26}Cl_{14}FeO_2S_2$ [1154.95 g/mol]. ^{1}**H-RMN** (250MHz, $CDCl_3$, δ(ppm)): 7.01 (s, 1H, CH); 6.90 (d, 1H, CH=CH, J = 16.33 Hz); 6.69 (d, 1H, CH=CH, J = 16.33 Hz); 4.90 (s, 2H, CH_2); 4.49 (s, 2H, C_5H_4); 4.36 (s, 2H, C_5H_4); 4.27 (s, 2H, C_5H_4); 4.22 (s, 2H, C_5H_4); 3.56 (t, 1H, CH, J = 7.41 Hz); 3.18 (q, 2H, CH_2, J = 7.19 Hz); 2.48 (m, 1H, CH_2, J = 6.26 Hz); 2.32 (t, 2H, CH_2, J = 7.52 Hz); 1.94 (m, 1H, CH_2, J = 6.74 Hz); 1.70 (m, 4H, CH_2, J = 7.6 Hz); 1.47 (m, 2H, CH_2, J = 7.7 Hz). **FT-IR** (KBr, ν(cm^{-1})): 2922 (s), 2854 (s), 1730 (s), 1631 (m), 1535 (w), 1458 (m), 1364 (s), 1336 (s), 1298 (s), 1274 (s), 1239 (s), 1163 (s), 1137 (s), 1084 (w), 1042 (m), 1027 (m), 987 (w), 957 (m), 928 (m), 863 (w), 827 (m), 807 (s), 714 (w), 686 (m). **LDI-TOF** (positive mode, m/z): 1153.8 $[M]^+$, 948.7 $[M-205.1]^+$.

7.5.8 Synthesis of 5-(1,2-dithiolan-3-yl)pentanoate of (*E*)-4-[2-(1'-methyl-ferrocen)ethen-1-yl]-2,3,5,6-(tetrachlorophenyl) bis(pentachlorophenyl) methyl radical (1)

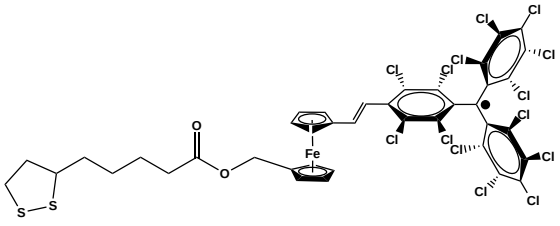

Procedure:

70 mg (72.5 μmol) of **7** were dissolved in 10 ml of anhydrous dichloromethane under inert conditions. 19.2 mg (93 μmol) of (±)−α−Lipoic acid dissolved in 1 ml of anhydrous dichloromethane were added. The mixture was stirred and cooled to 0° for 20 minutes. At the same time 22.9 mg (110.9 μmol) of DCC and 2.9 mg (23.9 μmol) of DMAP each of one, previously dissolved in 1 ml of anhydrous dichloromethane were mixed in a small round flask and cooled to 0° for 20 minutes. After that, the second mixture was added in the first one and maintained at 0° for 25 minutes more. The ice bath was removed and the reaction was left at room temperature for 31 h and 10 minutes. The mixture was washed with distilled water (3 x 7 ml), extracted with dichloromethane and dried with anhydrous magnesium sulfate ($MgSO_4$), filtered and the solvent evaporated under vacuum. The product was purified by a small-flash column chromatography of silica gel using a mixture of hexane/CH_2Cl_2/AcOEt (1:1:0,05) as eluent. Finally, 31.1 mg (37 %) of the pure product **1** were obtained.

Characterization: $C_{40}H_{25}Cl_{14}FeO_2S_2^{\bullet}$ [1153.94 g/mol]. **FT-IR** (KBr, ν(cm^{-1})): 2923 (m), 2853 (m), 2117 (w), 1729 (s), 1620 (m), 1510 (m), 1459 (m), 1365 (w), 1335 (s), 1319 (s), 1259 (s), 1157 (s), 1043 (m), 1028 (m), 987 (w), 958 (m), 946 (m), 932 (m), 865 (w), 814 (s), 734 (m), 710 (m), 672 (w). **LDI-TOF** (positive mode, m/z): 947.7 [M−206.2]$^+$.

7.5.9 Synthesis of (*NE,N'E*)-4,4⁰disulfanediyl bis(*N*-{1⁰2-4-[bis-(pentachlorophenyl)methyl]-2,3,5,6-tetrachlorophenylethen-1-yl-ferrocenylmethylene}aniline) (8H)

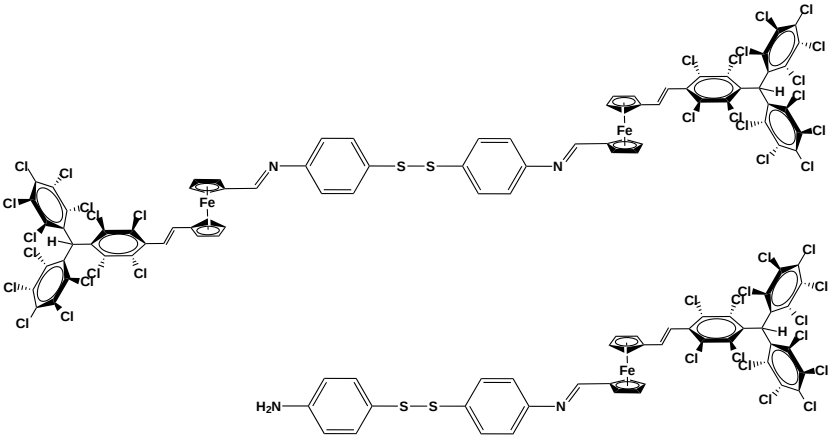

Procedure:

47.6 mg (49.3 μmol) of **4H** and 12.9 mg (103.6 μmol) of 4-aminothiophenol (4-ATP) were dissolved in 20 ml of anhydrous toluene into a round flask. A dean-stark system was mounted and the reaction was refluxed at 120 °C for 50 hours. After that, the solvent was evaporated under vacuum and a mixture of mono and bi-substituted molecules was obtained.

Characterization: $C_{76}H_{32}Cl_{28}Fe_2N_2S_2$ [2141.58 g/mol]. ^{1}H-RMN (250MHz, $CDCl_3$, δ(ppm)): 8.32 (s, 3H, CH=N); 7.18 (d, 12H, CH, J = 7.76 Hz); 7.07 (d, 6H, CH, J = 8.15 Hz); 7.00 (s, 3H, CH); 6.89 (d, 3H, CH=CH, J = 16.47 Hz); 6.70 (d, 3H, CH=CH, J = 16.47 Hz); 6.62 (d, 6H, CH, J = 8.43 Hz); 4.79 (s, 6H, C_5H_4); 4.53 (s, 12H, C_5H_4); 4.43 (s, 6H, C_5H_4); 3.79 (s, 6H, NH_2). **FT-IR** (KBr, ν(cm^{-1})): 2922 (m), 2852 (m), 1616 (s), 1593 (s), 1492 (s), 1462 (m), 1365 (m), 1337 (s), 1295 (s), 1216 (m), 1175 (m), 1137 (m), 1088 (w), 1042 (w), 860 (m), 820 (s), 808 (s), 759 (w), 728 (m), 714 (w), 694 (m). **LDI-TOF** (positive mode, m/z): 2141 $[M]^+$, 1193 $[M-948]^+$, 1069 $[M-1072]^+$.

7.6 Synthesis and characterization of octamethylated Fc–PTM derivatives

7.6.1 Synthesis of (*E*)-4-octamethylferrocenylvinylene-2,3,5,6-(tetrachlorophenyl)bis(pentachlorophenyl) methane (3-H)†

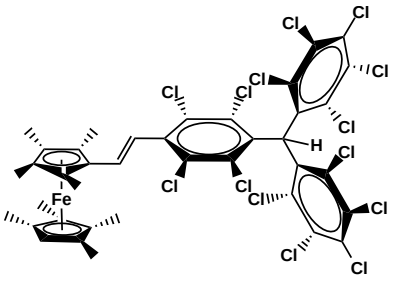

Procedure:

515.0 mg (587.5 μmol) of protonated phosphonate PTM derivative (**20**) were dissolved and stirred in 80 ml of anhydrous THF under an inert atmosphere of argon. Then, the reaction was cooled down to -78 °C using an acetone/$CO_{2(s)}$ bath and 156.8 mg (1397.0 μmol) of potassium *tert*-butoxide were added to form the ylide. The reaction was stirred and kept at -78 °C for 15 minutes. Then, the orange solution was heated up to 0 °C by changing the dewar recipient for an ice bath, and 210.8 mg (646.2 μmol) of 1-formyl-2,2′,3,3′,4,4′-octamethylferrocene were added. After reacting for 60 hours, the mixture was acidified with a 2M solution of hydrochloridric acid and extracted with 4 portions of 25 ml of chloroform. The orange phase was washed with water, dried with anhydrous magnesium sulfate, filtrated, and the solvent was evaporated under reduced pressure. Finally, the product was purified by column chromatography of silica gel using a mixture of hexane and diethyl ether as eluent (1:1). 511.3 mg (83%) of the final product **3-H** were obtained.

Characterization: $C_{39}H_{27}Cl_{14}Fe$ [1047.82 g/mol]. **^{1}H-RMN** (250MHz, $CDCl_3$, δ(ppm)): 7.03 (s, 1H, CH); 6.94 (d, 1H, CH=CH, J =16.38 Hz); 6.70 (d, 1H, CH=CH, J =16.38 Hz); 3.48 (s, 1H, CH); 1.93 (s, 6H, CH_3); 1.80 (s, 6H, CH_3); 1.66 (s, 12H, CH_3). **FT-IR** (KBr, ν(cm^{-1})): 2961 (m), 2914 (s), 2854 (s), 1728 (w), 1623 (s), 1538 (w), 1447 (w), 1420 (w), 1368 (s), 1335 (s), 1300 (s), 1272 (m), 1241 (m), 1214 (w), 1191 (w), 1187 (w), 1138 (m), 1116 (w), 1083 (w), 1027 (s), 971 (s), 937 (w), 923 (w), 871 (w), 843 (w), 807 (s), 748 (w), 714 (w), 685 (m). **LDI-TOF** (positive mode, m/z): 1047 $[M]^+$, 1014 $[M-33]^+$, 977 $[M-70]^+$.

†Synthesized by Dr. Judit Guasch

7.6.2 Synthesis of (*E*)-4-octamethylferrocenylvinylene-2,3,5,6-(tetrachlorophenyl)bis(pentachlorophenyl) methyl anion (3a)‡

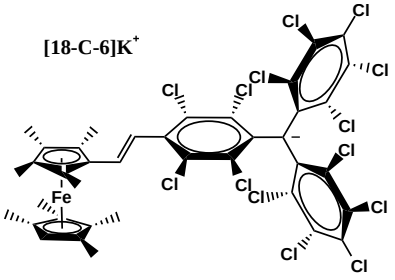

Procedure:

175.0 mg (166.9 μmol) of **3H**, 48.5 mg (183.5 μmol) of crown ether (18-C-6) and 156.8 mg (1817.7 μmol) of potassium hydroxide were dissolved and stirred in 80 ml of CH_2Cl_2 under an inert atmosphere of argon. After 24 hours, the unreacted potassium hydroxide was filtrated and the solvent evaporated under reduced pressure. The product was washed with cold hexane. Finally, 190.0 mg of product **3a** (84%) were obtained.

Characterization: $C_{51}H_{50}Cl_{14}FeKO_6$ [1350.22 g/mol (with 18-C-6)]. **FT-IR** (KBr, $\nu(cm^{-1})$): 2897 (m), 1597 (m), 1539 (w), 1503 (m), 1472 (m), 1453 (w), 1352 (s), 1284 (m), 1248 (m), 1205 (w), 1103 (s), 1027 (m), 960 (s), 867 (w), 835 (m), 806 (m), 721 (w), 687 (m), 662 (w). **LDI-TOF** (positive mode, m/z): 1048 $[M-302.2]^+$, 1014 $[M-336.2]^+$, 977 $[M-373.2]^+$, 942 $[M-408.2]^+$.

‡Synthesized by Dr. Judit Guasch

7.6.3 Synthesis of (*E*)-4-octamethylferrocenylvinylene-2,3,5,6-(tetrachlorophenyl)bis(pentachlorophenyl) methyl radical (3) [☒]

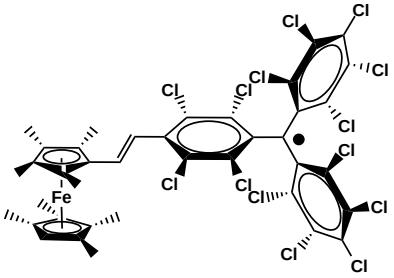

Procedure:

150.0 mg (111.0 μmol) of **3a** were dissolved in 85 ml of anhydrous CH_2Cl_2 (passed through activated alumina in order to deactivate the acidic points of the solvent) in strict inert conditions (series of vaccum/argon at -70 °C). Then, 21.6 mg (111.0 μmol) of silver tetrafluoroborate were added under vigorous stirring. In the next 30 minutes, the solution changed its color from purple to brown while a grey precipitate was formed (Ag^0). Finally, the solution was filtrated to eliminate the silver and was extracted with a solution of potassium hydroxide to eliminate the crown ether. Finally, the organic phase was dried and 214.0 mg (70%) of the dyad **3** were obtained.

Characterization: $C_{39}H_{26}Cl_{14}Fe^{\bullet}$ [1046.81 g/mol]. **FT-IR** (KBr, $\nu(cm^{-1})$): 2902 (m), 2865 (m), 1607 (m), 1536 (w), 1474 (m), 1416 (w), 1372 (w), 1351 (m), 1333 (s), 1287 (w), 1262 (m), 1135 (w), 1103 (s), 1025 (s), 962 (s), 873 (w), 838 (m), 808 (m), 734 (w), 712 (w), 690 (w), 666 (w). **LDI-TOF** (positive mode, m/z): 1047 $[M]^+$, 1014 $[M-33]^+$, 976 $[M-71]^+$.

[☒]Synthesized together with Dr. Judit Guasch

7.6.4 Synthesis of (*E*)-4-[2-(1-formyl-2,2-,3,3-,4,4-,5,5-octamethyl-ferrocen)ethen-1-yl]-2,3,5,6-tetrachlorophenyl-bis(2,3,4,5,6-pentachlorophenyl)methane (6H)[¶4]

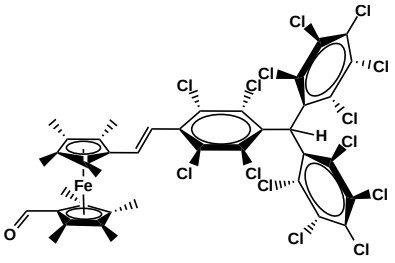

Procedure:

100 mg (0.89 mmol) of potassium *tert*-butoxide and 368 mg (0.42 mmol) 4-[bis(2,3,4,5,6-pentachlorophenyl)methyl]2,3,5,6-tetra-chlorobenzyl(triphenyl)phosphonium bromide were suspended in 8 ml of dry THF at −78 °C and stirred for 30 min. The cooling bath was removed and after 15 min the resulting orange ylide suspension was cooled again. Then, 100 mg (0.28 mmol) of 2,2-,3,3-,4,4-,5,5- octamethylferrocene-1,1-biscarbaldehyde dissolved in 2 ml of dry THF, were added slowly and the mixture was stirred for a further 72 hours at ambient temperature after which 5 ml of 2N HCl was added. The crude product was extracted with two portions of 50 ml of $CHCl_3$, the organic layer was washed three times with 50 ml of water, dried over Na_2SO_4 and evaporated under reduced pressure. Finally, chromatographic purification with silica and *n*-hexane/$CHCl_3$ (1:1) yielded 240 mg (75%) of the desired product **6H**.

Characterization: $C_{40}H_{28}Cl_{14}FeO$ [1075.83 g/mol]. **^{1}H-RMN** (250MHz, $CDCl_3$, δ(ppm)): 10.0 (1H, CHO); 7.0 (s, 1H, methine); 6.83 (d, 1H, J_{trans} = 16.9 Hz, vinyl); 6.65 (d, 1H, J_{trans} = 16.9 Hz, vinyl); 2.0, 1.9, 1.78, 1.75 (s, each 6H). **FT-IR** (KBr, ν(cm^{-1})): 2954 (m), 2907 (m), 2857 (m), 1729 (w), 1664 (s), 1629 (s), 1536 (w), 1448 (w), 1414 (m), 1370 (s), 1335 (s), 1298 (s), 1262 (s), 1212 (w), 1183 (w), 1136 (m), 1118 (m), 1075 (m), 1025 (s), 973 (s), 939 (w), 863 (m), 843 (w), 807 (s), 746 (w), 716 (m), 684 (s). **LDI-TOF** (negative mode, m/z): 1074 [M]$^-$, 1004 [M−70]$^-$.

[¶]Synthesized by Christian Sporer

7.6.5 Synthesis of (*E*)-4-[2-(1′-formyl-2′,2′′,3′,3′′,4′,4′′,5′,5′′-octamethyl-ferrocen)ethen-1-yl]-2,3,5,6-tetrachlorophenyl-bis(2,3,4,5,6-pentachlorophenyl)methyl radical (6)

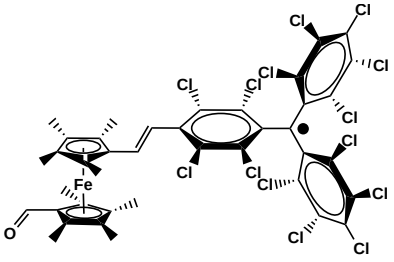

Procedure:

70 mg (65 μmol) of **6H** were dissolved in 12 ml of dry CH_2Cl_2 previously filtered through a column with basic alumina. Then, 31 μL (65 μmol) of tetrabutylammonium hydroxide solution ≈40% in water (TBAH) dissolved in 0.5 ml of dry CH_2Cl_2 were added. The solution was stirred for 6 hours under red light. After that, 15.4 mg 90.7 μmol) of silver nitrate ($AgNO_3$) dissolved in 0.5 ml of acetonitrile were added and the reaction was left for 1 hour and 15 minutes. The dark brown solution was filtered by a flash column to eliminate the rest of metallic silver and the solvent was evaporated under vacuum. 63 mg of pure radical **6** were obtained.

Characterization: $C_{40}H_{27}Cl_{14}FeO^{\bullet}$ [1075.82 g/mol]. **FT-IR** (KBr, ν(cm^{-1})): 2949 (m), 2910 (m), 2856 (m), 1664 (s), 1620 (m), 1511 (w), 1452 (w), 1412 (w), 1375 (s), 1333 (s), 1263 (s), 1104 (s), 1027 (s), 965 (s), 841 (m), 816 (m), 734 (m), 712 (m), 685 (m), 667 (m). **LDI-TOF** (negative mode, m/z): 1074 $[M]^-$, 1004 $[M-70]^-$.

7.7 Synthesis and characterization of Fc derivatives

7.7.1 Synthesis of ferrocenylmethyl 5-(1,2-dithiolan-3-yl) pentanoate (5)

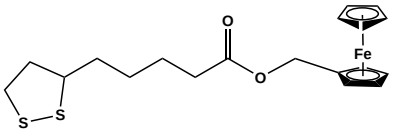

Procedure:

101.0 mg (467.5 μmol) of ferrocenemethanol were dissolved in 11 ml of anhydrous dichloromethane under inert conditions. 115.6 mg (560.3 μmols) of $(\pm)-\alpha-$Lipoic acid dissolved in 1 ml of anhydrous dichloromethane were added. The mixture was stirred and cooled to 0 °C for 25 minutes. At the same time 142.0 mg (688.2 μmols) of DCC and 15.3 mg (136.4 μmols) of DMAP each of one, previously dissolved in 1 ml of anhydrous dichloromethane were mixed in a small round flask and cooled to 0 °C for 25 minutes. After that, the second mixture was added in the first one and maintained at 0 °C for 20 minutes more. The ice bath was removed and the reaction was left at room temperature for 42 hours minutes. The mixture was washed with distilled water (3 x 5 ml), extracted with dichloromethane and dried with anhydrous magnesium sulfate ($MgSO_4$), filtered and the solvent evaporated under vacuum. The product was purified by a small-flash column chromatography of silica gel using a mixture of hexane/CH_2Cl_2/AcOEt (1:1:0,05) as eluent. Finally, 59 mg (31 %) of the pure product ***5*** were obtained.

Characterization: $C_{19}H_{24}FeO_2S_2$ [404.37 g/mol]. **^{1}H-RMN** (250MHz, $CDCl_3$, δ(ppm)): 4.89 (s, 2H, CH2); 4.27 (s, 4H, C_5H_4); 4.16 (s, 5H, C_5H_5); 3.59 (m, 1H, CH); 3.22 (m, 2H, CH_2); 2.50 (m, 1H, CH_2); 2.32 (t, 2H, CH_2, J = 7.11 Hz); 1.95 (m, 1H, CH_2); 1.71 (m, 4H, CH_2); 1.50 (m, 2H, CH_2). **FT-IR** (KBr, ν(cm^{-1})): 3092 (w), 2922 (m), 2865 (w), 1727 (s), 1445 (m), 1409 (m), 1377 (m), 1334 (m), 1236 (s), 1165 (s), 1103 (s), 1028 (s), 998 (s), 946 (m), 922 (m), 878 (w), 809 (s), 746 (s). **LDI-TOF** (positive mode, m/z): 404 $[M]^+$, 414 $[M+10]^+$.

7.8 Surfaces functionalization

7.8.1 Preparation of gold substrates

Glass slides were cut into small pieces (different sizes) according to the need in the Electron Microscopy Sample Preparation Service at Institut Catalá de Nanociència i Nanotecnologia (ICN2).

Clean procedure

Glass substrates were immersed in a solution of piranha for 1 hour. After that, they were removed and thoroughly washed with distillate water. Then they were washed with acetone and isopropanol, HPLC grade. Dried under a nitrogen current and placed in a glass support by using tape.
Silicon substrates were only washed with series of solvent (CH_2Cl_2, acetone, ethanol and isopropanol).

Evaporation conditions

Freshly cleaned glass and silicon substrates were loaded in the metal evaporator and 5 nm of Cr and 50 nm of Au were thermally evaporated.

7.8.2 Surface cleaning protocol

All the glass material used for SAMs preparation was cleaned in a Hellmanex II solution (1 % v/v in Mili-Q water), after 3 h the material was thoroughly washed with Mili-Q water and dried.
All gold substrates were first rinsed with different solvents of high purity grade (dichloromethane, acetone and ethanol) and sonicated in each one for 7 minutes, and dried under nitrogen stream. Then, the clean substrates were placed in a UV ozone chamber for 20 minutes to remove any organic dirt, afterwards they were immediately immersed in ethanol HPLC for a minimum period of 30 minutes. The substrates were rinsed with ethanol and isopropanol and dried under argon stream just before to be immersed in the solution of the desired D–A dyad to form the

corresponding SAM. The gold substrates on mica were not sonicated by follow the same procedure of cleaning.

7.8.3 Preparation of SAMs by the two-step approach

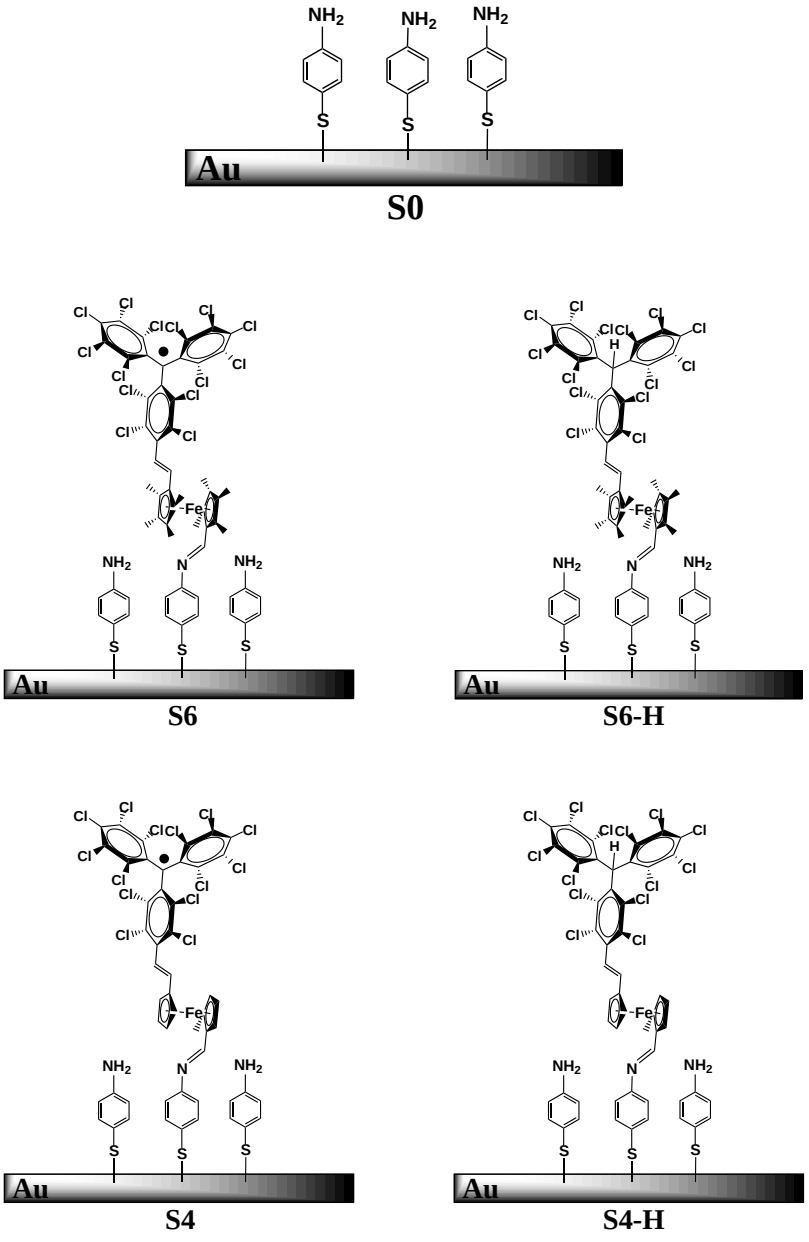

The functionalization of gold surfaces using the "two-step approach starts with the formation of the amino-terminated monolayer **S0**. To prepare **S0**, a freshly clean gold substrate was immersed in an ethanolic solution 10 mM of 4-aminothiophenol (4-ATP) molecules under an argon atmosphere. The gold substrate was left for

24 hours and then it was thoroughly rinsed with ethanol HPLC grade and dried under an nitrogen stream. **S0** was immediately immersed in a solution [1 mM] of the corresponding octamethylated or non-methylated Fc–PTM derivative (6 and 6H or 4 and 4H, respectively) under inert conditions. Two different solvent were used: dry toluene and trimethyl orthoformate (Tmof). The substrate was left for 24 and 48 hours under an argon atmosphere. Finally the new D–A SAMs (**S6**, **S6-H**, **S4** and **S4-H**) were rinsed with dry toluene or Tmof and dried under an argon stream. All the preparation process was made under red light conditions.

7.8.4 Preparation of SAMs by one-step approach

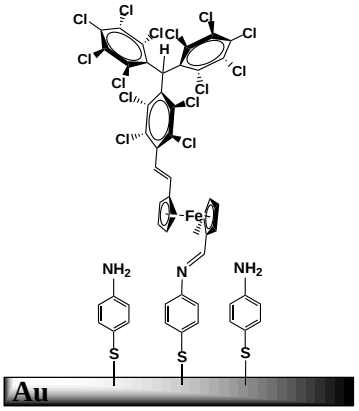

S8-H

S8-H SAM S8-H was prepared by immersion of a freshly cleaned gold substrate in a 1 mM solution of **8H** in toluene for 24 hours. After that the SAM was rinsed with dry toluene and dried under an argon current.

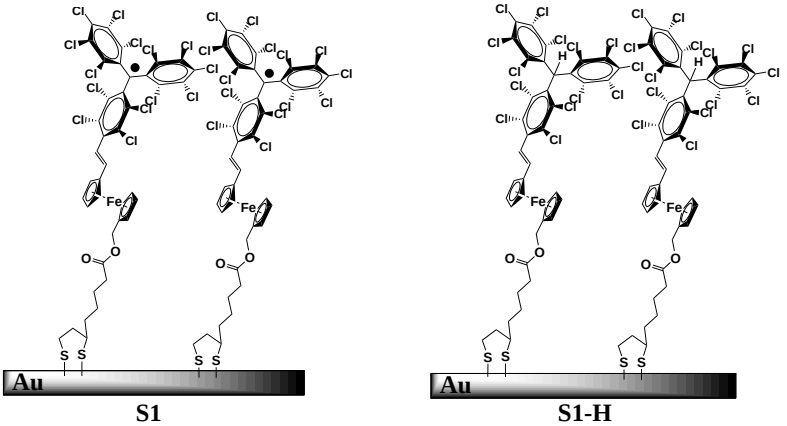

S1 **S1-H**

S1 and **S1-H** were prepared on Au substrates by immersion of the freshly cleaned substrates in a 1 mM solution of **1** and **1-H** dyads, respectively in absence of light and under argon atmosphere. The solvent used in both cases was freshly anhydrous toluene. The samples were maintained at 40 ° during the first hour and afterwards they were left at room temperature for 48 h. The functionalized gold substrates were rinsed thoroughly with anhydrous toluene in order to remove any physisorbed material and finally they were dried under argon stream.

Bibliography

[1] N. Nerngchamnong, L. Yuan, D.-C. Qi, J. Li, D. Thompson, and C. A. Nijhuis, "The role of van der Waals forces in the performance of molecular diodes.," *Nature nanotechnology*, vol. 8, no. 2, pp. 113–8, 2013.

[2] M. Ballester, J. Veciana, J. Riera, J. Castañer, R. Concepción, and O. Armet, "Inert Carbon Free Radicals. 7. "The (Kinetic) Reverse Effect" and Relevant Synthesis of New Monofunctionalized Triphenylmethyl Radicals and Their Nonradical Counterparts," *The Journal of organic chemistry*, vol. 51, pp. 2472–2480, 1986.

[3] C. Rovira, D. Ruiz-Molina, O. Elsner, J. Vidal-Gancedo, J. Bonvoisin, J. P. Launay, and J. Veciana, "Influence of topology on the long-range electron-transfer phenomenon.," *Chemistry - A European Journal*, vol. 7, no. 1, pp. 240–50, 2001.

[4] C. Sporer, I. Ratera, D. Ruiz-Molina, J. Vidal Gancedo, K. Wurst, P. Jaitner, C. Rovira, and J. Veciana, "Synthesis, X-ray structure, EPR and optical properties of a ferrocene substituted polychlorotriphenylmethyl radical," *Journal of Physics and Chemistry of Solids*, vol. 65, no. 4, pp. 753–758, 2004.

"Strength does not come from physical capacity. It comes from an indomitable will"

Mahatma Gandhi

8

Conclusions

This Thesis has been focused on the design, synthesis and nanostructuration of molecular materials based on donor–acceptor (D–A) open-shell systems.

The electronic bistability phenomena of the octamethylated Fc^8–PTM dyad **3** has been studied, demonstrating that in bulk, the proportion of the zwitterionic state is higher for this dyad in comparison with its analogous non-methylated Fc–PTM dyad **2**. The enhancement of the donor capability of the Fc unit based on the substitution of eight methyl groups was probed by the shift of its redox potential in comparison with the non-methylated system, as well as by the lower energy at which appeared the intramolecular electron transfer band in the UV-Vis-NIR spectrum. Interestingly, it was observed that in solution, playing with the polarity of different solvents we were able to stabilize one (neutral) or other (zwitterionic) stable electronic state of dyad **3**. It is noteworthy that using solvent of intermediate polarity it has been possible to observe the cohexistance of both electronic states, indicative of the true bistability of this system.

On the other hand, different derivatives based on the Fc–PTM dyad were used to prepare self-assembled monolayers (SAMs) on gold substrates using the bottom-up approach. SAMs prepared by means of the two-step strategy using an

imine condensation reaction were not stable to study their electronic properties neither to look for possible applications. However, SAMs prepared through the one-step strategy using Fc–PTM derivatives obtained from an esterification reaction were stable.

From the study of the electronic structure of SAMs **S1** was probed that once the molecules are bonded to the gold surface only the neutral state of the molecules is present. The no observation of bistability when passing from 3D (crystalline) to 2D structures (SAMs) was attributed to the loss of cooperative effect of intermolecular electrostatic interactions. Although dyad **1** is a good candidate to study the molecular switching induced by soft external stimuli like temperature and solvents, once it is nanostructured as an array of oriented dipoles on a surface we only observed a temperature induced and reversible partial charge transfer but not a true bistability with the complete electron transfer from the Fc to the PTM unit. In fact, when the Fc–PTM dyad **1** is nanostructured on a surface as a SAM (2D), the intermolecular electrostatic interactions are working against the intramolecular electron transfer (IET) that give place to the bistability phenomena observed in solid state (3D). To stabilize the bidimensional system it is required a reorganization of the energy levels of the system which take place against the D–A IET in order to get an electronically stable system. This is the reason why, in spite of the dipole moments of dyad **1** and **1H** no big modification of the work function of the gold was observed. This fact is also related to the high effect of depolarization and the reorganization of the energy levels that take place inside the bidimensional systems.

Finally, transport measurements of these SAMs in junctions of the type Au-SAM//Ga_2O_3/EGaIn show that SAM **S1** present high current density but does not show current rectification since the single unoccupied molecular orbital (SUMO) more localized on the PTM unit is participating in the charge transport at both bias applied (forward and reverse). Interestingly, the closed-shell SAM **S1-H** showed a high rectification ratio when −2.0 V (forward bias) were applied, which was attributed to the participation of the highest occupied molecular orbital (HOMO) localized over the Fc unit in the charge transport once the energy barrier imposed

by the lowest unoccupied molecular orbital (LUMO) is overcome at such voltage.

Generally, thanks to the possibility that offer molecular materials, through organic synthesis, to tune its molecular structure, in the framework of this Thesis it has been possible to study not only how the molecular structure influence the bistability phenomena but also how the dimensionality of the system influence their electronic properties. Such influences are important to be taken into account if we are interested to move forward towards applications using these kinds of systems. Moreover, the results obtained in this Thesis, contribute to the development of new molecules with interesting properties to be potentially used as active components in molecular electronics.

Appendices

A

Study of the degradation of organic molecules bonded to Au by synchrotron radiation

Since Fc–PTM D–A self-assembled monolayers contain carbon atoms with different binding energy due to their own chemical environment, this element was used to follow the degradation of the organic molecules bonded on gold substrates as effect of the synchrotron radiation. C1s high-resolution spectrum was taken at a photon energy of 500 eV. Different scans were measurements in the same point until to see any change as it is shown in Figure A.1.

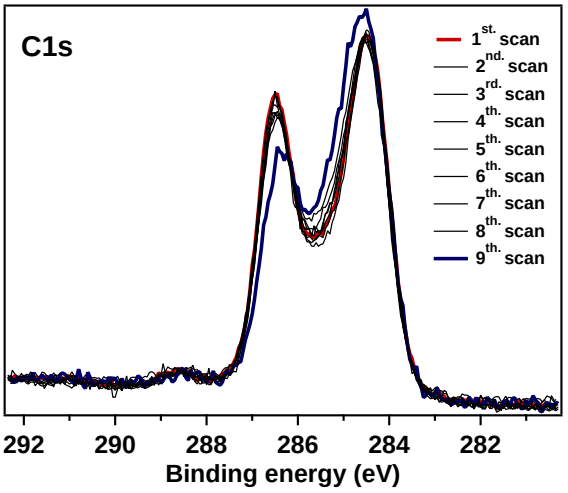

Figure A.1: High resolution photoemission spectra of C1s. Effect of the radiation.

It was observed that after 20 - 30 minutes of irradiation, the samples starts to show some degree of degradation. The peak observed at around 284.5 increase its intensity while the peak around 286.5 eV diminish it. Additionally, the separation between them decrease. After this observation, the sample was exposed for more time until to see a higher degree of degradation which clearly is observed in the blue line HR-PES spectrum of C1s showed in Figure A.2.

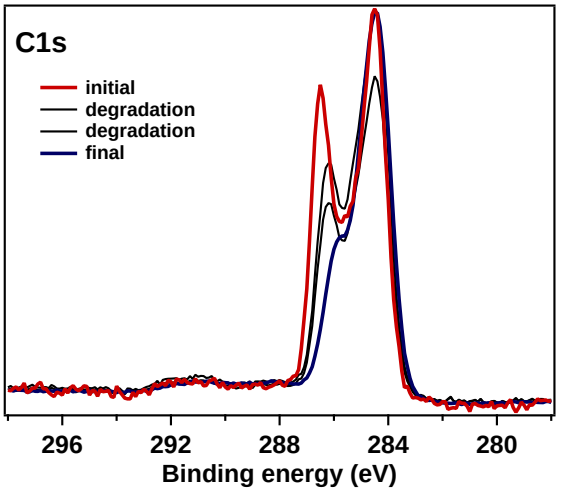

Figure A.2: High resolution photoemission spectra of C1s. Higher degree of degradation.

The effect of the temperature was also controlled by the spectrum of C1s. Until 120 °C the sample (**S1**) does not show any signal of degradation. However at 150 °C, the C1s spectrum (Figure A.3) was very similar to that obtained for the

sample degraded by the radiation.

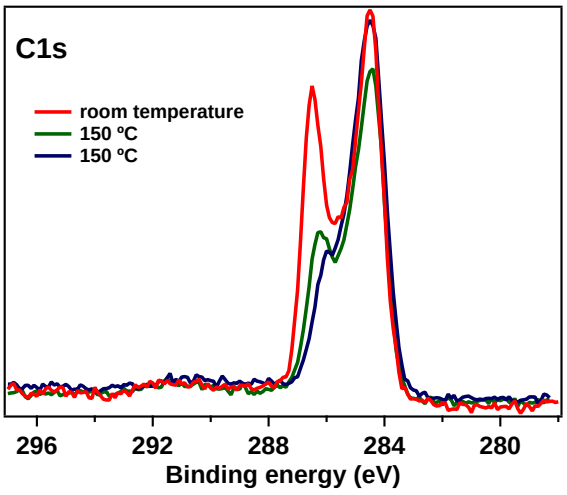

Figure A.3: High resolution photoemission spectra of C1s. Effect of the temperature.

Then to avoid the degradation of the organic molecules attached to the surface, each measurement reported in Chapter 4 was performed in a different spot of the sample.

B

Surface analysis techniques

B.1 Polarization-Modulation Infrared Reflection Adsorption Spectroscopy (PM-IRRAS)

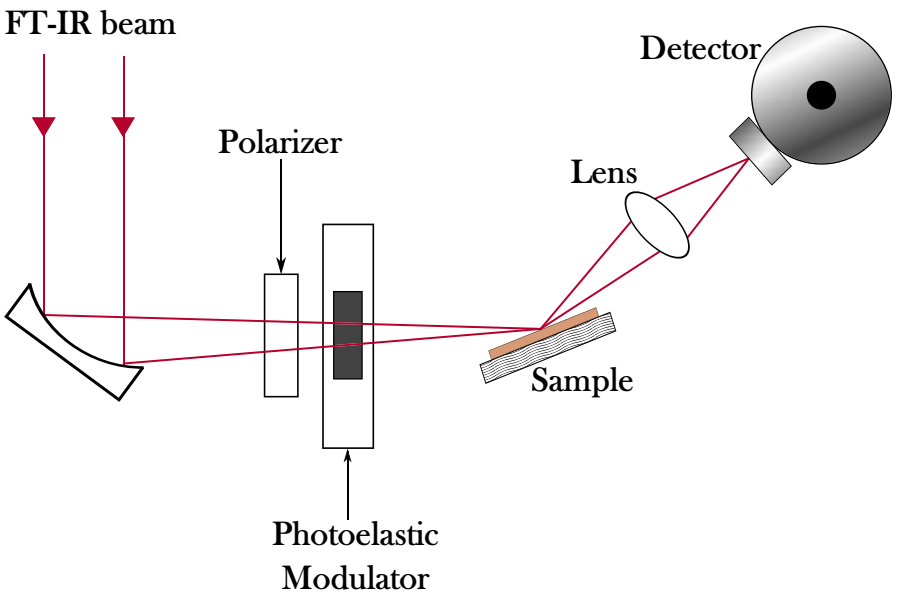

Figure B.1: Polarization-Modulation Infrared Reflection Adsorption Spectroscopy (PM-IRRAS) layout.

Polarization-Modulation Infrared Reflection Adsorption Spectroscopy (PM-IRRAS) is a very sensitive surface technique that allows the study of the molecular orientation and the chemical composition of thin films and monolayers. This technique is based on the selective absorption of s- and p-polarized light by molecules on a substrate when a high grazing incident angle is used. In a typical PM-IRRAS experiment two light modulations are applied simultaneously. One by the FT-IR interferometer and the other by the photoelastic modulator[1].

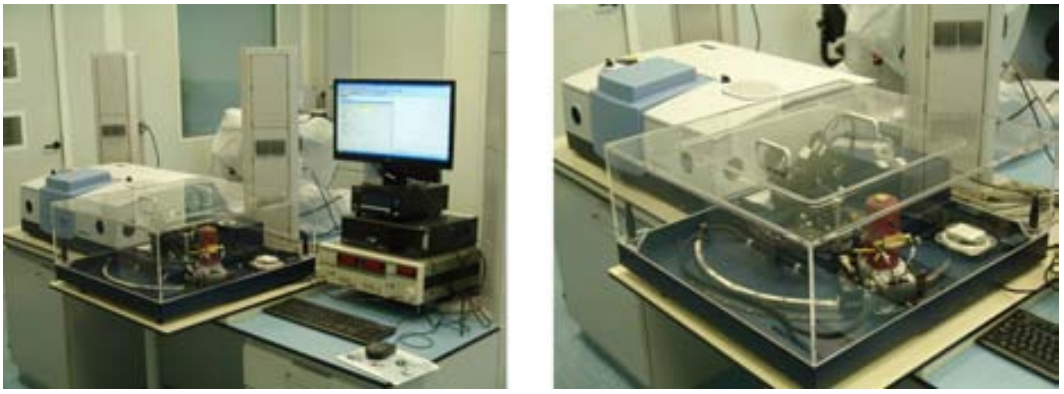

Figure B.2: PM-IRRAS equipment.

In a simple way, the process begins with the directional of a collimated infrared light onto an off-axis parabolic mirror with a long focal length. Then, the light beam passes through a polarizer and subsequently through a photo-elastic modulator (PEM) before to be focused onto the sample. Finally, the beam is collected with an infrared lens and focused onto the detector element[2]. Molecules grafted on metal surfaces only interact with the p-polarized infrared radiation which enhances its absorption allowing to increase the sensitivity of the measurement. However under this condition (high grazing angle of incidence) the absorption of s-polarized radiation is virtually zero. Then using selection rules at the surface is possible to infer about the average molecular orientation and conformation of molecules in SAMs[1]. Moreover the background absorption associated with the atmospheric environment do not mask the bands corresponding to the sample[2].

B.2 Contact Angle (CA)

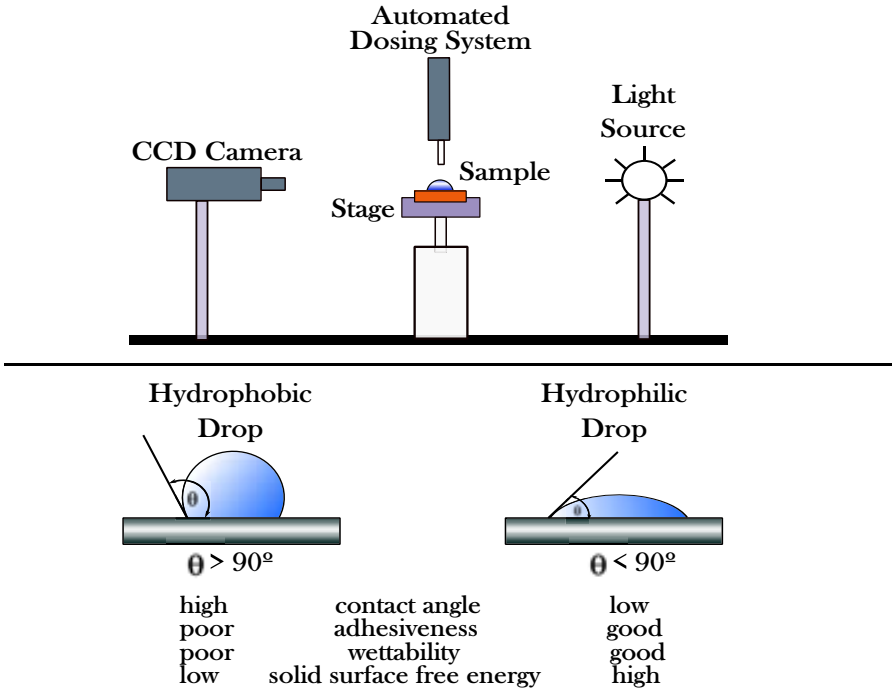

Figure B.3: Typical Contact Angle measurement setup.

The measurement of contact angles is fairly important for the majority of the wetting studies[3]. The contact angle (θ) is the angle formed between the tangent plane of the surface of a solid and a liquid at the wetting perimeter. The wetting perimeter is most commonly referred to as the wetting line at the three-phase zone (solid, liquid, gas). The most commonly used technique is the sessile drop method, using a contact angle goniometer, which uses an optical system to capture the profile of the liquid droplet on a solid substrate. A typical system uses a high-resolution camera and software to capture and analyse the contact angle[4]. The smaller the angle, the better the liquid is said to wet the solid, so for complete wetting is assumed a contact angle of zero degrees. Conversely, nonwettitg suggest a contact angle of 180 °. A value of $\theta > 90°$ implies poor wetting and low solid surface free energy, whereas $\theta < 90^o$ implies partial wetting and good adhesiveness[3].

B.3 Cyclic Voltammetry (CV)

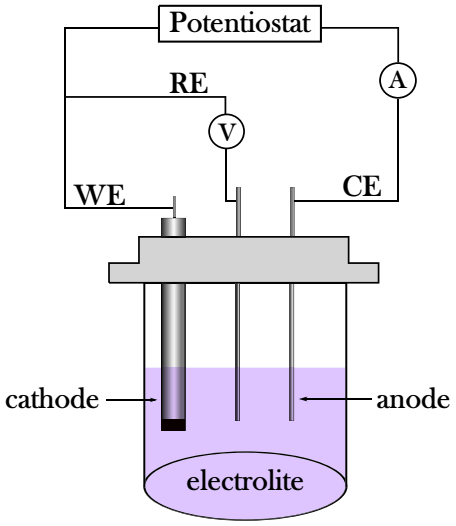

Figure B.4: Typical Cyclic Voltammetry measurement setup.

Cyclic voltammetry is an electrochemical technique that sweep a potential in a range while the current is measured of a redox event[5]. The voltage across the working and counter electrode (WE-CE) is controlled by the potentiostat which has to adjust such potential in order to maintain the potential difference between the working and reference electrodes (WE-RE) according to the desired potential at any time[6].

In CV experiments the WE potential has a triangular potential sweep configuration. Thus, it goes from a start potential value to a set final value and then it returns back to the initial potential maintaining a constant potential sweep rate which can range from few mV to hundred mV[6]. The voltammogram obtained determines the potentials at which different electrochemical processes occur and allows to shed light on the kinetics of electrochemical reactions taking place at electrode surfaces.

B.4 Atomic Force Microscopy (AFM)

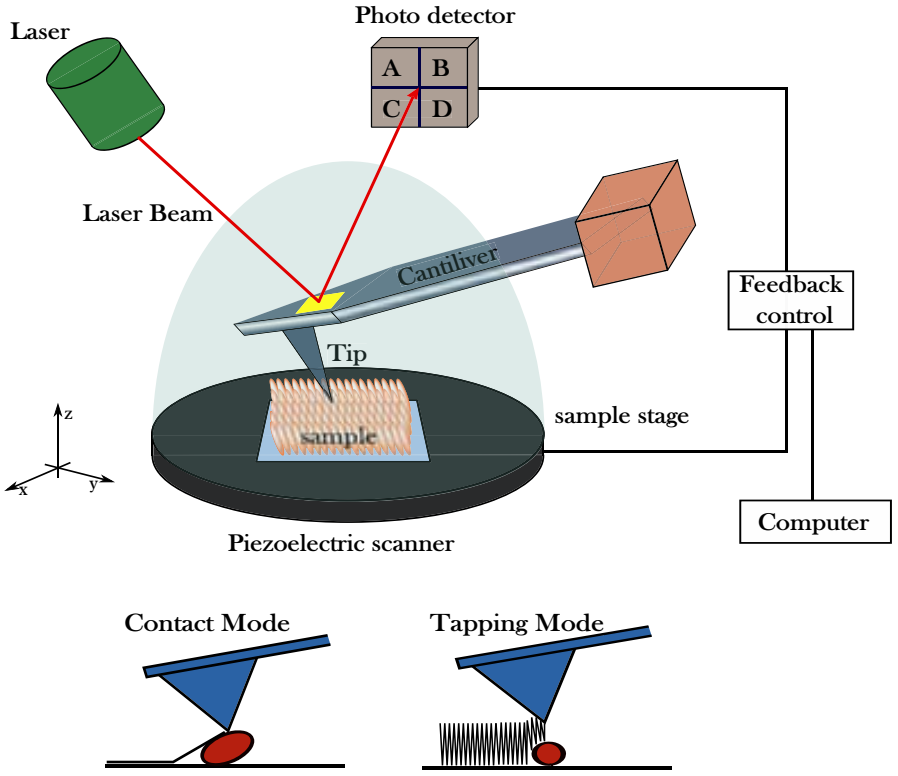

Figure B.5: Atomic Force Microscope setup.

Local electronic properties became accessible after the development of scanning probe microscopy (STM) by Binning *et al.* in 1981 at IBM Zurich. Based on quantum mechanical tunnelling between a conductive surface and an atomically sharp metallic tip, STM is well known to be the first instrument to generate real-space images of surfaces with atomic resolution and has triggered the development of new classes of STM-related microscopes[4], like the Atomic force microscopy (AFM) which nowadays is a basic technique and inevitable tool for all nanoscopic research, and is also known as scanning force microscopy (SFM). AFM, like all other scanning probe microscopes (SPM) works by scanning with a probe very close to the surface of the sample. It basically operates in two modes constant height or constant force by measuring attractive or repulsive forces between the tip and the sample, respectively[7]. Then the basic principle for all SPMs is that a sharp probe is scanned across a sample surface by means of piezoelectric transducers, while certain signals are recorded for every single point. Information is recorded

in the so-called near-field, so the resolution is no longer diffraction-limited. Topographical information – in principle, down to atomic resolution – can be obtained in real space. The working principle of an AFM is based on the deflection of a very sensitive cantilever due to repulsive forces. Such deflection is measured by using a laser beam when the sample is scanned. The x, y and z scanned positions performed by a piezoelectric translator. The computerised system controls xyz translations and records the reflected laser beam signal. Topographic pictures of the recorded data are constructed by dedicated software[4].

B.5 Kelvin Probe Force Microscopy (KFFM)

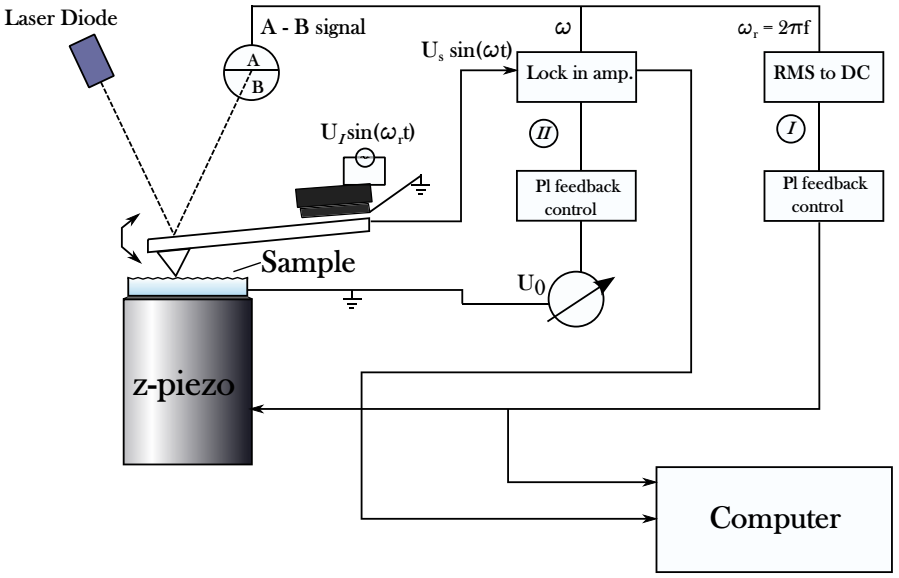

Figure B.6: Kelvin Probe Force Microscopy setup.

Kelvin Probe Force Microscopy (KFFM) was developed by Lord Kelvin in 1898 for the measurement of surface potentials[8]. This technique measures the contact potential difference (CPD) between a reference electrode and a sample.[9]. The sample corresponds to one plate of a parallel plate capacitor, with a known metal forming the other plate[8]. The CPD between these two materials is given by the difference of their work functions as shown Equation B.1.

$$V_{CPD} = -(\phi_1 - \phi_2)/e \tag{B.1}$$

Where ϕ_1 and ϕ_2 are the work functions of the conductors. Basically, in KPFM technique, a periodic vibration between the two plates at a frequency w gives an alternating current (ac) with the same frequency w when the two plates have different work functions. The technique depends on detecting the zero point of the ac while an additional bias voltage is applied between the two plates until the electric field between them disappears; thus the CPD can be measured by $V_{CPD} = -V_{bias}$[9].

B.6 X-ray Photoelectron Spectroscopy (XPS)

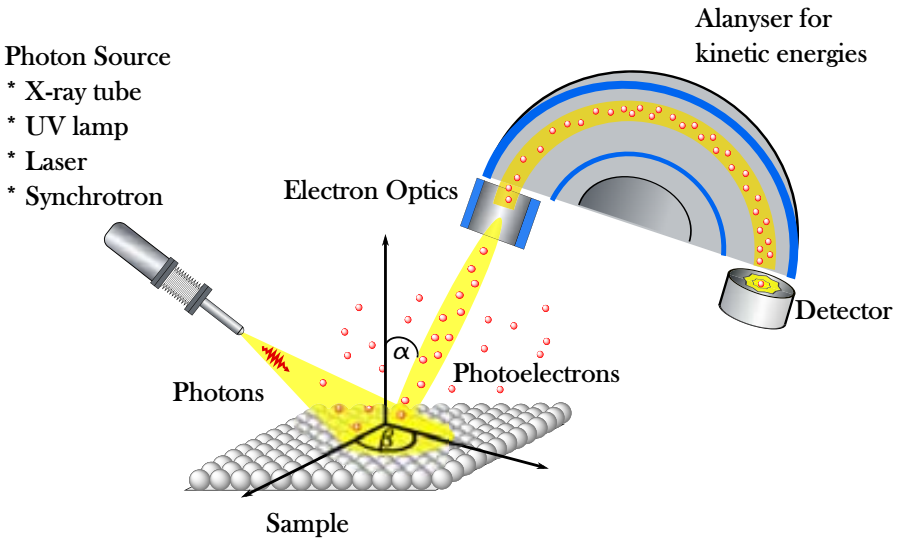

Figure B.7: X-ray Photoelectron Spectroscopy (XPS) schematic.

X-ray photoelectron spectroscopy (XPS) was developed as a surface analysis technique in the mid-60s by Siegbahn *et al.* at the University of Uppsala, to measure the elemental composition, chemical stoichiometry, chemical state, and electronic state of the elements that are present basically at the surface of a substrate. XPS spectra is obtaining by using very-high-energy "photon" to penetrate the material surface and "dig-out" the electrons that bond in the inner "core"-level orbital, the electrons generated in this manner are called x-ray photoelectrons. As the photoelectrons are recorded together with their kinetic energies (KE) and by analysing the later, the bonding energy of electrons is calculated; then the material from which the electrons escape is inferred. XPS is a very surface-sensitive technique, because photoelectrons free of inelastic collisions are only from the top 1 to 10 nm

of the material analysed, despite the fact that x-rays can penetrate much deeper into a material[4,10].

B.7 Time-of-Flight Secondary Ion Mass Spectrometry (ToF-SIMS)

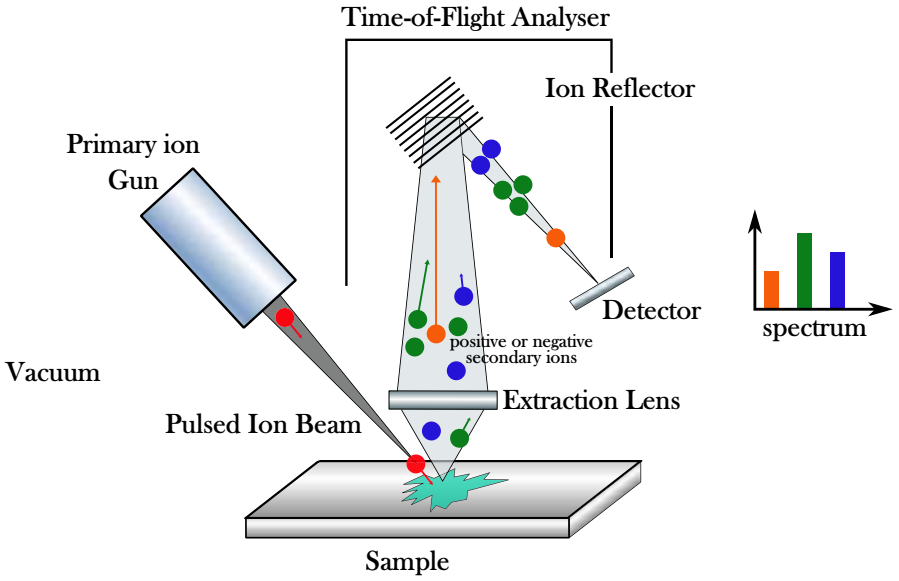

Figure B.8: Time-of-Flight Secondary Ion Mass Spectrometry (ToF-SIMS) schematic.

Time-of-Flight Secondary Ion Mass Spectroscopy (ToF-SIMS) is an analytical technique used to study the composition of solid surfaces and thin films, by focusing a pulsed beam of primary ions (typically Cs or Ga) on the surface to be analysed, producing secondary ions in a sputtering process. The particles obtained are accelerated into a time-of-flight tube and subsequently their mass is determined by measuring the time at which reach a detector. Then, ToF-SIMS is a qualitative technique which through analysing the secondary ions gives information about the molecular and elemental species present on the surface[11].

Bibliography

[1] M. S. Bradley, "A New Approach to Quantitative Spectral Conversion of PM-IRRAS : Theory , Experiments , and Performance Comparisons with Conven-

tional IRRAS," *Thermo Fisher Scientific*, vol. 2, no. 0, pp. 1–2, 2008.

[2] B. L. Frey, R. M. Corn, and S. C. Weibel, "Polarization-modulation. Approaches to Reflection-Absorption Spectroscopy.pdf," John Wiley & Sons, Inc., 2002.

[3] T. Tadros, "Contact Angle," in *Encyclopedia of Colloid and Interface Science SE - 55* (T. Tadros, ed.), p. 147, Springer Berlin Heidelberg, 2013.

[4] S. Zhang, L. Li, and A. Kumar, *Materials characterization techniques.* CRC Press, 2009.

[5] A. L. Eckermann, D. J. Feld, J. a. Shaw, and T. J. Meade, "Electrochemistry of redox-active self-assembled monolayers.," *Coordination chemistry reviews*, vol. 254, pp. 1769–1802, Aug. 2010.

[6] A. J. Bard, L. R. Faulkner, E. Swain, and C. Robey, *Electrochemical Methods. Fundamentals and Applications.* New York: John Wiley & Sons, Inc., second ed., 2001.

[7] G. Kaupp, "Atomic Force Microscopy," in *Atomic Force Microscopy, Scanning Near-field Optical Microscopy and Nanoscratching SE - 1*, pp. 1–86, Springer Berlin Heidelberg, 2006.

[8] S. Sadewasser and T. Glatzel, eds., *Kelvin Probe Force Microscopy. Measuring and compensating electrostatic forces.* New York: Springer.

[9] M. Fujihira, "Kelvin Probe Force Microscopy of Molecular Surfaces," *Annual Review of Materials Science*, vol. 29, pp. 353–380, Aug. 1999.

[10] M. Sardela, *Practical Materials Characterization.* Springer, 2014.

[11] J. Comelles, *Biochemical Gradients on Poly(methyl-methacrylate) surfaces.* PhD thesis, Universitat de Barcelona, 2010.

Index